



**Politecnico  
di Torino**

**ScuDo**

Scuola di Dottorato ~ Doctoral School

WHAT YOU ARE, TAKES YOU FAR

Doctoral Dissertation  
Doctoral Program in Mechanical Engineering (33<sup>th</sup> Cycle)

# Space Exploration Robotic Systems

Sample chain analysis and development  
for Enceladus surface acquisition

By

**Dario Riccobono**

\* \* \* \* \*

## **Supervisors:**

Prof. Nicola Amati, Politecnico di Torino

Prof. Giancarlo Genta, Politecnico di Torino

Dr. Scott J. Moreland, NASA Jet Propulsion Laboratory – Caltech

## **Doctoral Examination Committee:**

Prof. Nicola Amati, Politecnico di Torino

Prof. Giancarlo Genta, Politecnico di Torino

Prof. José Andrade, Referee, California Institute of Technology (Caltech)

Brett Kennedy, Referee, NASA Jet Propulsion Laboratory – Caltech

Prof. Renato Galluzzi-Aguilera, Tecnológico de Monterrey

Dr. Angelo Bonfitto, Politecnico di Torino

Prof. Sanjarbek Ruzimov, Turin Polytechnic University in Tashkent

Politecnico di Torino

2021

## **Declaration**

I hereby declare that, the contents and organization of this dissertation constitute my own original work and does not compromise in any way the rights of third parties, including those relating to the security of personal data.

Dario Riccobono  
2021

\* This dissertation is presented in partial fulfillment of the requirements for **Ph.D. degree** in the Graduate School of Politecnico di Torino (ScuDo).

# Summary

Saturn's moon Enceladus is among the most promising candidates in the Solar System to host life beyond Earth. Observations from the *Cassini* mission suggest that Enceladus contains a global ocean beneath its thick ice shell. Moreover, *Cassini* directly observed active cryovolcanism since material from the subsurface ocean is ejected through surface fractures in the South polar region. Enceladus' plume consists of vapor and particles that are deposited on the surface. The presence of complex organic materials, and the abundant geothermal energy from the interior and within the South polar terrain provide evidence for habitability and the prospect that life may have emerged and still be present on Enceladus.

A potential future lander mission to Enceladus is currently under investigation at NASA Jet Propulsion Laboratory (JPL). The research presented in this dissertation is part of a NASA JPL Strategic Research and Technology Development (RTD) effort to develop and mature a sample chain for Enceladus surface acquisition for in-situ measurements to Technology Readiness Level (TRL) 5. In this context, it is desirable to develop a sample chain to provide 1 cc to 5 cc volume samples to science instruments from the very shallow surface material in the top 1 cm, in order to acquire the freshest material deposited on surface from plume fallback.

Ph.D. research presented in this dissertation supported JPL's RTD activity by pursuing the following objectives.

- To define the high-level requirements on the sampling system to guarantee the stability of the lander while performing the sampling operation.
- To investigate and characterize sample collection and transfer operations in the Enceladus gravity, cryogenic, and vacuum environmental conditions.

- To provide sample chain design guidelines to fulfill sample acquisition requirements.

The definition of high-level requirements was driven by a novel analytical design tool conceived and developed for trade space exploration during early conceptual and preliminary design phases, where a rapid and broad evaluation is required for a very high number of configurations and boundary conditions. The tool rapidly determines the preliminary design envelope of a sampling apparatus to guarantee the stability condition of the lander. The tool also provides the capability to infer high-level requirements concerning other elements of the lander critical to its stability, such as the footpads.

The investigation and characterization of sample transport and collection is achieved by developing a model based on the Discrete Element Method (DEM). DEM is a numerical simulation technique for computing the motion and effect of a large number of particles. A set of analysis metrics is developed to characterize the granular material flow generated during the sampling operation. The analysis metrics are devised to be used for both numerical analysis and experimental testing, providing a framework for apples-to-apples comparison. Most sensitive model parameters are determined through a sensitivity analysis and then directly measured via independent tests performed by using custom designed apparatus.

The investigation and characterization of sample transfer is achieved by developing analytical tools to study the flow of particles dispersed into a gas with the aim to pneumatically transfer the sample to the scientific instrument. The exploration of design space is performed to determine the optimal design parameters to achieve a dilute phase transport of the sample.

Results of previously described investigations were adopted to drive the design of sample chain elements that were subsequently prototyped and subject to verification testing and maturation to TRL 4.

A test campaign is planned for DEM model validation and Dual-Rasp sampling system and sample collection verification to achieve TRL 5 via parabolic flights in 1%g Earth's gravity and vacuum conditions.

Finally, a two DOF RA was designed and developed with integrated sampling system, sample collection, and pneumatic sample transfer systems to a notional science instrument chamber with the aim to perform end-to-end sample chain verification in 1g Earth's gravity and Enceladus-like thermal vacuum environment to achieve TRL 5.



# Acknowledgment

I would like to acknowledge Prof. Giancarlo Genta, for the enthusiastic support, guidance, and mentoring during my entire academic career. I would like to thank Prof. Nicola Amati, for the patience and support.

I would like to acknowledge Dr. Scott Moreland and Dr. Paul Backes, for giving to me the extraordinary opportunity of daring mighty things and living one of the most amazing experiences of my life at JPL.

I also wish to express my appreciation to Dr. Cinzia Zuffada, for opening JPL's amazing universe to young explorers, including me.

I would like to thank JPL's folks Mircea Badescu, Alex Brinkman, Tyler Okamoto, Michael Hans, Joshua Krohn and Phillipe Tosi, for supporting the research activity.

This research was carried out at the Jet Propulsion Laboratory, California Institute of Technology, and was sponsored by the JPL Visiting Student Research Program and the National Aeronautics and Space Administration.

Finally, and most importantly, I would like to thank those closest to me. I will always be grateful to my family and friends for all the moral and loving support through both the good times and the hard times, and for their unshakable confidence in me.

A very special thank you goes to you, Jasmine. Thank you for giving me tireless encouragement and unconditional love, and for sharing with me some of the most precious moments of my life. Thank you for helping me to travel beyond my horizons, and for showing me what makes this only life truly worth living. Exploration is impossible without a home base, and you were my one.



*Per aspera ad astra*



# Contents

List of Tables .....	iv
List of Figures .....	viii
List of Symbols, Abbreviations and Acronyms .....	xx
1 Introduction .....	1
1.1 Robotic systems for planetary exploration: historical overview and future perspectives .....	1
1.2 Roadmap to ocean worlds .....	3
1.3 A potential lander mission to Enceladus: science and technology ....	4
1.4 Problem statement and dissertation objectives .....	9
1.5 Dissertation overview .....	10
2 Definition of sampling system requirements .....	11
2.1 MISTRAL: A design tool for robotic systems involved in sampling operations 12	
2.1.1 Structure of the tool .....	12
2.1.2 Analysis model .....	14
2.1.3 Application to NASA's Phoenix Mars lander mission .....	30
2.2 Application of MISTRAL to potential Enceladus lander mission ...	37
3 Investigation of sampling system concepts .....	44
3.1 Introduction .....	44
3.2 Simulants .....	47
3.3 IBARM manipulation testbed .....	50
3.4 Full-face drill .....	51
3.5 Drive tube .....	53
3.6 Ultrasonic scoop .....	57
3.7 Rasp .....	63
3.8 Dual-Rasp .....	65
4 Investigation of sample collection .....	67

---

4.1	Introduction.....	67
4.2	Approach.....	68
4.2.1	Continuum approach .....	68
4.2.2	Discrete approach.....	69
4.3	Dual-Rasp sampling system.....	78
4.3.1	Characterization of granular flow .....	78
4.3.1.1	Numerical DEM model .....	79
4.3.1.2	Analysis metrics .....	88
4.3.1.3	Sensitivity analysis of DEM model parameters .....	93
4.3.1.4	Sensitivity analysis of sampling system parameters .....	109
4.3.1.5	Measurement of DEM model parameters.....	118
4.3.2	DEM-driven design and verification of sample collection system 131	
4.3.3	Future work .....	157
4.4	Ultrasonic scoop sampling system.....	161
4.4.1	Analysis method.....	162
4.4.2	Case studies .....	167
5	Investigation of sample transfer and deposit .....	174
5.1	Introduction.....	174
5.2	Approach.....	175
5.2.1	Empirical approach .....	176
5.2.2	Theoretical approach .....	179
5.3	Integrated sample chain testbed .....	182
5.4	Sample transfer system applied to Full-face drill sampling system 184	
5.5	Sample transfer system applied to Rasp sampling system .....	191
5.6	Sample transfer system applied to Dual-Rasp sampling system ...	196
5.7	Sample measurement .....	209
5.8	Ocean Worlds Life Surveyor Project.....	213
	Conclusions.....	214
	References.....	216







# List of Tables

<b>Table 2.1</b> Overview of the main robotic lander configurations adopted in space exploration. ....	15
<b>Table 2.2</b> Force peaks registered during Phoenix Mars lander operations. The name highlights the denomination of the excavation site followed by a number indicating the reference sol (Mars day). ....	31
<b>Table 2.3</b> Values of MISTRAL parameters for the Phoenix lander case study. ....	33
<b>Table 2.4</b> Data point values converted according to the input required to build the DE. ....	35
<b>Table 2.5</b> Values of MISTRAL parameters for the Enceladus lander case study. ....	39
<b>Table 4.1</b> DEM model input parameters sorted by contact mechanics model. ....	87
<b>Table 4.2</b> DEM model input parameters sorted by category. ....	87
<b>Table 4.3</b> Values of environmental parameter and Dual-Rasp cutting heads parameters for the sensitivity analysis of DEM model parameters. These values are common to all simulations. ....	96
<b>Table 4.4</b> DEM computation parameters. ....	97
<b>Table 4.5</b> Values of particle parameters and paired parameters for the sensitivity analysis of DEM model parameters. Baseline values are highlighted in red. ....	98
<b>Table 4.6</b> DEM simulation matrix for the sensitivity analysis of DEM model parameters. All baseline simulations (highlighted in red) are included for completeness. ....	100
<b>Table 4.7</b> Values of variable parameters for the sensitivity analysis of DEM model parameters. Baseline values are highlighted in red. ....	100
<b>Table 4.8</b> Sensitivity analysis of DEM model parameters. Delta-values for velocity magnitude analysis metric. ....	105
<b>Table 4.9</b> Sensitivity analysis of DEM model parameters. Delta-values for elevation dispersion angle analysis metric. ....	105
<b>Table 4.10</b> Sensitivity analysis of DEM model parameters. Delta-values for azimuth dispersion angle analysis metric. ....	106
<b>Table 4.11</b> Values of parameter np within the definition of FOM3. ....	107

<b>Table 4.12</b> Sensitivity analysis of DEM model parameters. Results about velocity magnitude metrics.....	107
<b>Table 4.13</b> Sensitivity analysis of DEM model parameters. Results about elevation dispersion angle metrics.....	108
<b>Table 4.14</b> Sensitivity analysis of DEM model parameters. Results about azimuth dispersion angle metrics.....	108
<b>Table 4.15</b> Global results of the sensitivity analysis of DEM model parameters.....	109
<b>Table 4.16</b> Values of DEM parameters and environmental parameter for the sensitivity analysis of sampling system parameters. These values are common to all simulations.....	110
<b>Table 4.17</b> Values of the parameters of Dual-Rasp cutting heads for the sensitivity analysis of sampling system parameters. Baseline values are highlighted in red.....	111
<b>Table 4.18</b> DEM simulation matrix for the sensitivity analysis of sampling system parameters. All baseline simulations (highlighted in red) are included for completeness.....	112
<b>Table 4.19</b> Values of variable parameters for the sensitivity analysis of sampling system parameters. Baseline values are highlighted in red.....	113
<b>Table 4.20</b> Sensitivity analysis of sampling system parameters. Delta-values across trend lines for velocity magnitude analysis metric.....	114
<b>Table 4.21</b> Sensitivity analysis of sampling system parameters. Delta-values across trend lines for elevation dispersion angle analysis metric.....	115
<b>Table 4.22</b> Sensitivity analysis of sampling system parameters. Delta-values across trend lines for azimuth dispersion angle analysis metric.....	115
<b>Table 4.23</b> Sensitivity analysis of sampling system parameters. Results about velocity magnitude metrics.....	116
<b>Table 4.24</b> Sensitivity analysis of sampling system parameters. Results about elevation dispersion angle metrics.....	116
<b>Table 4.25</b> Sensitivity analysis of sampling system parameters. Results about azimuth dispersion angle metrics.....	117
<b>Table 4.26</b> Global results of the sensitivity analysis of sampling system parameters.....	117
<b>Table 4.27</b> Materials considered for DEM model validation.....	118
<b>Table 4.28</b> Properties of YSZ and alumina particles.....	120
<b>Table 4.29</b> Values of COR between YSZ / alumina particles and Al 6061-T6.....	131

---

<b>Table 4.30</b> Parameters of the Dual-Rasp cutting heads and environmental parameter for the DEM-MBD co-simulation of sample collection system. ....	139
<b>Table 4.31</b> Particle parameters for the DEM-MBD co-simulation of sample collection system.....	140
<b>Table 4.32</b> Paired parameters for the DEM-MBD co-simulation of sample collection system.....	140
<b>Table 4.33</b> Parameters of sample transport guide for the DEM-MBD co-simulation of sample collection system. ....	141
<b>Table 4.34</b> Parameters of the collection cup for the DEM-MBD co-simulation of sample collection system. ....	141
<b>Table 4.35</b> Ambient analogue materials adopted for sample collection system verification campaign. ....	156
<b>Table 4.36</b> Results of sample collection system verification campaign.....	156
<b>Table 4.37</b> Computation parameters for DEM-MBD co-simulation of ultrasonic scoop sample chain steps. ....	164
<b>Table 4.38</b> Parameters of the ultrasonic scoop and environmental parameter for DEM-MBD co-simulation of ultrasonic scoop sample chain steps.....	164
<b>Table 4.39</b> Particle parameters for DEM-MBD co-simulation of ultrasonic scoop sample chain steps. ....	165
<b>Table 4.40</b> Paired parameters for DEM-MBD co-simulation of ultrasonic scoop sample chain steps. ....	165
<b>Table 4.41</b> Values of acceleration disturbances measured at scoop’s location using IBARM while performing sample chain steps.....	167
<b>Table 5.1</b> Results of the analysis of TRL 3 pneumatic sample transfer system applied to the Full-face drill sampling system.....	189
<b>Table 5.2</b> Results of the analysis of TRL 3 pneumatic sample transfer system applied to the Rasp sampling system.....	194
<b>Table 5.3</b> Results of the analysis of TRL 4 pneumatic sample transfer system applied to the Dual-Rasp sampling system.....	199
<b>Table 5.4</b> Main features of TRL 5 pneumatic sample transfer system.....	209
<b>Table 5.5</b> Methods for indirect measurement of volumetric concentration of solids in pneumatic conveying pipelines [246].....	210
<b>Table 5.6</b> Methods for indirect measurement of solids’ velocity in pneumatic conveying pipelines [246].....	210
<b>Table 5.7</b> Trade space study on sample measurement technologies. ....	211



# List of Figures

<b>Figure 1.1</b> Evolution with time of the cone penetration resistance of ice plume deposit analogs at several temperatures [39].	6
<b>Figure 1.2</b> Predicted cone penetration resistance of icy plume deposits as a function of temperature and sintering time. Black contours are for the best-fit activation energy value. Dashed and dotted contours illustrate the effect of the uncertainty on activation energy. For legibility, these contours are only shown for the 10-5 (white) and 100 MPa (red) cone penetration resistance levels. Modified after [39].	7
<b>Figure 1.3</b> NASA definition of Technology Readiness Levels [52].	8
<b>Figure 2.1</b> Block diagram of MISTRAL.	13
<b>Figure 2.2</b> Free body diagram (XY plane view) for the 3-legged lander. Qualitative scheme, not to scale.	17
<b>Figure 2.3</b> Main geometric parameters (XY plane view) for the 3-legged lander. Qualitative scheme, not to scale.	18
<b>Figure 2.4</b> Free body diagram and main geometric parameters (XZ plane view) for the 3-legged lander. Qualitative scheme, not to scale.	18
<b>Figure 2.5</b> Free body diagram and main geometric parameters (YZ plane view) for the 3-legged lander. Qualitative scheme, not to scale.	19
<b>Figure 2.6</b> Free body diagram (XY plane view) for the 4-legged lander. Qualitative scheme, not to scale.	19
<b>Figure 2.7</b> Main geometric parameters (XY plane view) for the 4-legged lander. Qualitative scheme, not to scale.	20
<b>Figure 2.8</b> Free body diagram and main geometric parameters (XZ plane view) for the 4-legged lander. Qualitative scheme, not to scale.	20
<b>Figure 2.9</b> Free body diagram and main geometric parameters (YZ plane view) for the 4-legged lander. Qualitative scheme, not to scale.	21
<b>Figure 2.10</b> Vectors joining the lander's footpads for the 3-legged lander. Qualitative scheme, not to scale.	23
<b>Figure 2.11</b> Vectors joining the lander's footpads for the 4-legged lander. Qualitative scheme, not to scale.	24
<b>Figure 2.12</b> Example of convex objective functions.	27
<b>Figure 2.13</b> Some sampling system configurations that might be explored in MISTRAL by changing the $\beta$ angle.	29

---

<b>Figure 2.14</b> Engineering model of the Phoenix lander RA and ISAD. Credits: NASA/University of Arizona .....	30
<b>Figure 2.15</b> Phoenix lander worst-case scenario. The lander is inclined about the Y axis and pulled downhill during backhoe operations. Qualitative scheme, not to scale. ....	32
<b>Figure 2.16</b> Phoenix lander configuration. The sampling spot lies inside the area delimited by the green lines. Qualitative scheme, not to scale. ....	33
<b>Figure 2.17</b> Plot of the DE of Phoenix lander together with the data points..	36
<b>Figure 2.18</b> Enceladus lander worst-case scenario. The lander is inclined about the Y axis and pushed downhill during sampling operation. Qualitative scheme, not to scale. ....	37
<b>Figure 2.19</b> 3-legged lander configuration for the Enceladus lander case study. Qualitative scheme, not to scale.....	38
<b>Figure 2.20</b> 4-legged lander configuration for the Enceladus lander case study. Qualitative scheme, not to scale.....	38
<b>Figure 2.21</b> DE of 3-legged lander for the Enceladus lander case study. The ground slope is reported in absolute values for convenience. ....	40
<b>Figure 2.22</b> DE of 4-legged lander for the Enceladus lander case study. The ground slope is reported in absolute values for convenience. ....	41
<b>Figure 2.23</b> Use of the DE for system design. Example for the 3-legged lander configuration.....	43
<b>Figure 3.1</b> Steps of a typical sample chain.....	44
<b>Figure 3.2</b> The Icy Bodies Simulation (IBoS) chamber designed and fabricated at JPL to produced and evolve Enceladus surface icy analogues.....	48
<b>Figure 3.3</b> Enceladus simulants. Fine-grained pervious concrete (Top). Very fine-grained pervious concrete (Middle). Sintered cryogenic ice (Bottom).....	49
<b>Figure 3.4</b> IBARM manipulation testbed.....	50
<b>Figure 3.5</b> Front face drill bit with linear teeth array design (Top) and 3D printed metal test bits (Bottom).....	52
<b>Figure 3.6</b> Test of the full-face drill bit with linear teeth arrays.....	52
<b>Figure 3.7</b> Full-face drill bit with curved teeth array (Left) and fabricated prototype integrated into the testbed (Right).....	53
<b>Figure 3.8</b> Drive tube sample collection and transfer system main components.....	54
<b>Figure 3.9</b> Drive tube sample collection and transfer system main components integrated into a housing.....	55

<b>Figure 3.10</b> Drive tube in sampling configuration (Left) and after sample acquisition and separation (Right). .....	56
<b>Figure 3.11</b> Implemented drive tube components (Left), assembled (Middle), and sample tube with collected sample (Right). .....	57
<b>Figure 3.12</b> Piezoelectric-driven ultrasonic sampling system. ....	58
<b>Figure 3.13</b> Sampling system in chopping configuration. ....	60
<b>Figure 3.14</b> Sampling tool in sampling configuration. ....	61
<b>Figure 3.15</b> Sampling system at the end of sample acquisition. ....	61
<b>Figure 3.16</b> Sampling system in the sample transfer configuration (Left) and scoop being scraped against the sample transfer chamber (Right). ....	62
<b>Figure 3.17</b> Prototype of the ultrasonic sampling system provided with two different types of scoop. Curved (Top) and straight (Bottom). The curved scoop helped the mitigation of some drawbacks of the straight version, namely the higher reactive loads and the higher difficulty to handle the sample during sample chain steps. ....	62
<b>Figure 3.18</b> Rasp sampling system. ....	64
<b>Figure 3.19</b> Prototype of the Rasp sampling system. Close-up rotary cutting bit is shown. ....	64
<b>Figure 3.20</b> The Dual-Rasp sampling system combines the capability to sample a wide range of surface material strengths with the advantage to require low average preload. ....	65
<b>Figure 3.21</b> The Dual-Rasp involved in sampling operations. ....	66
<b>Figure 3.22</b> Dual-Rasp cutters. The two counter-rotating, rasp-type cutting heads remove the pristine material and throw it up between them via momentum transfer. ....	66
<b>Figure 4.1</b> DEM calculation cycle. ....	70
<b>Figure 4.2</b> Soft contact of spherical particles in discrete simulations. ....	71
<b>Figure 4.3</b> Example of forces and moments acting on a particle during contact. ....	72
<b>Figure 4.4</b> Example of contact detection methodology. ....	74
<b>Figure 4.5</b> Particle's shape determination through roundness and sphericity chart [154]. ....	75
<b>Figure 4.6</b> Example of polyhedral shapes: a) 7 vertexes, 10 faces; b) 9 vertexes, 14 faces; c) 11 vertexes, 18 faces; d) 100 vertexes, 196 faces [155]. ....	75
<b>Figure 4.7</b> Example of super-quadratic particles [156]. ....	76
<b>Figure 4.8</b> Example of real particle scans modeled by using multi-sphere clumps [149]. ....	76

---

<b>Figure 4.9</b> Side view of granular material flow generated by the action of the Dual-Rasp sampling system while performing sampling operations. ....	79
<b>Figure 4.10</b> Graphic representation of contact mechanics models [171]. ....	86
<b>Figure 4.11</b> Velocity magnitude analysis metric. Top: side view of DEM-simulated granular material flow generated by the Dual-Rasp cutting heads with indication of velocity vectors. Bottom: plot of velocity magnitude distribution, including indication of the percentile of particles in a certain range of velocity magnitude values. ....	90
<b>Figure 4.12</b> Elevation dispersion angle analysis metric. Top: side view of DEM-simulated granular material flow generated by the Dual-Rasp cutting heads with indication of elevation dispersion angle. Bottom: plot of elevation dispersion angle distribution, including indication of the percentile of particles in a certain range of elevation dispersion angle values. ....	91
<b>Figure 4.13</b> Azimuth dispersion angle analysis metric. Top: top view of DEM-simulated granular material flow generated by the Dual-Rasp cutting heads with indication of azimuth dispersion angle. Bottom: plot of azimuth dispersion angle distribution, including indication of the percentile of particles in a certain range of azimuth dispersion angle values. ....	92
<b>Figure 4.14</b> Post-processing methodology of DEM simulation data. ....	93
<b>Figure 4.15</b> Front view of counter-rotating Dual-Rasp cutting heads (Top left). Side view (Top right) and surface mesh (Bottom) of a single cutting head. ....	97
<b>Figure 4.16</b> Lonestar5 cabinets [185]. ....	101
<b>Figure 4.17</b> Lonestar5 system architecture [185]. ....	102
<b>Figure 4.18</b> Inclined plane testbed (a). Detail of the bottom face of the particle plate with three particles glued to it (b). YSZ particles shown as a reference (c). ....	122
<b>Figure 4.19</b> Inclined plane testbed shown in inclined position. ....	122
<b>Figure 4.20</b> Particle plate. ....	123
<b>Figure 4.21</b> Standard deviation as function of sample size for measurement of particle-tool coefficient of static friction of YSZ particles. ....	123
<b>Figure 4.22</b> Standard deviation as function of sample size for measurement of particle-tool coefficient of static friction of alumina particles. ....	124
<b>Figure 4.23</b> Particle drop testbed. ....	125
<b>Figure 4.24</b> Particle drop test setup including the ultra-high speed camera. ....	125
<b>Figure 4.25</b> Representative frames of particle drop test sequence, as recorded by the ultra-high speed camera. 1) and 2) show the particle falling toward the tool	

plate. 3) shows the contact between particle and tool plate. 4) shows particle bounce.....	126
<b>Figure 4.26</b> Example of a typical drop test data plot. Particle's vertical velocity vs. time is shown, indicating downward motion, upward motion, and particle-plate contact.....	126
<b>Figure 4.27</b> Standard deviation as function of sample size for measurement of particle-tool coefficient of restitution considering YSZ particles dropped from 150 mm. ....	128
<b>Figure 4.28</b> Standard deviation as function of sample size for measurement of particle-tool coefficient of restitution considering YSZ particles dropped from 300 mm. ....	128
<b>Figure 4.29</b> Standard deviation as function of sample size for measurement of particle-tool coefficient of restitution considering YSZ particles dropped from 450 mm. ....	129
<b>Figure 4.30</b> Standard deviation as function of sample size for measurement of particle-tool coefficient of restitution considering alumina particles dropped from 150 mm. ....	129
<b>Figure 4.31</b> Standard deviation as function of sample size for measurement of particle-tool coefficient of restitution considering alumina particles dropped from 300 mm. ....	130
<b>Figure 4.32</b> Standard deviation as function of sample size for measurement of particle-tool coefficient of restitution considering alumina particles dropped from 450 mm. ....	130
<b>Figure 4.33</b> DEM-MBD co-simulation of first design iteration of sample collection system implementing direct collection into a volume. Particles trajectories are shown in red. Please note that the collection volume is cross sectioned to show the inside. Side view shown. ....	133
<b>Figure 4.34</b> DEM-MBD co-simulation of second design iteration of sample collection system implementing the guide concept to deflect particles toward the collection cup. Please note that both the guide and the collection cup are cross sectioned to show the inside. Side view shown. ....	133
<b>Figure 4.35</b> Examples of geometries with reflection and focusing properties. From top to bottom: parabola, ellipse, and rotunda. ....	135
<b>Figure 4.36</b> Guide design based on the ellipsoid geometry. View of the elevation plane showing the focusing effect on particles' trajectories. ....	136

<b>Figure 4.37</b> Guide design based on the ellipsoid geometry. View of the azimuth plane showing the focusing effect on particles' trajectories. The transparent orange element represents the collection cup. ....	136
<b>Figure 4.38</b> 3D representation of the sample collection system model, including the ellipsoidal guide (black), the collection cup (orange) and the Dual-Rasp cutting heads (light blue). ....	137
<b>Figure 4.39</b> Dual-Rasp granular flow characterization in 1g Earth's environment. Results show the dispersion of the analysis metrics including 25 <sup>th</sup> percentile (green), 50 <sup>th</sup> percentile (yellow), and 75 <sup>th</sup> percentile (red). ....	142
<b>Figure 4.40</b> Sample collection system design for 1g Earth's environment driven by DEM-MBD co-simulation results. Granular flow dispersion in the elevation plane is shown, including 25 <sup>th</sup> percentile (green area), 50 <sup>th</sup> percentile (yellow area), and 75 <sup>th</sup> percentile (red area). ....	143
<b>Figure 4.41</b> Sample collection system design for 1g Earth's environment driven by DEM-MBD co-simulation results. Granular flow dispersion in the azimuth plane is shown, including 25 <sup>th</sup> percentile (green area), 50 <sup>th</sup> percentile (yellow area), and 75 <sup>th</sup> percentile (red area). ....	143
<b>Figure 4.42</b> DEM-MBD co-simulation of sample collection system in 1g Earth's environment. ....	144
<b>Figure 4.43</b> Dual-Rasp granular flow characterization in 1%g Enceladus' environment. Results show the dispersion of the analysis metrics including 25 <sup>th</sup> percentile (green), 50 <sup>th</sup> percentile (yellow), and 75 <sup>th</sup> percentile (red). ....	146
<b>Figure 4.44</b> Sample collection system design for 1%g Enceladus' environment driven by DEM-MBD co-simulation results. Granular flow dispersion in the elevation plane is shown, including 25 <sup>th</sup> percentile (green area), 50 <sup>th</sup> percentile (yellow area), and 75 <sup>th</sup> percentile (red area). ....	147
<b>Figure 4.45</b> Sample collection system design for 1%g Enceladus' environment driven by DEM-MBD co-simulation results. Granular flow dispersion in the azimuth plane is shown, including 25 <sup>th</sup> percentile (green area), 50 <sup>th</sup> percentile (yellow area), and 75 <sup>th</sup> percentile (red area). ....	147
<b>Figure 4.46</b> DEM-MBD co-simulation of the sample collection system in 1%g Enceladus' environment. ....	148
<b>Figure 4.47</b> Concept #1 of collection cup design provided with labyrinth-style sample retention features. General architecture. ....	149
<b>Figure 4.48</b> Concept #1 of collection cup design provided with labyrinth-style sample retention features. Potential particles' trajectories. Qualitative scheme..	150

---

<b>Figure 4.49</b> Concept #1 of collection cup design provided with labyrinth-style sample retention features. DEM-MBD co-simulation. ....	150
<b>Figure 4.50</b> Concept #2 of collection cup design provided with labyrinth-style sample retention features. Potential particles' trajectories. Qualitative scheme..	151
<b>Figure 4.51</b> Concept #3 of collection cup design provided with labyrinth-style sample retention features. Potential particles' trajectories. Qualitative scheme..	151
<b>Figure 4.52</b> Concept #2 of collection cup design provided with labyrinth-style sample retention features. DEM-MBD co-simulation. ....	152
<b>Figure 4.53</b> Concept #3 of collection cup design provided with labyrinth-style sample retention features. DEM-MBD co-simulation. ....	152
<b>Figure 4.54</b> Concept #4 of collection cup design provided with grid-style sample retention features. Side view of the integrated design (left). Top view of the collection cup (right).....	153
<b>Figure 4.55</b> Concept #4 of collection cup design provided with grid-style sample retention features. DEM-MBD co-simulation. ....	153
<b>Figure 4.56</b> Integrated CAD model of the sample collection system composed of the Dual-Rasp sampling system, the ellipsoid-shaped guide, and the collection cup provided with grid-style sample retention features.....	155
<b>Figure 4.57</b> Integrated prototype of the Dual-Rasp sampling system and the sample collection system composed of the ellipsoid-shaped guide and the collection cup. This prototype also integrates the pneumatic sample transfer system into the collection cup design (further details provided in paragraph 5.6). .....	155
<b>Figure 4.58</b> Typical parabolic flight sequence [218]. ....	158
<b>Figure 4.59</b> Vacuum chamber testbed including Dual-Rasp sampling system, sample collection system and surface analogue. ....	159
<b>Figure 4.60</b> Particle tracking software used for post-processing of high-speed recordings of the granular flow generated by a single Dual-Rasp cutting head. Particles are identified by green cross symbols, while particles' trajectories are identified by red lines. ....	159
<b>Figure 4.61</b> Sample transport of approximately 10 $\mu\text{m}$ particles in 1 atm conditions.....	160
<b>Figure 4.62</b> Sample transport of approximately 10 $\mu\text{m}$ particles in 0.05 atm conditions.....	160
<b>Figure 4.63</b> CAD model of vacuum chamber testbed for parabolic flight. Testbed includes the Dual-Rasp sampling system, the sample collection system,	

and the surface analogues. Vacuum chamber surrounding the assembly not shown for convenience.....	161
<b>Figure 4.64</b> CAD model of curved scoop.....	162
<b>Figure 4.65</b> Basic scoop motion steps. Scooping (1-2), ascend from surface (2-3), move to lander (3-4), and deposit into science instruments (5).....	163
<b>Figure 4.66</b> Plots of acceleration disturbances measured at scoop's location using IBARM while performing sample chain steps.....	166
<b>Figure 4.67</b> Case study 1, 1g Earth's gravity and full RA's stiffness. Position disturbance functions shown at each sample chain step: scooping (SCP), ascend from surface (ASC), move to lander (MTL), and deposit (DPS). ....	168
<b>Figure 4.68</b> Case study 1, 1g Earth's gravity and full RA's stiffness. DEM-MBD simulation of sample chain steps performed by the ultrasonic scoop is shown, including sampling (A), ascend from surface (B), move to lander (C), and deposit (D). ....	169
<b>Figure 4.69</b> Case study 2, 10%g Earth's gravity and 10% full RA's stiffness. Position disturbance functions shown at each sample chain step: scooping (SCP), ascend from surface (ASC), move to lander (MTL), and deposit (DPS). ....	170
<b>Figure 4.70</b> Case study 2, 10%g Earth's gravity and 10% full RA's stiffness. DEM-MBD simulation of sample chain steps performed by the ultrasonic scoop is shown, including sampling (A), ascend from surface (B), move to lander (C), and deposit (D). ....	171
<b>Figure 4.71</b> Case study 3, 1%g Earth's gravity (i.e. Enceladus conditions) and 1% full RA's stiffness. Position disturbance functions shown at each sample chain step: scooping (SCP), ascend from surface (ASC), move to lander (MTL), and deposit (DPS).....	172
<b>Figure 4.72</b> Case study 3, 1%g Earth's gravity (i.e. Enceladus conditions) and 1% full RA's stiffness. DEM-MBD simulation of sample chain steps performed by the ultrasonic scoop is shown, including sampling (A), ascend from surface (B), move to lander (C), and deposit (D).....	173
<b>Figure 5.1</b> Phase diagram for dilute phase vertical pneumatic transport [234].	178
<b>Figure 5.2</b> Phase diagram for dilute phase horizontal pneumatic transport [234].....	179
<b>Figure 5.3</b> Example of state diagram representing flow regimes in disperse systems and defined through the use of non-dimensional parameters.....	181

- 
- Figure 5.4** Example of state diagram for liquid-solid and for non-pressurized gas-solid systems. The heavy solid lines represent gas-solid systems, while the heavy dotted lines represent liquid-solid systems [241]. ..... 182
- Figure 5.5** Qualitative scheme of the pneumatic sample transfer system for both the Full-face and Rasp sampling systems. The sampling systems dock with the pneumatic sample transfer system in two points to close the pneumatic circuit. .... 183
- Figure 5.6** Qualitative scheme of the pneumatic sample transfer system for the Dual-Rasp sampling system. The sampling system docks with the pneumatic sample transfer system only in one point to close the pneumatic circuit. .... 183
- Figure 5.7** Full-face drill sampling system with integrated pneumatic sample transfer features..... 184
- Figure 5.8** Integrated sample chain architecture for Full-face drill sampling system. Sampling position shown. Qualitative scheme, not to scale..... 185
- Figure 5.9** Integrated sample chain architecture for Full-face drill sampling system. Sample transfer position shown. Qualitative scheme, not to scale..... 186
- Figure 5.10** Pneumatic sample transfer system within the integrated sample chain testbed. Configuration for Full-face drill and Rasp sampling systems shown. Robotic arm (IBARM) and sampling systems not shown. .... 186
- Figure 5.11** Cross-section of pneumatic sample transfer system applied to the Full-face drill sampling system. Bold blue arrows represent the flow of gas, while bold orange arrows represent the flow of gas/solids mixture. .... 187
- Figure 5.12** Block diagram of the software tool developed for pneumatic sample transfer system analysis and design..... 188
- Figure 5.13** Nitrogen phase diagram [242]. ..... 189
- Figure 5.14** End-to-end sample chain operations for the Full-face drill sampling system. Top picture shows Full-face drill in sampling position. Middle picture shows the Full-face drill in an intermediate position prior to completion of docking operation. Bottom picture shows the Full-face drill docked to sealed interfaces and in sample transfer position..... 190
- Figure 5.15** Rasp sampling system with integrated pneumatic sample transfer features..... 191
- Figure 5.16** Integrated sample chain architecture for Rasp sampling system. Sampling position shown. Qualitative scheme, not to scale..... 192
- Figure 5.17** Integrated sample chain architecture for Rasp sampling system. Sample transfer position shown. Qualitative scheme, not to scale. .... 193

- Figure 5.18** Cross-section of pneumatic sample transfer system applied to the Rasp sampling system. Bold blue arrows represent the flow of gas, while bold orange arrows represent the flow of gas/solids mixture. .... 193
- Figure 5.19** End-to-end sample chain operations for the Rasp sampling system. Top picture shows the Rasp in sampling position. Middle picture shows the Rasp in an intermediate position prior to completion of docking operations. Bottom picture shows the Rasp docked to sealed interfaces and in sample transfer position..... 195
- Figure 5.20** Dual-Rasp sampling system with integrated pneumatic sample transfer features. Collection chamber’s door shown in partially open position. . 196
- Figure 5.21** Integrated sample chain architecture for Dual-Rasp sampling system. Sampling position shown. Qualitative scheme, not to scale..... 197
- Figure 5.22** Integrated sample chain architecture for Dual-Rasp sampling system. Sample transfer position shown. Qualitative scheme, not to scale..... 197
- Figure 5.23** Cross-section of pneumatic sample transfer system applied to the Dual-Rasp sampling system. Bold blue arrow represents the flow of gas, while bold orange arrows represent the flow of gas/solids mixture. .... 198
- Figure 5.24** End-to-end TRL 4 sample chain operations for the Dual-Rasp sampling system. Top picture shows the Dual-Rasp in sampling position. Bottom picture shows the Dual-Rasp docked to sealed interface and in sample transfer position. In this case, the science instrument chamber is represented by a soft bag supported by a rigid cylindrical structure. .... 200
- Figure 5.25** Artistic concept of the Enceladus lander. .... 202
- Figure 5.26** Sample collection in the Dual-Rasp TRL 5 sample chain. The sample material removed from the surface flows from the Dual-Rasp, through the guide into the collection chamber provided with sample retention features. .... 202
- Figure 5.27** Preparation to sample transfer in the Dual-Rasp TRL 5 sample chain. Once the sample is collected into the collection chamber (Top), the guide moves on top of it to enable pneumatic sample transfer to science instrument chamber (Bottom). .... 203
- Figure 5.28** Pneumatic sample transfer in the Dual-Rasp TRL 5 sample chain. Once the collection volume is closed by the guide, the gas is released into the inlet pneumatic line, flows through the guide and into the collection chamber (red arrows). The mix of gas and sample exits the collection chamber through the outlet pneumatic line to reach the science instrument chamber (orange arrows). .... 204

---

<b>Figure 5.29</b> Prototype of science instrument chamber for TRL 5 pneumatic sample transfer system. ....	204
<b>Figure 5.30</b> CFD analysis of gas flow from inlet, through the guide and into the collection chamber. Front (Left) and side (Right) cross-section views representing streamlines are showed. ....	205
<b>Figure 5.31</b> Main components of a typical rotary union joint [243]. ....	205
<b>Figure 5.32</b> <i>TRL 5 sample chain elements, including RA, Dual-Rasp sampling, sample collection, and sample transfer systems.</i> ....	206
<b>Figure 5.33</b> Architecture of TRL 5 pneumatic sample transfer system. ....	207
<b>Figure 5.34</b> Helium phase diagram [245]. ....	207
<b>Figure 5.35</b> State diagram of gas/solids dispersion for TRL 5 pneumatic sample transfer system. ....	208
<b>Figure 5.36</b> Flow properties along the TRL 5 pneumatic sample transfer system, namely gas density $\rho_f$ , gas velocity $U_f$ , and gas Mach number $M_f$ ....	208
<b>Figure 5.37</b> Working principle of microwave Doppler technique for measuring concentration and velocity of particles in a pneumatic conveying system. The sensor emits microwaves and measures the Doppler-shift energy of microwaves reflected by particles in the gas/sample dispersion flowing in the pneumatic line. Doppler-shift energy relates to flow rate of particles. ....	212
<b>Figure 5.38</b> Cumulative voltage vs. sample mass correlation for microwave Doppler technique applied to BLC 110 analogue material. Various flow conditions are represented, also showing a correlation between voltage and flow velocity. ....	212



# List of Symbols, Abbreviations and Acronyms

## Latin symbols

$C_G$	Lander Center of Gravity
$E_p$	Particle Young's modulus
$E_r$	Margin of error
$E_t$	Surface geometry Young's modulus
$E^*$	Equivalent Young's modulus
$e_{pp}$	Particle-particle coefficient of restitution
$e_{pt}$	Particle-surface coefficient of restitution
$F_p$	Lander weight vector
$F_n$	Normal force between two contacting particles
$F_s$	Sampling force vector
$F_t$	Tangential force between two contacting particles
$G$	Solids feed rate
$G_t$	Gap between Dual-Rasp cutting heads
$E^*$	Equivalent shear modulus
$g$	Gravity acceleration
$I_t$	Inclination of Dual-Rasp cutting heads with respect to horizontal
$k_n$	Elastic constant for normal contact.
$k_t$	Elastic constant for tangential contact
$L_t$	Length of Dual-Rasp cutting heads
$m^*$	Equivalent mass
$N_t$	Number of teeth of Dual-Rasp cutting heads

$n_0$	Estimate of minimum sample size
$O_t$	Outer diameter of Dual-Rasp cutting heads
$R_r$	Rolling radius
$R_t$	Dual-Rasp rotational velocity
$R^*$	Equivalent radius of the contacting particles
$T_c$	Critical timestep
$T_{cR}$	Critical Rayleigh timestep
$U_{CH}$	Chocking velocity
$U_{salt}$	Saltation velocity
$V_t$	Dual-Rasp vertical plunging velocity
$Z$	Value of the Z-distribution

## Greek symbols

$\gamma_n$	Viscoelastic damping constant for normal contact.
$\gamma_g$	Global ground slope angles about Y axis
$\gamma_s$	Local ground slope angle about Y axis at the sampling spot
$\gamma_t$	Viscoelastic damping constant for tangential contact
$\delta_n$	Normal overlap distance between two contacting particles
$\dot{\delta}_n$	Normal component of the relative velocity between two contacting particles
$\delta_t$	Tangential overlap distance between two contacting particles
$\dot{\delta}_t$	Tangential component of the relative velocity between two contacting particles
$\delta_g$	Global ground slope angles about X axis
$\delta_s$	Local ground slope angle about X axis at the sampling spot

---

$\mu_r$	Coefficient of rolling friction
$\mu_{rpp}$	Particle-particle coefficient of rolling friction
$\mu_{rpt}$	Particle-surface coefficient of rolling friction
$\mu_{spp}$	Particle-particle coefficient of static friction
$\mu_{spt}$	Particle-surface coefficient of static friction
$\nu_p$	Particle Poisson's ratio
$\nu_t$	Surface geometry Poisson's ratio
$\rho_p$	Particle density
$\rho_t$	Surface geometry density
$\sigma$	Estimate of standard deviation
$\omega$	Angular velocity of particle

## Abbreviations

wrt	With respect to
3D	Three dimensional

## Acronyms

API	Application Programming Interface
CDT	Constant Directional Torque
CFD	Computational Fluid Dynamics
COR	Coefficient Of Restitution
COTS	Commercial Off-The Shelf
CPT	Cone Penetration Test

CPU	Central Processing Unit
DE	Design Envelope
DEM	Discrete Element Method
DOF	Degree of Freedom
EPSD	Elastic-Plastic Spring-Dashpot
FEM	Finite Element Method
FOM	Figure-of-Merit
fps	Frames per second
GPU	Graphics Processing Unit
MBD	Multi-Body Dynamics
MPI	Message-Passing Interface
M3Tk	Mobility Mechanics Modeling Toolkit
XFEM	Extended Finite Element Method
GCR	Galactic Cosmic Rays
HPC	High Performance Computing
ISAD	Icy Soil Acquisition Device
JPL	Jet Propulsion Laboratory
LAMMPS	Large-scale Atomic/Molecular Massively Parallel Simulator
LIGGGHTS	LAMMPS Improved for General Granular and Granular Heat Transfer Simulations
LEO	Low Earth Orbit
LRF	Lander Reference Frame
LS5	Lonestar5
MD	Molecular Dynamics
NASA	National Aeronautics and Space Administration
OWLS	Ocean Worlds Life Surveyor

RA	Robotic Arm
RARF	Robotic Arm Reference Frame
RPM	Revolutions Per Minute
RTD	Research and Technology Development
STL	Standard Tessellation Language
TACC	Texas Advanced Computing Center
TAG	Touch-And-Go
TRL	Technology Readiness Level
UCS	Unconfined Compressive Strength
VTK	Visualization ToolKit
VUV	Vacuum UltraViolet
YSZ	Yttria Stabilized Zirconia

# Chapter 1

## 1 Introduction

### 1.1 Robotic systems for planetary exploration: historical overview and future perspectives

Robots are machines designed to perform tasks and jobs with different levels of autonomy. Robotics is the engineering discipline concerning conceptualization, design, manufacturing, and operation of robots. As a highly multidisciplinary discipline, robotics involves mechanics, electronics, computer science, artificial intelligence, mechatronics, including nanotechnology and bioengineering.

Robots were originally introduced for performing pre-defined, fully controlled tasks within production lines of industrial factories, contributing to the worldwide diffusion of industrial mass-production of goods. Nowadays, research efforts focus on robots capable of higher levels of autonomy in performing tasks that require to interact with dynamic environments including humans, such as in offices, homes, and hospitals, or for medical applications.

Robots are also widely used in space since the beginning of the space exploration history, as they represent an efficient and, in most cases, the only chance to explore other worlds. In fact, humans would require very special equipment to survive in the harsh and prohibitive space and planetary environments, including extreme temperature variations, vacuum or very high atmospheric pressures, corrosive atmospheres, ionizing radiation, and very fine dust. Special equipment only suited for the particular conditions found in Low Earth Orbit (LEO) were successfully used, still within the protective shield of geomagnetic field. Humans were able to also survive on the surface of the Moon, but only for short periods. Therefore, human exploration of Solar System is still out of our grasp.

On the other hand, robots require far less countermeasures to survive the harsh conditions of space, thus are perfectly suited for travelling very long distances in deep space and exploring other worlds. Space robots include orbiters, landers, and rovers capable to orbit other planetary bodies, land, and rove on

them, respectively. Tasks assigned to space robots gradually increased in complexity over time, especially for space missions to the surface of planetary bodies such as planets, moons, asteroids, and comets. These tasks range from complex manipulation activities for performing sample acquisition and handling to rough terrain traversing, thus requiring sensing and perception capabilities to aid guidance, navigation, and control and in a natural unstructured environment. Moreover, the communication time-delay between a robotic system in space and a human operator on Earth can achieve tens of minutes or even hours, thus requiring advanced autonomous capabilities to safely manage robot operations. Therefore, any robotic system involved in space exploration must possess the versatility to handle many different potential scenarios, including not nominal and unexpected ones.

Robotic systems such as landers and rovers have been a crucial component for the exploration of planetary bodies since the beginning of the space exploration history. The Soviet Union's lander Luna 9 was the first human-made object performing a soft landing on the surface of a planetary body (i.e. the Moon) in 1966. Since then, fleets of robotic systems have explored our cosmic neighborhood, touching down on several planetary bodies, and pushing the limits of our knowledge of Solar System.

Robotic exploration began with several missions to the Moon continuing to the present day, from the U.S. and Soviet Union's probes of the 1960s and 1970s to the more recent Chinese missions of Chang'e program [1] [2]. In the inner Solar System, several of the Soviet Union's lander missions visited Venus in the 1970s and 1980s, such as the probes of the Venera and Vega programs. A notable case is represented by the U.S. Pioneer Venus Multiprobe that delivered one large and three smaller probes to the surface of Venus. One of the probes survived on the surface for over one hour. Among planetary bodies, Mars was a historic privileged target of space exploration with several missions including orbiters, rovers, and landers. In 1971, Soviet Union's probes Mars 2 and Mars 3 were the first probes achieving the surface of Mars, both carrying a small, tethered rover. Because of some malfunctions, they were not able of returning useful data. In 1976, the U.S. landers Viking 1 and 2 were the first probes returning useful data from the surface of Mars [3], followed by the U.S. landers Mars Pathfinder in 1997 [4] and Phoenix in 2008 [5]. The U.S. InSight lander, which touched down in late 2018, is the most recent of a long series of Mars lander missions [6]. In the outer Solar System, Saturn's moon Titan was the only planetary body of the outer Solar System visited by a landing mission to date. The European lander Huygens, part of the Cassini-Huygens mission, touched down on Titan in 2005 [7]. About small Solar System bodies, various landing missions also visited comets and asteroids. In 2001, the NEAR spacecraft performed the first landing on a small Solar System body, asteroid 433 Eros. The European mission Rosetta first delivered a lander, named Philae, on the surface of the comet 67P/Churyumov-Gerasimenko in 2014 [8]. On the other hand, MASCOT and MINERVA-II were

the first landers/hoppers landing on asteroid Ryugu as part of the Japanese mission Hayabusa 2 in late 2018 [9].

Proposed future missions include significant robotic contributions for planetary science and astrobiology in either the inner and the outer Solar System, including planetary bodies such as Mars, comets, asteroids, and ocean worlds [10].

## 1.2 Roadmap to ocean worlds

An ocean world is a planetary body with a current liquid ocean which might or might not be global. The Earth is an ocean world used as a reference. Jupiter's moon Europa and Saturn's moons Enceladus and Titan are explicitly identified as ocean worlds. Europa and Enceladus showed evidence of subsurface oceans communicating with both the surface and the seafloor, thus receiving energy which is important for habitability considerations. The presence of subsurface oceans on Titan is not supported by obvious evidence since they are expected to be covered by a thick ice crust, thus making difficult any communication with the surface. However, Titan has active cycles of surface liquids in contact with a wide range of organic species, which could present the characteristics for prebiotic chemistry and, potentially, the first steps toward life.

Other planetary bodies of the Solar System, such as Neptune's moon Triton, Pluto, Ceres, and Saturn's moon Dione, are considered candidate ocean worlds based on limited observations from robotic missions.

Main relevant questions to address about the exploration of ocean worlds include [11]:

1. Understanding where/why oceans are present.
2. Characterize ocean environments in these known ocean worlds.
3. Characterize their habitability.
4. Search for extant life.

High-priority targets of potential future robotic exploration missions that would address these questions include:

- Europa: Habitability mission. Europa Clipper is in progress [12], and a Europa Lander study is in progress [13].
- Titan: Habitability and/or ocean characterization mission. Dragonfly mission has been selected as the next New Frontiers class mission and is currently under development [14].
- Enceladus: Search-for-life mission. Plume flyby missions [15] and lander missions for in-situ analysis of plume fallback are currently under investigation.

### 1.3 A potential lander mission to Enceladus: science and technology

Part of the content of the present paragraph was published in [16].

Enceladus is among the most promising candidates in the Solar System to host life beyond Earth. Observations from the *Cassini* mission, including gravity data and accurate rotation measurements showing a physical libration [17], suggest that Enceladus contains a global ocean beneath its thick ice shell [18]. Moreover, *Cassini* directly observed active cryovolcanism since material from the subsurface ocean is ejected through surface fractures in the South polar region, named Tiger Stripes [19] [20]. Local thermal anomalies with a temperature up to 180K are observed in the Tiger Stripes region [21] [22] [23], while the rest of the South polar terrain is significantly colder (around 30-50K) [24]. Tidal shear heating within the ice shell is likely the origin of the plumes and thermal anomalies [25] [26]. Observations from the *Voyager* mission and analysis of *Cassini* data suggest that the plume is a phenomenon persisting for decades and perhaps even longer [27] [28] [29].

Enceladus' plume consists of vapor and particles; the particles are approximately micron-size and mostly comprised of water ice feeding Saturn's E ring [30]. A subset of the particles (i.e. about 40%) also contain percent-level NaCl and other salts by mass [31] [32] and a separate subset (i.e. about 4%) contain complex organic materials, also at the percent-level by mass [33]. The vapor phase of the plume includes ammonia, carbon dioxide, low-mass organics including CH<sub>4</sub>, <sup>40</sup>Ar [34], and molecular H<sub>2</sub> [35]. <sup>40</sup>Ar is formed from the radioactive decay of <sup>40</sup>K, which suggests a direct connection between the silicate interior and the exosphere. H<sub>2</sub> and CH<sub>4</sub> are strongly suggestive of ongoing hydrothermal activity, as it would leave the interior and escape in a short period of time. The moderately high pH derived for the ocean [36], the presence of complex organic materials, and the abundant geothermal energy from the interior and within the South polar terrain provide evidence for habitability and the prospect that life may have emerged and still be present on Enceladus [37] [38] [39]. *Cassini* observations of particles in the Enceladus plume and the E ring enabled the determination of their grain size distribution and their trajectories, and the modeling of their deposition rate back on Enceladus surface. The mean radius of equivalent-sphere particles determined from imaging is  $3.1 \pm 0.5 \mu\text{m}$  [40]. The Cassini Cosmic Dust Analyzer characterized the vertical structure of the plume, from which a particle ejection model was established [41]. The deposition of plume particles could then be computed as function of particle size, source location, and location on the Enceladus surface [30] [42]. Particles in the range 0.1–5  $\mu\text{m}$  are expected to dominate the plume deposits. The average deposition rate is on order of 1  $\mu\text{m}/\text{year}$  but can be greater than 0.1 mm/year in locations close to jet sources [30] [42]. This is roughly consistent with a separate model that

suggests 68-93% of all plume particles are deposited on the surface [43]. Plume particles, in Enceladus' exosphere or on its surface, could contain traces of life or biosignatures [43] [44]. The observations collected all strongly suggest the presence of the fundamental ingredients to sustain life: a subsurface liquid water ocean, an energy source heating the ocean from the interior, and necessary chemical elements [31] [32] [34] [35] [38] [39] [45].

In comparison to Jupiter's moon Europa, the radiation environment on the Enceladus surface is benign, thus enabling preservation of organic molecules on the surface for relatively long timescales. Both particle and ultraviolet radiation can have degradative effects on biosignatures. Uniquely on Enceladus, these effects are modulated by the continuing deposition of fresh plume particles, which scatter or absorb radiation and shield buried particles. The flux of magnetospheric particle radiation at Enceladus is relatively low. While studies on the particle irradiation at Enceladus are not available, it is possible to use the radiation environment of Saturn's moon Mimas as a worst-case analog for Enceladus. On the most irradiated location on Mimas, the time to reach 100 eV/16 amu electron dose accumulation (a standard unit representing a chemically significant dose) is about 1 million years at a depth of 1 mm [46]. Thus, shallow material in regions of plume deposition will be minimally processed. Galactic Cosmic Rays (GCRs) deliver radiation doses that are many orders of magnitude lower than that from magnetospheric particles, thus do not need to be considered as a degradation mechanism on the short timescales appropriate to Enceladus' continually deposited plume particles. Solar ultraviolet irradiation can also degrade organic biosignatures. Generally, the most damaging radiation is in the Vacuum UltraViolet (VUV), below approximately 150 nm. Light at these wavelengths and below has absorption lengths (the distance light travels before its intensity decreases by a factor of 1/e) in single crystal water ice of less than 0.1  $\mu\text{m}$  [47]. This indicates that organic molecules embedded within micron-sized plume grains will be almost entirely shielded from damaging VUV radiation. Continuing deposition on the surface would provide additional shielding.

Longer wavelength ultraviolet radiation is also damaging to organic molecules. For example, the photolytic half-lives of the amino acids glycine and phenylalanine are 6.5 and 4.5 years at 206 nm, and 5 and 1 years at 254 nm, respectively, under Solar flux levels representative of Europa's surface [36]. Note that the Solar flux at Enceladus would be 3.3 times less than at Europa. Absorption lengths for photons at these wavelengths are approximately 1 m in a pure block of water ice. However, scattering models [48] show penetration depths of 250 and 500  $\mu\text{m}$  at 210 and 300 nm in a non-porous medium of isotropically scattering 60  $\mu\text{m}$  ice grains. Scattering, and thus penetration depths, would be even shorter in a medium composed of smaller particles, as expected at Enceladus. The conclusion is that at locations on Enceladus where deposition rates are high (0.1 mm/year and higher), the deposition of plume particles would effectively shield amino acids from photolytic degradation. It is expected that

most other organic molecular biosignatures would have photolytic half-lives comparable to amino acids.

Plume deposits are expected to consist initially of fine-grained ice particles loosely in contact, forming a granular and non-cohesive material. This material would then slowly sinter over time and presumably become more consolidated [37, 38]. The mechanical properties of plume deposits and how they evolve over time are at present not well constrained.

A recent laboratory study [39] investigated the evolution in strength upon sintering of fine-grained ice particles with diameters comparable to Enceladus' plume particles. Cone penetration resistance measurements were obtained as a function of time and at different temperatures (Figure 1.1). An Arrhenius analysis of the strengthening rates yielded an activation energy of 24.3 kJ/mol, which was then used to predict the strength evolution of plume deposits under Enceladus and Europa's surface conditions (Figure 1.2). Based on these results, plume deposits on Enceladus are expected to be poorly consolidated. It would take at least 100 My from plume deposits to develop a resistance of 1 MPa under Enceladus' nominal surface conditions. Deposits near the Tiger Stripes, where strengthening rates would be much higher, would also be covered by fresh unconsolidated particles at a rate up to about 1 mm/year [30] [42].

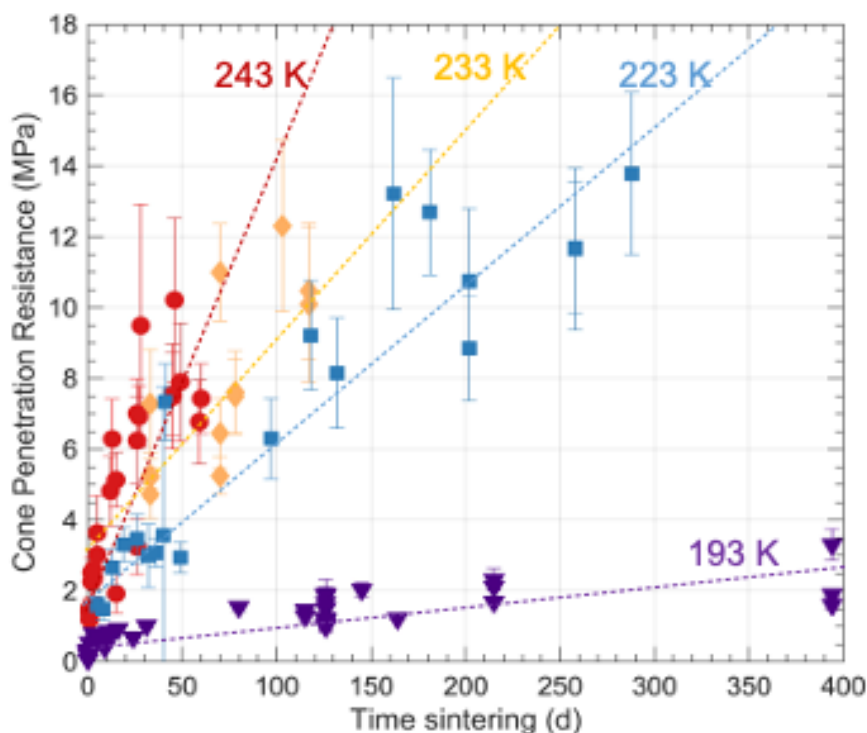


**Figure 1.1** Evolution with time of the cone penetration resistance of ice plume deposit analogs at several temperatures [39].

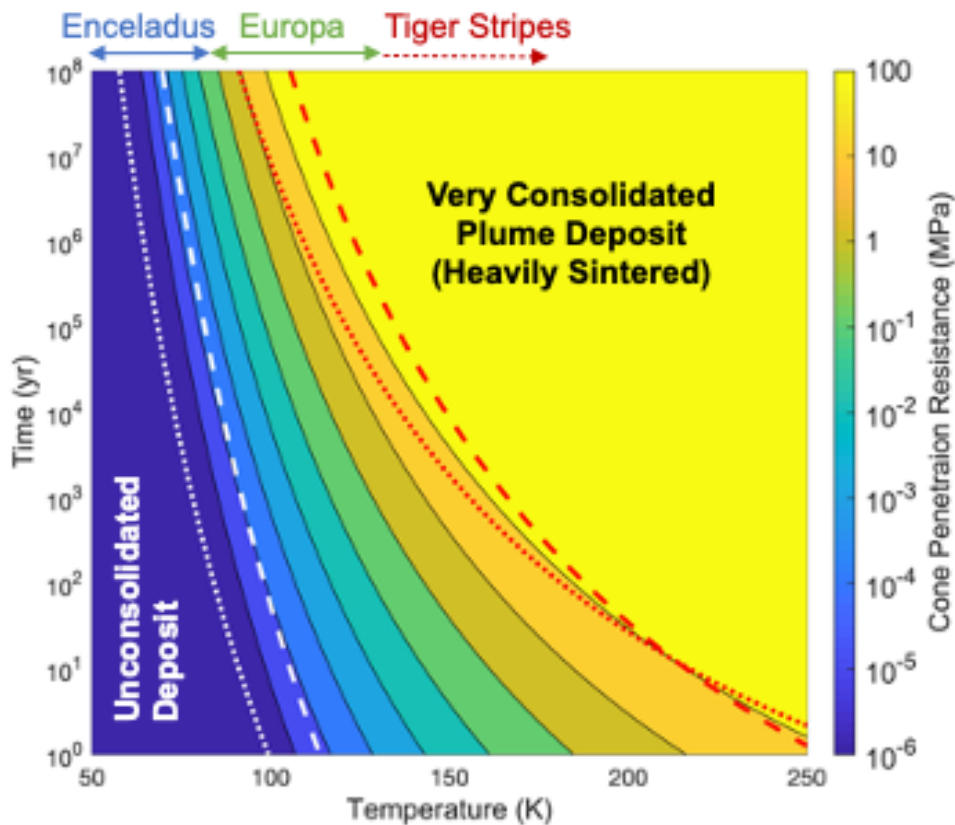


**Figure 1.2** Predicted cone penetration resistance of icy plume deposits as a function of temperature and sintering time. Black contours are for the best-fit activation energy value. Dashed and dotted contours illustrate the effect of the uncertainty on activation energy. For legibility, these contours are only shown for the 10-5 (white) and 100 MPa (red) cone penetration resistance levels. Modified after [39].

Mission concepts have previously proposed to capture particles in the plume itself [49]. Landed mission concepts, in some ways similar to the Europa Lander [50], would have their own challenges and foreseeably be costly. However, they would avoid hypervelocity capture that might potentially affect the mass spectral signature of plume materials. Landed mission concepts could be able to acquire much larger amounts of materials than plume fly-through concepts, allowing higher sensitivity to trace constituents, and enabling the conduction of a larger number of replicate analyses, thereby providing greater robustness of science results [51].

A potential future lander mission to Enceladus is currently under investigation at NASA Jet Propulsion Laboratory (JPL). The research presented in this dissertation is part of a NASA JPL Strategic Research and Technology Development (RTD) effort to develop and mature a sample chain for Enceladus surface acquisition for in-situ measurements to Technology Readiness Level (TRL) 5, according to the NASA definition summarized in Figure 1.3 [52] [53]. In

the context of such a lander mission it is desirable to develop a sample chain (i.e. the sequence of steps to acquire a sample from its pristine environment) to provide 1 cc to 5 cc volume samples to science instruments from the very shallow surface material in the top 1 cm, in order to acquire the freshest material deposited on surface from plume fallback.

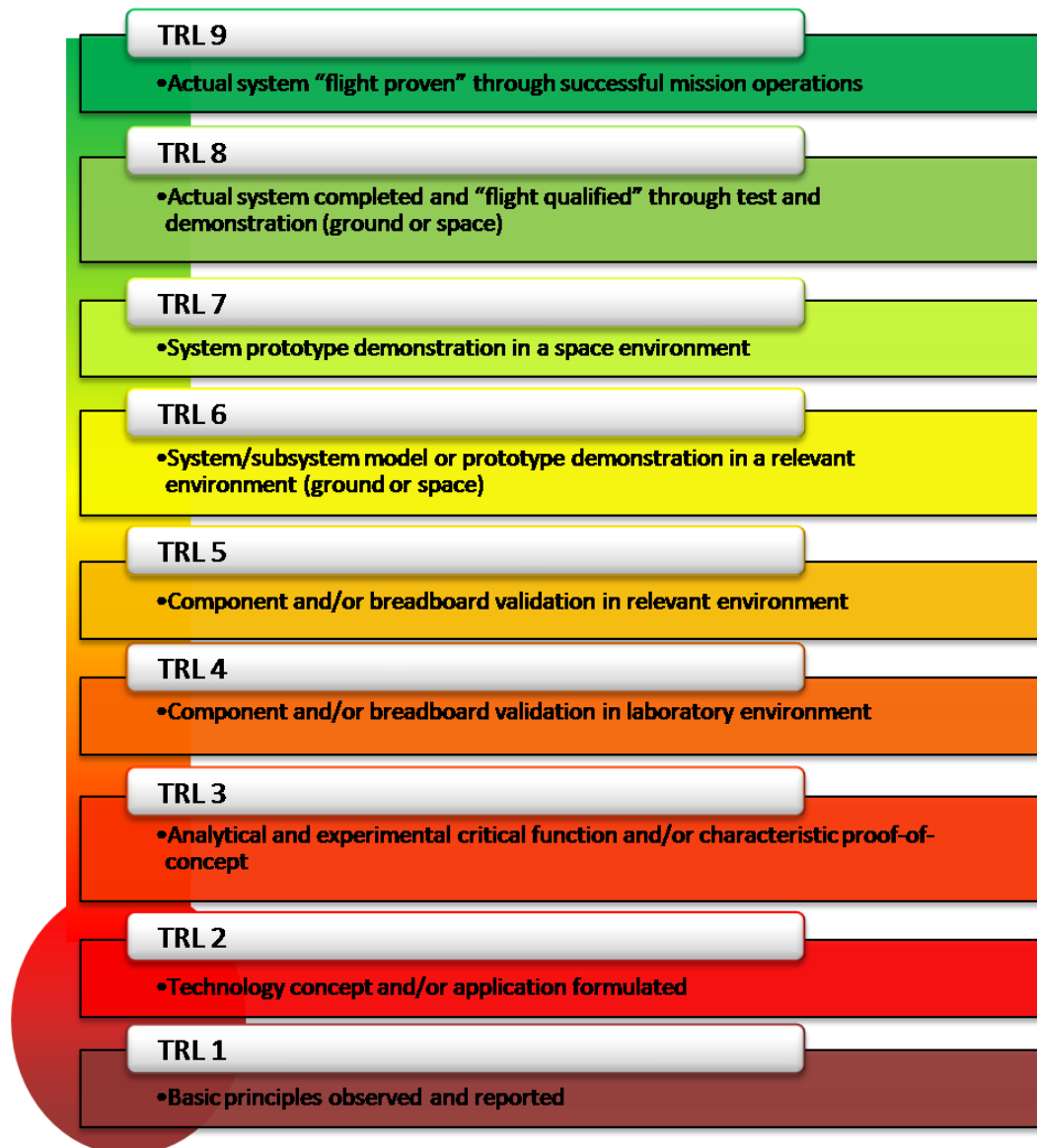


*Figure 1.3 NASA definition of Technology Readiness Levels [52].*

## 1.4 Problem statement and dissertation objectives

In the context of a lander mission to the surface of Enceladus, the low gravity (1% Earth's), cryogenic, and vacuum environment represents a unique challenge for lander stability, surface sampling and sample handling. From the perspective of lander stability, even small forces applied to the lander could weaken its stability, potentially causing the lander to lift or slide downhill. From the perspective of surface sampling and sample handling, dynamics of particles constituting the sample tend to be dominated by particle-particle forces (i.e. interaction between particles) and particle-surface forces (i.e. interaction between particles and the surface of other bodies such as the sampling tool or the sample collection cup), instead of being dominated by gravity force. As a result, particles show an extremely low tendency to settle and the resulting high tendency of spreading in a very sparse fashion moving on long ballistic trajectories, in such a way particles look having a random motion, similar to the behavior of a gas.

Dissertation focuses on the analysis and development of the sample chain for a potential lander mission to the surface of Enceladus that would collect material from plume fallback for in-situ analysis.

Ph.D. research supported JPL's RTD activity by pursuing the following objectives.

1. To define the high-level requirements on the sampling system to guarantee the stability of the lander while performing the sampling operation.
2. To investigate and characterize sample collection and transfer operations in the Enceladus gravity, cryogenic, and vacuum environmental conditions.
3. To provide sample chain design guidelines to fulfill sample acquisition requirements.

Objective 1 is achieved by developing a novel analytical design tool conceived for trade space exploration during early conceptual and preliminary design phases, where a rapid and broad evaluation is required for a very high number of configurations and boundary conditions. The tool rapidly determines the preliminary design envelope of a sampling apparatus to guarantee the stability condition of the lander. The tool also provides the capability to infer high-level requirements concerning other elements of the lander critical to its stability, such as the footpads.

Objective 2 concerning the investigation and characterization of sample transport and collection is achieved by developing a model based on the Discrete Element Method (DEM). DEM is a numerical simulation technique for computing the motion and effect of a large number of particles, treated as unique entities in such a way the behavior of the bulk material arises from particle-particle and

particle-surface interactions. A set of analysis metrics is developed to characterize the granular material flow generated during the sampling operation. The analysis metrics are devised to be used for both numerical analysis and experimental testing, providing a framework for apples-to-apples comparison. Most sensitive model parameters are determined through a sensitivity analysis and then directly measured via independent tests performed by using custom designed apparatus.

The investigation and characterization of sample transfer is achieved by developing analytical tools to study the flow of particles dispersed into a gas with the aim to pneumatically transfer the sample to its destination (i.e. the scientific instrument). The exploration of design space is performed to determine the optimal design parameters to achieve a dilute phase transport of the sample.

Objective 3 is achieved by the extrapolation of design guidelines from previous described investigations to achieve the optimal design of sample chain elements.

## 1.5 Dissertation overview

Dissertation is organized as follows.

Chapter 1 provides an historical overview and future perspectives on robotic systems applied to space exploration with focus on the roadmap to robotic exploration of ocean worlds and specifically to the science and technology of a potential future lander mission to the surface of Enceladus.

Chapter 2 addresses the novel analytical design tool developed for trade space exploration of robotic systems involved in sampling operations, including application of the tool to determination of sampling system requirements to guarantee lander's stability.

Chapter 3 addresses the investigation of sampling system concepts developed, prototyped, and tested for Enceladus surface acquisition.

Chapter 4 addresses the investigation of sample collection operations, including methods and models developed to study the interaction between sampling system and soil, the resulting granular material flow and collection dynamics. Design process of sample chain elements for sample collection, prototyping, and testing are included.

Chapter 5 addresses the investigation of sample transfer and deposit operations, including methods and models developed to study pneumatics as a technique for sample transfer. Design process of sample chain elements for sample transfer and deposit, prototyping, and testing are included.

Chapter 0 presents conclusions about the research activity and perspectives for future work.

# Chapter 2

## 2 Definition of sampling system requirements

Part of the content of the present Chapter was published in [54].

As introduced in paragraph 1.4, the Enceladus low gravity environment provides unique challenges for surface sample acquisition. One of them is represented by the severe limit on the allowable reacted load from the sampling system to the lander.

To guarantee a nominal sampling operation, crucial to mission success, it is required that the forces generated by the sampling system do not affect the stability of the whole robotic system (e.g. a lander). The traditional approach to investigate various concepts for a robotic mission involved in sampling operations relies on the preliminary definition of a set of potential sampling tool candidates [55]. Therefore, ad-hoc analyses on the stability of the whole robotic system must be performed every time a design parameter is modified. E.g. physical and geometrical characteristics of the robotic system, properties related to the environment, physical and geometrical features of the sampling tool [56] [57] [58]. At a higher level, the same process must be repeated every time a new sampling tool and a new configuration of the whole robotic system is investigated. Existing literature focuses on the sampling tool design [59] [60], not including the influence of the whole robotic system and the surrounding environment. On the other hand, COTS (Commercial Off-The Shelf) simulation tools, such as multi-body dynamics tools, allow to address complex systems. However, using such tools for building a full design space that includes the variation of several parameters cannot be performed in an automatic fashion, and is thus significantly time consuming and requires a not negligible workload. Such tools would not be suited for rapid preliminary evaluation of the design space for several different configurations and boundary conditions, which is a typical need for studies that require broad trades. COTS simulation tools are well suited for detailed design of a very restricted number of solutions. In order to make this process more time-

effective and reliable, a systematic effort was made to develop MISTRAL (MultiDisciplinary deSign Tool for Robotic sAmpLing), a novel tool that supports the definition of the high-level requirements of a robotic system involved in sampling operations.

## **2.1 MISTRAL: A design tool for robotic systems involved in sampling operations**

MISTRAL is conceived for trade space exploration during early conceptual and preliminary design phases, where a rapid and broad evaluation is required for a high number of configurations and boundary conditions. The tool determines the preliminary Design Envelope (DE) of a sampling system to guarantee the stability condition of the whole robotic system. The tool implements a 3D (three-dimensional) analytical model capable to reproduce several scenarios, accepting various input parameters such as physical and geometrical characteristics of the robotic system, properties related to the environment (i.e. gravity, physical and geometrical properties of the terrain) and features related to the sampling system (i.e. geometry, applied forces). Moreover, the model includes coupling effects among these parameters. This feature can be exploited to infer multidisciplinary high-level requirements concerning several other elements of the investigated system, such as robotic arms (RAs) and footpads. In this context, the DE is a graphical representation of the parameter variation, a key element for obtaining a comprehensive and rapid overview of the design space. Once the design space is defined by using MISTRAL, high-level trade-offs are conducted to narrow the range of variables. At this point, more detailed evaluation of sampling operation can be conducted on a narrower range of design variables by performing further studies that exploit more accurate models, simulation tools and experimental tests. These further activities support the identification of design branches that will be the subject of a series of medium/low level trade-offs and selections down to specific design points to analyze and test at very high detail, until a single, final solution is identified and verified.

### **2.1.1 Structure of the tool**

MISTRAL is conceived as a tool to determine the preliminary DE of a sampling apparatus to guarantee the stability condition of the whole robotic system according to the investigated scenario.

Figure 2.1 shows the block diagram of the tool. The process starts with the scenario definition where the user inputs all relevant parameters to characterize the scenario under investigation. The first group of inputs includes physical and geometrical properties of the robotic system. In the case of considering a lander, geometrical properties include main dimensions and positioning of body, legs, and

RA. Physical properties include the mass of the lander and the position of its center of mass. The second group of inputs includes the properties of the environment, such as the local gravitational acceleration and the characteristics of the terrain in terms of friction and slope distribution. The third group of inputs includes the physical and geometrical properties of the sampling system. Parameters such as the geometry of the sampling system and the applied forces can be provided. The fourth group of inputs includes the required margins for the stability of the whole robotic system.

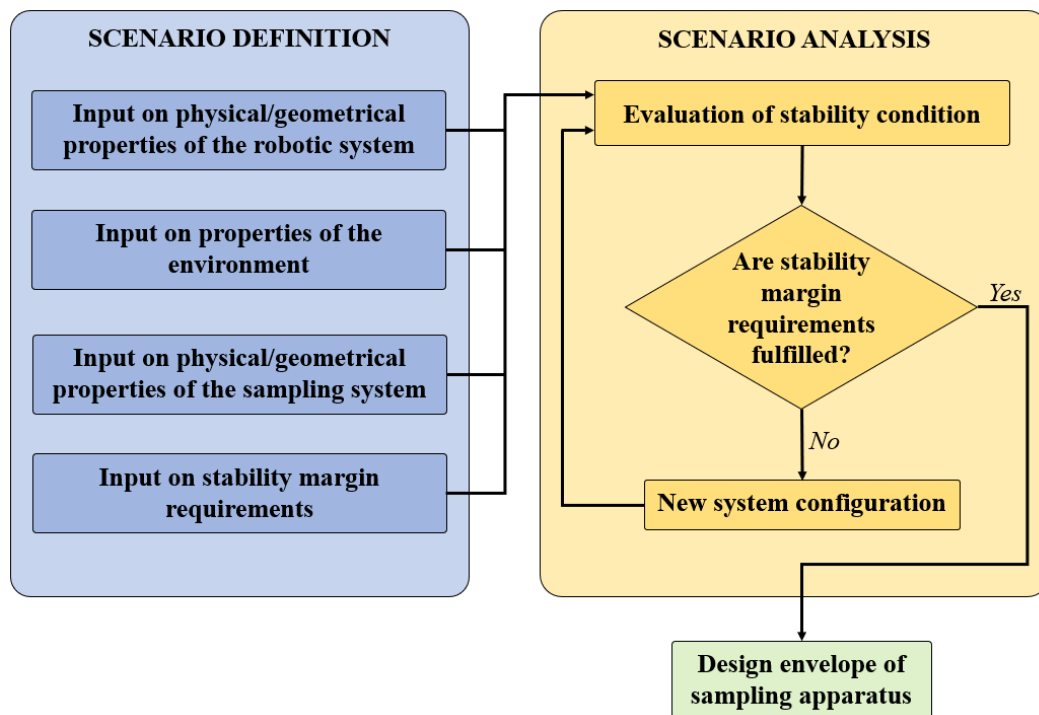


*Figure 2.1* Block diagram of MISTRAL.

The second phase of the process is the scenario analysis. The analysis model uses the inputs to evaluate the stability condition of the robotic system by solving a set of equations, as extensively explained in paragraph 2.1.2. In the case of a lander, the equilibrium condition depends on the reaction forces the terrain applies to the footpads. The reaction forces are related to several parameters, such as the lander weight, which depends on its mass and on local gravitational acceleration, the morphology and the physical characteristics of the terrain (i.e. slope distribution and friction), the sampling force applied to the terrain and the way it is applied, which depends on sampling tool geometry. The tool performs an optimization procedure to determine the maximum allowed magnitude of the sampling force that prevents the lander changing its equilibrium state, according to the stability margins provided by the user. The stability margins are defined

with respect to the reaction forces required to keep the equilibrium condition of the lander.

This process outputs the DE of the sampling apparatus according to the scenario under investigation. The DE refers to a delimited range of the parameters within which the lander maintains its equilibrium condition within the defined stability margins.

### 2.1.2 Analysis model

The 3D analytical model was developed to study the static equilibrium of a lander with the aim to determine the DE within which the sampling system should be designed. The model provides an indication on the maximum allowed sampling force magnitude that prevents the lander changing its equilibrium state. To achieve this goal, the model computes the three Cartesian components of the reaction forces acting on each lander's footpad. The evaluation of the reaction forces enables the determination of the DE of the sampling apparatus according to the investigated scenario. Rotational stability is not explicitly addressed because it is usually anticipated by lifting of the legs, which is a stability limit addressed. E.g. to get a single leg supporting most of the weight, the other legs must lift off the ground first. By preventing legs from lifting off the ground, rotational stability issues are usually avoided. Nevertheless, rotational stability will be explicitly considered for the inclusion in the tool in future developments.

The presented approach allows the evaluation of the lander's reaction to generic external loads having components along the three Cartesian axes, meaning that

- Lander's weight  $\mathbf{F}_p$  has three components. This is the effect of the general ground slope angles about X axis ( $\delta_g$ ) and Y axis ( $\gamma_g$ ), as shown from Figure 2.2 to Figure 2.9.
- Sampling force  $\mathbf{F}_s$  has three components. This considers three effects. The first one is the effect of the inclination of the sampling force with respect to the ground. The second one is the effect of placing the sampling spot off-axes, as shown from Figure 2.2 to Figure 2.9. The third one is the effect of the local ground slope angles about X axis ( $\delta_s$ ) and Y axis ( $\gamma_s$ ). The local ground slope angles are related to the local geometry of the ground at the sampling spot, which in turn influences the direction of the sampling force.
- Center of Gravity ( $C_G$ ) of the lander is off-axes.

Two different lander configurations are considered, 3-legged lander equipped with three footpads arranged as a regular triangle shape, and 4-legged lander equipped with four footpads arranged as a square. Both configurations are

plausible in the context of the Enceladus lander mission study considered, and consistent with some of the most common architectures for legged landers, as shown in Table 2.1.

**Table 2.1** Overview of the main robotic lander configurations adopted in space exploration.

Lander name	Landing configuration	Body configuration	RA configuration	Notes	Reference
Mars Pathfinder	1 point of contact with the surface arranged as a flat landing platform	Non-regular hexagon	Not applicable	The lander carried a small rover on the surface.	[4]
Beagle-2	1 point of contact with the surface arranged as a flat landing platform	Shallow bowl	4 rotational DOFs	The RA was designed to perform scientific instrument and sampling system deployment to the surface.	[61]
Venera 13, 14	1 point of contact with the surface arranged as a ring-shaped landing platform	Cylinder	1 rotational DOF	The RA performed scientific instrument deployment to the surface. The lander was equipped with a sampling system that operated at its location, fixed to the lander's body.	[62]
Surveyor 3, 4, 5, 6, 7	3 points of contact with the surface arranged as a regular triangle shape	Regular triangle	1 linear and 2 rotational DOFs	On Surveyor 3, 4 and 7, the RA performed sampling system deployment to the surface and supported sampling operations. On Surveyor 5 and 6, the RA performed scientific instrument deployment to the surface.	[63] [64] [65] [66] [67]
Viking 1, 2	3 points of contact with the surface arranged as a regular triangle shape	Non-regular hexagon	1 linear and 2 rotational DOFs	The RA performed sampling system deployment to the surface, supported sampling operations and delivered the sample collected to the scientific instrument.	[3] [68] [69]

Mars Polar Lander	3 points of contact with the surface arranged as a regular triangle shape	Regular hexagon	4 rotational DOFs	The RA was designed to perform sampling system deployment to the surface, to support sampling operations and deliver the sample collected to the scientific instrument.	[70]
Phoenix	3 points of contact with the surface arranged as a regular triangle shape	Regular hexagon	4 rotational DOFs	The RA performed sampling system deployment to the surface, supported sampling operations and delivered the sample collected to the scientific instrument.	[5]
Philae	3 points of contact with the surface arranged as a regular triangle shape	Non-regular hexagon	Not applicable	The lander was equipped with a sampling system that was designed to operate at its location, fixed to the lander's body. The lander body had a 1 rotational DOF about the vertical, central joint of the 3-leg landing gear.	[71]
InSight	3 points of contact with the surface arranged as a regular triangle shape	Regular hexagon	4 rotational DOFs	The RA performs scientific instrument deployment to the surface.	[6]
Luna 16, 20, 24	4 points of contact with the surface arranged as a rectangle shape	Cylinder	1 linear DOF	The RA performed sampling system deployment to the surface and supported sampling operations.	[72] [73] [74]

To easily link the position of the footpads to the geometric characteristics of the body, it was assumed that the 3-legged lander has a hexagonal body, while the 4-legged lander has an octagonal body. It should be noted that any shape of the lander body can be used, since it is only an easy method to link the geometric characteristics of the lander to the position of its footpads, which in turn determines the effect of the reaction forces on the lander stability. It should be noted also that any arrangement of the legs can be studied by adjusting the position of the footpads. As an example, it would be possible to select the three main loaded legs in a legged lander with more than three legs and switch between

them to explore the DE assuming the borderline case has a single leg that comes to no load (e.g. a 4-legged lander always tilts slightly, although soft regolith mediates this behavior).

The Lander's Reference Frame (LRF) is placed at the ground level, while the origin of LRF is aligned with the geometric center of the lander's body. The resulting free body diagrams are shown from Figure 2.2 to Figure 2.5 for the 3-legged lander, and from Figure 2.6 to Figure 2.9 for the 4-legged lander.

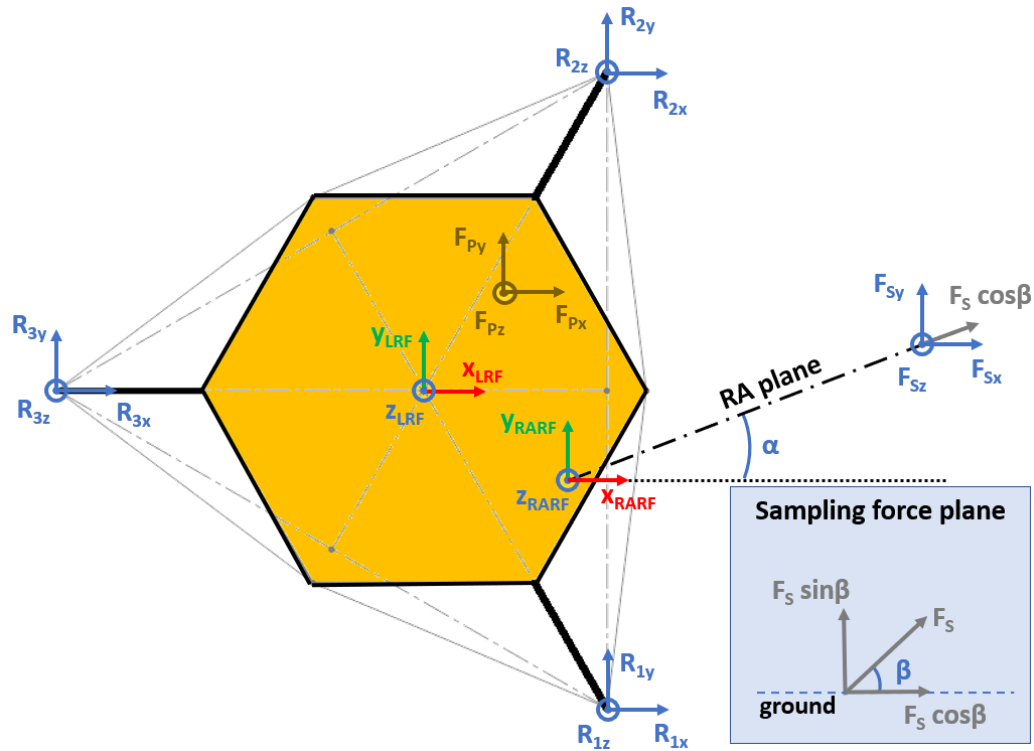


**Figure 2.2** Free body diagram (XY plane view) for the 3-legged lander. Qualitative scheme, not to scale.

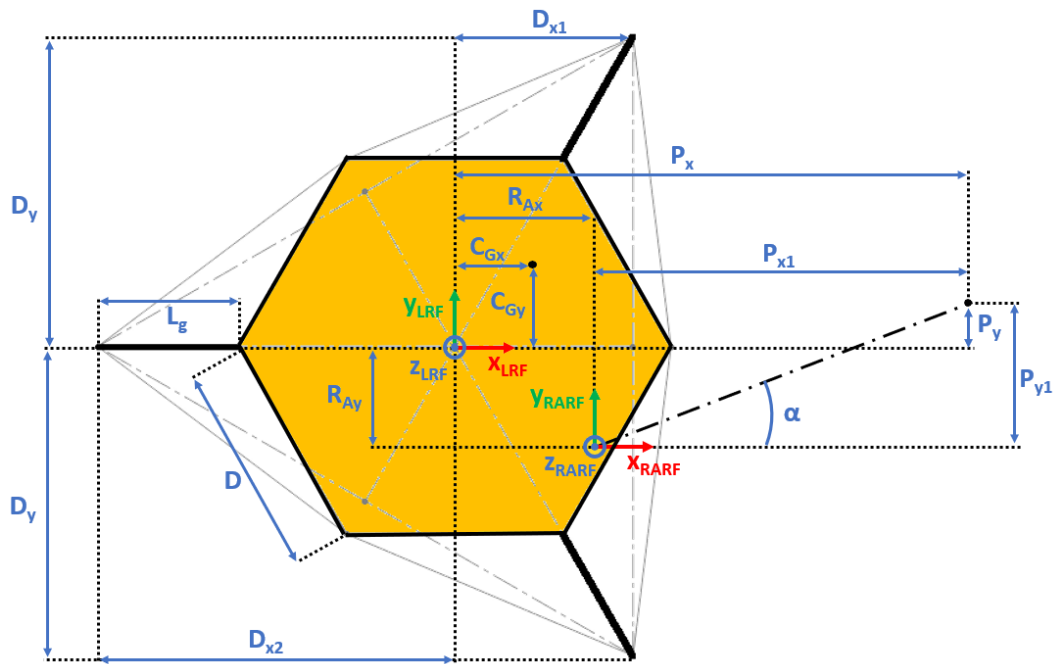


**Figure 2.3** Main geometric parameters (*XY plane view*) for the 3-legged lander. Qualitative scheme, not to scale.

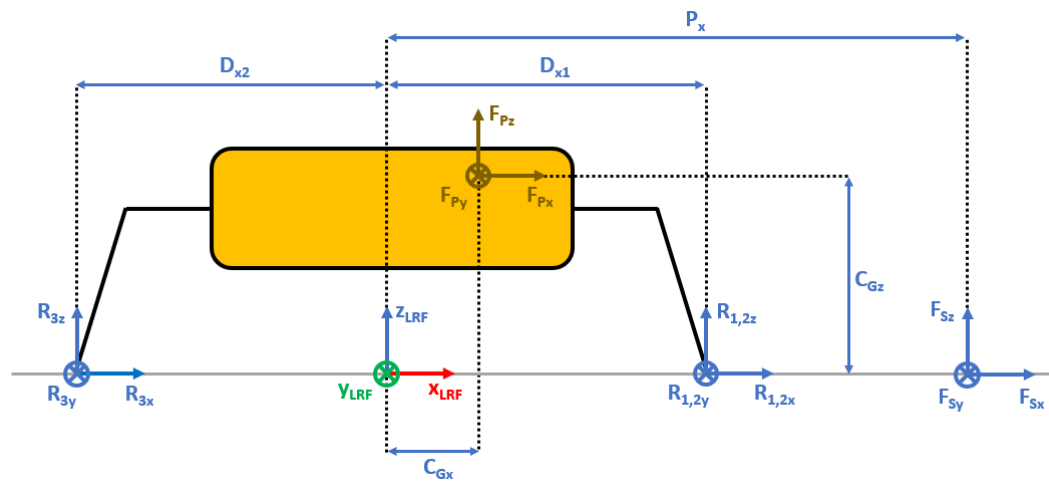


**Figure 2.4** Free body diagram and main geometric parameters (*XZ plane view*) for the 3-legged lander. Qualitative scheme, not to scale.

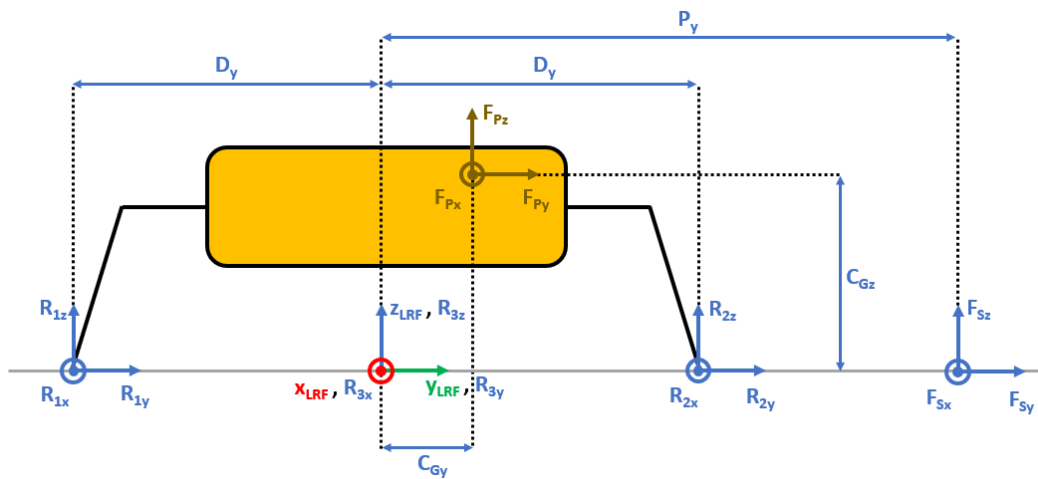


**Figure 2.5** Free body diagram and main geometric parameters ( $YZ$  plane view) for the 3-legged lander. Qualitative scheme, not to scale.

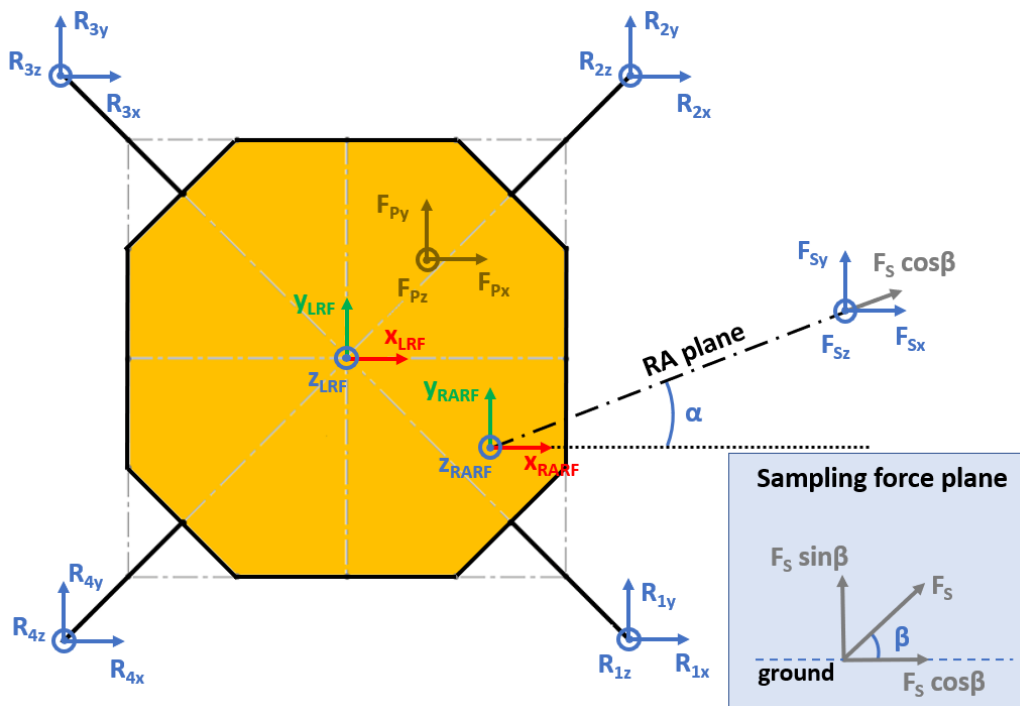


**Figure 2.6** Free body diagram ( $XY$  plane view) for the 4-legged lander. Qualitative scheme, not to scale.

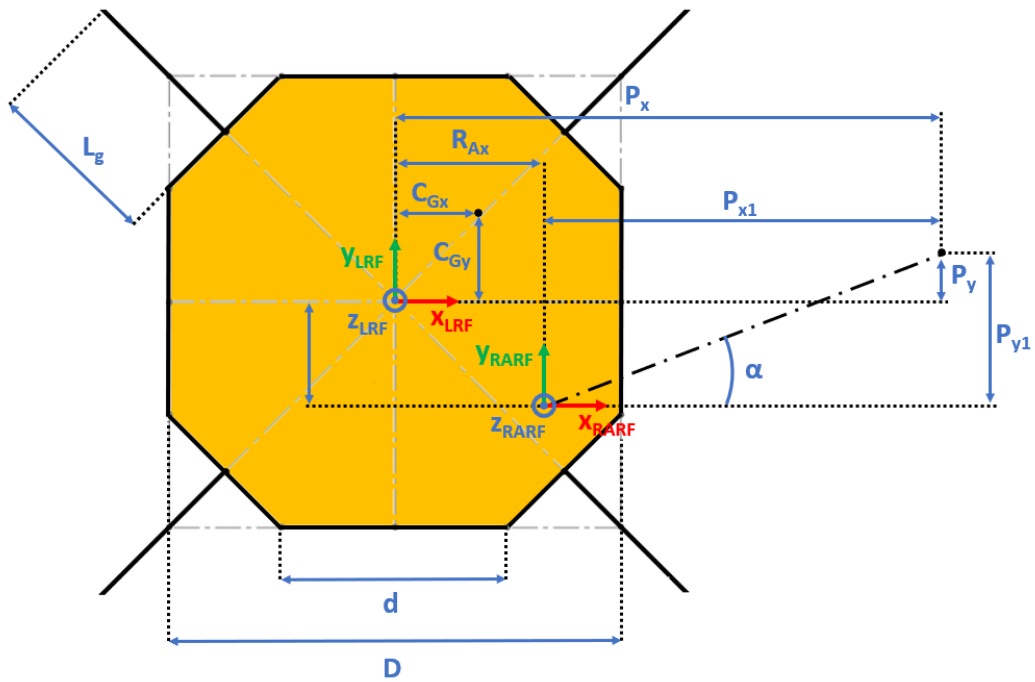


**Figure 2.7** Main geometric parameters (XY plane view) for the 4-legged lander. Qualitative scheme, not to scale.

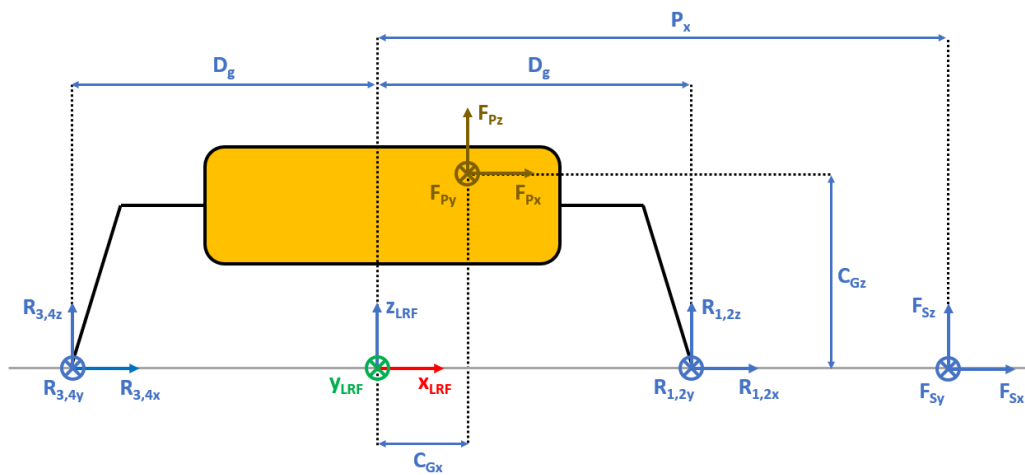


**Figure 2.8** Free body diagram and main geometric parameters (XZ plane view) for the 4-legged lander. Qualitative scheme, not to scale.

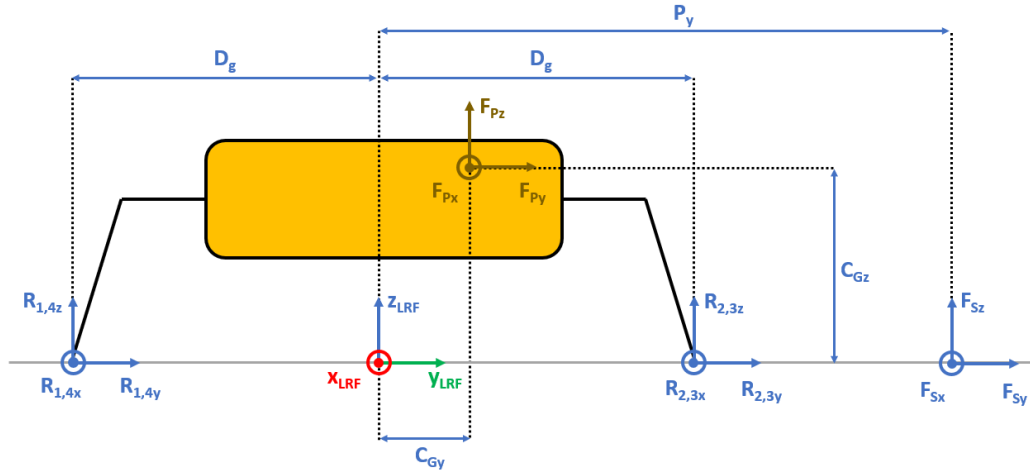


**Figure 2.9** Free body diagram and main geometric parameters (YZ plane view) for the 4-legged lander. Qualitative scheme, not to scale.

Hereafter, bold printing indicates vectors while non-bold printing indicates scalars.

$R_{n_{x,y,z}}$  are the Cartesian components of the reaction force acting on the  $n$ -th lander's footpad ( $n = 1, 2, 3, 4$ ).

Given the assumption on the lander's body shape (i.e. hexagon for the 3-legged lander, octagon for the 4-legged lander) and footpads arrangement (i.e. regular triangle for the 3-legged lander, square for the 4-legged lander), the position of the footpads is defined via the parameters  $D_{x_{1,2}}$  and  $D_y$  for the 3-legged lander, and  $D_g$  for the 4-legged lander. It should be noted that those parameters are linked to the geometric parameters  $D$ ,  $d$  and  $L_g$ , defining the general configuration of the lander's body and footpads (Figure 2.2 to Figure 2.9).

$F_{p_{x,y,z}}$  are the Cartesian components of the lander's weight  $F_p$ . The position of the  $C_G$  is defined via the geometric parameters  $C_{G_{x,y,z}}$ .

$R_{A_{x,y}}$  define the position of the RA on the lander's deck. Such geometric parameters also define the origin of the Robotic Arm Reference Frame (RARF).

$F_{s_{x,y,z}}$  are the Cartesian components of the sampling force  $F_s$ . The sampling force is applied to the sampling spot, localized with respect to LRF and RARF via the geometric parameters  $P_{x,y}$  and  $P_{x_1,y_1}$ , respectively. Eq. (2.1–2.2) relate geometric parameters  $P_{x,y}$ ,  $P_{x_1,y_1}$  and  $R_{A_{x,y}}$ .

$$P_x = R_{Ax} + P_{x_1} \quad (2.1)$$

$$P_y = R_{Ay} + P_{y_1} \quad (2.2)$$

In Figure 2.2 and Figure 2.6, the line joining the origin of RARF to the sampling spot represents a plane containing the RA and perpendicular to the XY plane. The sampling force  $F_s$  lies on the sampling force plane, which is oriented according to both the position of the RA and the local geometry of the ground at the sampling spot.

$\alpha$  is the orientation of the RA plane with respect to the XZ plane (i.e. a rotation about the Z axis of RARF), defined as  $\tan \alpha = P_{y_1}/P_{x_1}$ .

$\beta$  is the angle of the sampling force  $F_s$  with respect to the ground, located in the sampling force plane.

The vector components of the sampling force  $F_s$  are computed by defining the local ground slope angles about X axis ( $\delta_s$ ) and Y axis ( $\gamma_s$ ) of RARF. A rotation matrix is defined for the rotation about the X axis, Y axis and the Z axis, according to Eq. (2.3–2.5), respectively. The rotation matrices are applied to the base sampling force vector  $\mathbf{S} = F_s [\cos \beta, 0, \sin \beta]$  to obtain its components, according to Eq. (2.6).

$$\Gamma_s = \begin{bmatrix} 1 & 0 & 0 \\ 0 & \cos \delta_s & -\sin \delta_s \\ 0 & \sin \delta_s & \cos \delta_s \end{bmatrix} \quad (2.3)$$

$$\Delta_s = \begin{bmatrix} \cos \gamma_s & 0 & \sin \gamma_s \\ 0 & 1 & 0 \\ -\sin \gamma_s & 0 & \cos \gamma_s \end{bmatrix} \quad (2.4)$$

$$A_s = \begin{bmatrix} \cos \alpha & -\sin \alpha & 0 \\ \sin \alpha & \cos \alpha & 0 \\ 0 & 0 & 1 \end{bmatrix} \quad (2.5)$$

$$\mathbf{F}_s = A_s \Gamma_s \Delta_s \mathbf{S} \quad (2.6)$$

The vector components of the lander's weight  $F_p$  are computed by defining the general ground slope angles about X axis ( $\delta_g$ ) and Y axis ( $\gamma_g$ ) of LRF. A rotation matrix is defined for both the rotation about the X axis and the Y axis, according to Eq. (2.7–2.8), respectively. The rotation matrices are applied to the base weight vector  $\mathbf{W} = [0, 0, -F_w]$  to obtain the vector components of the lander's weight, according to Eq. (2.9).  $F_w = mg$  is the base weight force, where  $m$  is the lander's mass and  $g$  is the gravitational acceleration.

$$\Gamma_g = \begin{bmatrix} 1 & 0 & 0 \\ 0 & \cos \delta_g & -\sin \delta_g \\ 0 & \sin \delta_g & \cos \delta_g \end{bmatrix} \quad (2.7)$$

$$\Delta_g = \begin{bmatrix} \cos \gamma_g & 0 & \sin \gamma_g \\ 0 & 1 & 0 \\ -\sin \gamma_g & 0 & \cos \gamma_g \end{bmatrix} \quad (2.8)$$

$$\mathbf{F}_p = \Gamma_g \Delta_g \mathbf{W} \quad (2.9)$$

Eq. (2.10–2.11) show the vector form of the systems of equations to compute the reaction forces acting on the footpads for a 3-legged and a 4-legged lander, respectively. Lines 1-2 in Eq. (2.10–2.11) derive from the free body diagrams and represent equilibrium conditions with respect to LRF.

Line 3 in Eq. (2.10) represents the geometric conditions imposed by assuming that the lander behaves as a rigid body. This means that the relative distance between the footpads does not change. The geometric conditions bring to the assumption that the regular triangle shape does not change. There are several ways to define a regular triangle. The one selected is to impose that each side of the triangle has a constant length equal to the other ones, as shown in Figure 2.10.

Lines 3-5 in Eq. (2.11) represent the geometric conditions imposed by assuming that the lander behaves as a rigid body. This means that the relative distance between the footpads does not change. The geometric conditions bring to the assumption that the square shape does not change. There are several ways to define a square. The one selected is to impose that each diagonal has a constant length equal to the other one (line 3). Moreover, the two diagonals are imposed to be perpendicular each other, similarly for the sides of the square (line 4), as shown in Figure 2.11. Finally, all the footpads are imposed to lie on the same plane (line 5). This is obtained by imposing that the determinant of matrix  $A$  (i.e. the matrix defining the equation of a plane passing through the four footpads) is equal to zero.

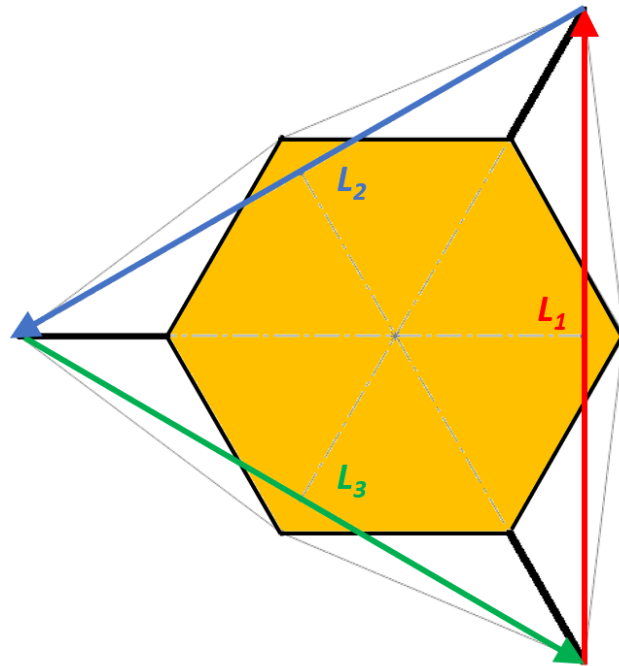


**Figure 2.10** Vectors joining the lander's footpads for the 3-legged lander. Qualitative scheme, not to scale.

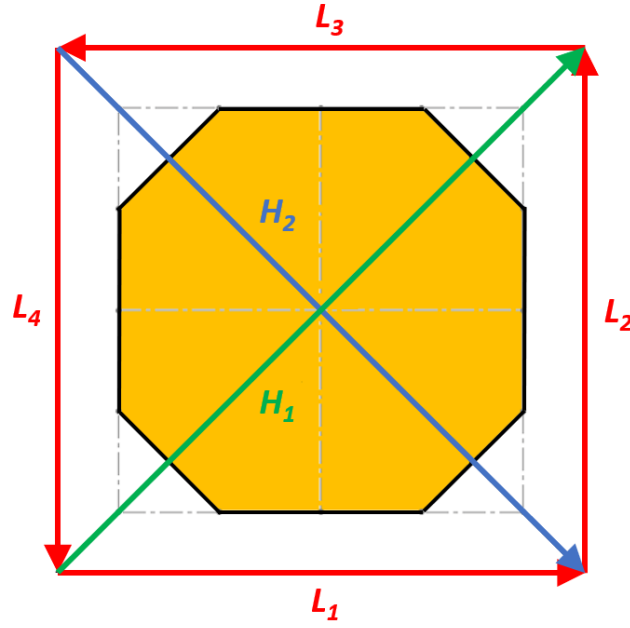


**Figure 2.11** Vectors joining the lander's footpads for the 4-legged lander. Qualitative scheme, not to scale.

$$\begin{cases} \sum_{n=1}^3 \mathbf{R}_n + \mathbf{F}_s + \mathbf{F}_p = 0 \\ \sum_{n=1}^3 \mathbf{D}_n \times \mathbf{R}_n + \mathbf{D}_s \times \mathbf{F}_s + \mathbf{D}_p \times \mathbf{F}_p = 0 \\ \|\mathbf{L}_1\|_2 = \|\mathbf{L}_2\|_2 = \|\mathbf{L}_3\|_2 = c \end{cases} \quad (2.10)$$

$\mathbf{R}_n = (R_{n_x}, R_{n_y}, R_{n_z})$  Reaction force vector acting on  $n$ -th footpad

$\mathbf{F}_s = (F_{s_x}, F_{s_y}, F_{s_z})$  Sampling force vector

$\mathbf{F}_p = (F_{p_x}, F_{p_y}, F_{p_z})$  Lander weight vector

$\mathbf{D}_1 = \mathbf{D}_2 = (D_{x_1}, D_y, 0)$  Footpads position vector 1

$\mathbf{D}_3 = (D_{x_2}, 0, 0)$  Footpads position vector 2

$\mathbf{D}_s = (P_x, P_y, 0)$  Sampling spot position vector

$\mathbf{D}_p = (C_{G_x}, C_{G_y}, C_{G_z})$  Center of Gravity position vector

$D_{x_1} = (D + L_g) \sin \frac{\pi}{6}$  X coordinate of footpads 1-2, dependent on lander geometric parameters  $D$  and  $L_g$  (Figure 2.2 to Figure 2.5)

$D_{x_2} = (D + L_g)$	X coordinate of footpad 3, dependent on lander geometric parameters $D$ and $L_g$ (Figure 2.2 to Figure 2.5)
$D_y = (D + L_g) \sin \frac{\pi}{3}$	Y coordinate of footpads 1-2, dependent on lander geometric parameters $D$ and $L_g$ (Figure 2.2 to Figure 2.5)
$c = 2D_y$	Length of each side of the regular triangle having the footpads as vertices
$\left\{ \begin{array}{l} \sum_{n=1}^4 \mathbf{R}_n + \mathbf{F}_s + \mathbf{F}_p = 0 \\ \sum_{n=1}^4 \mathbf{D}_n \times \mathbf{R}_n + \mathbf{D}_s \times \mathbf{F}_s + \mathbf{D}_p \times \mathbf{F}_p = 0 \\ \ \mathbf{H}_1\ _2 = \ \mathbf{H}_2\ _2 = b \\ \mathbf{H}_1 \cdot \mathbf{H}_2 = \mathbf{L}_1 \cdot \mathbf{L}_2 = \mathbf{L}_3 \cdot \mathbf{L}_4 = 0 \\  A  = 0 \end{array} \right. \quad (2.11)$	
$\mathbf{R}_n = (R_{n_x}, R_{n_y}, R_{n_z})$	Reaction force vector acting on $n$ -th footpad
$\mathbf{F}_s = (F_{s_x}, F_{s_y}, F_{s_z})$	Sampling force vector
$\mathbf{F}_p = (F_{p_x}, F_{p_y}, F_{p_z})$	Lander weight vector
$\mathbf{D}_1 = \mathbf{D}_2 = \mathbf{D}_3 = \mathbf{D}_4 = (D_g, D_g, 0)$	Footpads position vector
$\mathbf{D}_s = (P_x, P_y, 0)$	Sampling spot position vector
$\mathbf{D}_p = (C_{G_x}, C_{G_y}, C_{G_z})$	Center of Gravity position vector
$D_g = (c + L_g) \sin \frac{\pi}{4}$	X, Y coordinate of footpads 1-4, dependent on lander geometric parameters $D$ , $d$ and $L_g$ (Figure 2.6 to Figure 2.9)
$b = 2(c + L_g)$	Length of the diagonal of the square having the footpads as vertices, dependent on lander geometric parameters $D$ , $d$ and $L_g$ (Figure 2.6 to Figure 2.9)
$c = \frac{D}{2} \left( \sqrt{2} - \cos \frac{\pi}{4} \right) + \frac{d}{2} \cos \frac{\pi}{4}$	Constant adopted to simplify the notation, dependent on lander geometric parameters $D$ and $d$ (Figure 2.6 to Figure 2.9)

To exploit the geometric conditions in Eq. (2.10–2.11), it is required to link those equations with the variables to be computed (i.e. the reaction forces  $R$ ). For this reason, the point of contact between each footpad and the ground was modeled via three springs along the three Cartesian axes. It is assumed that the springs have all the same constant stiffness  $k$ . Given this assumption, it was found that the physical solution of Eq. (2.10–2.11) is independent on the value of the spring stiffness. The reaction forces can be related to the displacement  $d$  of the lander's footpads via Eq. (2.12).

$$R = k d \quad (2.12)$$

The goal is the evaluation of the maximum allowed magnitude of the sampling force  $F_s$  that prevents the lander changing its equilibrium state. Therefore, the sampling force  $F_s$  represents the independent variable, while the reaction forces represent the dependent variable. Eq. (2.10–2.11) were symbolically solved to get the explicit dependence of the reaction forces from the sampling force,  $R_n = f(F_s)$ . The maximum allowed sampling force is defined such that the reaction forces  $R_n$  do not overcome a certain pre-defined limit force. According to Eq. (2.13–2.14), the limit force is computed by defining a margin for the reaction forces. The limit force  $L_{xy}$  is applied to prevent the lander from sliding in the XY plane. The limit force  $L_z$  is applied to prevent the lander from lifting off the XY plane (i.e. the ground).

The limit force  $L_{xy}$  is defined by applying a margin  $M_{xy}$  with respect to the friction force  $F_a$ , which is the boundary for the incipient motion of the lander. According to Eq. (2.15), the friction force is defined with respect to the Z component of the  $n$ -th reaction force through the coefficient of friction  $\mu$  between the lander's footpad and the ground. The limit force  $L_z$  is defined by applying a margin  $M_z$  with respect to a pre-defined minimum value for the Z component of the reaction force ( $K_z$ ).

Margins  $M_{xy}$  and  $M_z$  can get any positive real value, where a value equal to 0 means a margin of 0%, a value of 1 means a margin of 100%, etc.

$$L_{xy} = \frac{F_a}{(1 + M_{xy})} \quad (2.13)$$

$$L_z = K_z(1 + M_z) \quad (2.14)$$

$$F_a = \mu R_{nz} \quad (2.15)$$

The limit force  $L_{xy}$  depends on the sampling force  $F_s$  through the Z component of the reaction force  $R_{nz}$ . On the other hand, the limit force  $L_z$  is pre-defined.

The maximum allowed magnitude of the sampling force  $F_s$ , named  $F_{s_{max}}$ , is evaluated by minimizing the objective functions defined by Eq. (2.16–2.17).

$$J_{xy} = (L_{xy} - R_{n_{xy}})^2 \quad (2.16)$$

$$J_z = (L_z - R_{n_z})^2 \quad (2.17)$$

Where  $R_{n_{xy}} = \sqrt{R_{n_x}^2 + R_{n_y}^2}$

The objective functions are convex, meaning that they have a global minimum (Figure 2.12). The minimization problem is defined according to Eq. (2.18–2.19).

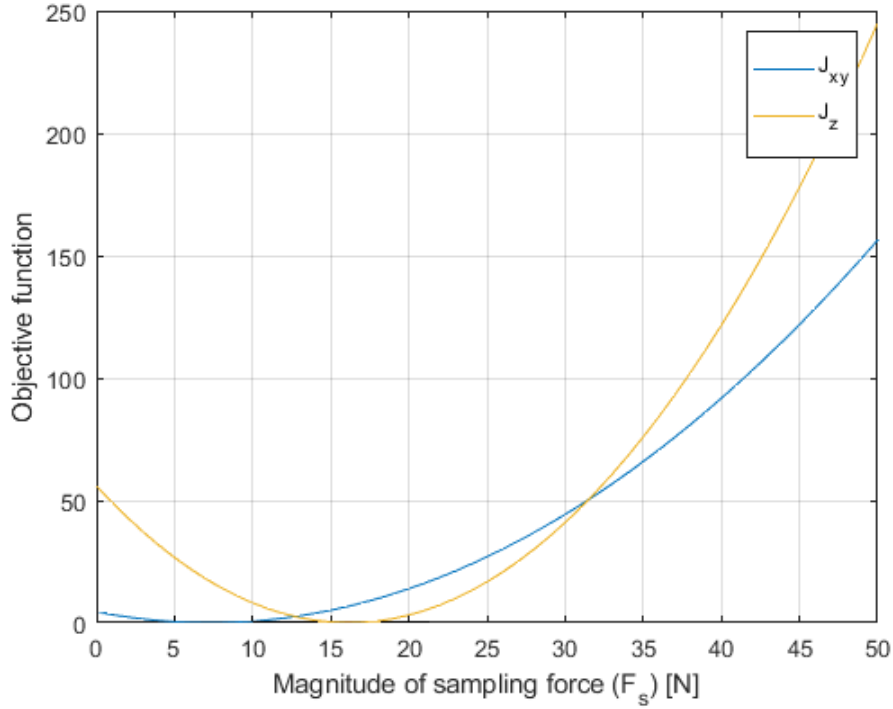


**Figure 2.12** Example of convex objective functions.

$$(F_{s_{max}})_{xy} = \min_{F_s} J_{xy}(F_s) \text{ such that } F_{s_1} < F_s < F_{s_2} \quad (2.18)$$

$$(F_{s_{max}})_z = \min_{F_s} J_z(F_s) \text{ such that } F_{s_1} < F_s < F_{s_2} \quad (2.19)$$

The minimization problem is solved by using the MATLAB function `fminbnd`, which finds the minimum of a single-variable function on a fixed interval [75] [76]. As a conservative approach, the minimum value among the two

computed by solving the minimization problems is selected, according to Eq. (2.20).

$$F_{smax} = \min \left( (F_{smax})_{xy}, (F_{smax})_z \right) \quad (2.20)$$

$F_{smax}$  is obtained with respect to a specific condition, since all the parameters (i.e. environmental, physical, geometrical) except the sampling force  $F_s$  are defined prior solving the minimization problem. At different environmental, physical, or geometrical conditions correspond different values of  $F_{smax}$ . By exploring the parameters' space, it is possible to derive the DE of the lander. Three kinds of parameters are used to define the DE: dependent, independent and boundary.

The dependent parameters represent the output whose variation is used to determine the equilibrium condition. In this case, the dependent parameters are the reaction forces  $R_n$  acting on the lander's footpads. The margin  $M_{xy}$  on the value of the friction force  $F_a$  is used to define the limit  $L_{xy}$  of the DE in the XY plane. In fact, the friction force determines the boundary for the incipient motion of the lander. On the other hand, the margin  $M_z$  on the null value of the Z component of the reaction force is used to define the limit  $L_z$  of the DE along the Z axis. In fact, the null value represents the boundary for the incipient lifting of the lander.

The independent parameters represent inputs that affect the dependent parameters, in this case represented by the magnitude of the sampling force  $F_s$ .

The boundary parameters represent all the inputs not directly involved in the minimization process. Such parameters include.

- **Environmental parameters**
  - Gravitational acceleration ( $g$ )
  - General ground slope about X, Y axes ( $\delta_g, \gamma_g$ )
  - Local ground slope about X, Y axes at the sampling spot ( $\delta_s, \gamma_s$ )
  - Footpad-to-ground coefficient of friction ( $\mu$ )
- **Physical and geometrical parameters of the lander**
  - Mass ( $m$ )
  - Length of the leg's projection in the XY plane ( $L_g$ )
  - Length of the body's side ( $D$ )
  - Cartesian components of the  $C_G$  position ( $C_{G_{x,y,z}}$ )
  - Margin on the reaction forces ( $M_{xy,z}$ )

- **Physical and geometrical parameters of the sampling**
  - Cartesian components of the position of the sampling spot ( $P_{x,y}$ )
  - Inclination of the sampling force with respect to the ground ( $\beta$ )

By changing the boundary parameters, it is possible to explore several environmental conditions as well as several physical and geometrical configurations related to both lander and sampling (Figure 2.13). Among potential sampling systems, it should be mentioned that highly dynamic systems such as drills are probably less suited to the application of the technique presented in this dissertation. Future developments of the tool will aim to include the capability to address the investigation of such sampling systems.

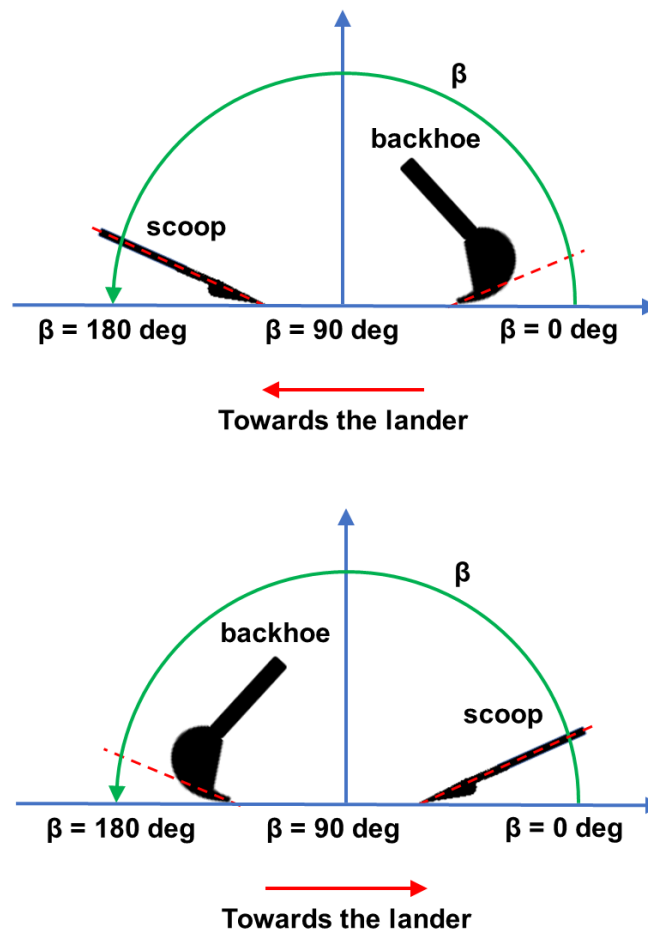


**Figure 2.13** Some sampling system configurations that might be explored in MISTRAL by changing the  $\beta$  angle.

### 2.1.3 Application to NASA's Phoenix Mars lander mission

This paragraph presents the application of MISTRAL to real mission data from the NASA's Phoenix Mars lander.

The Phoenix lander touched down on 25 May 2008 in the Green Valley, a high latitude Mars region, and operated until 2 November 2008, acquiring data during 152 sols (Mars days) of operations. The Phoenix lander was equipped with a 2.4 m RA with an Icy Soil Acquisition Device (ISAD) (Figure 2.14). The ISAD is composed by a scoop capable of excavating trenches, a scraper blade for hard soils and a rasp tool [77] [78].

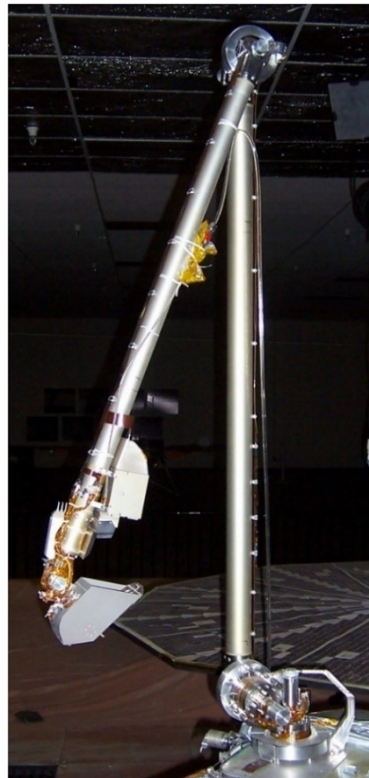


**Figure 2.14** Engineering model of the Phoenix lander RA and ISAD. Credits: NASA/University of Arizona

Several trenches were excavated and resistive forces during backhoe operations were derived. The highest forces registered during mission operations are shown in Table 2.2.

**Table 2.2** Force peaks registered during Phoenix Mars lander operations. The name highlights the denomination of the excavation site followed by a number indicating the reference sol (Mars day).

Name	Force magnitude [N]	Force component	Reference
Dodo-Goldilocks 116-1	70	Normal to surface	[77] [78]
Dodo-Goldilocks 116-2	75	Normal to surface	[79]
Stone Soup 74, 76, 85, 88	100	Total force in the excavation plane	[79]

The procedure presented here aims to check that the force peaks lie inside the DE of the Phoenix lander, as obtained by using MISTRAL. Therefore, the first step is the computation of the DE. The values of the MISTRAL parameters are shown in Table 2.3.

It was assumed that the body of the Phoenix lander has a regular hexagonal shape. Given this assumption, the length of the body's side ( $D$ ) was derived from [80].

The length of the leg's projection in the XY plane ( $L_g$ ) was assumed from [78] by considering a proportion with respect to the lander's deck diameter [80].

The X, Y components of the  $C_G$  position ( $C_{G_{x,y}}$ ) were assumed coincident with the LRF origin, while the Z component ( $C_{G_z}$ ) was assumed by considering the lander's height [80].

The lander's mass was derived from [80].

The sampling system of the Phoenix lander is a backhoe. The inclination of the sampling force with respect to the ground ( $\beta$ ) was derived from [79] and converted according to the convention of Figure 2.13.

A 100% margin on X, Y, Z components of the reaction forces ( $M_{x,y,z}$ ) was assumed.

The general slope of the ground was assumed only about Y axis ( $\gamma_g$ ), while the slope about X axis ( $\delta_g$ ) was assumed negligible. The local slopes of the ground at the sampling spot ( $\gamma_s, \delta_s$ ) were also assumed negligible.

The footpad-to-ground coefficient of friction ( $\mu$ ) was derived from the angle of internal friction of the soil ( $\varphi$ ) through the Coulomb's law  $\mu = \tan \varphi$  [81]. Since the angle of internal friction is  $38 \text{ deg} \pm 5 \text{ deg}$  [79], the coefficient of friction was found varying in the range  $0.65 \div 0.93$ .

The sampling spot was assumed varying within the RA workspace derived from [78]. The workspace is delimited by an upper and a lower end, and by an inner and an outer circular sector centered in the RARF origin (Figure 2.16). The inner and outer circular sectors have a radius of 1.52 m and 2.14 m, respectively. The radius of the outer circular sector was derived from [78], while the radius of the inner circular sector was assumed by considering a proportion with respect to the outer radius. The upper and lower ends were assumed spanning across a 90 deg angle.

The scenario assumed for the Phoenix lander is shown in Figure 2.15 and Figure 2.16. Such a situation might be considered a worst-case scenario, since the lander is pulled downhill by the RA.

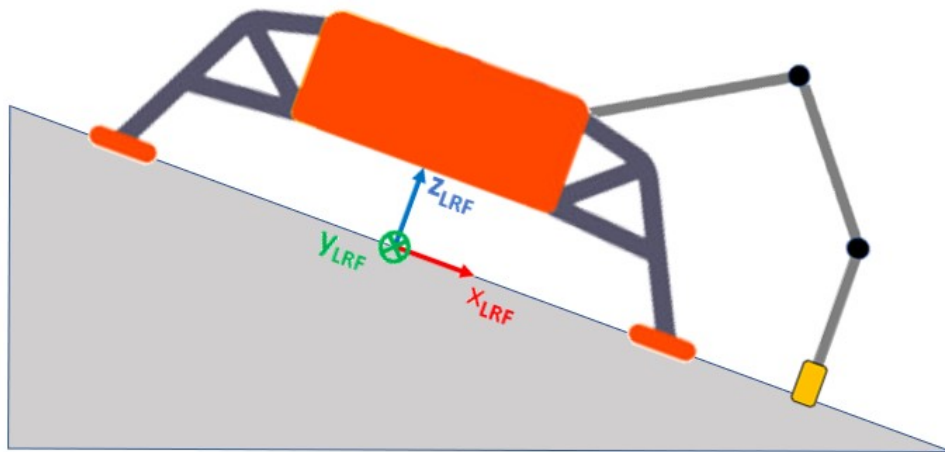


**Figure 2.15** Phoenix lander worst-case scenario. The lander is inclined about the Y axis and pulled downhill during backhoe operations. Qualitative scheme, not to scale.

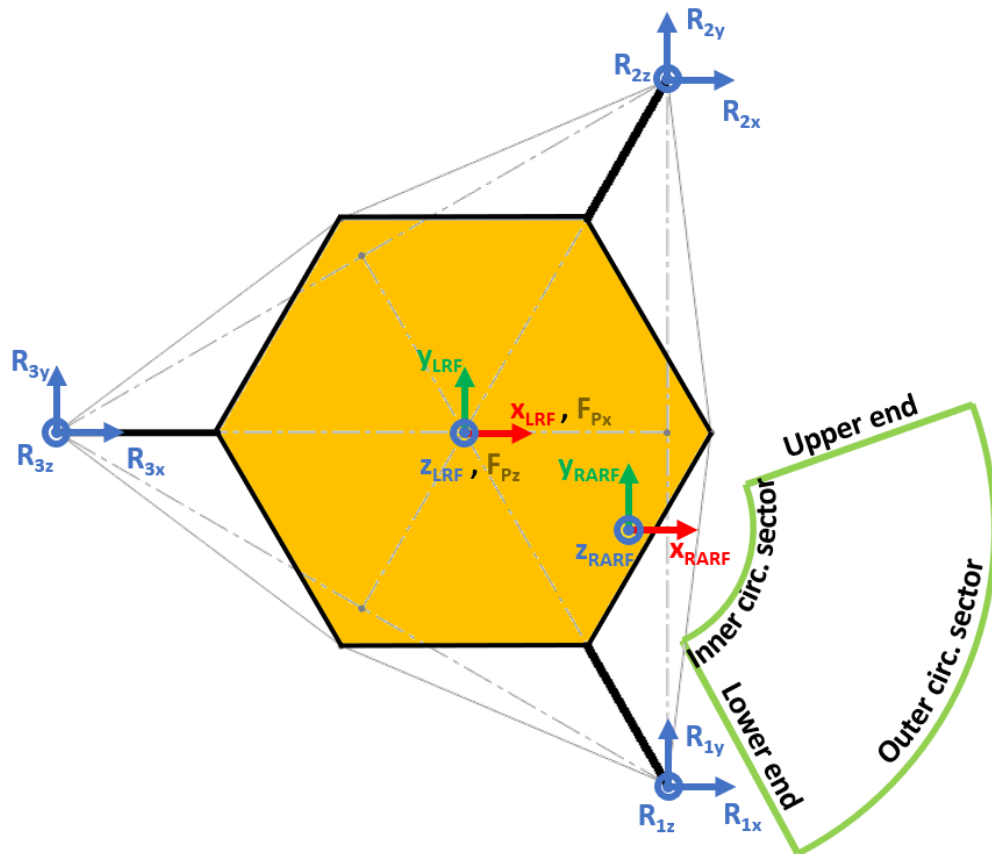


**Figure 2.16** Phoenix lander configuration. The sampling spot lies inside the area delimited by the green lines. Qualitative scheme, not to scale.

**Table 2.3** Values of MISTRAL parameters for the Phoenix lander case study.

Constant parameters	
Environmental parameters	Value
Gravitational acceleration ( $g$ )	3.72 m/s <sup>2</sup>
Slope of the ground about X axis ( $\delta_g$ )	0 deg
Local slope of the ground about X axis at the sampling spot ( $\delta_s$ )	0 deg
Local slope of the ground about Y axis at the sampling spot ( $\gamma_s$ )	0 deg
Physical and geometrical parameters of lander	Value
Length of the leg's projection in the XY plane ( $L_g$ )	0.2 m
Length of the body's side ( $D$ )	0.75 m

[X, Y, Z] components of the $C_G$ position ( $C_{G_{x,y,z}}$ )	[0, 0, 1] m
Margin on the reaction forces ( $M_{xy,z}$ )	[1, 1]
Mass ( $m$ )	350 kg
<b>Physical and geometrical parameters of sampling</b>	<b>Value</b>
Inclination of the sampling force with respect to the ground ( $\beta$ )	33.9 deg
<b>Variable parameters</b>	
<b>Environmental parameters</b>	<b>Range</b>
Slope of the ground about Y axis ( $\gamma_g$ )	(0 ÷ 20) deg
Footpad-to-ground coefficient of friction ( $\mu$ )	0.65 ÷ 0.93
<b>Physical and geometrical parameters of sampling</b>	<b>Range</b>
[X, Y] components of the position of the sampling spot ( $P_{x_1,y_1}$ )	Derived according to the definition of the RA workspace.

The DE obtained by using MISTRAL is shown in Figure 2.17, where each line represents the locus of the points where the magnitude of the sampling force  $F_s$  is maximum, according to the defined margin. The DE was defined with respect to the ground slope since this environmental parameter is particularly crucial to surface operations. Several max- $F_s$  lines were obtained by changing the variable parameters within the defined ranges. The DE is defined as the area underlying a max- $F_s$  line. The DE of the Phoenix lander was selected as the area underlying the lowest max- $F_s$  line, considered as a worst-case scenario (light blue area in Figure 2.17).

To plot data points reported in Table 2.2, they have to be first converted to represent the total magnitude of the sampling force, according to the input required to build the DE. Since the original Stone Soup point represents the total force in the excavation plane, it was assumed that it already represents the required input. On the other hand, the original Dodo-Goldilocks points  $F_{s_o}$  represent the normal force, so they have to be converted into the required input through the inclination of the sampling force with respect to the ground ( $\beta$ ). The new value  $F_{s_n}$  is obtained through the equation  $F_{s_n} = F_{s_o} / \sin \beta$ . The values of the plotted data points are reported in Table 2.4.

The ground slope selected to plot the data points has a value of 7 deg, reported as the average value at the landing site [82] [83].

Figure 2.17 shows that the data points lie inside the DE of the Phoenix lander, confirming the quality of the tool's results even considering the worst-case scenario.

**Table 2.4** Data point values converted according to the input required to build the DE.

Name	Force magnitude [N]
Dodo-Goldilocks 116-1	125.5
Dodo-Goldilocks 116-2	134.5
Stone Soup 74, 76, 85, 88	100

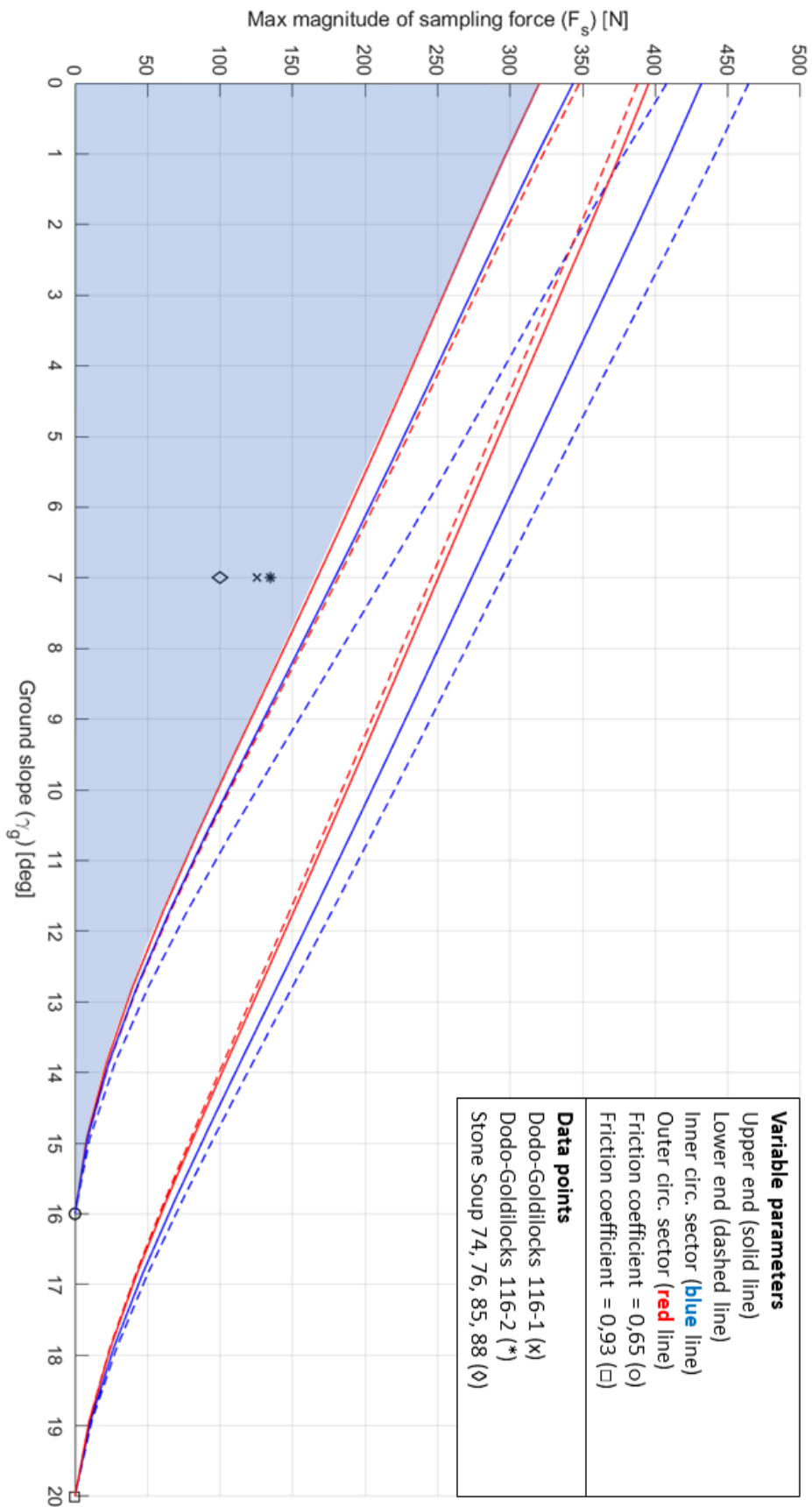


Figure 2.17 Plot of the DE of Phoenix lander together with the data points.

## 2.2 Application of MISTRAL to potential Enceladus lander mission

This paragraph presents the application of MISTRAL to a potential Enceladus lander mission.

The Enceladus low gravity environment represents a great challenge for lander stability because of the severe limit on the allowable reacted load from the sampling system to the lander. Therefore, a critical task is the evaluation of the effect of the forces the sampling system might apply to the lander while performing the sampling operations.

Two lander configurations were studied, a 3-legged and a 4-legged lander. The variable parameters selected are the lander's mass, the distance of the sampling spot and the footpad-to-ground coefficient of friction. By exploring the space of the variable parameters, it is possible to derive the DE.

The scenario under investigation is shown from Figure 2.18 to Figure 2.20, and it was assumed to be a worst-case scenario, since the lander is pushed downhill by the RA. The RARF is assumed being coincident with the LRF, and the sampling force plane is aligned with the X axis. The goal is to avoid the lander to slide downhill, so the friction force along X axis is the driver to calculate the max sampling force within the defined margin.

Values chosen for model parameters are shown in Table 2.5.

DEs obtained are shown in Figure 2.21 and Figure 2.22.

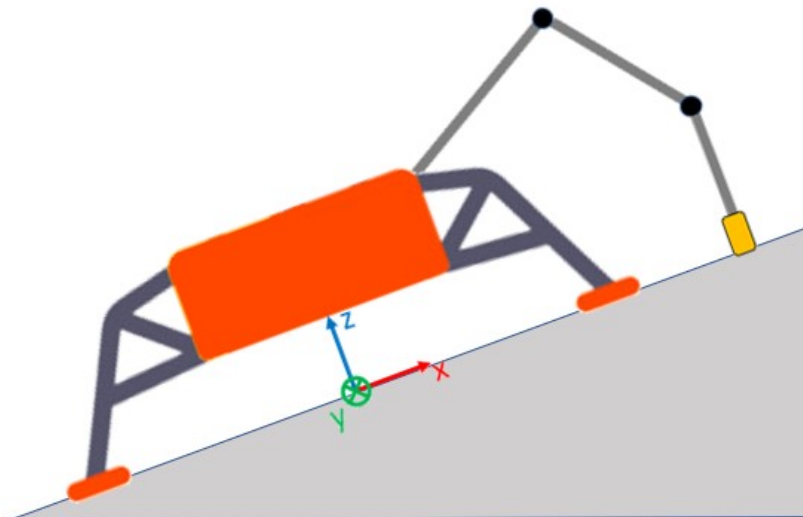


**Figure 2.18** Enceladus lander worst-case scenario. The lander is inclined about the Y axis and pushed downhill during sampling operation. Qualitative scheme, not to scale.

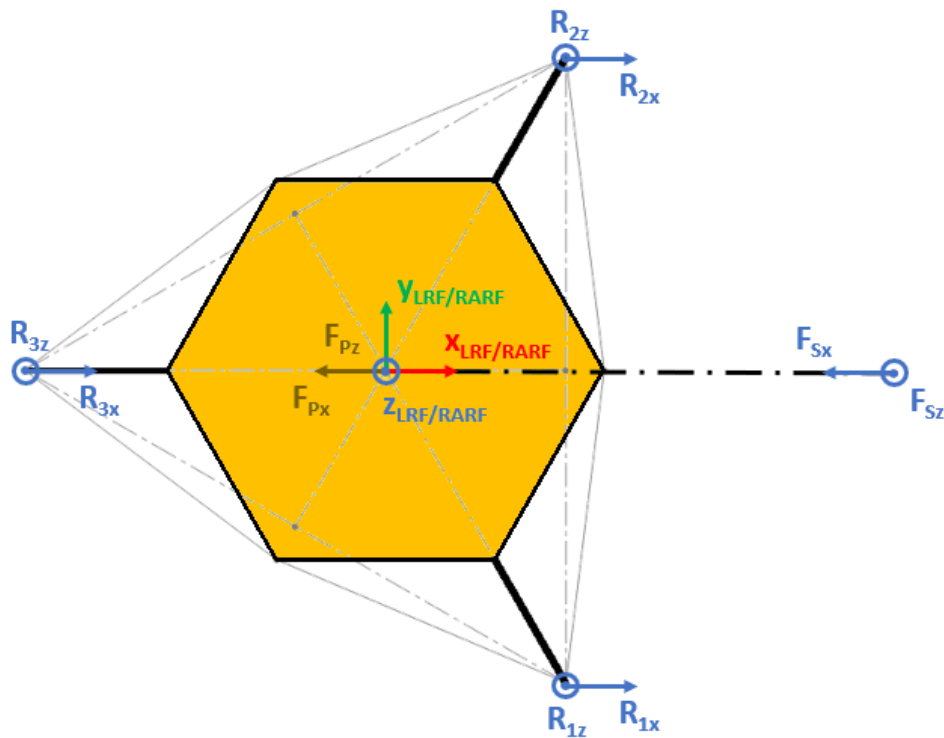


**Figure 2.19** 3-legged lander configuration for the Enceladus lander case study. Qualitative scheme, not to scale.

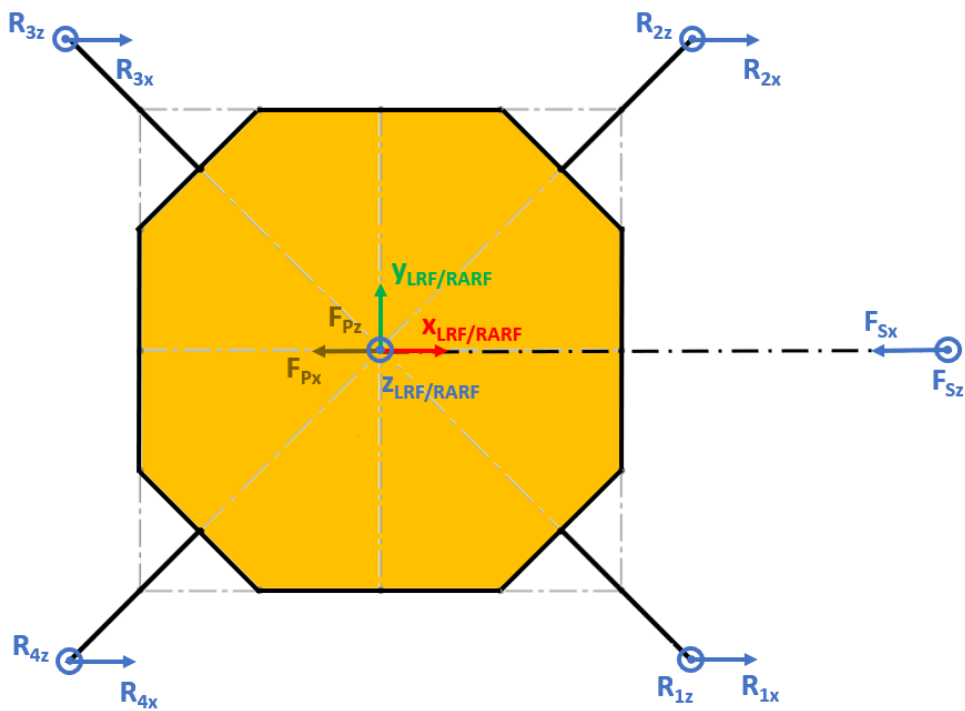


**Figure 2.20** 4-legged lander configuration for the Enceladus lander case study. Qualitative scheme, not to scale.

**Table 2.5** Values of MISTRAL parameters for the Enceladus lander case study.

Constant parameters	
Environmental parameters	Value
Gravitational acceleration ( $g$ )	0.113 m/s <sup>2</sup>
Slope of the ground about X axis ( $\delta_g$ )	0 deg
Local slope of the ground about X axis at the sampling spot ( $\delta_s$ )	0 deg
Local slope of the ground about Y axis at the sampling spot ( $\gamma_s$ )	0 deg
Physical and geometrical parameters of lander	Value
Length of the leg's projection in the XY plane ( $L_g$ )	0.5 m
Length of the body's side ( $D$ )	1 m
[X, Y, Z] components of the $C_G$ position ( $C_{G_{x,y,z}}$ )	[0, 0, 1] m
Margin on the reaction forces ( $M_{xy,z}$ )	[1, 1]
Physical and geometrical parameters of sampling	Value
Y component of the position of the sampling spot ( $P_y$ )	0 m
Inclination of the sampling force with respect to the ground ( $\beta$ )	175 deg
Variable parameters	
Environmental parameters	Range
Slope of the ground about Y axis ( $\gamma_g$ )	(0 ÷ -20) deg
Footpad-to-ground coefficient of friction ( $\mu$ )	0.5 ÷ 1
Physical and geometrical parameters of lander	Range
Mass ( $m$ )	(300 ÷ 500) kg
Physical and geometrical parameters of sampling	Range
X component of the position of the sampling spot ( $P_x$ )	(2 ÷ 6) m

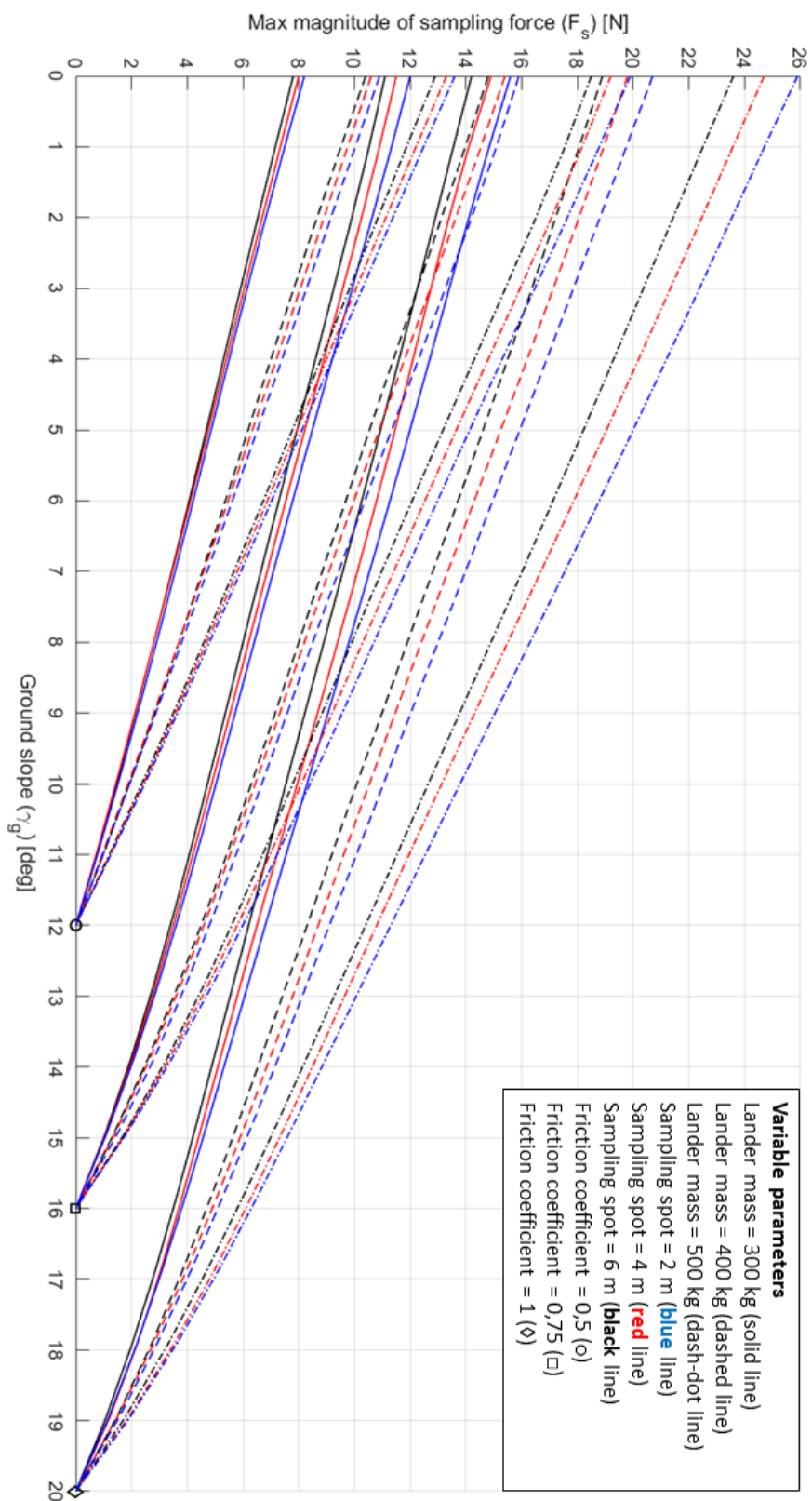
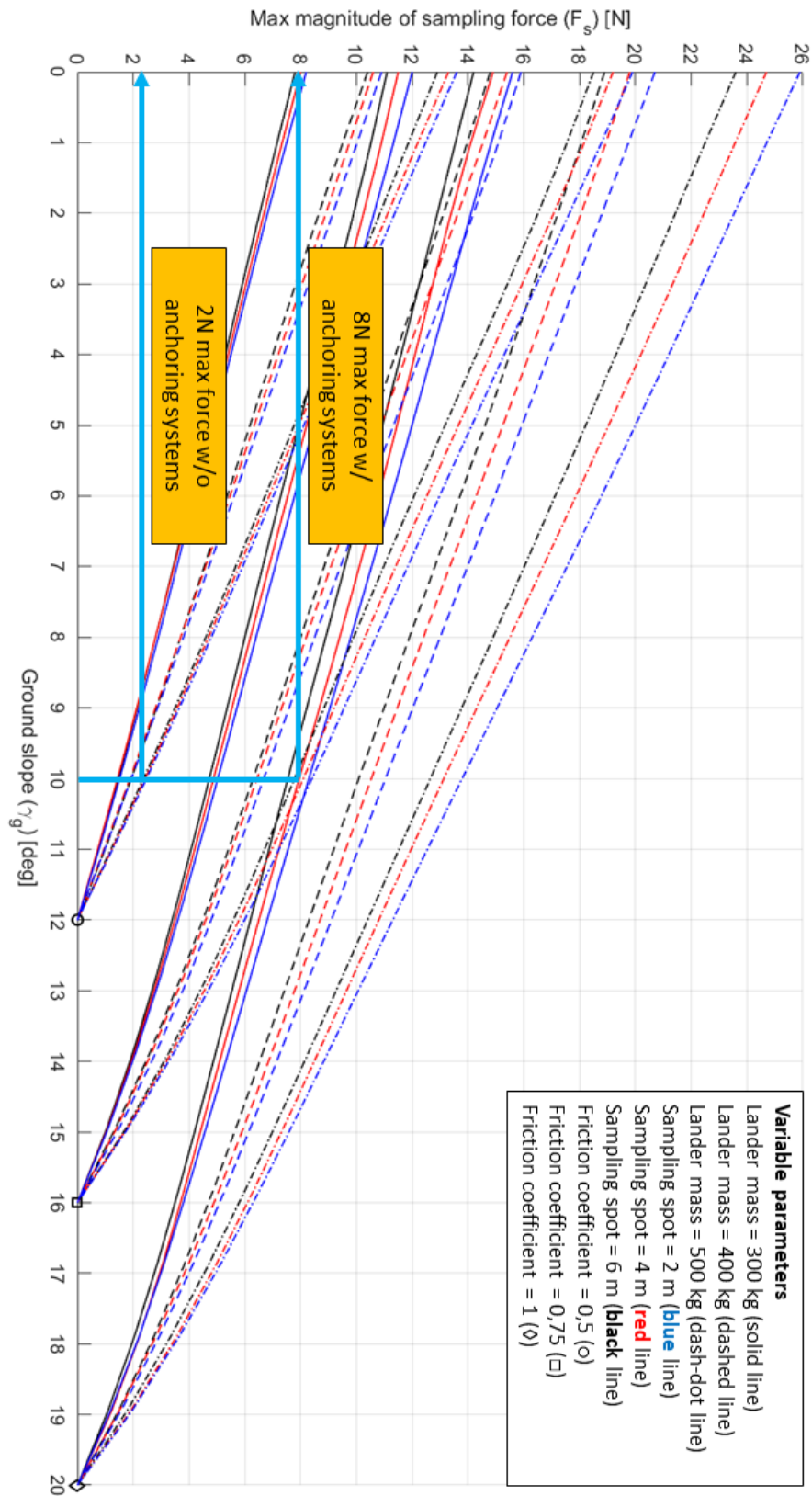


Figure 2.21 DE of 3-legged lander for the Enceladus lander case study. The ground slope is reported in absolute values for convenience.



DE plots were conceived to rapidly assess the high-level requirements of a sampling system. However, benefits of using MISTRAL are much greater. Since the model used to build the DE considers the coupling among sampling parameters, lander parameters, and environmental parameters, it is possible to use the plots to infer high-level requirements concerning other lander systems.

From plots of Figure 2.21 and Figure 2.22 it is possible to derive not only a requirement on the sampling system, but also a requirement on the footpads, a critical system to guarantee lander's stability. By assuming a lander's mass of 500 kg, a 2-m-long RA, and an average ground slope of 10 deg, it is possible to derive that a footpad-to-ground coefficient of friction equal to 0.5 allows an incredibly low maximum  $F_s$  (i.e. about 2 N). By increasing the coefficient of friction to 0.75 it is possible to sustain a maximum  $F_s$  four times greater (i.e. about 8 N) (Figure 2.23). A higher footpad-to-ground coefficient of friction can be achieved by adding heated pins as anchoring system with the purpose to increase resistance to lander footpad sliding. These heated pins (6 mm diameter and 80 mm long) create a V-shaped hole in the ice for the pins to rest in. Preliminary laboratory testing showed the interaction can be modelled as a point sliding up a frictionless slope (due to radiation, the walls are not vertical). This turns into the definition of a requirement for both the sampling system (i.e. maximum allowed sampling force of about 8 N) and the lander system (i.e. footpad-to-ground coefficient of friction of about 0.75).



**Figure 2.23** Use of the DE for system design. Example for the 3-legged lander configuration.

# Chapter 3

## 3 Investigation of sampling system concepts

Part of the content of the present chapter was published in [55] [84].

### 3.1 Introduction

The sample chain is the sequence of steps (Figure 3.1) to acquire a sample from pristine environment and is typically composed of the following phases.

- *Sampling*, that is the operation of breaking up and/or disturbing the pristine material to get the sample.
- *Collection*, that is the operation of gathering the sample.
- *Transfer*, that is the operation of transporting the sample from one location to another.
- *Measurement*, that is the operation of measuring the quantity of sample collected in terms of mass, volume, etc.
- *Deposit*, that is the operation of delivering the sample to its destination (e.g. a science instrument, a storing capsule, etc.)

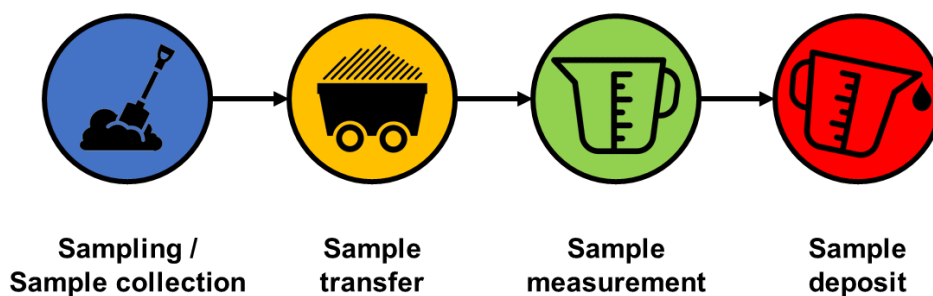


*Figure 3.1 Steps of a typical sample chain.*

This chapter focuses on the investigation of sampling systems required to fulfill the requirements of the first phase (i.e. sampling) of the sample chain.

As shown in previous chapters, the low surface gravity of Enceladus represents a new challenge for surface sampling that is not met by sampling systems developed for microgravity (e.g. comets and asteroids) or higher gravity (e.g. Europa 13%g, Moon 16%g, or Mars 38%g) environments.

A study was conducted to explore various sampling systems that could be used by an in-situ lander mission. The focus was on devices that operate with a low reaction force, entail low energy consumption, are robust to low gravity and are compatible with stringent planetary protection and contamination control requirements. Several sampling devices were developed or adapted and then tested in simulated conditions that resemble the Enceladus surface properties. The combination of the low deposition rate of plume fallback material and the very low surface temperature (i.e. approximately 80 K) results in a very slow sintering rate. As a consequence, the surface material is likely weak and highly porous [42] [85]. To account for potentially greater sintering rates and the resulting wide range of surface material strengths, the sampling system was developed to be able to sample surface materials between 400 kPa and 12 MPa CPT (Cone Penetration Test) and 40-95% porosity [85].

The sample acquisition requirements identified fall in the following categories and are summarized below.

- Science instrument (OS)
- Sample integrity (SI)
- Astrobiology science (AS)
- Engineering, Environment, Architecture (EE)

### **Sample**

- Acquire and transfer at least 10 samples (OS)
- Acquire sample within 10 mm depth (AS)
- Sample particle longest linear length will be no greater than 5mm (OS)
- Samples volumes will be between 1 cc and 5 cc (OS)
- Verify sample volume delivered to the science instrument (SI)
- At least 60% of sample will be acquired within 10 mm of the surface (AS)

### **Sample integrity**

- Sample will be maintained below 140 K (SI)
- Sampling system shall be contamination control compatible (SI)
- No more than 25% of sample particles can have shortest dimension smaller than 50 $\mu$ m (AS)

### Surface mechanical properties

- Be able to acquire sample from material with the following range of properties (full range of properties described by simulant suite)
- Sub-rounded to angular granular material (SP)
- Porosity between 40% and 95% (SP)
- Weak, rounded, unconsolidated material, of zero effective sintering (SP)
- Non-cohesive material low end strength of 400 kPa CPT, 95% porosity (SP)
- Cohesive material high end strength of 12 MPa CPT, 40% porosity (SP)

### Science instrument interface

- Deliver to and be compatible with JPL's OWLS instrument to be located on lander with minimal and allowable interface requirements to be levied on the OWLS instruments (OS). Further details about OWLS instrument are presented in paragraph 5.8.

### Hardware System, Environments and Spacecraft

- Produce a reaction force to lander less than 8 N horizontal (see full allowable loads envelope for combined force charts) (EE)
- Consume low energy compatible with a battery powered surface phase (EE)
- Sampling operation and hardware compatible with Enceladus surface environment, including vacuum,  $0.113 \text{ m/s}^2$  gravity and 70 K (EE)

The potentially strong material of 12 MPa precludes the use of sampling systems that only work for weak materials such as the TAGSAM sampler of the OSIRIS-REx mission or the CAESAR comet surface sample return mission sampling system [86] [87]. The requirement of low reacted force to the lander precludes the use of sampling systems that require higher reacted loads such as the Mars Science Laboratory powder drill (i.e. 300 N preload) [88] and the proposed Europa Lander mission baseline counter-rotating saws and rasp with currently assumed 50 N maximum reacted loads. The BiBlade developed for comet surface sampling [89] [90] and Brush Wheel Sampler developed for asteroid surface sampling [91] were designed for higher reacted loads that are available in a Touch-And-Go (TAG) mission architecture where spacecraft inertia reacts sampling forces in the order of 1000s N. The Rosetta mission Philae lander rotary drill SD2 would only acquire very weak material, and as a drill, would be poorly suited for collecting surface material [92]. The Phobos Grunt mission had the CHOMIK percussive drive tube sampler [93], but as a drive tube it is designed

to primarily collect subsurface samples. The requirement on low sampling depth and particle size precludes the use of sampling systems based on momentum transfer such as the bullets fired by the Hayabusa 2 mission to break up and loft particles into a collection canister [94].

## 3.2 Simulants

A fundamental step in the development of a sampling system is the definition of appropriate simulants and analogues representative of the surface properties expected. Enceladus surface evolved in unique environmental conditions (i.e. vacuum, cryogenic temperatures and solar irradiation) that are difficult to reproduce on Earth for simulant production and sampling system verification testing. For this reason, the first objective was to produce simulants in ambient conditions (i.e. standard temperature, pressure and illumination) that can be made representative of the Enceladus surface properties by investigating related micron-scale ice particle sintering [85]. The design and production of the mechanical strength of the simulant was based on the description of potential Enceladus surface microstructure morphology. These simulants were intended to be preliminary and to aid in early sampling system testing prior to intensive study of laboratory ice analogues.

The simulant parameters were chosen based on the best understanding of Enceladus' range of possible surface properties, and specifically considering the needs of the sampling tools under development (e.g. considering strong and very weak materials for worst case scenarios) in making these choices.

The simulants were developed to have the following microstructure properties.

- Granular, cohesive type bulk structure.
- Micro-structure to be of particles bonded to neighboring touching particles (i.e. necking type shape to contacting particles).
  - About 10-100  $\mu\text{m}$  grain size with narrow size range (poorly graded).
  - Rounded or sub-rounded particle shape.
  - Particles of high strength material.
  - Particle-particle bonding method to be high strength and brittle while maintaining adequate minimum necking and porosity.
  - Brittle failure.
  - 35 to 45% porosity.

A specific value of strength was not prescribed since laboratory measurements of Enceladus icy analogues have not been made yet. There are efforts currently underway at JPL to produce such analogs and to measure

strength in-situ within the Icy Bodies Simulation (IBoS) environmental chamber (Figure 3.2). The IBoS chamber was designed and fabricated for use in generating and evolving icy body materials to represent the Enceladus surface. Micron-scale particles will be produced and subject to Enceladus thermal and vacuum conditions and the evolving mechanical properties will be measured via cone penetrometer.

Four pervious concrete mixes were selected as ambient simulants. Two were of about 100  $\mu\text{m}$  mean particle size (i.e. very fine-grained) and two were of about 400  $\mu\text{m}$  mean particle size (i.e. fine-grained). Each of the grain size simulants had a 2.5 MPa and 4.5 MPa UCS (Unconfined Compressive Strength), 2 inches cube in compression (Figure 3.3).

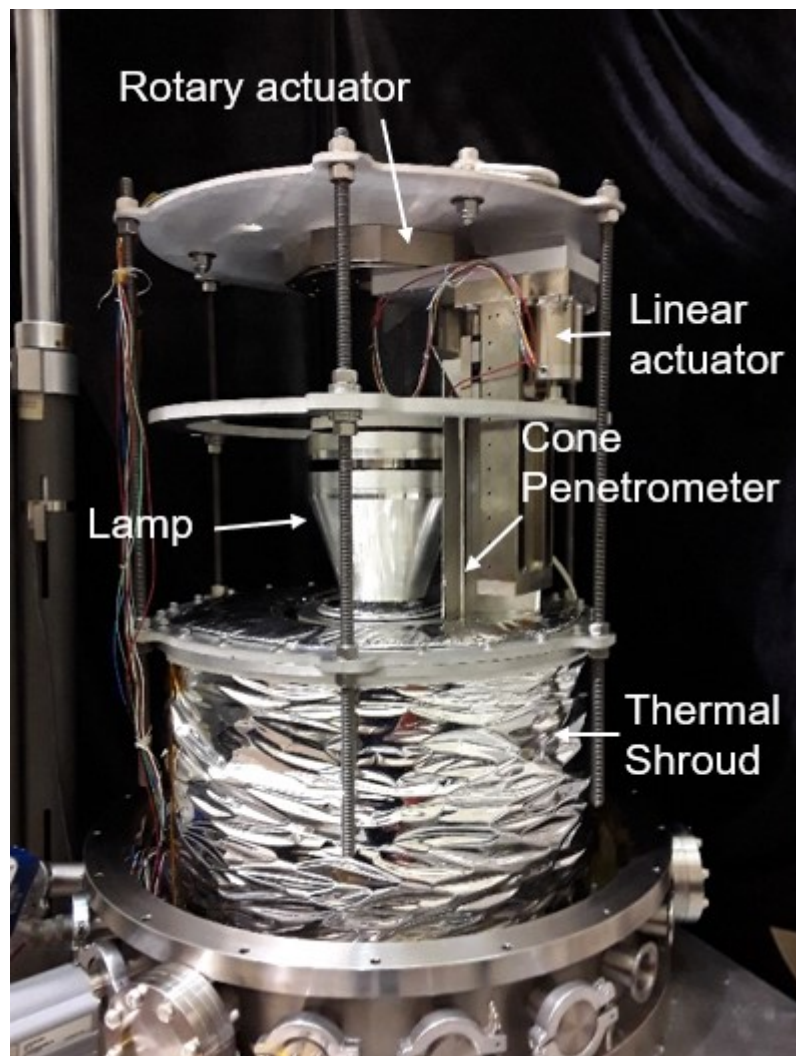


**Figure 3.2** The Icy Bodies Simulation (IBoS) chamber designed and fabricated at JPL to produce and evolve Enceladus surface icy analogues.



**Figure 3.3** *Enceladus simulants. Fine-grained pervious concrete (Top). Very fine-grained pervious concrete (Middle). Sintered cryogenic ice (Bottom).*

### 3.3 IBARM manipulation testbed

A 3 DOF robotic arm, named Icy Body ARM (IBARM), was developed and fabricated to evaluate all sampling systems on the same testbed (Figure 3.4). The manipulation testbed was equipped with two force-torque sensors and a weight off-loading mechanism. The force-torque sensors are configured in base-mounted and wrist-mounted locations to measure sampling loads and analyze force signal attenuation through the sampling arm to the lander. The weight off-loading mechanism is used to reduce the joint torques during sampling operations and instrumented with a load cell to enable full free-body load estimation on the arm. The arm has a mounting interface after the wrist force-torque sensor to accommodate a number of various sampling tools.

The kinematics, controls, and operator interfaces for the manipulation testbed are provided by JPL's CASAH (Controls and Autonomy for Sample Acquisition and Handling) software system [95]. Basic arm behaviors, like joint motion and task-space motion, are used to provide a set of motion primitives for sampling operations. Force control behaviors were developed to help limit the arm loads during sampling by slowing down the forward progress of the tool as a function of low-pass filtered wrist forces. Compared to open-loop control, force control showed from 13% to 70% load reduction using low strength simulants, depending on the sampling tool considered.

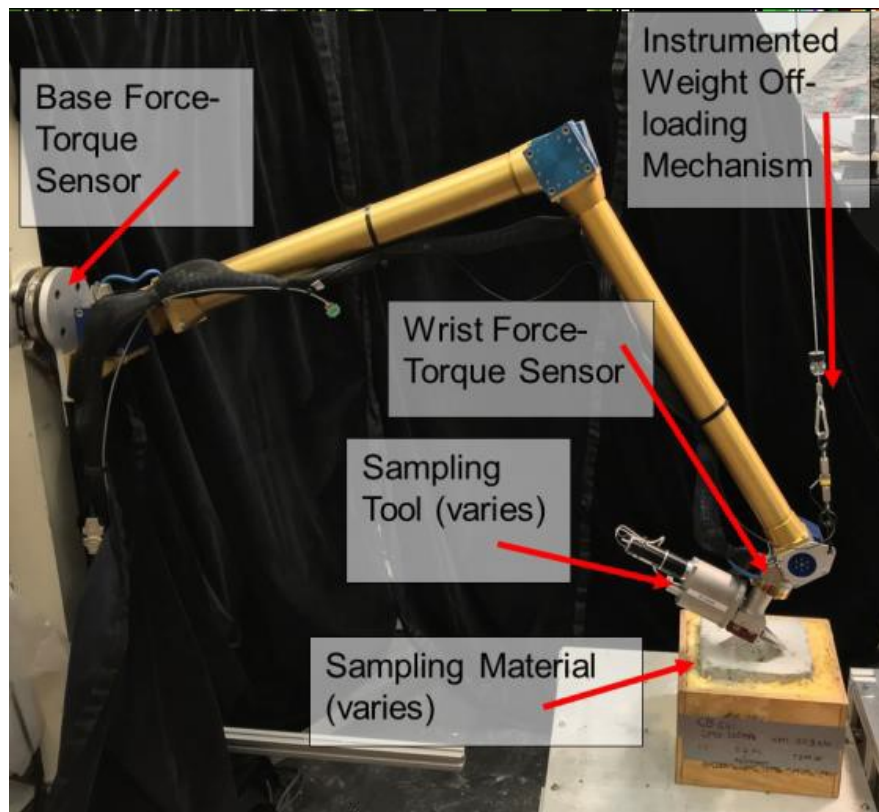


*Figure 3.4 IBARM manipulation testbed.*

### 3.4 Full-face drill

One of the investigated sampling systems was a rotary hammer tool with a powder bit with full-face cutting ability that drives the cuttings toward the bit rotation axis and stores the cuttings inside the bit. A rotary hammer tool allows operation with low weight-on-bit and low torque. The bit cutting teeth configuration allows for low torque from the driving tool. A conical bit and a cylindrical bit shapes were tested. The cylindrical bit was tested in two teeth arrays configurations and was also designed to enable efficient pneumatic transfer of collected cuttings (further details are presented in paragraph 5.4). In one configuration, the teeth are aligned in straight line segments, parallel to each other and located behind the symmetry plane going through the central bit axis in the rotation direction (Figure 3.5). In between the two rows of teeth there is an additional center tooth to complete the full front face coverage. Locating the teeth behind the symmetry plane causes the cuttings to be driven toward the central axis where the collection holes are located. The offset distance and the rotational speed are design parameters that need to be considered to assure that the cuttings are driven toward the bit central axis.

The inside of the bit creates a cavity for storing the cuttings during drilling. The top of the bit can be configured with a spring-loaded lid and access ports. A spring-loaded lid would allow the cuttings to be pushed out of the bit in case of overflowing to prevent compacting cuttings inside the bit. The access ports would allow the bit to interface with other devices for cuttings removal for sample transfer or bit cleaning. The bit has vertical features that allow the impact to be transferred to the cutting teeth more efficiently. During testing, the bit cavity was filled with cuttings but a lot more cuttings were driven outside the hole (Figure 3.6).



**Figure 3.5** Front face drill bit with linear teeth array design (Top) and 3D printed metal test bits (Bottom).



**Figure 3.6** Test of the full-face drill bit with linear teeth arrays.

In another configuration, the bit frontal face is a concave surface and the teeth placement follow an arc or parabola segment where the angle of the tangent to the locating curve with the central symmetry plane is proportional to the radial distance from the central axis (Figure 3.7). Driving the cuttings toward the central axis assures low strength material surface sample collection. The bit was designed with a lid that can shape the internal bit cavity for sample retention during drilling and subsequent sample transfer using pneumatics. In a first fabricated configuration for pneumatic sample transfer, the cavity inside the bit is shaped to increase the efficiency of cuttings removal from inside the bit to transfer it to other devices. The bit was able to collect cuttings during the test and the cuttings were transferred using a pneumatic system. The tool was tested in various simulants ranging from unconsolidated sand to 5.4 MPa UCS with preload measured in the 6 N to 10 N. The bit was able to collect sample of 2.2 cc to 2.8 cc volume.

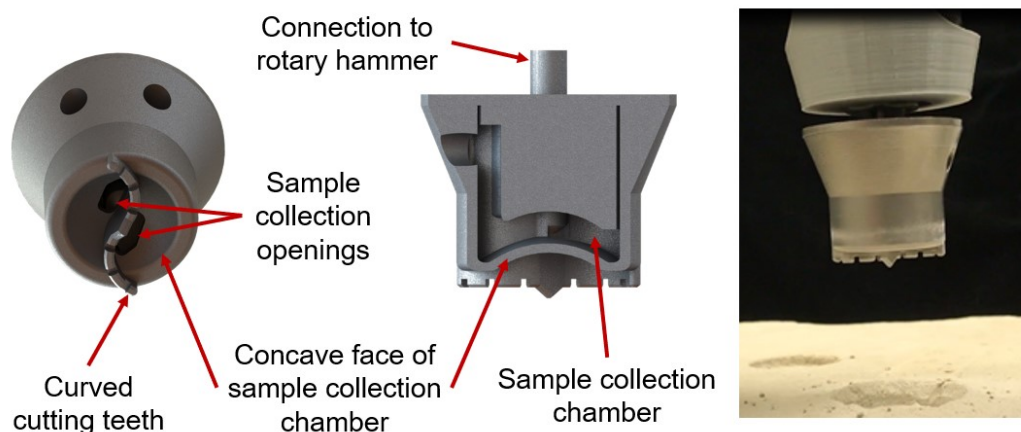


**Figure 3.7** Full-face drill bit with curved teeth array (Left) and fabricated prototype integrated into the testbed (Right).

### 3.5 Drive tube

Another sampling system investigated was based on a drive tube specifically designed for sample collection and transfer of shallow surface material. It includes a set of drive tubes, means of driving them into the ground for sample collection, a storage mechanism and means to load them in front of the drive mechanism and a means to transfer them. The main components of the sampling system are shown in Figure 3.8 and integrated into a housing in Figure 3.9. The drive tube includes a sample tube, a sample tube sheath, and a sample retention mechanism (Figure 3.10). The sample tube sheath is shaped as a cylinder with a flange at the top and a through axial hole. At the bottom end, the hole diameter is smaller with a shoulder between the large diameter section and small diameter section. The

shoulder can have a groove to aid in the passive control of the sample retaining mechanism shape. The bottom end of the sheath can have chamfers on both inner and outer edges or only on one edge. The chamfers geometry is dictated by the scope of the sheath to collect more or less of the sample material that is being penetrated. The sample tube is shaped as a cylinder with a flange at the upper end to support impact from the anvil and transfer the load to the tip of the sacrificial sheath and tube and to interface with the slot in the anvil. The outer diameter of the sample tube is smaller than the large inner diameter of the sheath and the inner diameter is larger or the same size as the smaller inner diameter of the sheath. At the bottom end, the sample tube has the sample retention mechanism.

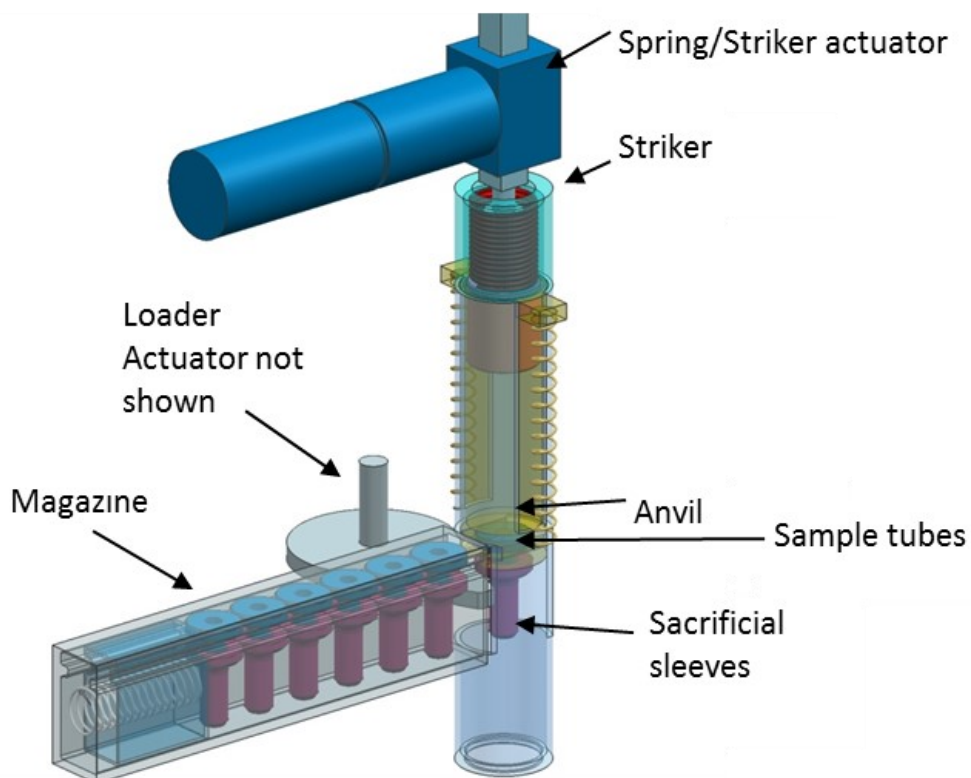


**Figure 3.8** Drive tube sample collection and transfer system main components.

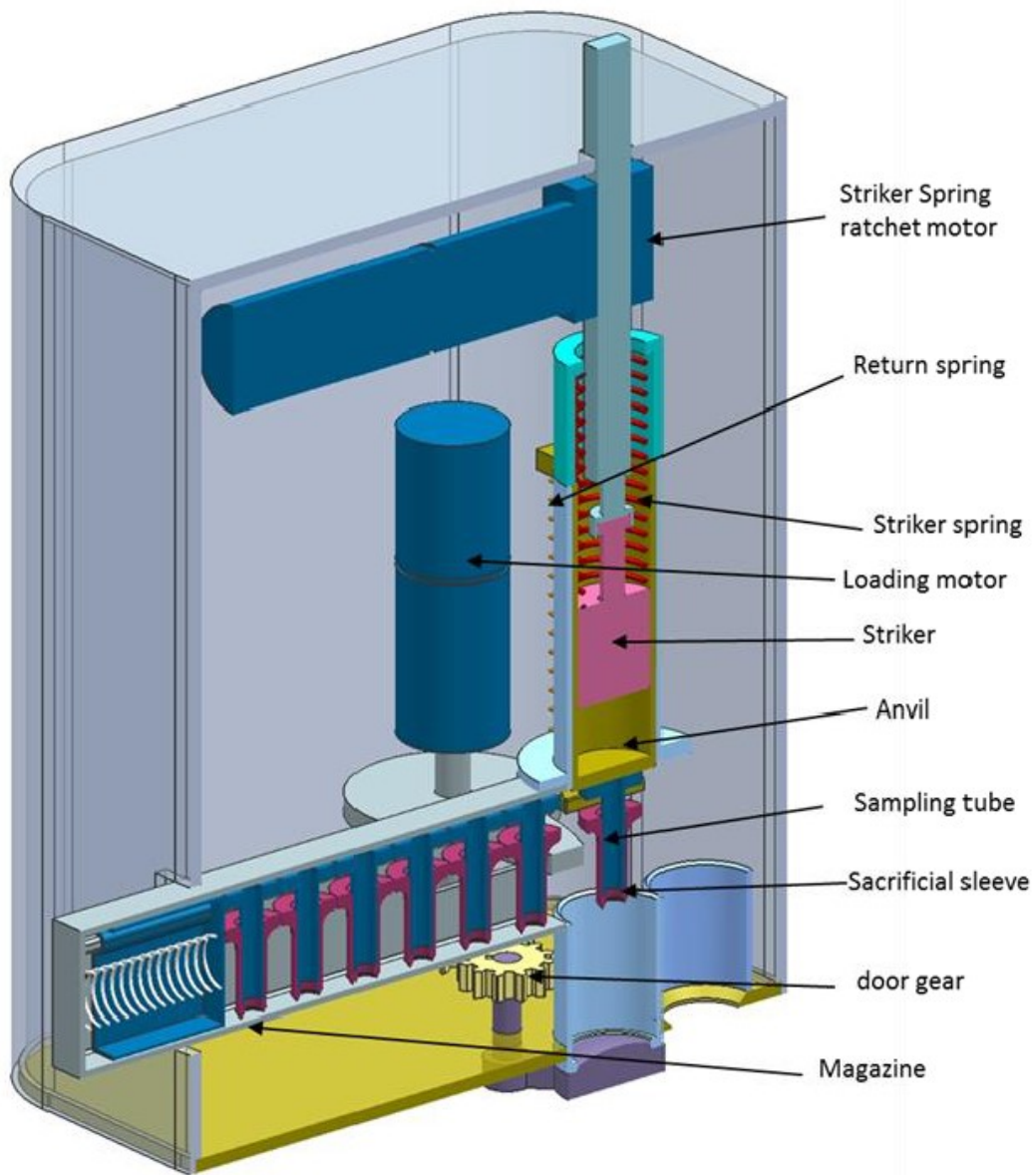


**Figure 3.9** Drive tube sample collection and transfer system main components integrated into a housing.

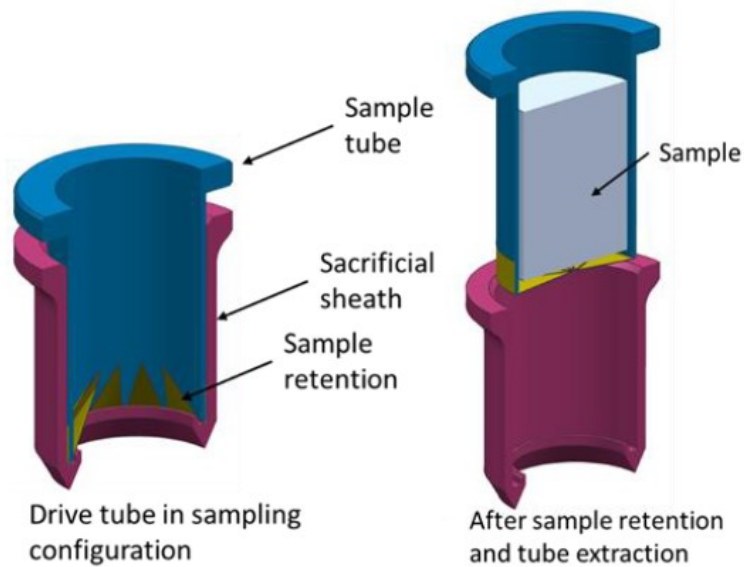


**Figure 3.10** Drive tube in sampling configuration (Left) and after sample acquisition and separation (Right).

One configuration of the retention mechanism is a fish trap with flexible fingers extending radially from the edge of the sample tube to the central axis. When the sample tube is inserted into the sheath against the bottom sheath shoulder the fingers deform toward the sample tube wall, leaving the central part of the tube open. Having the fingers open allows the tube to sample low penetration resistance material such as fluffy snow or powder. When the sample tube is extracted from the sheath, the fingers are released and retake their relaxed position, closing the bottom opening of the sample tube.

The drive tubes are stored in a linear or circular cartridge where a preloaded spring pushes them toward the drive mechanism axis. An actuator driven cam mechanism is used to load one drive tube at a time into the drive mechanism, hold the other drive tubes into the cartridge, and slide the sample tube after sampling away from the drive mechanism axis for sample transfer.

The drive mechanism consists of a guide tube with a bottom baseplate, an anvil with a bottom slot for accommodating the sample tube flange, an extraction spring mounted between the guide tube and the anvil, a hammer and a drive spring, and a linear actuator with a gripper to engage the hammer and preload the drive spring. For sampling, the hammer is retracted to preload the drive spring, a new sample tube is loaded into the anvil slot, and the sampler is placed with the base plate against the surface of the material to be sampled. The hammer is released, the drive spring accelerates the hammer that impacts the anvil and drives the drive tube into the sampled material, preloading the extraction/return spring. The anvil is stopped by the baseplate and the compressed extraction/return spring retrieves the anvil with the sample tube. The sacrificial sheath will remain in the ground during the sample tube extraction. When the sample tube separates from

the drive tube sheath, the sample retention mechanism gets activated retaining the sample in the sample tube. After the sample tube extraction, the sampler is docked with the sample receiving station and the sample tube containing the sample is transferred to the sample handling subsystem. The sample can be processed inside the sample tube as is the case for dry volatiles extraction or wet organics extraction. Having the sample enclosed in the sample tube with a known geometry makes the sample handling better determined. Components of the drive tube sampling system were fabricated and tested in the lab (Figure 3.11) using an impact mass. The drive tube sampling system can work with an impact driver or a percussive mechanism. The primary concern with the drive tube concept was the ability to acquire sample from strongest material, e.g. 12MPa UCS.



**Figure 3.11** Implemented drive tube components (Left), assembled (Middle), and sample tube with collected sample (Right).

### 3.6 Ultrasonic scoop

Another sampling system investigated was a piezoelectric-driven device that can collect a predefined volume of sample and requires 1 DOF for operation. The sampler has two ends where different configuration end-effectors can be attached. In the shown configuration, one end includes a scoop and the other includes a surface preparation tool (i.e. a chopper) (Figure 3.12). The piezoelectric actuator is attached to a joint of a robotic arm that can serve as both deployment mechanism and for tool operation. A passive detent-driven mechanism can be attached to the same joint as the tool and can serve as a stopper to ease sample collection and function as a scoop lid. The stopper has detent-controlled positioning and can be moved in different positions using the joint actuator and the sampling tool.

The tool includes a double-ended piezoelectric actuator that can have different attachments at the two ends, a mounting interface, and a stopper mechanism. The piezoelectric actuator includes a single or double piezoelectric stack preloaded between a set of two horns, an interface part for mounting, and different or identical end effector tools attached to the horn's tips. The two end effector tools can be run at the horn's resonant frequencies and at their own frequency. The piezoelectric stacks are driven by an AC electric field and can produce oscillations into the horns. The horns geometry can be configured to amplify the stacks vibrations' amplitude. The actuator can have an additional mass excited to produce lower frequency and higher energy impact to the end effector tools.

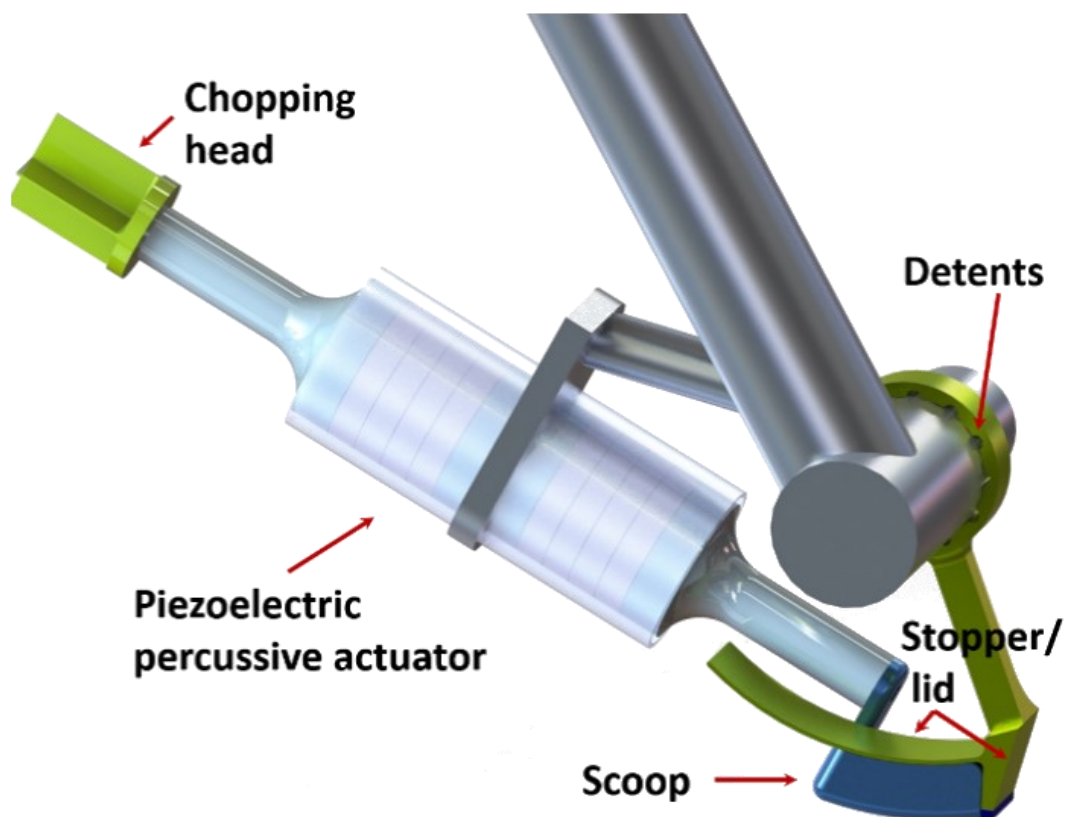


*Figure 3.12 Piezoelectric-driven ultrasonic sampling system.*

The piezoelectric material used for actuator fabrication can be a material that specifically targets the sampling location environmental conditions such as, for example, cryogenic piezoelectric materials for outer planets sampling and high temperature piezoelectric materials for Venus applications.

In the current implementation, one end effector tool consists of a scoop with curved bottom. The scoop symmetry plane can be mounted inline or offset from the horn symmetry planes. The center of the circle that defines the scoop bottom curvature is configured to be identical with the axis of the mounting joint which allows the device to be operated by only one actuator. The stop link includes the

lid rigidly attached to the link. In a different implementation, the lid can be attached to the stop link using a flexure that makes possible the use of a scoop without an axial offset. The other end-effector tool consists of a chopping tool with flat faces oriented along the piezoelectric actuator axis. This can be used to penetrate the surface and break the material in smaller chunks needed by the science instrument requirements.

For sampling, the following steps can be implemented.

- *Step 1* – Surface preparation (chopping). The deploying robotic arm uses the wrist joint to rotate the tool to move the stop link out of the way and orient the tool with the chopping head against the surface area to be sampled. The piezoelectric tool can be activated to cut slots in the sampling area making it easier for the scoop to collect the sample and pre-sizing the sampled material to the instrument requirements (Figure 3.13).
- *Step 2* – Position tool for sampling. The wrist joint rotates the tool to position the stop link in the sampling orientation, then moves the sampling tool away from the stop link. The stop link is loaded against the ground in the sampling area. The tool is rotated so it touches the ground and the lid covers the scoop (Figure 3.14).
- *Step 3* – Sampling. The tool has the piezoelectric actuator activated and is rotated using the wrist joint only until it touches the stop link. The wrist joint actuator can be controlled to maintain a maximum applied torque or a predefined rotation speed. The power to drive the piezoelectric actuator can also be controlled (Figure 3.15).
- *Step 4* – Sample transfer. After the sampling process is completed, the robotic arm can follow a succession of predefined movements to move the stop link away from a position that would interfere with the sample transfer process while maintaining the scoop in a horizontal position to prevent sample loss. An on-board camera can be used at this time to acquire an image of the scoop with the sample to assess the sample including verifying adequate volume. The scoop is aligned with the delivery location for sample transfer. A scraper can be provided at the delivery location so the scoop can be moved against the scraper to remove the collected sample material from the scoop (Figure 3.16). The piezoelectric actuator can be activated at a lower power level to ease the sample separation from the scoop. After the sample transfer process is completed, the arm can move the tool to a stowing position or perform another sampling operation.

A series of chopping tools configurations were fabricated and tested using two ultrasonic transducers. Tested configurations were flat blade, cross blade, and circular cutter. All cutters were able cut the medium strength consolidated

simulant with a preload of 7 to 10 N but were not able to penetrate the higher strength simulant (5.4 MPa UCS). Figure 3.17 shows prototypes of the ultrasonic sampling system realized for lab testing.

Further analysis of the piezoelectric actuated scoop in Enceladus gravity conditions indicated that there would be risk of the particles bouncing away from the scoop during sample acquisition and out of the scoop during the sample transfer process due to arm accelerations (further details are presented in paragraph 4.4). Also, a higher strength surface material would require a higher preload for the piezoelectric scoop concept.

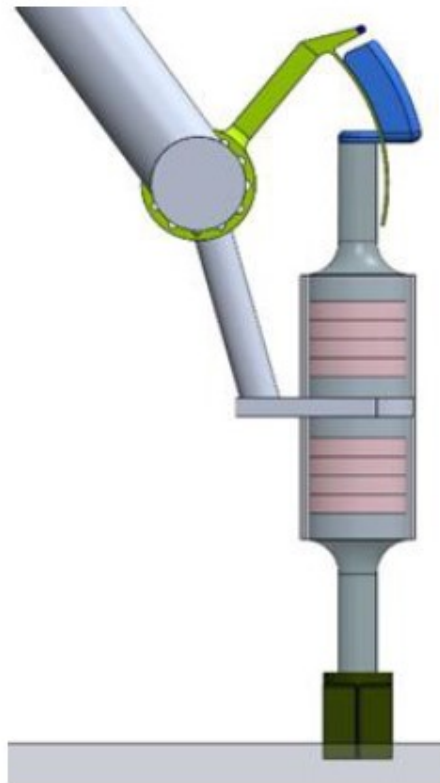


*Figure 3.13 Sampling system in chopping configuration.*

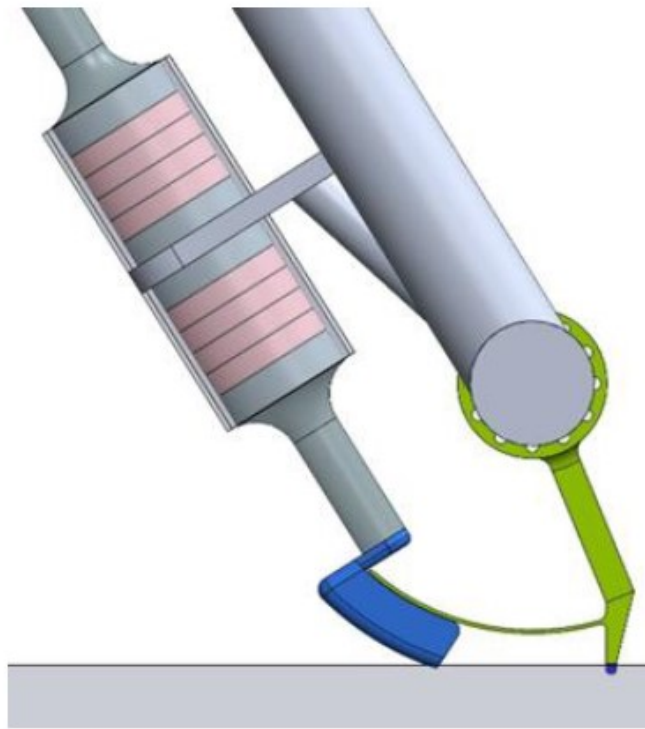


*Figure 3.14 Sampling tool in sampling configuration.*

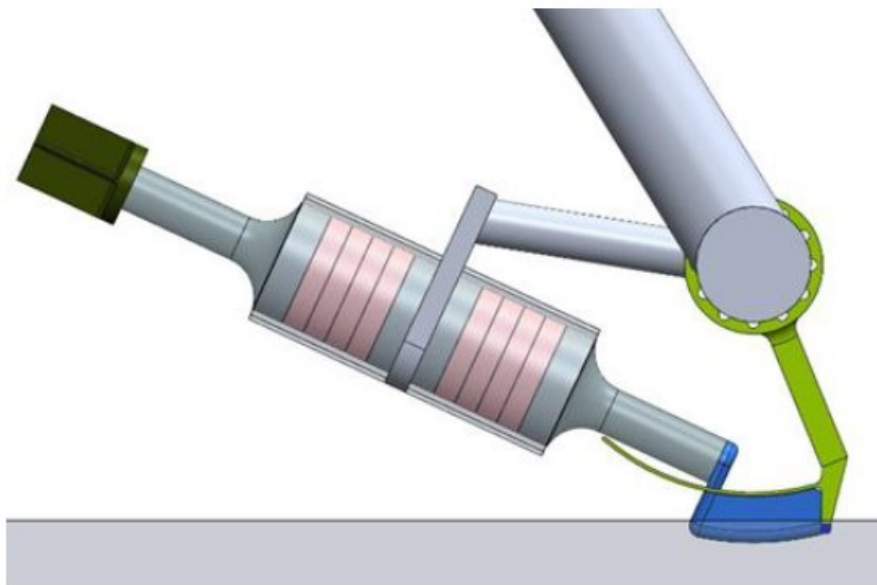


*Figure 3.15 Sampling system at the end of sample acquisition.*

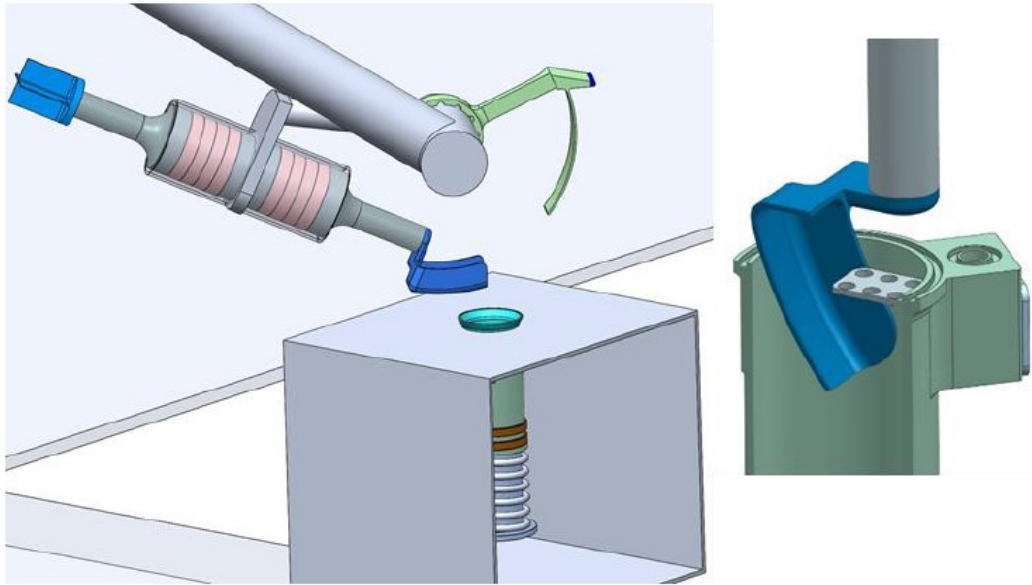


**Figure 3.16** Sampling system in the sample transfer configuration (Left) and scoop being scraped against the sample transfer chamber (Right).



**Figure 3.17** Prototype of the ultrasonic sampling system provided with two different types of scoop. Curved (Top) and straight (Bottom). The curved scoop helped the mitigation of some drawbacks of the straight version, namely the higher reactive loads and the higher difficulty to handle the sample during sample chain steps.

### 3.7 Rasp

A rotary cutter-based sampling system was developed and tested. This system relies on high cutter rotational rates to impart momentum into cuttings that are flung into a sample collection chamber located immediately above the spinning cutter. Later the acquired sample can be transferred from the collection chamber to its destination (i.e. the scientific instrument placed on the lander).

The Rasp sampling system (Figure 3.18 and Figure 3.19) is based on the NASA's Phoenix Mars Lander mission Icy Soil Acquisition Device (ISAD) [96]. The ISAD consists of a scoop and a rasp bit. The spring-loaded rasp bit design and sample cuttings capture strategy was leveraged from this heritage system.

A rasp-based sampling system is well suited to Enceladus surface sampling application for the following reasons. First, the Rasp is robust to excavation and capturing material of a wide range of strength (from loose to very hard). Secondly, the momentum transfer type sample capture, performs increasingly well at lower gravity. The rasp bit easily imparts adequate momentum into excavated particles to flying the material into the collection cup. Lastly, the reaction forces are very low compared to other potential sampling systems while cutting into hard, icy material due to small cutter tooth engagement with the ground and the fly-wheel momentum effect of the high-speed bit.

Due to the low gravity environment found on Enceladus, dumping of the sample that is located in the collection cup would not be possible. The Enceladus gravity is sufficiently low that it cannot be relied upon to provide enough force to overcome small scale forces such as electrostatic and friction when attempting to transfer the material out of the sampler and into the potential instrument. The Rasp sampling system was therefore designed for a pneumatic transfer which is capable to move the sample in low gravity (further details are presented in paragraph 5.5).

The Rasp was demonstrated to meet all requirements including collection of low-end and high-end strength material. It was tested in unconsolidated material, medium strength, and high strength material with a preload of 6 N to 8 N and was able to collect 1.5 cc material.

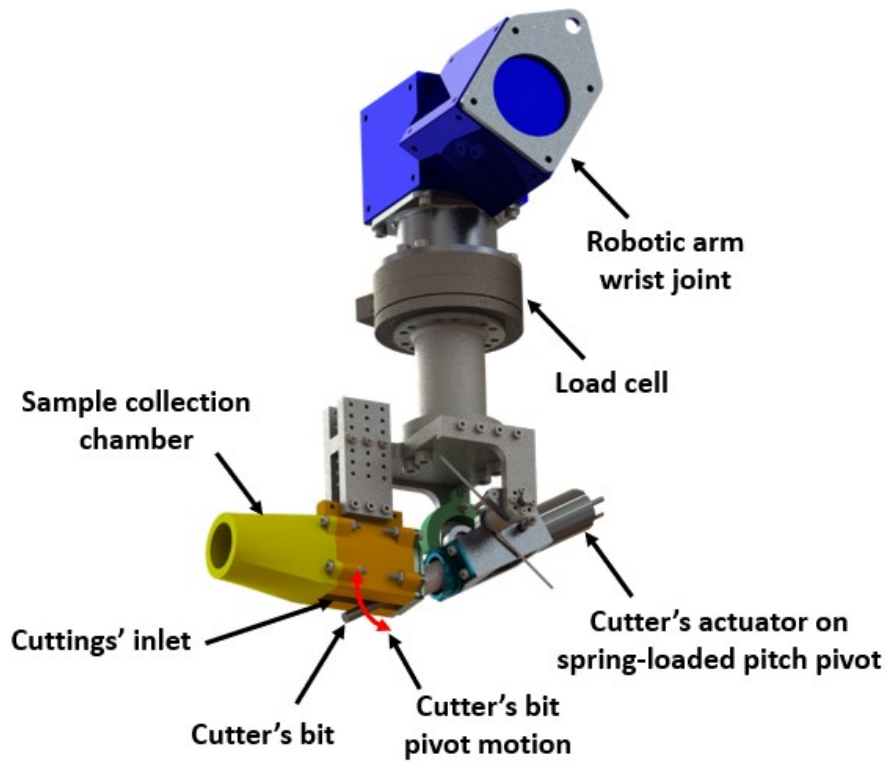


*Figure 3.18 Rasp sampling system.*

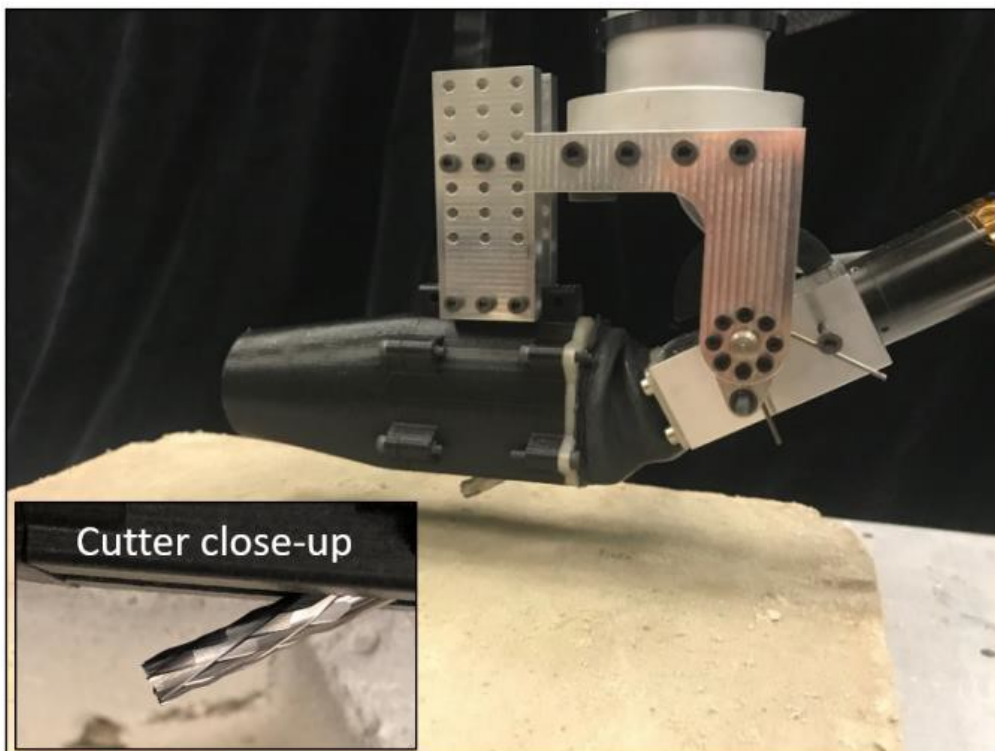


*Figure 3.19 Prototype of the Rasp sampling system. Close-up rotary cutting bit is shown.*

### 3.8 Dual-Rasp

To cope with the several challenges of surface sampling on Enceladus, including the wide range of potential surface material strengths, the limit on the allowable reacted load, and the low gravity environment, a novel sampling system, named Dual-Rasp, was devised and developed (Figure 3.20 and Figure 3.21). The Dual-Rasp sampler is provided with two counter-rotating, rasp-type cutting heads (Figure 3.22). These are suited to acquire samples from very strong surface materials, as shown by the Mars Phoenix mission, where a single rasp-type cutting head was implemented to sample hard icy surfaces [96]. On the other hand, the Brush-wheel sampler concept used counter-rotating brushes to acquire loose material by throwing it between them into a collection chamber [91]. The Dual-Rasp combines these concepts to obtain a sampling system that is capable to acquire samples from weak to high strength materials with the great advantage to require low average preload.

The Dual-Rasp acquires sample by exploiting the rasping action of the two cutting heads to remove the pristine material, thus achieving a momentum transfer that throws the material up between them in a controlled path for collection into a chamber.

The Dual-Rasp was selected as the baseline sampling system for the Enceladus lander mission concept. Following chapters will present further details and discussion regarding Dual-Rasp integration in the whole sample chain.

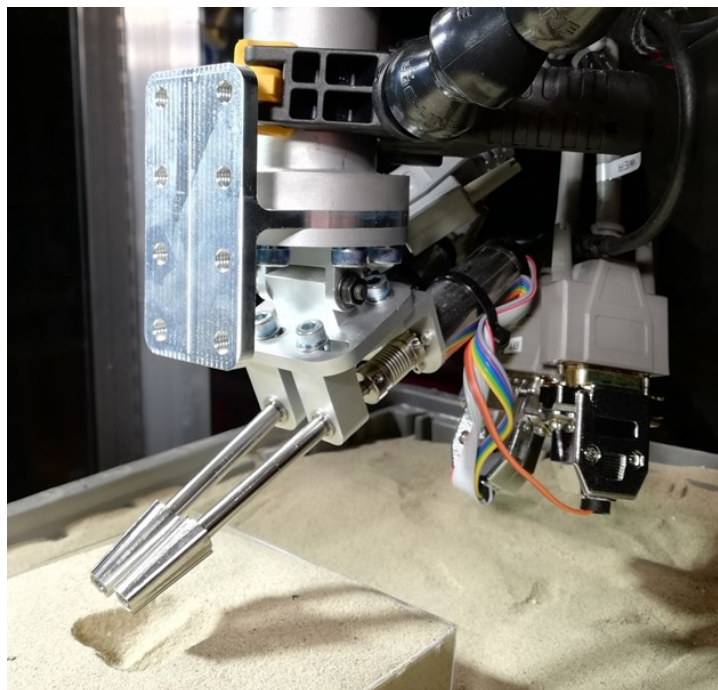


**Figure 3.20** The Dual-Rasp sampling system combines the capability to sample a wide range of surface material strengths with the advantage to require low average preload.

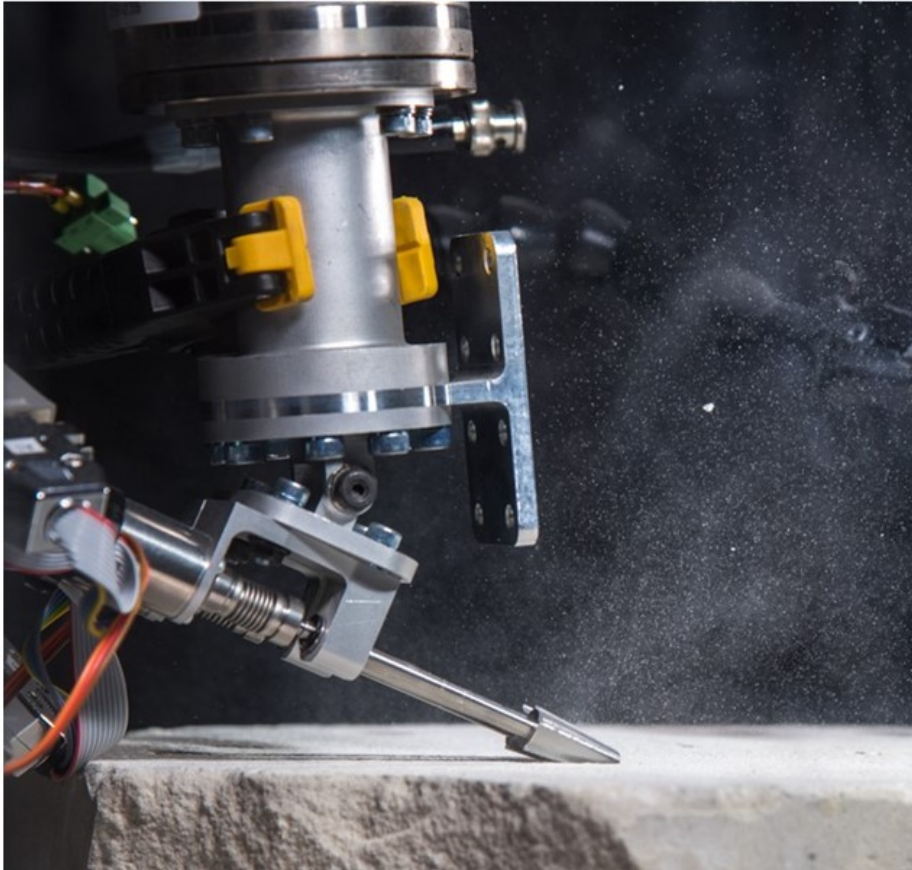


*Figure 3.21 The Dual-Rasp involved in sampling operations.*



*Figure 3.22 Dual-Rasp cutters. The two counter-rotating, rasp-type cutting heads remove the pristine material and throw it up between them via momentum transfer.*

# Chapter 4

## 4 Investigation of sample collection

Part of the content of the present chapter was published in [55] [84].

### 4.1 Introduction

As introduced in previous chapter, the sample chain is typically composed of the following phases.

- *Sampling*, that is the operation of breaking up and/or disturbing the pristine material to get the sample.
- *Collection*, that is the operation of gathering the sample.
- *Transfer*, that is the operation of transporting the sample from one location to another.
- *Measurement*, that is the operation of measuring the quantity of sample collected in terms of mass, volume, etc.
- *Deposit*, that is the operation of delivering the sample to its destination (e.g. a science instrument, a storing capsule, etc.)

The previous chapter addressed the first phase of the sample chain (i.e. sampling) by presenting the sampling system concepts developed to perform the operation of breaking up and/or disturbing the Enceladus pristine material to obtain a surface sample. This chapter focuses on the second phase of the sample chain (i.e. sample collection) by introducing the strategies developed and the analysis conducted to study the operation of gathering the sample. One of the main challenges of the Enceladus low gravity vacuum environment, is represented by the significant difficulty to handle the sample because of the extremely low tendency of the particles to settle and the resulting high tendency of spreading in a very sparse fashion. In a higher gravity vacuum environment, gravity force tends to dominate over the forces resulting from the interaction among the particles (i.e. particle-particle forces) and the forces between particles and other bodies (i.e. particle-surface forces). As a result, gravity significantly determines particle

dynamics and bulk material behavior. E.g. particles tend to quickly settle down and move along short ballistic trajectories. In a low gravity, vacuum environment such as the one found on Enceladus, gravity force tends to be negligible if compared to particle-particle and particle-surface forces. As a result, particle-particle and particle-surface forces significantly determine particle dynamics and bulk material behavior. E.g. particles do not tend to settle down and move along very long ballistic trajectories. Those trajectories can be considered straight if compared to the characteristic dimension of the investigated problem (i.e. the dimensions of the sampling system), in such a way the particles look having a random linear motion, similar to a perfect gas.

Some past missions used the great advantages of a higher local gravity for sample collection, since it is possible to exploit the natural tendency of particles to easily settle down and rest in the desired collection volume. On Enceladus it is not possible to rely on gravity for sample collection because of the challenging operations of getting the sample into the collection volume and ensuring that it is retained in there. For this reason, accurate strategies need to be investigated to guarantee a sufficient control over the natural tendency of particles to spread.

## 4.2 Approach

To study the dynamics of an assembly made of a great number of particles with the purpose of developing efficient handling strategies, special analysis methods are required. These methods can be grouped into two main approaches: continuum and discrete.

### 4.2.1 Continuum approach

Methods based on continuum mechanics can be used to study granular materials [97] but modeling the large displacements and deformations typical of granular flows, especially in a very disperse state, is particularly challenging. In fact, these methods consider matter as a continuum that occupies the entire space, thus distinct particles do not exist. Continuum approaches are implemented through various numerical techniques. The most widely used is the Finite Element Method (FEM) [98] [99] [100] [101]. To analyze the problem under investigation, FEM discretizes the large domain of interest into smaller finite elements. To do so, the method subdivides the domain by using a mesh. The method then approximates the equations that describe the problem to be studied at the local element level. This process results into a local system of equations for each element. Local systems of equations are then transformed into a global system of equations through a transformation of coordinates to determine the final solution of the problem. Classical FEM is not well suited to analyze typical discontinuous

problems, as in problems with large deformations, fracture mechanics, boundary layer, or particle dynamics. The process of re-meshing the discontinuous surfaces as they evolve (e.g. fracture propagation) might help to get around the limitation in some specific cases, but with a significant computational cost and potential projection errors [102] [103]. For this reason, the classical FEM has been enriched in several ways to overcome these drawbacks. As an example, the Extended Finite Element Method (XFEM) introduces discontinuous functions to avoid re-meshing of discontinuous surfaces, thus reducing computational cost and projection errors [104] [105].

Tentative to gradually remove the dependence on the mesh and its related drawbacks led to the so called meshfree methods, also applied to modeling of granular materials, still with some challenges if compared to pure discrete methods [106] [107] [108]. These methods do not rely on mesh but are rather based on nodes and their interaction with all neighbors. As a result, nodes have no longer a fixed number of predefined neighbors. Instead, nodes can move in the domain of interest because of the mutual interactions according to the specified set of equations for the investigated problem.

#### 4.2.2 Discrete approach

Molecular Dynamics (MD) is a simulation method that pushes forward the concept of individual nodes free to move in the simulation domain. MD is a discrete numerical method born to analyze the motion of atoms and molecules in large assemblies [109] [110] [111]. Particles are treated as unique entities that can interact each other. Forces between particles are determined using interatomic potentials or molecular mechanics force fields. Particles' motion is determined by numerically solving Newton's equations of motion. Particles' accelerations are obtained from individual forces' balance, and then integrated to obtain particle's velocity and position step by step. MD results particularly suited for the simulation of large assemblies of particles, a task that is impossible to carry out analytically. Main benefits of this method include the significant insight on motion's dynamics at particle's level, as well as the possibility to study the behavior of particle's assembly as it arises from interactions at particle's level. Main drawback is represented by the significant computational cost deriving by the need to numerically solve the equations of motions step by step and for each single particle in the simulation. The diffusion of parallel cloud computing has mitigated the problem with the result of making this method more appealing. In fact, cloud technologies have widened and made easier and cost-affordable the access to the High Performance Computing (HPC) resources required to perform MD simulations [112] [113] [114].

A numerical method closely related to MD is the Discrete Element Method (DEM) [115] [116] [117] [118], a widely accepted technique particularly suited to

address engineering problems about granular and discontinuous materials, such as granular flows, powder mechanics, and tool-soil interaction [119] [120] [121] [122] [123] [124]. Moreover, DEM is often coupled with continuum-based methods such as Computational Fluid Dynamics (CFD) to model fluid-particle interaction [125] [126] [127]. Compared to MD, DEM includes particles' rotational DOF, in such a way particles have full 6 DOF. DEM also introduces specific models for granular materials, and is often capable to include complex particle's geometries, such as polyhedral. Since DEM treats each particle as a distinct entity, the bulk material behavior emerges from the mutual interaction of all particles in the assembly. As a result, DEM is capable to capture the solid/fluid dual behavior of granular media. Main advantages of using a discrete approach, such as DEM, over a continuum approach include the capability to capture particle level behavior which often affects bulk behavior, the capability to accurately model micromechanics, and the difficulty of using constitutive laws typical of the continuum approach. Similarly to MD, DEM exploits contact mechanics models to determine forces at particle-particle and particle-surface contacts. Newton's equations of motion are then applied to the force balance of each particle to determine its acceleration. Particle's velocity and position are then obtained by integration (Figure 4.1). This process is repeated at each timestep of the simulation to update the state vector of each particle, including information on particle's position, linear/angular velocity, and linear/angular acceleration.

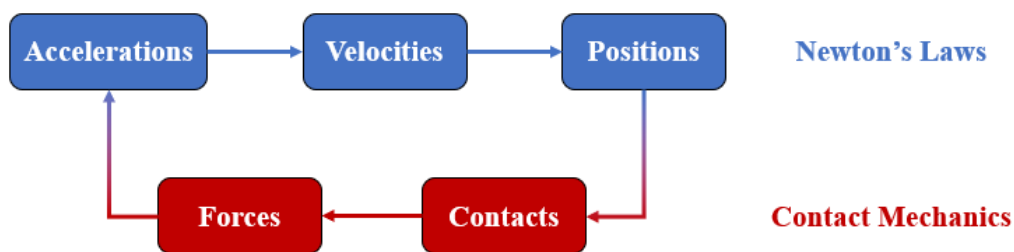


*Figure 4.1 DEM calculation cycle.*

Two methods of discrete simulations are usually available: hard contact and soft contact. In hard contact simulations, particles are rigid bodies, contact forces are considered impulsive, and only one contact at a time is possible. In soft contact simulations, the most common and accurate, particles are rigid bodies, but small overlaps are allowed. The entity of the overlap is evaluated from particles' size and relative position. This enables a more accurate evaluation of contact forces and simultaneous contacts are possible.

In soft contact simulations, calculation of particle's motion starts by considering the state vector of each particle involved. When two particles come into contact with initial velocities  $v_1$  and  $v_2$  (Figure 4.2), contact forces  $F_1$  and  $F_2$  are determined, based on the entity of the overlap and on contact mechanics

model adopted. Newton's equations of motion for rotation and translation, Eq. (4.1) and Eq. (4.2), respectively, are then solved to determine particles' motion in terms of acceleration, velocity and position. Forces acting on a single particle during contact can be of different nature, such as weight force ( $F_g$ ), contact force ( $F_c$ ), and bonding force ( $F_{nc}$ ) with other particles (Figure 4.3). At every time step, velocity and position of each particle are updated via numerical integration of Newton's laws, according to Eq. (4.3–4.4), where  $m$  is particle's mass,  $I$  is particle's moment of inertia,  $F$  and  $M$  are forces and torques acting on the particle, respectively, while  $\dot{v}$  and  $\dot{\omega}$  are particle's linear and rotational acceleration, respectively. In soft contact simulations, particles' overlap is evaluated along two different directions, resulting in normal overlap and tangential overlap. Normal overlap is evaluated along the line joining the centers of two particles (i.e. normal line), while the tangential overlap is evaluated along the line perpendicular to the normal line and passing through the contact point. As a result, two types of forces are considered, normal contact forces and tangential contact forces.

$$m\dot{v} = \sum F \quad (4.1)$$

$$I\dot{\omega} = \sum M \quad (4.2)$$

$$x(t + \Delta t) = x(t) + v(t) \Delta t \quad (4.3)$$

$$v(t + \Delta t) = v(t) + a(t) \Delta t \quad (4.4)$$

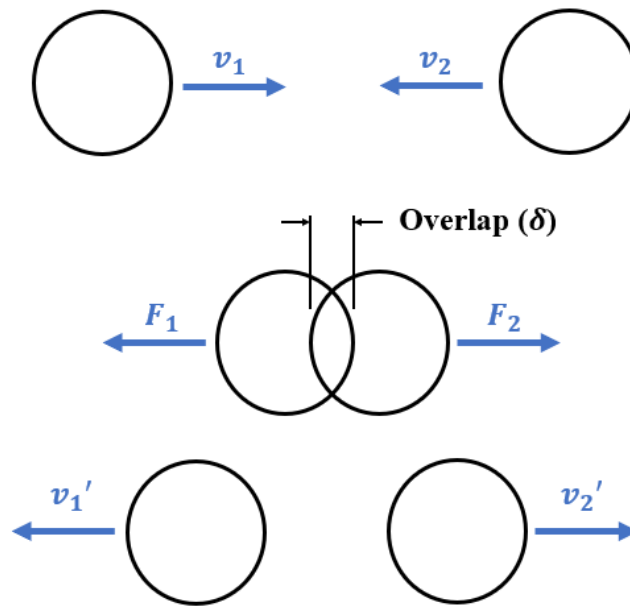


**Figure 4.2** Soft contact of spherical particles in discrete simulations.

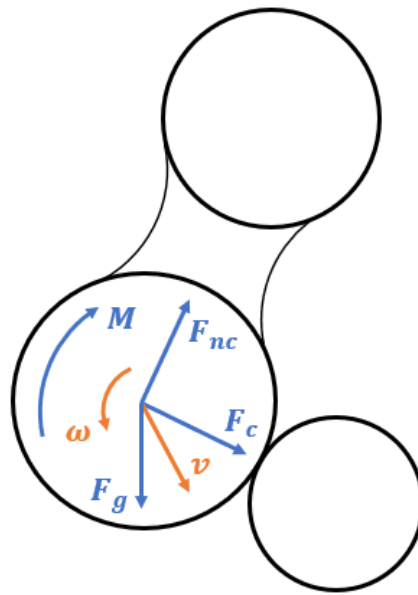


**Figure 4.3** Example of forces and moments acting on a particle during contact.

Several models based on contact mechanics are available to evaluate contact forces in the following domains:

- *Normal / tangential contact.* Models in these domains enable the evaluation of frictional forces between two particles in normal and tangential direction. These models account for the overlap and relative velocity between interacting particles in normal and tangential direction. Among most common models there are:
  - *Hookean model* [128] [129] [130] [131] [132] [133] [134], where a force with an elastic term proportional to overlap distance (i.e. linear function of overlap distance), and a damping term proportional to relative velocity is added.
  - *Hertzian model* [128] [129] [130] [131] [132] [133] [134], where a force with an elastic term proportional to overlap area (i.e. non-linear function of overlap distance), and a damping term proportional to relative velocity is added.
- *Rotational contact.* Models in this domain enable the evaluation of rotational frictional force between two particles. Real particles have non-regular shapes that introduce a rolling friction due to physical phenomena such as interlocking. Modeling real particle's shapes is highly demanding from a computational standpoint, so spherical particles are usually preferred. Therefore, to reproduce rolling friction effects on spherical particles, these models add an additional torque contribution aiming to simulate the effect of real particle's shape [135] [136]. Among most common models:

- *CDT (Constant Directional Torque) model* [137] [138], where a purely elastic additional torque proportional to overlap distance is added.
- *EPSD (Elastic-Plastic Spring-Dashpot) model* [137] [138], where an additional torque with an elastic term proportional to overlap distance, and a damping term proportional to relative velocity is added.
- *Cohesion*. Models in this domain enable the evaluation of several types of inter-particle interactions tending to maintain the contact between particles. Inter-particle interactions include capillary and a viscous forces as result of the presence of liquid bridges between particles, electrostatic and electromagnetic forces, and cohesion forces. Among most common models:
  - *Easo capillary viscous model* [139] [140] [141] [142] [143], where an additional normal force with a capillary term and a viscous term is added, caused by a liquid bridge film between particles. The model is also capable to solve for the transfer of surface liquid from one particle to the other as the bridge breaks up.
  - *JKR (Johnson-Kendall-Roberts) model* [144] [145] [146] [147] [148], where an additional normal force tending to maintain the contact is added. The force is proportional to particle contact area and to cohesion energy density.

To apply contact models, contact detection must be performed first. DEM codes usually check relative position between the elements of the simulation (i.e. particles and surface geometries) by performing a grid-based search in the domain. Figure 4.4 shows an example of contact detection methodology. This operation is computationally expensive and scales up in a non-linear manner with the number of elements in the simulation, as well as with the size of the elements (i.e. particularly sensitive to the size of particles), the size of the simulation domain, the presence of non-regular particle's shapes, etc.

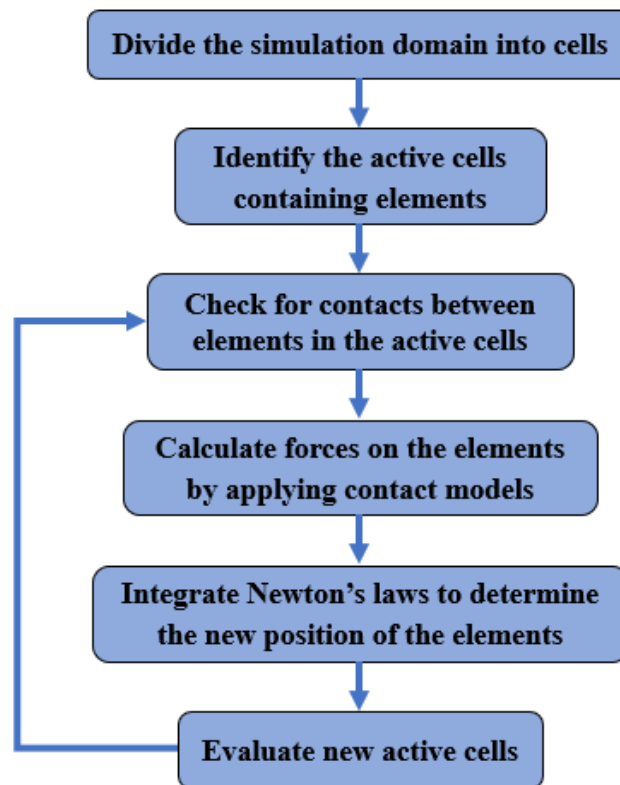


**Figure 4.4** Example of contact detection methodology.

Particle's shape was mentioned as one of the main reasons for the high computation resources required to perform DEM simulations. On the other hand, a particle's shape not sufficiently accurate could lead to misleading or wrong results. A tradeoff between particle's shape accuracy and computational cost must be performed in such a way a representative model is obtained at a reasonable computational cost. Real particle's shape can be characterized by using two parameters, sphericity and roundness (Figure 4.5) and can be approximated in several ways [149] [150] [151] [152] [153].

- *Sphere*. Modeling particles as single spheres is the most simple and elementary method to approximate particle's shape.
- *Polyhedral*. Particles are modeled as polyhedral composed of flat faces joined by corners and edges (Figure 4.6).
- *Super-quadratic*. Particle's shape is modeled by using superquadratic functions (Figure 4.7), defined as  $\left(\frac{x}{a}\right)^m + \left(\frac{y}{b}\right)^m + \left(\frac{z}{c}\right)^m = 1$
- *Multi-sphere*. Particle's shape is modeled by overlapping single spheres (Figure 4.8). This method enables to capture particle's irregularity by maintaining a good computational efficiency. Furthermore, main contact models are verified for spherical particles, thus can be extended to multi-sphere particles with confidence.

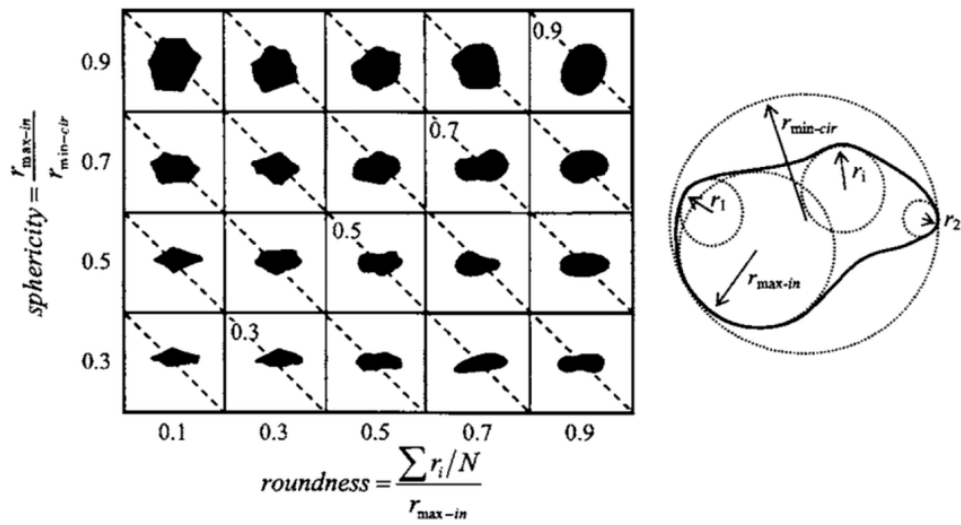


**Figure 4.5** Particle's shape determination through roundness and sphericity chart [154].

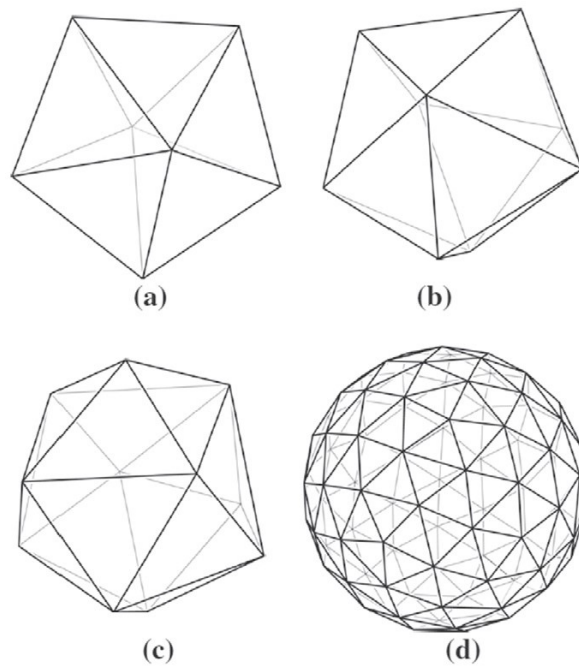


**Figure 4.6** Example of polyhedral shapes: a) 7 vertexes, 10 faces; b) 9 vertexes, 14 faces; c) 11 vertexes, 18 faces; d) 100 vertexes, 196 faces [155].

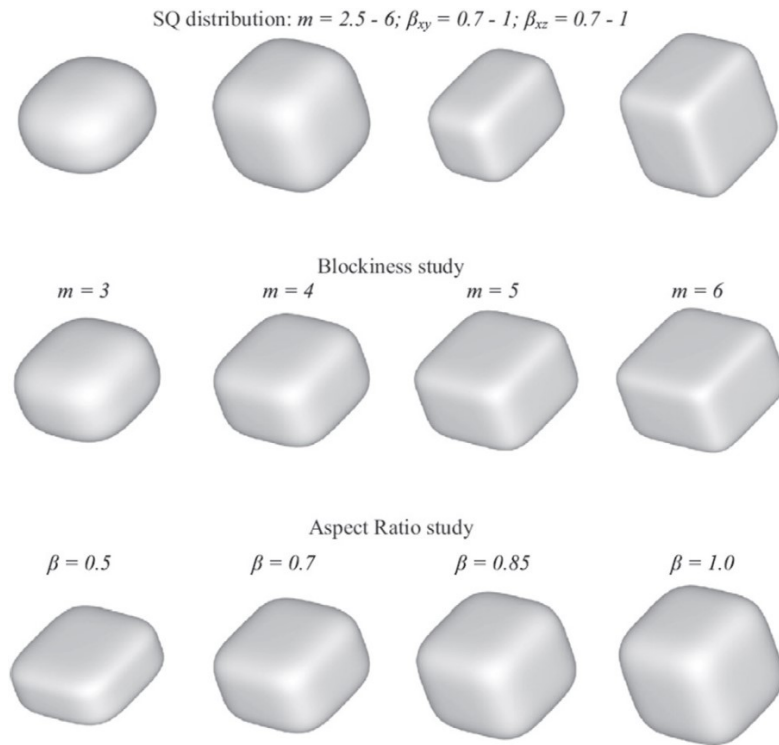


**Figure 4.7** Example of super-quadratic particles [156].

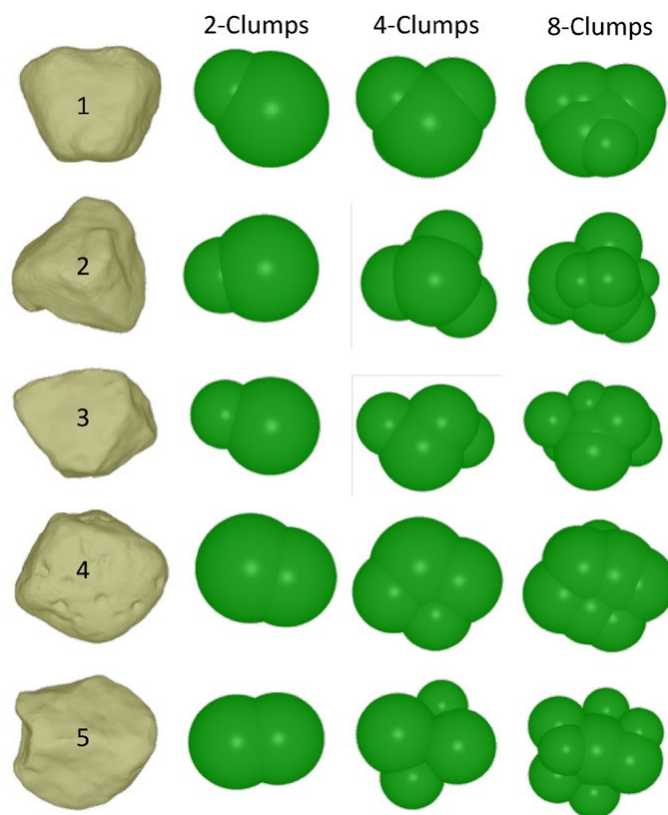


**Figure 4.8** Example of real particle scans modeled by using multi-sphere clumps [149].

Particle's shape is only one of the input parameters required to setup a DEM simulation. An accurate set of material input parameter values is also required to be able to make accurate predictions. This is probably the toughest and most challenging aspect in DEM modeling, and could require the largest effort in a DEM simulation project.

DEM parameters include properties of the particles, properties of the surface geometries the particles can interact with, paired properties (i.e. particle-particle properties, and particle-surface properties), and common properties (e.g. environmental properties). Particle's properties include for example Young's modulus, Poisson's ratio, density, size, and shape. Properties of surface geometries include for example Young's modulus and Poisson's ratio. Paired properties include for example coefficient of static friction, coefficient of restitution (COR), and coefficient of rolling friction. Common properties include for example the gravitational acceleration. Parameters are dependent on the DEM models, thus different DEM codes might implement different models and parameters.

Two main approaches are commonly adopted in the literature for the evaluation of DEM input parameters [157]. The first approach can be referred to as the Bulk Calibration Approach and exploits either in-situ or laboratory experiments to measure bulk material properties. The same experiments are then reproduced in DEM simulations as closely as possible. DEM parameters' values are then changed iteratively until the simulated material behavior matches the experimental result. A potential drawback of this approach is that the simulation result is affected by several different parameters. Since different combinations of the same parameters can lead to the same result, the solution is not unique. The consequence is that the material calibration obtained through this process might be dependent on the specific application and there is no guarantee that it will be accurate for another. Moreover, DEM models attribute a physical meaning to the parameters. Since there are different combinations of DEM parameters that potentially lead to the same result, the physical meaning of the parameters might be lost through this approach. A good practice is to choose a calibration experiment that is different from the final application to model. In fact, if the final application is used to perform the calibration of DEM parameters, then the result is just a sensitivity analysis and would not enable the prediction of material behavior for the final application.

The second approach to evaluate DEM input parameters can be referred to as the Direct Measuring Approach, and directly measures the parameters' values at particle or contact level. This approach might be very difficult to apply, depending on the parameter to measure and on the particle size. Most common research focused on particles at millimeter scale and above. Another challenge is represented by the fact that a high accuracy in the measurement of the parameters at particle level would not necessarily lead to an accurate result in predicting the bulk material behavior. This results from the inherent inaccuracies of particle's

shape model and contact model adopted. As already mentioned, it is very difficult to model particle's shape and size with sufficient accuracy due to both modeling and computational limitations. As a result, particle size is often increased, and particle shape is significantly simplified. Only special cases that involve simplistic shapes such as spheres in the context of controlled laboratory experiments can really take advantage of this approach. The main benefit of using direct measurement is that properties' values are independent on the DEM model or the specific DEM code adopted.

### **4.3 Dual-Rasp sampling system**

As presented in paragraph 3.8, the Dual-Rasp sampling system was developed to cope with the several challenges of surface sampling on Enceladus, including the wide range of potential surface material strengths, the limit on the allowable reacted load, and the low gravity environment. The Dual-Rasp sampling system exploits the counter-rotating motion of its rasp cutters to remove the surface material and throw the cuttings into a collection chamber. Sample collection is then achieved by transferring momentum from cutters to cuttings, thus generating a granular material flow. Since a successful sample collection relies on the ability of the Dual-Rasp to generate such a granular material flow, it is of key importance understating how the process works to make predictions on how it might work in the Enceladus environment, thus providing guidelines for sample chain design.

#### **4.3.1 Characterization of granular flow**

The Dual-Rasp ability to generate a granular material flow was observed in laboratory experiments by using high-speed cameras to record the sampling operation. Figure 4.9 shows a frame from a high-speed recording of the sampling operation performed by using the Dual-Rasp sampling system. In this case, the Dual-Rasp is operated at about 10000 RPM, and the granular material adopted is unconsolidated quartz sand in the 100-1000  $\mu\text{m}$  grain size rage. On the other hand, the Dual-Rasp cutters are about 30 mm long. The picture shows a disperse flow that looks concentrating in a column of material originating at the tip of the cutters. To better understand how this process works, it is required to model and quantitatively characterize the granular flow. This information can be adopted to obtain an insight on the phenomenon, thus supporting the development of strategies to enable successful sample collection into a chamber.

DEM is a method particularly suited to model such a phenomenon, since it can capture the complex dynamics of a large assembly of distinct particles subject to a high number of mutual interactions and interactions with other surfaces (e.g. sampling system's cutters, collection chamber, etc.). The following paragraph

describes the DEM-based numerical model developed to investigate the tool-soil interaction and the resulting granular material flow while performing surface sample acquisition.

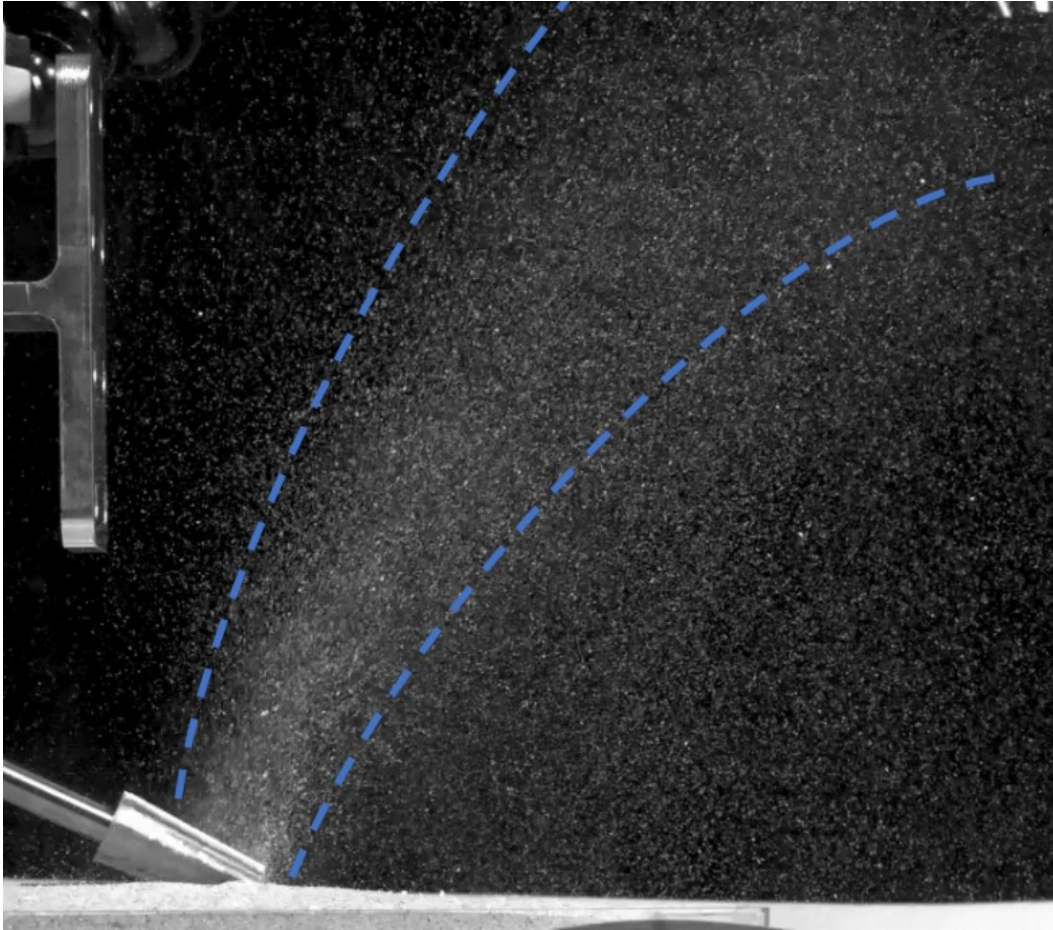


*Figure 4.9* Side view of granular material flow generated by the action of the Dual-Rasp sampling system while performing sampling operations.

#### 4.3.1.1 Numerical DEM model

The analysis of the interaction between particles and moving surfaces (e.g. sampling system, collection chamber, etc.) requires a co-simulation between DEM, simulating particles' assembly, and Multi-Body Dynamics (MBD), simulating the action of the Dual-Rasp sampling system, as well as the motion of other surfaces.

The open-source software LIGGGHTS® (LAMMPS Improved for General Granular and Granular Heat Transfer Simulations) [158] was adopted as DEM simulation engine. As the name suggests, LIGGGHTS® is a DEM particle simulation software that improves its ancestor LAMMPS (Large-scale Atomic/Molecular Massively Parallel Simulator), a classical molecular dynamics

simulation engine specialized on materials modeling. LIGGGHTS® exploits a highly scalable, efficient parallelization using Message-Passing Interface (MPI) techniques and a spatial-decomposition of the simulation domain, also providing accelerated performance on CPUs and GPUs. The software supports import and handling of complex geometries, including STL surfaces geometries, and VTK tetrahedral volume meshes. Also, it supports a variety of particle-particle contact mechanics models, including tangential history, non-sphericity, and cohesion. Efficient MPI supports a tight coupling with fellow simulation engines for co-simulation, including CFD-DEM simulations [159] and Lagrange-Euler coupling in general.

NASA JPL's software Mobility Mechanics Modeling Toolkit (M3Tk) [160] was adopted as MBD simulation engine. M3Tk exploits cutting edge multibody dynamics algorithms for high fidelity mathematical modeling of robotic systems dynamics. The tool is coupled with collision detection algorithms and contact mechanics models and enables modeling of interaction between robotic systems and the environment, as well as concurrent 3D visualization and rapid model development.

Since actual particle's shape of Enceladus surface material grains is not known, the DEM simulation model implements spherical particles for ease of validation via experimental testing. Main benefit is a significantly reduced computational cost of the simulations. The DEM model exploits the following contact mechanics models to evaluate forces/torques acting on particles.

- Hertz-Mindlin model for normal-tangential contact [128] [129] [130] [131] [132] [133] [134].
- Elastic-Plastic Spring-Dashpot (EPSD2) model for rotational contact [137] [138]. It should be noted that the rotational contact model is used in place of the real particle's shape to simulate its effect [135] [136].
- Cohesionless particles were considered, as loose material represents the low-end of the range of Enceladus surface material properties considered and the worst-case scenario in terms of particles' dispersion and sample handling.

The Hertz contact model is used to describe the normal contact between two particles. The normal force  $F_{n_{ij}}$  between  $i$ -th particle and  $j$ -th particle is evaluated when the distance  $r$  between the centers of the two particles having radii  $R_i$  and  $R_j$  is less than their contact distance  $d = R_i + R_j$ . The force is calculated according to Eq. (4.5)

$$F_{n_{ij}} = k_n \delta_{n_{ij}} - \gamma_n \dot{\delta}_{n_{ij}} \quad (4.5)$$

Where

- $k_n$  Elastic constant for normal contact.
- $\delta_{n_{ij}}$  Normal overlap distance between the two contacting particles,  $\delta_n = d - r$
- $\gamma_n$  Viscoelastic damping constant for normal contact.
- $\dot{\delta}_{n_{ij}}$  Normal component of the relative velocity between the two contacting particles.

The normal force has two terms, a spring force that is a linear function of normal overlap between the two contacting particles, and a damping force that is a linear function of normal relative velocity between the two contacting particles, thus a non-linear function of normal overlap.

The elastic constant for normal contact  $k_n$  is defined according to Eq. (4.6), while the viscoelastic damping constant for normal contact  $\gamma_n$  is defined according to Eq. (4.7)

$$k_n = \frac{4}{3} E^* \sqrt{R^* \delta_n} \quad (4.6)$$

$$\gamma_n = -2 \sqrt{\frac{5}{6}} \beta \sqrt{S_n m^*} \geq 0 \quad (4.7)$$

Where

$E^*$  Equivalent Young's modulus,  $E^* = \left( \frac{1-\nu_i^2}{E_i} + \frac{1-\nu_j^2}{E_j} \right)^{-1}$  where  $\nu$  is the Poisson's ratio and  $E$  is the Young's modulus of the  $i$ -th particle and  $j$ -th particle, respectively.

$R^*$  Equivalent radius of the contacting particles,  $R^* = \left( \frac{1}{R_i} + \frac{1}{R_j} \right)^{-1}$  where  $R$  is the radius of the  $i$ -th particle and  $j$ -th particle, respectively.

$m^*$  Equivalent mass,  $m^* = \left( \frac{1}{m_i} + \frac{1}{m_j} \right)^{-1}$  where  $m$  is the mass of the  $i$ -th particle and  $j$ -th particle, respectively. The particle mass is calculated by using the defined density  $\rho$  and the volume of the particle is derived by the defined radius  $R$ .

Terms  $S_n$  and  $\beta$  of the viscoelastic damping constant  $\gamma_n$  are defined according to Eq. (4.8 – 4.9)

$$S_n = 2E^* \sqrt{R^* \delta_n} \quad (4.8)$$

$$\beta = \frac{\ln e}{\sqrt{\ln^2 e + \pi^2}} \quad (4.9)$$

Where  $e$  is the coefficient of restitution between  $i$ -th particle and  $j$ -th particle. It should be noted that this parameter is defined per particle type pair. Therefore, in the case of considering two types of particle  $i$  and  $j$  (i.e. two different materials) to represent the soil material and the sampling tool material, then the values of coefficients  $e_{ii}$ ,  $e_{ij} = e_{ji}$ ,  $e_{jj}$  must be defined.

The Mindlin-Deresiewicz contact model is used to describe the tangential contact between two particles. The tangential force  $F_{tij}$  between  $i$ -th particle and  $j$ -th particle is evaluated when the distance  $r$  between the centers of the two particles having radii  $R_i$  and  $R_j$  is less than their contact distance  $d = R_i + R_j$ . The force is calculated according to Eq. (4.10)

$$F_{tij} = k_t \delta_{tij} - \gamma_t \dot{\delta}_{tij} \quad (4.10)$$

Where

$k_t$  Elastic constant for tangential contact.

$\delta_{tij}$  Tangential overlap distance between the two contacting particles,  $\delta_t = d - r$

$\gamma_t$  Viscoelastic damping constant for tangential contact.

$\dot{\delta}_{tij}$  Tangential component of the relative velocity between the two contacting particles.

The tangential force has two terms, a shear force that is a linear function of tangential overlap between the two contacting particles, and a damping force that is a linear function of tangential relative velocity between the two contacting particles, thus a non-linear function of tangential overlap. The shear force term also considers the duration of the tangential overlap between the two particles during contact, thus it is a history effect.

The Coulomb friction criterion truncates the tangential force if it exceeds a critical value defined by Eq. (4.11)

$$F_t \leq \mu_s F_n \quad (4.11)$$

Where  $\mu_s$  is the coefficient of static friction between  $i$ -th particle and  $j$ -th particle, respectively. It should be noted that this parameter is defined per particle

type pair. Therefore, in the case of considering two types of particle  $i$  and  $j$  (i.e. two different materials) to represent the soil material and the sampling tool material, then the values of the coefficients  $\mu_{ii}, \mu_{ij} = \mu_{ji}, \mu_{jj}$  must be defined.

The elastic constant for tangential contact  $k_t$  is defined according to Eq. (4.12), while the viscoelastic damping constant for tangential contact  $\gamma_t$  is defined according to Eq. (4.13)

$$k_t = 8G^* \sqrt{R^* \delta_n} \quad (4.12)$$

$$\gamma_t = -2 \sqrt{\frac{5}{6}} \beta \sqrt{S_t m^*} \geq 0 \quad (4.13)$$

Where

$G^*$  Equivalent shear modulus,  $G^* = \left( \frac{2(2-\nu_i)(1+\nu_i)}{E_i} + \frac{2(2-\nu_j)(1+\nu_j)}{E_j} \right)^{-1}$  where  $\nu$  is the Poisson's ratio and  $E$  is the Young's modulus of particle types  $i$ -th and  $j$ -th respectively.

$R^*$  Equivalent radius of the contacting particles,  $R^* = \left( \frac{1}{R_i} + \frac{1}{R_j} \right)^{-1}$  where  $R$  is the radius of the particle types  $i$ -th and  $j$ -th, respectively.

$m^*$  Equivalent mass,  $m^* = \left( \frac{1}{m_i} + \frac{1}{m_j} \right)^{-1}$  where  $m$  is the mass of the  $i$ -th particle and  $j$ -th particle, respectively. The particle mass is calculated by using the defined density  $\rho$  and the volume of the particle is derived by the defined radius  $R$ .

Terms  $S_t$  and  $\beta$  of the viscoelastic damping constant  $\gamma_t$  are defined according to Eq. (4.14 – 4.15)

$$S_t = 8G^* \sqrt{R^* \delta_t} \quad (4.14)$$

$$\beta = \frac{\ln e}{\sqrt{\ln^2 e + \pi^2}} \quad (4.15)$$

Where  $e$  is the coefficient of restitution between  $i$ -th particle and  $j$ -th particle. It should be noted that this parameter is defined per particle type pair. Therefore, in the case of considering two types of particle  $i$  and  $j$  (i.e. two different materials) to represent the soil material and the sampling tool material, then the values of coefficients  $e_{ii}, e_{ij} = e_{ji}, e_{jj}$  must be defined.

The Elastic-Plastic Spring-Dashpot (EPSD2) contact model is used to describe the rotational contact between two contacting particles. The model adds an additional torque contribution defined according to Eq. (4.16)

$$M_{r_{ij}} = -\frac{\omega_i - \omega_j}{|\omega_i - \omega_j|} \mu_r R_r F_n \quad (4.16)$$

Where

$\omega_i$  Angular velocity of  $i$ -th particle.

$\omega_j$  Angular velocity of  $j$ -th particle.

$\mu_r$  Coefficient of rolling friction, defined as  $\mu_r = \tan \alpha$ . The angle  $\alpha$  is called angle of rolling resistance which is the maximum angle of a slope on which the rolling resistance torque counterbalances the torque produced by gravity acting on the body.

$R_r$  Rolling radius, defined as  $R_r = \frac{R_i R_j}{R_i + R_j}$ , where  $R_i$  and  $R_j$  are the radii of  $i$ -th particle and  $j$ -th particle, respectively.

$F_n$  Normal force between contacting particles.

It should be noted that this parameter is defined per particle type pair. Therefore, in the case of considering two types of particle  $i$  and  $j$  (i.e. two different materials) to represent the soil material and the sampling tool material, then the values of the coefficients  $\mu_{r_{ii}}, \mu_{r_{ij}} = \mu_{r_{ji}}, \mu_{r_{jj}}$  must be defined.

Figure 4.10 shows a graphical representation of contact mechanics models implemented into the DEM simulation model.

Table 4.1 summarizes the input parameters required by the DEM simulation model sorted by the contact mechanics model adopted. The rows denote the membership to a certain contact mechanics model, whereas the columns separate the different contributions to each model.

Table 4.2 summarizes all input parameters required by the DEM simulation model sorted by category (i.e. surface geometry, particle, paired, environmental). Since the paired parameters are defined by pairs, the subscript **pt** defines the particle-surface parameters, while the subscript **pp** defines the particle-particle parameters).

Several DEM codes used in geomechanics applications, including LAMMPS/LIGGGHTS [112] [161], use the second order velocity-Verlet integration scheme to integration Newton's equations of motion [162]. This numerical integration method is conditionally stable, meaning that it is numerically stable only when the timestep is less than a critical timestep  $T_c$ . If this condition is fulfilled, small perturbations of the initial parameters will not amplify to big changes in the final solution. Two main approaches are typically found in the literature to determine  $T_c$  for DEM simulations. The first approach relies on the oscillation period of a 1 DOF system, while the second approach considers the

velocity of Rayleigh waves. In the 1 DOF system approach, a spring-mass system is considered and  $t_c$  was originally evaluated via Eq. (4.17) [115]

$$T_{c_{1DOF}} = 2\sqrt{\frac{m}{k}} \quad (4.17)$$

Further developments led to Eq. (4.18) [163]

$$T_{c_H} = 2\alpha \sqrt{\frac{m_{min}}{k_{max}}} \quad (4.18)$$

Where  $m_{min}$  is the minimum mass,  $k_{max}$  is the maximum normal/tangential contact stiffness, and  $\alpha$  is a parameter that considers multiple contacts for each mass.

Since most DEM simulation models use the Hertzian contact model, the contact stiffness depends on the overlap distance, thus there will be several different spring stiffnesses in the DEM simulation at a given timestep. For this reason, Eq. (4.19) was proposed as a modification of Eq. (4.17) and was implemented in LS-DYNA code [164].

$$T_{c_J} = 0.2\pi \sqrt{\frac{m_{min}}{E}} \sqrt{\frac{\beta}{3(1+2\nu)}} \quad (4.19)$$

Where  $E$  is the particle Young's modulus and  $\beta$  is a stiffness penalty parameter.

A similar formulation was also proposed for the critical timestep associated with rotational motion, according to Eq. (4.20) [165]

$$T_{c_T} = 2 \sqrt{\frac{2m_{min}}{5k_t}} \quad (4.20)$$

Where  $k_t$  is the tangential spring stiffness.

The velocity of Rayleigh waves is considered a more suited approach to determine the critical timestep when the Hertzian contact model is used, mainly because the contact model is non-linear [166] [167] [168] [169]. This approach considers critical the time for a Rayleigh wave to pass through a sphere during contact. In fact, excessive overlaps between particles can lead to disturbance waves. Eq. (4.21) was proposed to determine  $T_{c_R}$  based on this approach.

$$T_{cR} = \frac{\pi R \sqrt{\frac{\rho}{G}}}{0.1631\nu + 0.8766} \quad (4.21)$$

Where  $\rho$  is the particle density,  $G$  is the particle shear stiffness, and  $\nu$  is the particle Poisson's ratio. Since the Hertzian model has been adopted for the DEM simulation model implemented, the Rayleigh critical timestep was considered as an estimate to determine the simulation timestep to use. In particular, the simulation timestep was selected by multiplying  $T_{cR}$  by a factor between 0.2 and 0.4, as suggested in the literature to prevent numerical stability issues [164] [170].

Newton's equations of motion are solved at each timestep by performing NVE integration to update position, velocity, and angular velocity for finite-size spherical particles. NVE integration keeps constant the number of particles (i.e. "N"), the volume (i.e. "V"), and the energy (i.e. "E") of the system. As a result, the sum of kinetic and potential energy of the system is conserved. This integration scheme creates a system trajectory consistent with the microcanonical ensemble.

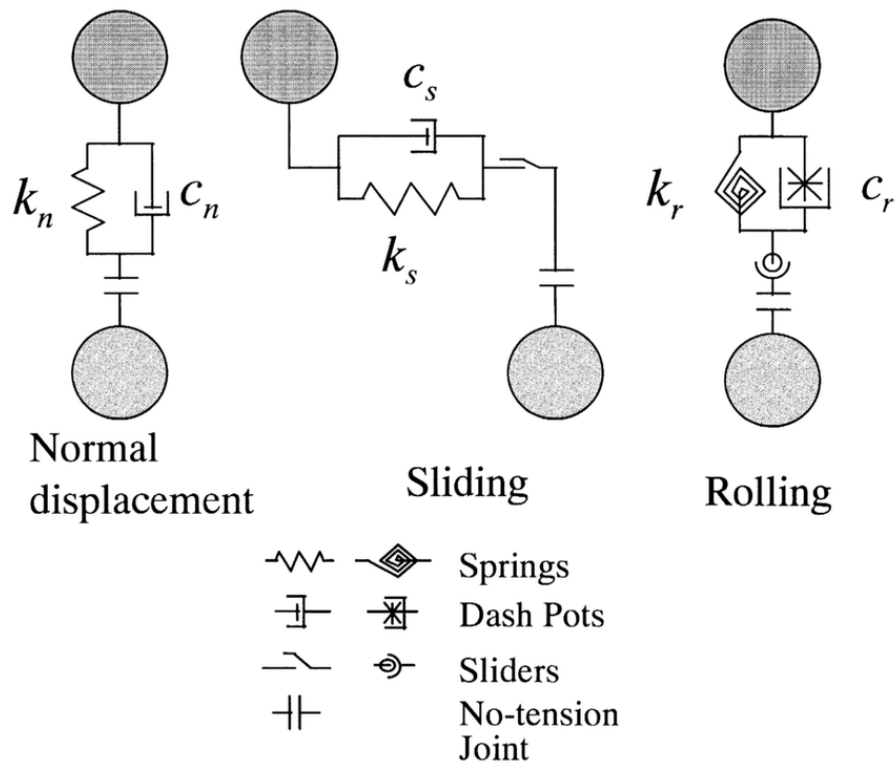


**Figure 4.10** Graphic representation of contact mechanics models [171].

**Table 4.1** DEM model input parameters sorted by contact mechanics model.

		Contribution		
		Elastic	Dissipative	Inertial
Contact model	Normal contact (Hertz model)	$E, \nu$	$e$	$\rho$
	Tangential contact (Mindlin-Deresiewicz model)	$E, \nu$	$e, \mu_s$	$\rho$
	Rotational contact (EPSD2 model)	$(E, \nu)$	$\mu_r, (e)$	$(\rho)$

**Table 4.2** DEM model input parameters sorted by category.

Category					
		Surface geometry	Particle	Paired	Environmental
Parameter	Young's modulus ( $E_t$ )		Young's modulus ( $E_p$ )	$pp$ coefficient of static friction ( $\mu_{s_{pp}}$ )	Gravitational acceleration ( $g$ )
	Poisson's ratio ( $\nu_t$ )		Poisson's ratio ( $\nu_p$ )	$pt$ coefficient of static friction ( $\mu_{s_{pt}}$ )	
			Density ( $\rho_p$ )	$pp$ coefficient of rolling friction ( $\mu_{r_{pp}}$ )	
			Diameter ( $D_p$ )	$pt$ coefficient of rolling friction ( $\mu_{r_{pt}}$ )	
				$pp$ coefficient of restitution ( $e_{pp}$ )	
				$pt$ coefficient of restitution ( $e_{pt}$ )	

### 4.3.1.2 Analysis metrics

To understand how the Dual-Rasp sampling system enables momentum transfer to particles, how granular material flow develops and how the Dual-Rasp sampling system performs, it is required to define a set of metrics providing a quantitative characterization of the granular material flow.

Since the granular material flow would follow a ballistic motion in an environment with no atmosphere such as the one found on Enceladus, similar metrics to those required to characterize the projectile ballistic motion were chosen.

- *Velocity magnitude.* This metric highly affects cuttings' trajectories, together with the direction of the velocity vector, defined through the following two metrics. Since the granular material flow is made of a number of cuttings, the statistical distribution of the velocity magnitude among cuttings is evaluated with the possibility of determining the percentile of cuttings in a certain range of velocity magnitude values (Figure 4.11).
- *Elevation and Azimuth dispersion angles.* These two metrics complete the minimum set of information required to characterize the granular material flow in the 3D space. To determine cuttings' trajectories, the information on velocity magnitude must be coupled with the information on the direction of velocity vector. This information is provided through elevation and azimuth angles, thus enabling a full 3D spatial characterization of the granular material flow. The elevation dispersion angle is defined with respect to the horizontal direction (i.e. X-axis in Figure 4.12), while the azimuth dispersion angle is defined with respect to the longitudinal symmetry axis of the Dual-Rasp sampling system (i.e. green dashed line in Figure 4.13). Since the granular material flow has a certain dispersion, the spatial dispersion angle is also included into the definition of these two metrics. Again, since the granular material flow is made of a number of cuttings, the statistical distribution of the spatial dispersion angles among cuttings is evaluated with the possibility of determining the percentile of cuttings in a certain range of dispersion angle values (Figure 4.12 and Figure 4.13).

The analysis metrics are conceived to characterize both the simulated and the experimental granular material flow to obtain the same data products enabling apples-to-apples comparison and ease of validation.

A typical DEM simulation outputs a log file with a certain frequency defined by the user. The log files contain information about each particle of the simulation

at a certain timestep, including ID, type, cartesian position components, and cartesian velocity components. A tool for post-processing simulation log files to extrapolate the analysis metrics from a simulation was coded to automate the process. Post-processing focuses on a user-defined control volume, that is a subdomain of simulation domain. Post-processing outputs the distribution of the analysis metrics, also providing the so-called *filling bands*, a range of values of the analysis metrics containing a certain percentage of particles. The information on filling bands supports the identification of requirements for system's design.

Figure 4.14 shows the methodology applied to post-process DEM simulation data for extraction of analysis metrics.

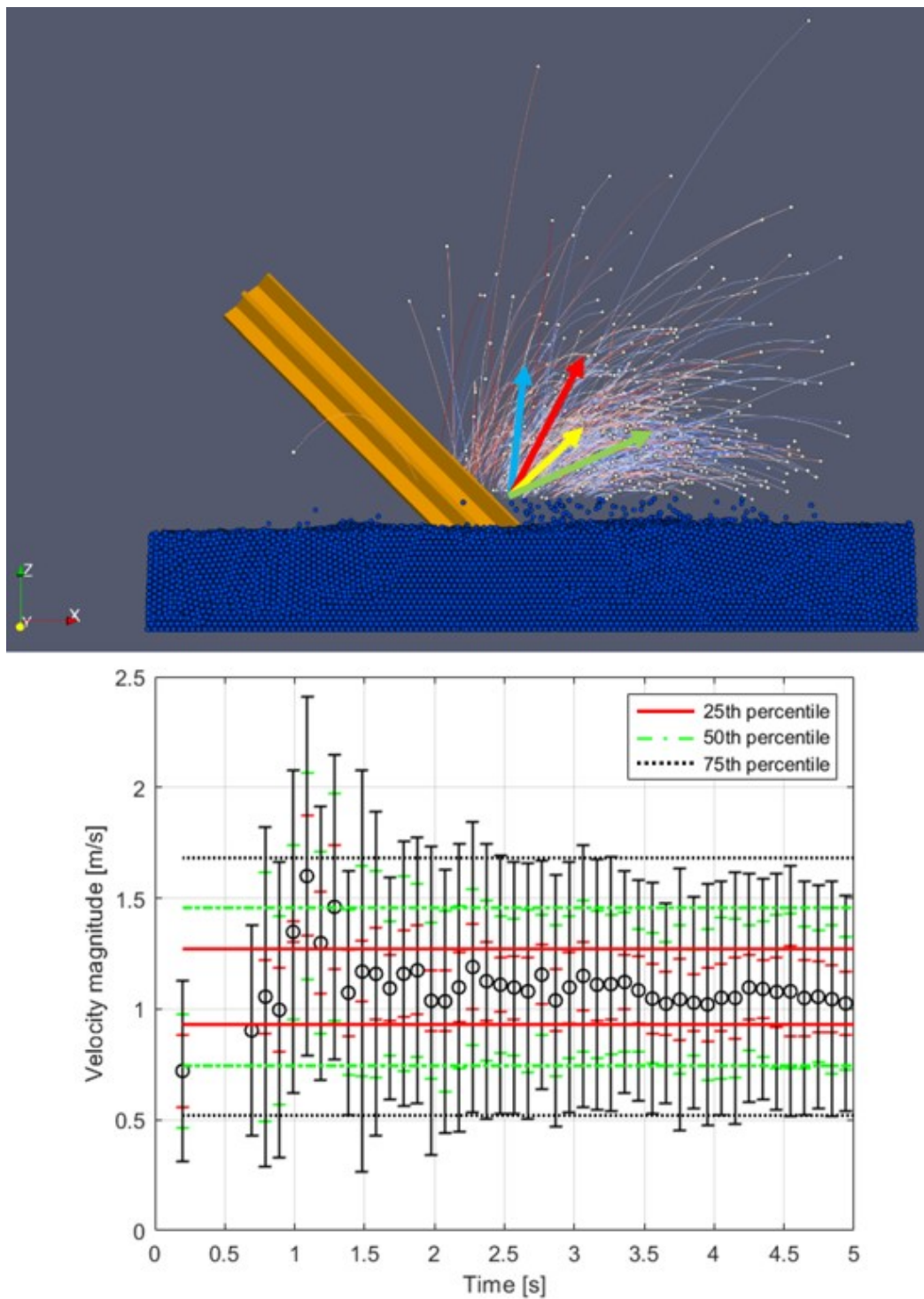


**Figure 4.11** Velocity magnitude analysis metric. Top: side view of DEM-simulated granular material flow generated by the Dual-Rasp cutting heads with indication of velocity vectors. Bottom: plot of velocity magnitude distribution, including indication of the percentile of particles in a certain range of velocity magnitude values.

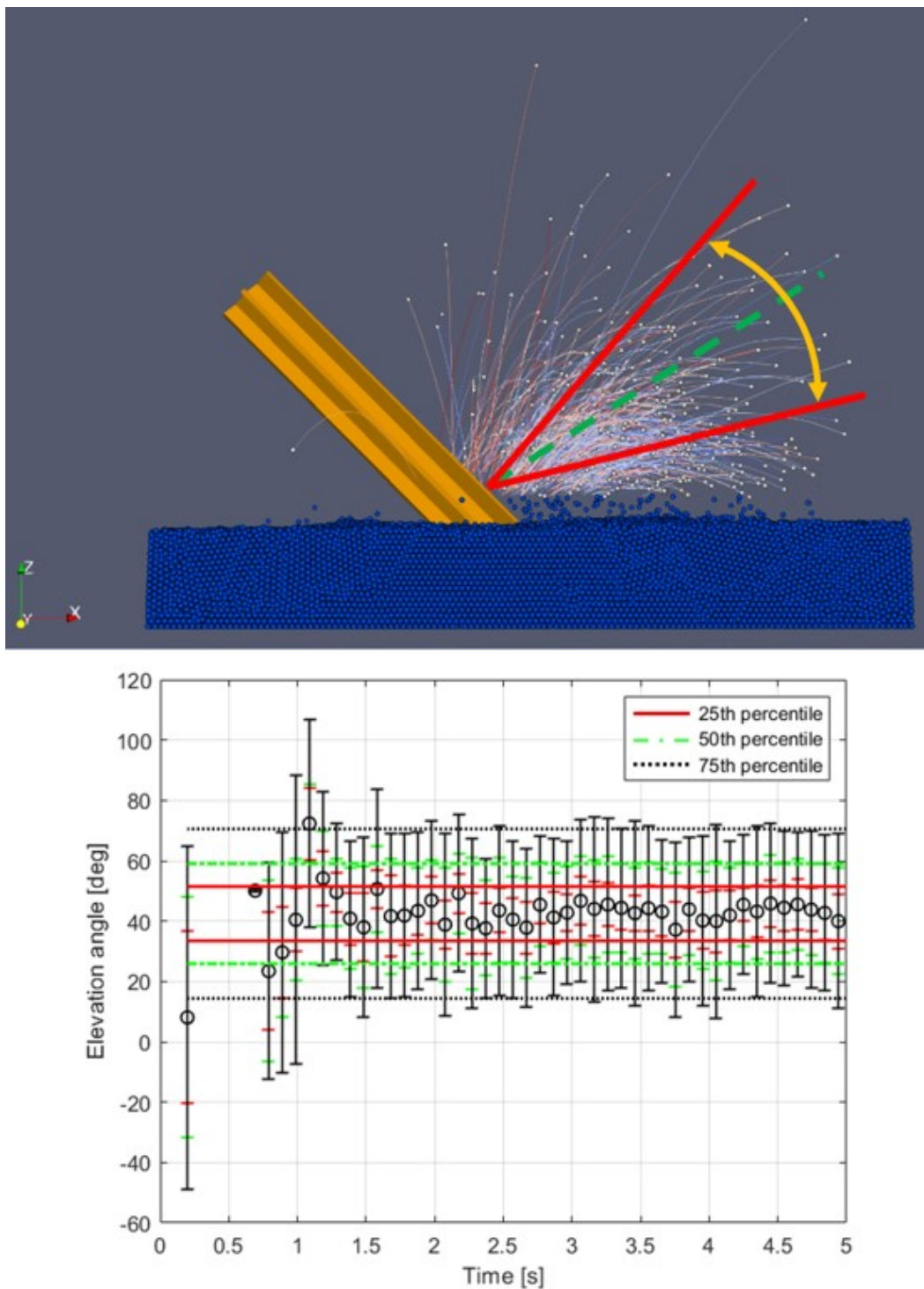


**Figure 4.12** Elevation dispersion angle analysis metric. Top: side view of DEM-simulated granular material flow generated by the Dual-Rasp cutting heads with indication of elevation dispersion angle. Bottom: plot of elevation dispersion angle distribution, including indication of the percentile of particles in a certain range of elevation dispersion angle values.

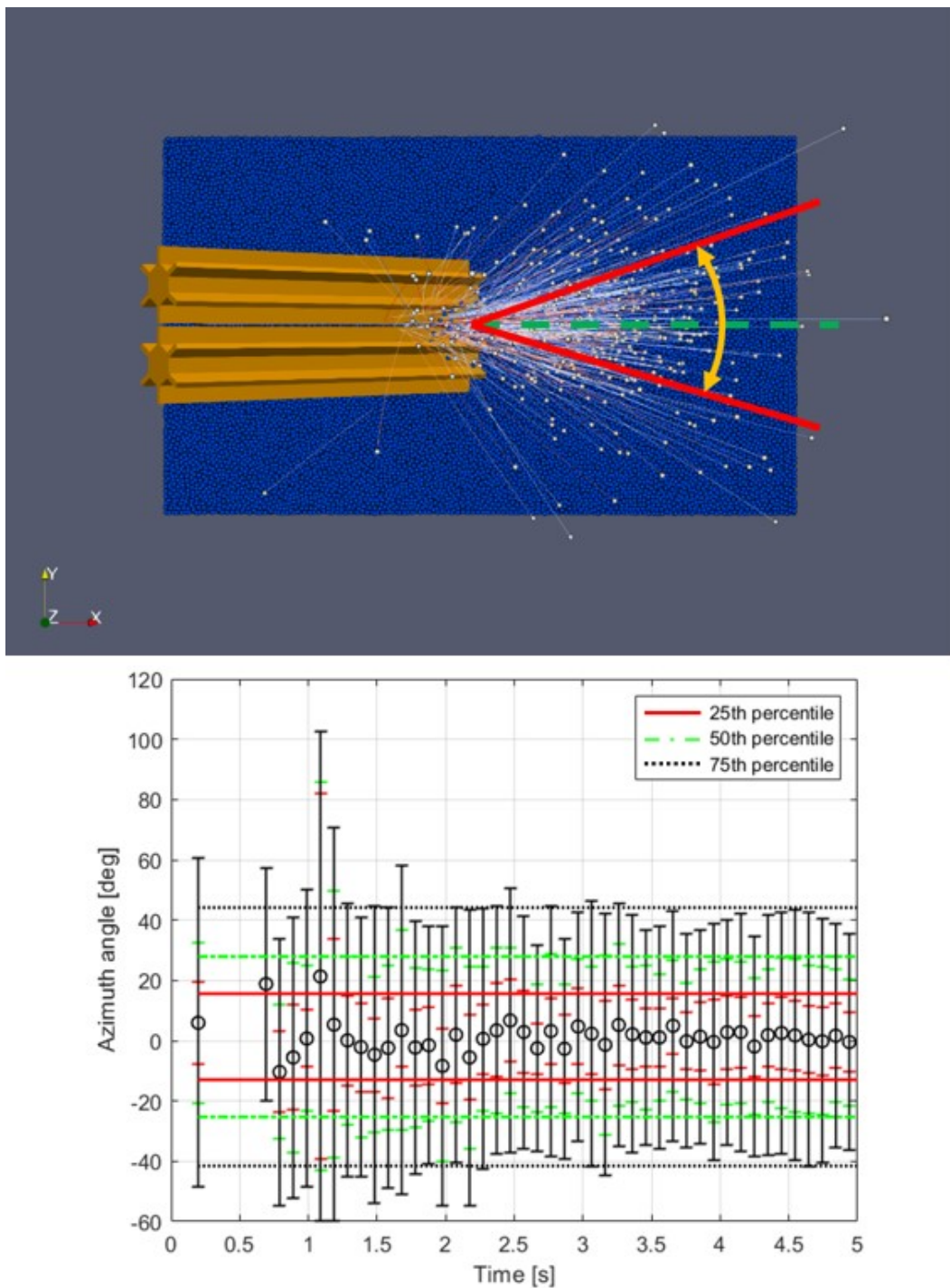


**Figure 4.13** Azimuth dispersion angle analysis metric. Top: top view of DEM-simulated granular material flow generated by the Dual-Rasp cutting heads with indication of azimuth dispersion angle. Bottom: plot of azimuth dispersion angle distribution, including indication of the percentile of particles in a certain range of azimuth dispersion angle values.

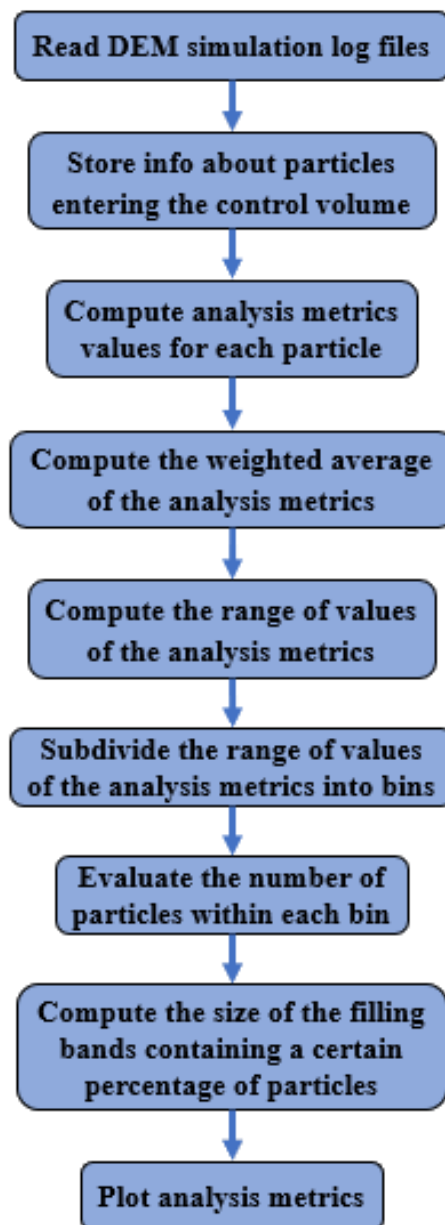


*Figure 4.14 Post-processing methodology of DEM simulation data.*

### 4.3.1.3 Sensitivity analysis of DEM model parameters

As shown in Table 4.2, thirteen input parameters are required to perform a DEM simulation. Among those parameters, surface geometry parameters and environmental parameter can be pre-defined. Surface geometry parameters (i.e. Young's modulus and Poisson's ratio) are defined by the material chosen for Dual-Rasp cutting heads, while environmental parameter is the gravitational acceleration. Last pre-defined input parameter is the particle diameter. Equivalent-sphere Enceladus particles are expected to be micron-sized, with an average diameter of about 10  $\mu\text{m}$  [40]. However, simulation of particles at the real grain

size would be too computationally demanding, thus requiring a scale up of the simulated particles [172] [173] [174] [175]. A particle diameter equal to 1 mm was found to be an adequate tradeoff between computational cost and accuracy. For model validation purposes, a real material composed of unconsolidated particles of the same size and shape as the simulated material (i.e. spherical particles of 1 mm diameter) was selected, as detailed in paragraph 4.3.1.5. DEM input parameters are then reduced to nine parameters related to both particles and paired interaction between particles and surface geometries. To further decrease the dimensionality of the DEM model, a sensitivity analysis was performed with the purpose of determining the most sensitive parameters influencing the granular material flow generated by the Dual-Rasp sampling system. The sensitivity analysis requires to:

1. Define a simulation baseline with a set of pre-defined parameters.
2. Define a range of values for each parameter reported below and included in the sensitivity analysis:
  - Particle Young's modulus ( $E_p$ )
  - Particle Poisson's ratio ( $\nu_p$ )
  - Particle density ( $\rho_p$ )
  - Particle-particle coefficient of static friction ( $\mu_{spp}$ )
  - Particle-surface coefficient of static friction ( $\mu_{spt}$ )
  - Particle-particle coefficient of rolling friction ( $\mu_{rpp}$ )
  - Particle-surface coefficient of rolling friction ( $\mu_{rpt}$ )
  - Particle-particle coefficient of restitution ( $e_{pp}$ )
  - Particle-surface coefficient of restitution ( $e_{pt}$ )
3. Perform DEM simulations by changing the parameters' values in the pre-defined range. The simulation aims to reproduce the sampling operation performed by the Dual-Rasp sampling system and the resulting granular material flow.
4. Evaluate parameters' sensitivity by extracting the analysis metrics from simulation results.
5. Identify most sensitive parameters influencing the granular material flow.

The simulation baseline includes the environmental parameter (i.e. gravitational acceleration), parameters related to the Dual-Rasp cutting heads, parameters related to the particles, and paired parameters related to the interaction between particles and surface geometries. Baseline values of environmental parameter and Dual-Rasp cutting heads parameters are common to all simulations and are summarized in Table 4.3. Since particles were scaled up because of computational constraints, a resolution parameter  $\Gamma$  was introduced to

appropriately describe the size of the particles with respect to the Dual-Rasp cutting heads [176] [177]. The resolution parameter determines the number of particles that come into contact at once with the minimal characteristic length  $L_{min}$  of the cutting heads. In this case, the minimal feature of the cutting heads that come into contact with the particles is the single tooth. Therefore, the minimal characteristic length  $L_{min}$  is equal to the length of the tooth. The resolution parameter  $\Gamma$  is thus defined according to Eq. (4.22)

$$\Gamma = \frac{L_{min}}{D_{max}} \quad (4.22)$$

Where  $D_{max}$  is the maximum particle diameter.

According to literature, values of the resolution parameter  $\Gamma \geq 2.5$  are found to be sufficient for systems with an architecture similar to the Dual-Rasp cutting heads [177] [178] [172]. Therefore, a resolution parameter  $\Gamma = 3$  was selected and the tooth length (i.e. the minimal characteristic length  $L_{min}$ ) was derived, given a particle diameter  $D_{max}$  equal to 1 mm. Figure 4.15 shows the model of the cutting head used in the DEM simulations. DEM computational parameters are reported in Table 4.4.

Values of particle parameters and paired parameters subject to the sensitivity analysis are summarized in Table 4.5. Values were selected to include granular material properties ranging from silica sand to pure ice [81] [149] [179] [180] [181] [182]. Most baseline values were selected as mid-range values. Baseline value for particle Young's modulus was selected to reduce the computational cost of simulations. Range of values for the coefficient of restitution was selected assuming that particles dissipate energy during collisions because of rotational motion, plastic deformation, and heat. For these reasons, the coefficient of restitution ranges from 0 (i.e. perfectly inelastic collision) to 1 (i.e. perfectly elastic collision). Range of values for the coefficient of rolling friction was selected considering particle's shape ranging from rounded/sub-rounded grains with negligible inter-locking to particles with low roundness and sphericity (e.g. jagged not spherical particles). Baseline value selected as the most plausible for the expected rounded/sub-rounded Enceladus ice grains [30] [40] [85].

**Table 4.3** Values of environmental parameter and Dual-Rasp cutting heads parameters for the sensitivity analysis of DEM model parameters. These values are common to all simulations.

<b>Parameters of Dual-Rasp cutting heads</b>	
<b>Geometry</b>	Cylindrical core with 6 straight uniformly spaced radial teeth
<b>Geometrical features and Position</b>	<ul style="list-style-type: none"> <li>• Core length: 30 mm</li> <li>• Core diameter: 7 mm</li> <li>• Tooth: 3 mm (length) x 1 mm (thickness)</li> <li>• Gap between cutting heads: 2 mm (at teeth's tip)</li> <li>• Inclination with respect to horizontal: 45 deg</li> </ul>
<b>Prescribed motion</b>	<ul style="list-style-type: none"> <li>• Vertical motion (plunging) velocity: 2 mm/s</li> <li>• Vertical motion (plunging) displacement: 10 mm</li> <li>• Rotational speed: 2000 RPM</li> </ul>
<b>Material (Al 6061-T6)</b>	<ul style="list-style-type: none"> <li>• Young's modulus (<math>E_t</math>): 68.9 GPa [183]</li> <li>• Poisson's ratio (<math>\nu_t</math>): 0.33 [183]</li> </ul>
<b>Mesh</b>	<ul style="list-style-type: none"> <li>• Shell surface mesh</li> <li>• 1 mm element size</li> <li>• 7706 total nodes</li> <li>• 3852 total elements</li> </ul>
<b>Environmental parameter</b>	
<b>Gravitational acceleration</b>	9.81 m/s <sup>2</sup>

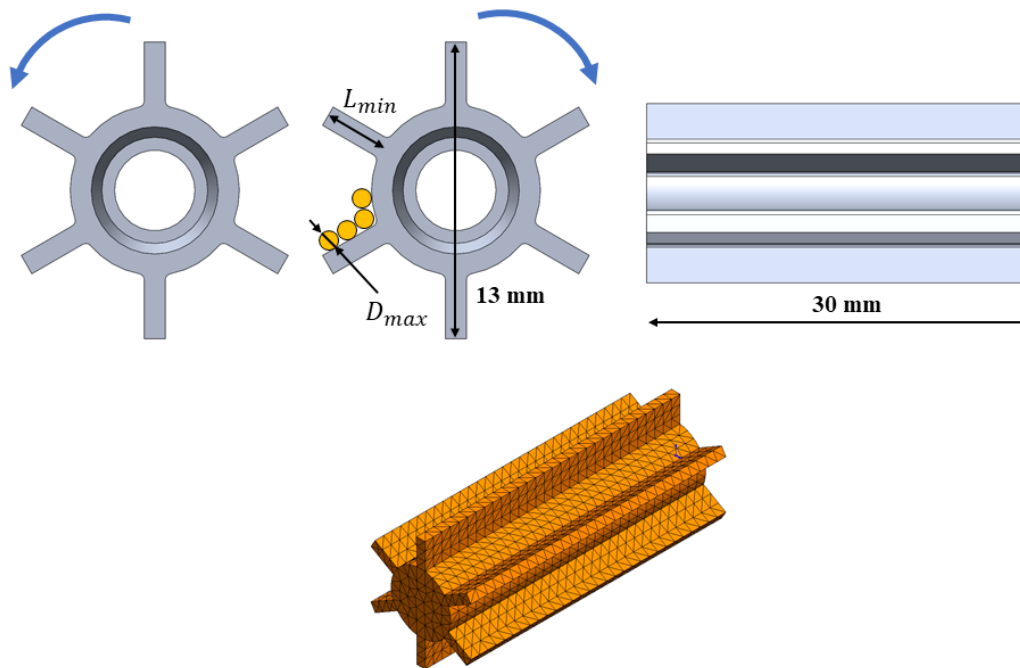


**Figure 4.15** Front view of counter-rotating Dual-Rasp cutting heads (Top left). Side view (Top right) and surface mesh (Bottom) of a single cutting head.

**Table 4.4** DEM computation parameters.

DEM computation parameters	
Integrator	NVE
Time step	0.5e-05 s
Number of steps	1.2e+05
Simulation time	5 s

**Table 4.5** Values of particle parameters and paired parameters for the sensitivity analysis of DEM model parameters. Baseline values are highlighted in red.

Particle parameters	
Shape / Shape distribution	<b>Sphere / Monodisperse</b>
Size / Size distribution	<b>1 mm diameter / Monodisperse</b>
Number of particles	<b>187500</b>
Size of particles' bed	<b>75 mm (length) x 75 mm (width) x 30 mm (height)</b>
Young's modulus ( $E_p$ )	[ <b>0.1</b> , 1, 10] GPa
Poisson's ratio ( $\nu_p$ )	[0.15, 0.25, <b>0.35</b> ]
Density ( $\rho_p$ )	[900 <b>3000</b> 6000] kg/m <sup>3</sup>
Paired parameters	
$pp$ coefficient of static friction ( $\mu_{spp}$ )	[0.1, <b>0.5</b> , 1]
$pt$ coefficient of static friction ( $\mu_{spt}$ )	[0.1, <b>0.5</b> , 1]
$pp$ coefficient of rolling friction ( $\mu_{rpp}$ )	[ <b>0.005</b> , 0.1, 0.3]
$pt$ coefficient of rolling friction ( $\mu_{rpt}$ )	[ <b>0.005</b> , 0.1, 0.3]
$pp$ coefficient of restitution ( $e_{pp}$ )	[0.1, <b>0.5</b> , 0.9]
$pt$ coefficient of restitution ( $e_{pt}$ )	[0.1, <b>0.5</b> , 0.9]

Given the range of values for the parameters involved in the sensitivity analysis, it is possible to define the simulation matrix of the sensitivity analysis. The simulation matrix is composed of simulation sets characterized by the investigation of a single parameter involved in the sensitivity analysis. Therefore, nine simulation sets are defined, each one including three simulations, one for each value assigned to the reference parameter. The simulation matrix is then composed of 27 simulations. However, some simulations are duplicated. In fact, it should be noted that each simulation set has one simulation out of the three (named *baseline simulation*) that has all baseline values of the parameters, resulting in a total of nine *baseline simulations*. All *baseline simulations* are identical across the simulation sets. Therefore, only one out of the nine *baseline*

*simulations* need to be performed. As a result, eight *baseline simulations* are removed from the simulation matrix, resulting in a total of 19 unique simulations required to perform the sensitivity analysis. The simulation matrix was developed by assuming that the parameters involved in the sensitivity analysis are independent each other. Table 4.6 and Table 4.7 show the simulation matrix and the values of variable parameters for the sensitivity analysis, respectively.

Because of the high computational cost required to perform DEM simulations, it is required to use HPC resources since personal computers or workstations are usually not suited for the intensive computations required by this type of simulation. For this reason, the resources of Texas Advanced Computing Center (TACC) were adopted to support all DEM simulations described in this dissertation. TACC is an advanced computing research center at University of Texas at Austin, United States, that provides several services, including a comprehensive ecosystem of cutting-edge HPC resources, visualization, data analysis, storage, archive, cloud, data-driven computing, connectivity, tools, Application Programming Interface (API), algorithms, consulting, and software [184]. TACC has several HPC systems available to satisfy the several needs of the science and technology community. The HPC system exploited to perform the DEM simulations described in this dissertation is called Lonestar5 (LS5) [185]. LS5 cabinets and system architecture are shown in Figure 4.16 and Figure 4.17, respectively. LS5 main system features are summarized below [186].

- 1252 Cray XC40 compute nodes, each with two 12-core Intel® Xeon® processing cores for a total of 30048 compute cores.
- 2 large memory compute nodes, each with 1 TB memory.
- 8 large memory compute nodes, each with 512 GB memory.
- 16 Nodes with NVIDIA K-40 GPUs.
- 5 PB DataDirect Networks storage system.
- Cray-developed Aries interconnect.

Each DEM simulation performed within the sensitivity analysis typically required 500 compute cores, 6 hours of computational time and produced up to 50 GB of raw data.

**Table 4.6** DEM simulation matrix for the sensitivity analysis of DEM model parameters. All baseline simulations (highlighted in red) are included for completeness.

Simulation Set AS	Simulation Set BS	Simulation Set CS
AS1 Baseline + AS2 AS3	BS1 Baseline + BS2 BS3	CS1 Baseline + CS2 CS3
Simulation Set DS	Simulation Set ES	Simulation Set FS
DS1 Baseline + DS2 DS3	ES1 Baseline + ES2 ES3	FS1 Baseline + FS2 FS3
Simulation Set GS	Simulation Set HS	Simulation Set MS
GS1 Baseline + GS2 GS3	HS1 Baseline + HS2 HS3	MS1 Baseline + MS2 MS3

**Table 4.7** Values of variable parameters for the sensitivity analysis of DEM model parameters. Baseline values are highlighted in red.

Parameter	Code	Value
Particle Young's Modulus ( $E_p$ )	AS1	0.1 GPa
	AS2	1 GPa
	AS3	10 GPa
Particle Poisson's ratio ( $\nu_p$ )	BS1	0.15
	BS2	0.25
	BS3	0.35
Particle density ( $\rho_p$ )	CS1	900 kg/m <sup>3</sup>
	CS2	3000 kg/m <sup>3</sup>
	CS3	6000 kg/m <sup>3</sup>
Particle-particle coeff. static friction ( $\mu_{spp}$ )	DS1	0.1
	DS2	0.5
	DS3	1

Particle-particle coeff. restitution ( $e_{pp}$ )	ES1	0.1
	<b>ES2</b>	<b>0.5</b>
	ES3	0.9
Particle-particle coeff. rolling friction ( $\mu_{r_{pp}}$ )	<b>FS1</b>	<b>0.005</b>
	FS2	0.1
	FS3	0.3
Particle-tool coeff. static friction ( $\mu_{s_{pt}}$ )	GS1	0.1
	<b>GS2</b>	<b>0.5</b>
	GS3	1
Particle-tool coeff. restitution ( $e_{pt}$ )	HS1	0.1
	<b>HS2</b>	<b>0.5</b>
	HS3	0.9
Particle-tool coeff. rolling friction ( $\mu_{r_{pt}}$ )	<b>MS1</b>	<b>0.005</b>
	MS2	0.1
	MS3	0.3



*Figure 4.16 Lonestar5 cabinets [185].*

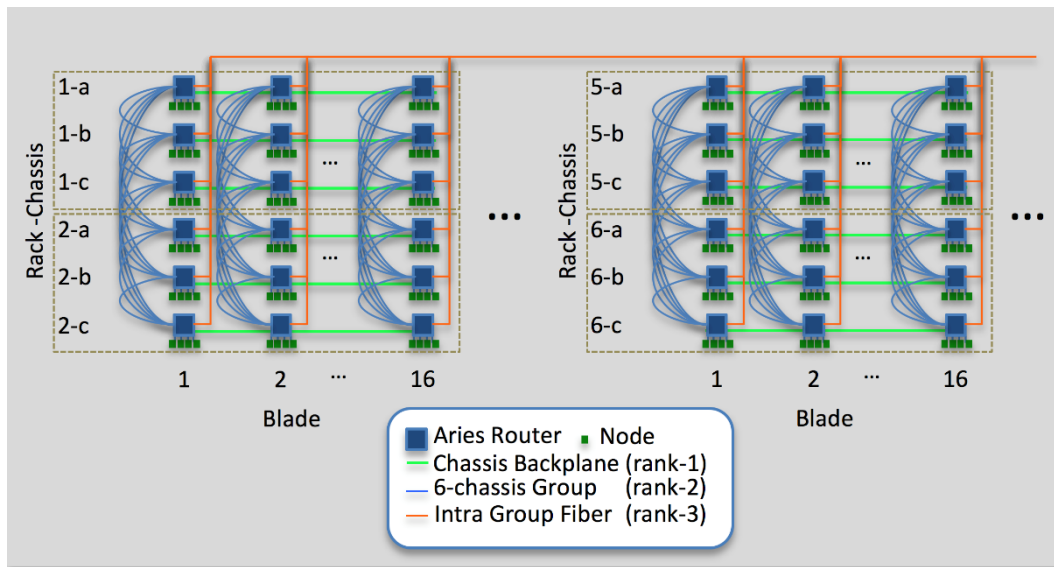


**Figure 4.17** Lonestar5 system architecture [185].

Raw DEM simulation data were post-processed to obtain the analysis metrics. Furthermore, average values of the analysis metrics were computed for the three values of the range defined for each parameter involved in the sensitivity analysis, and then fitted via linear trend functions. Delta-values across trend functions were computed for the average value, 25<sup>th</sup> percentile, 50<sup>th</sup> percentile, and 75<sup>th</sup> percentile of the analysis metrics of each parameter (Table 4.8, Table 4.9, and Table 4.10). Delta-values are the basis for the determination of most sensitive parameters, since they provide a quantitative indication about the influence of a parameter on the analysis metrics, thus on the granular material flow. To efficiently use these results and complete the sensitivity analysis, the Figure-of-Merit (FOM) approach was adopted [187] [188]. A FOM is a quantitative parameter used to characterize a device, system, or method, relative to its alternatives. In this context, FOMs are used to capture the characteristics of the parameters involved in the sensitivity analysis and facilitate direct comparison by using relative merits. FOMs should have some basic features, including:

- Be as discrete as possible, to compare relative values expected to be achieved by closely related parameters.
- Be as concise as possible, to facilitate direct comparison of parameters.
- Be as mutually independent as possible, to prevent cross coupling.
- Be as non-redundant as possible, to ensure that each metric is measuring a unique feature of the parameters.

Three FOMs were identified to facilitate comparison among parameters.  $FOM_1$  and  $FOM_2$  are related to relative and absolute delta-values, while  $FOM_3$  is related to the procedure to measure the parameters for real-world materials. In fact, the Direct Measurement Approach was selected to determine values of DEM input parameters. This approach requires to directly measure the parameters' values at particle or contact level, and might be very difficult to apply, depending on the parameter to measure and on the particle size. Only special cases that involve simplistic shapes such as spheres in the context of controlled laboratory experiments can really take advantage of this approach. For model validation purposes, a real material composed of unconsolidated particles of the same size and shape as the simulated material (i.e. spherical particles of 1 mm diameter) was selected, as detailed in paragraph 4.3.1.5. For this reason, the direct measurement can be applied and its benefits can be fully exploited, including the advantage that measured properties' values are independent on the DEM model or the specific DEM code adopted [157]. Follows below the detailed description and formulation of the three FOMs identified.

$FOM_1$  is named *relative delta* and captures how close the  $i$ -th delta-value  $\Delta_i$  is to the maximum delta-value  $\Delta_{max}$  for each analysis metric. Therefore,  $FOM_1$  characterizes the relative ratio between delta-values and is defined according to Eq. (4.23) and has a value between 0 (if  $\Delta_i = 0$ ) and 1 (if  $\Delta_i = \Delta_{max}$ ).

$FOM_2$  is named *absolute delta* and captures how much the  $i$ -th delta-value affects particle's trajectory. The higher is the delta-value, the higher is the influence on particle's trajectory.  $FOM_2$  has two different formulations for the velocity magnitude analysis metric (i.e.  $FOM_{2a}$ ) and for both the elevation and azimuth dispersion angles analysis metrics (i.e.  $FOM_{2b}$ ).

$FOM_{2a}$  involves delta-values  $\Delta_V$  related to velocity magnitude analysis metrics and is defined with respect to the theoretical tangential particle's velocity  $V_t$  provided by the Dual-Rasp cutting heads. The closer is the delta-value to the order of magnitude of  $V_t$ , the higher is the value of the  $FOM_{2a}$ , which is always between 0 and 1. Based on simulation baseline,  $V_t = 1.3146 \text{ m/s}$ .  $FOM_{2a}$  is defined according to Eq. (4.24). It should be noted that numerical values related to  $\Delta_V$  are expressed in  $\text{m/s}$  units.

$FOM_{2b}$  involves delta-values  $\Delta_D$  related to elevation and azimuth dispersion angle analysis metrics. The higher is the delta-value, the higher is the value of the  $FOM_{2b}$ , which is always between 0 and 1.  $FOM_{2b}$  is defined according to Eq. (4.25).

$FOM_3$  is named *parameters' measurement* and captures the difficulty in measuring the  $i$ -th parameter. The level of difficulty in measuring a certain parameter was evaluated by considering the number of published papers  $np$  about the direct measurement of such a parameter [157]. Values of parameter  $np$  are reported in Table 4.11.  $FOM_3$  is defined according to Eq. (4.26).

Each FOM is given a weight  $W_n$ , and it is assumed that all weights are equal to 1, meaning that all FOMs have the same merit. Finally, the total score  $S_i$  of the  $i$ -th parameter is obtained by applying Eq. (4.27), where  $FOM_n^i$  is the value of  $n$ -th FOM for the  $i$ -th parameter.

Results of sensitivity analysis for each analysis metric are reported in Table 4.12, Table 4.13, and Table 4.14, while Table 4.15 reports the global results of the sensitivity analysis, considering the average values of each analysis metric. Global results show a clear influence of particle-tool coefficient of static friction ( $\mu_{s_{pt}}$ ) and particle-tool coefficient of restitution ( $e_{pt}$ ) on granular material flow. These results are compatible with the tool-particle interaction that characterizes the Dual-Rasp action. In fact, the momentum transfer between cutting heads and particles takes place via collisions at microscale level. The efficiency of momentum transfer because of collisions is highly influenced by the coefficient of restitution between the two materials. As confirmed by the physics of collisions at particle level [189], the coefficient of restitution significantly determines the particles' velocity after collision, thus influencing the velocity magnitude metric. The efficiency of momentum transfer is also influenced by the coefficient of static friction between the two materials. In fact, the coefficient of static friction determines the tool-particle contact duration and the ability of particles to slide along the teeth of the cutting heads, thus influencing both particles' velocity and direction of particles' trajectories.

$$FOM_1 = \frac{|\Delta_i|}{\max|\Delta_i|} \quad (4.23)$$

$$FOM_{2a} = \begin{cases} 1 & \text{if } \Delta_V > 0.5 \quad (\Delta_V \cong V_t) \\ 0.75 & \text{if } 0.05 < \Delta_V \leq 0.5 \quad \left(\Delta_V \cong \frac{V_t}{10}\right) \\ 0.5 & \text{if } 0.005 < \Delta_V \leq 0.05 \quad \left(\Delta_V \cong \frac{V_t}{100}\right) \\ 0.25 & \text{if } \Delta_V \leq 0.005 \quad \left(\Delta_V \cong \frac{V_t}{1000}\right) \end{cases} \quad (4.24)$$

$$FOM_{2b} = \begin{cases} 1 & \text{if } \Delta_D > 45^\circ \\ 0.75 & \text{if } 30^\circ < \Delta_V \leq 45^\circ \\ 0.5 & \text{if } 15^\circ < \Delta_V \leq 30^\circ \\ 0.25 & \text{if } \Delta_V \leq 15^\circ \end{cases} \quad (4.25)$$

$$FOM_3 = \begin{cases} 1 & \text{if } np > 10 \text{ (soft difficulty measure)} \\ 0.5 & \text{if } 5 \leq np \leq 10 \text{ (medium difficulty measure)} \\ 0.25 & \text{if } np < 5 \text{ (hard difficulty measure)} \end{cases} \quad (4.26)$$

$$S_i = \frac{\sum_{n=1}^3 W_n FOM_n^i}{\sum_{n=1}^3 W_n} \quad (4.27)$$

**Table 4.8** Sensitivity analysis of DEM model parameters. Delta-values for velocity magnitude analysis metric.

Parameter	Average Vel. mag. [m/s]	25 <sup>th</sup> perc. Vel. mag. [m/s]	50 <sup>th</sup> perc. Vel. mag. [m/s]	75 <sup>th</sup> perc. Vel. mag. [m/s]
$E_p$	0.0307	-0.0105	0.0139	-0.0440
$\nu_p$	0.0441	-0.0096	0.0311	0.0322
$\rho_p$	-0.0059	0.0239	0.0185	-0.0152
$\mu_{spp}$	-0.0069	0.0156	0.0123	0.0564
$e_{pp}$	0.0468	0.0224	0.0175	0.0411
$\mu_{rpp}$	-0.0167	0.0232	-0.0103	-0.0011
$\mu_{spt}$	-0.0624	0.0090	-0.0315	-0.0188
$e_{pt}$	0.5110	0.2829	0.5339	0.7530
$\mu_{rpt}$	0.0000	0.0000	0.0000	0.0000

**Table 4.9** Sensitivity analysis of DEM model parameters. Delta-values for elevation dispersion angle analysis metric.

Parameter	Average Elev. angle [deg]	25 <sup>th</sup> perc. Elev. angle [deg]	50 <sup>th</sup> perc. Elev. angle [deg]	75 <sup>th</sup> perc. Elev. angle [deg]
$E_p$	-2.8684	2.5748	0.9137	0.0848
$\nu_p$	1.0396	-0.6054	0.4050	0.0686

$\rho_p$	0.5768	0.1496	0.2206	0.9162
$\mu_{s_{pp}}$	1.7208	-4.0828	-2.8452	-3.6408
$e_{pp}$	-0.7692	1.7724	2.6568	8.4191
$\mu_{r_{pp}}$	-0.0769	-1.1007	-2.6260	-2.3115
$\mu_{s_{pt}}$	1.9876	1.2440	1.4642	2.6399
$e_{pt}$	5.0007	5.0415	0.8724	-0.6285
$\mu_{r_{pt}}$	0.0000	0.0000	0.0000	0.0000

**Table 4.10** Sensitivity analysis of DEM model parameters. Delta-values for azimuth dispersion angle analysis metric.

Parameter	Average Az. angle [deg]	25 <sup>th</sup> perc. Az. angle [deg]	50 <sup>th</sup> perc. Az. angle [deg]	75 <sup>th</sup> perc. Az. angle [deg]
$E_p$	2.9520	6.1195	2.1060	3.4887
$\nu_p$	0.5070	-3.1248	-0.6976	-1.2183
$\rho_p$	-0.4206	-2.1094	0.9089	2.3878
$\mu_{s_{pp}}$	0.2791	2.1425	4.3977	7.5670
$e_{pp}$	-0.0081	6.2147	8.6385	9.9232
$\mu_{r_{pp}}$	-1.6412	-0.0479	-0.8535	1.4171
$\mu_{s_{pt}}$	5.7518	-0.1287	0.3523	-0.3998
$e_{pt}$	-2.8210	6.4295	7.4358	9.2699
$\mu_{r_{pt}}$	0.0000	0.0000	0.0000	0.0000

**Table 4.11** Values of parameter  $np$  within the definition of  $FOM_3$ .

Parameters	$np$
Particle Young's Modulus ( $E_p$ )	8
Particle Poisson's ratio ( $\nu_p$ )	0
Particle density ( $\rho_p$ )	2
Particle-particle coeff. static friction ( $\mu_{spp}$ )	5
Particle-particle coeff. restitution ( $e_p$ )	6
Particle-particle coeff. rolling friction ( $\mu_{rpp}$ )	2
Particle-tool coeff. static friction ( $\mu_{spt}$ )	16
Particle-tool coeff. restitution ( $e_t$ )	14
Particle-tool coeff. rolling friction ( $\mu_{rpt}$ )	5

**Table 4.12** Sensitivity analysis of DEM model parameters. Results about velocity magnitude metrics.

		Analysis Metrics			
		Average Vel. mag.	25 <sup>th</sup> perc. Vel. mag.	50 <sup>th</sup> perc. Vel. mag.	75 <sup>th</sup> perc. Vel. mag.
Parameters	Particle Young's Modulus ( $E_p$ )	0.35	0.35	0.34	0.35
	Particle Poisson's ratio ( $\nu_p$ )	0.28	0.26	0.27	0.26
	Particle density ( $\rho_p$ )	0.25	0.28	0.26	0.26
	$pp$ coeff. static friction ( $\mu_{spp}$ )	0.34	0.35	0.34	0.44
	$pp$ coeff. restitution ( $e_p$ )	0.36	0.36	0.34	0.35
	$pp$ coeff. rolling friction ( $\mu_{rpp}$ )	0.26	0.28	0.26	0.17
	$pt$ coeff. static friction ( $\mu_{spt}$ )	0.62	0.51	0.52	0.51
	$pt$ coeff. restitution ( $e_t$ )	1.00	0.92	1.00	1.00
	$pt$ coeff. rolling friction ( $\mu_{rpt}$ )	0.25	0.25	0.25	0.25

**Table 4.13** Sensitivity analysis of DEM model parameters. Results about elevation dispersion angle metrics.

		Analysis Metrics			
		Average El. angle	25 <sup>th</sup> perc. El. angle	50 <sup>th</sup> perc. El. angle	75 <sup>th</sup> perc. El. angle
Parameters	Particle Young's Modulus ( $E_p$ )	0.44	0.42	0.36	0.25
	Particle Poisson's ratio ( $\nu_p$ )	0.21	0.21	0.21	0.17
	Particle density ( $\rho_p$ )	0.19	0.18	0.19	0.20
	$pp$ coeff. static friction ( $\mu_{s_{pp}}$ )	0.32	0.52	0.58	0.39
	$pp$ coeff. restitution ( $e_p$ )	0.28	0.37	0.56	0.58
	$pp$ coeff. rolling friction ( $\mu_{r_{pp}}$ )	0.17	0.24	0.47	0.26
	$pt$ coeff. static friction ( $\mu_{s_{pt}}$ )	0.50	0.50	0.59	0.52
	$pt$ coeff. restitution ( $e_t$ )	0.62	0.75	0.52	0.44
	$pt$ coeff. rolling friction ( $\mu_{r_{pt}}$ )	0.25	0.25	0.25	0.25

**Table 4.14** Sensitivity analysis of DEM model parameters. Results about azimuth dispersion angle metrics.

		Analysis Metrics			
		Average Az. angle	25 <sup>th</sup> perc. Az. angle	50 <sup>th</sup> perc. Az. angle	75 <sup>th</sup> perc. Az. angle
Parameters	Particle Young's Modulus ( $E_p$ )	0.42	0.57	0.33	0.37
	Particle Poisson's ratio ( $\nu_p$ )	0.20	0.33	0.19	0.21
	Particle density ( $\rho_p$ )	0.19	0.28	0.20	0.25
	$pp$ coeff. static friction ( $\mu_{s_{pp}}$ )	0.27	0.36	0.42	0.50
	$pp$ coeff. restitution ( $e_p$ )	0.25	0.57	0.58	0.58
	$pp$ coeff. rolling friction ( $\mu_{r_{pp}}$ )	0.26	0.17	0.20	0.21
	$pt$ coeff. static friction ( $\mu_{s_{pt}}$ )	0.75	0.42	0.43	0.43
	$pt$ coeff. restitution ( $e_t$ )	0.58	0.75	0.70	0.73
	$pt$ coeff. rolling friction ( $\mu_{r_{pt}}$ )	0.25	0.25	0.25	0.25

**Table 4.15** Global results of the sensitivity analysis of DEM model parameters.

		Analysis Metrics		
		Velocity magnitude	Azimuth angle	Elevation angle
<b>Parameters</b>	Particle Young's Modulus ( $E_p$ )	0.35	0.42	0.44
	Particle Poisson's ratio ( $\nu_p$ )	0.28	0.20	0.21
	Particle density ( $\rho_p$ )	0.25	0.19	0.19
	$pp$ coeff. static friction ( $\mu_{spp}$ )	0.34	0.27	0.32
	$pp$ coeff. restitution ( $e_p$ )	0.36	0.25	0.28
	$pp$ coeff. rolling friction ( $\mu_{rpp}$ )	0.26	0.26	0.17
	$pt$ coeff. static friction ( $\mu_{spt}$ )	0.62	0.75	0.50
	$pt$ coeff. restitution ( $e_t$ )	1.00	0.58	0.62
	$pt$ coeff. rolling friction ( $\mu_{rpt}$ )	0.25	0.25	0.25

#### 4.3.1.4 Sensitivity analysis of sampling system parameters

A sensitivity analysis was also conducted on the parameters that characterize the cutting heads of the Dual-Rasp with the goal to provide guidelines for sampling system design. The sensitivity analysis requires to:

1. Define a simulation baseline with a set of pre-defined parameters.
2. Define a range of values for each parameter reported below and included in the sensitivity analysis
  - Number of teeth ( $N_t$ )
  - Length ( $L_t$ )
  - Outer diameter (measured at teeth's tip) ( $O_t$ )
  - Gap between cutters (measured at teeth's tip) ( $G_t$ )
  - Inclination with respect to horizontal ( $I_t$ )
  - Vertical (plunging) velocity ( $V_t$ )
  - Rotational velocity ( $R_t$ )
3. Perform DEM simulations by changing the parameters' values in the pre-defined range. The simulation aims to reproduce the sampling

operation performed by the Dual-Rasp sampling system and the resulting granular material flow.

4. Evaluate parameters' sensitivity by applying the analysis metrics to simulation results.
5. Identify the most sensitive parameters influencing the granular material flow.

The simulation baseline includes the environmental parameter (i.e. gravitational acceleration), parameters related to the Dual-Rasp cutting heads, parameters related to the particles, and paired parameters related to the interaction between particles and surface geometries. Baseline values of DEM parameters and environmental parameter are common to all simulations and are summarized in Table 4.16. Values of the parameters of Dual-Rasp cutting heads subject to the sensitivity analysis are summarized in Table 4.17.

**Table 4.16** Values of DEM parameters and environmental parameter for the sensitivity analysis of sampling system parameters. These values are common to all simulations.

Particle parameters	
Shape / Shape distribution	Sphere / Monodisperse
Size / Size distribution	1 mm diameter / Monodisperse
Number of particles	187500
Size of particles' bed	<ul style="list-style-type: none"> <li>• Length: 75 mm</li> <li>• Width: 75 mm</li> <li>• Height: 30 mm</li> </ul>
Young's modulus ( $E_p$ )	0.1 GPa
Poisson's ratio ( $\nu_p$ )	0.35
Density ( $\rho_p$ )	3000 kg/m <sup>3</sup>
Paired parameters	
$pp$ coefficient of static friction ( $\mu_{spp}$ )	0.5
$pt$ coefficient of static friction ( $\mu_{spt}$ )	0.5

<b><math>pp</math> coefficient of rolling friction (<math>\mu_{r_{pp}}</math>)</b>	0.005
<b><math>pt</math> coefficient of rolling friction (<math>\mu_{r_{pt}}</math>)</b>	0.005
<b><math>pp</math> coefficient of restitution (<math>e_{pp}</math>)</b>	0.5
<b><math>pt</math> coefficient of restitution (<math>e_{pt}</math>)</b>	0.5
<b>Environmental parameter</b>	
<b>Gravitational acceleration</b>	9.81 m/s <sup>2</sup>

**Table 4.17** Values of the parameters of Dual-Rasp cutting heads for the sensitivity analysis of sampling system parameters. Baseline values are highlighted in red.

<b>Parameters of Dual-Rasp cutting heads</b>	
<b>Prescribed motion</b>	<b>Vertical motion (plunging) displacement: 10 mm</b>
<b>Number of teeth (<math>N_t</math>)</b>	[2, 4, <b>6</b> ]
<b>Length (<math>L_t</math>)</b>	[ <b>30</b> , 40, 50] mm
<b>Outer diameter (<math>O_t</math>)</b>	[ <b>13</b> , 15, 17] mm
<b>Gap between cutting heads (<math>G_t</math>)</b>	[ <b>2</b> , 6, 10] mm
<b>Inclination wrt horizontal (<math>I_t</math>)</b>	[20, <b>45</b> , 70] deg
<b>Vertical (plunging) velocity (<math>V_t</math>)</b>	[ <b>2</b> , 3, 4] mm/s
<b>Rotational velocity (<math>R_t</math>)</b>	[ <b>2000</b> , 6000, 10000] RPM

Given the range of values for the parameters involved in the sensitivity analysis, it is possible to define the simulation matrix of the sensitivity analysis. The simulation matrix is composed of simulation sets characterized by the investigation of a single parameter involved in the sensitivity analysis. Therefore, seven simulation sets are defined, each one including three simulations, one for each value assigned to the reference parameter. The simulation matrix is then composed of 21 simulations. However, some simulations are duplicated. In fact, it should be noted that each simulation set has one simulation out of the three (named *baseline simulation*) that has all baseline values of the parameters, resulting in a total of seven *baseline simulations*. All *baseline simulations* are

identical across the simulation sets. Therefore, only one out of the seven *baseline simulations* need to be performed. As a result, six *baseline simulations* are removed from the simulation matrix, resulting in a total of 15 unique simulations required to perform the sensitivity analysis. The simulation matrix was developed by assuming that the parameters involved in the sensitivity analysis are independent each other. Table 4.18 and Table 4.19 show the simulation matrix and the values of variable parameters for the sensitivity analysis, respectively.

**Table 4.18** DEM simulation matrix for the sensitivity analysis of sampling system parameters. All baseline simulations (highlighted in red) are included for completeness.

Simulation Set AT	Simulation Set BT	Simulation Set CT
AT1 Baseline + AT2 <b>AT3</b>	<b>BT1</b> Baseline + BT2 BT3	<b>CT1</b> Baseline + CT2 CT3
Simulation Set DT	Simulation Set ET	Simulation Set FT
<b>DT1</b> Baseline + DT2 DT3	<b>ET1</b> Baseline + ET2 ET3	<b>FT1</b> Baseline + FT2 FT3
Simulation Set GT		
<b>GT1</b> Baseline + GT2 GT3		

**Table 4.19** Values of variable parameters for the sensitivity analysis of sampling system parameters. Baseline values are highlighted in red.

Parameter	Code	Value
Number of teeth	<b>AT1</b>	<b>2</b>
	AT2	4
	AT3	6
Length	<b>BT1</b>	<b>30 mm</b>
	BT2	40 mm
	BT3	50 mm
Outer diameter	<b>CT1</b>	<b>13 mm</b>
	CT2	15 mm
	CT3	17 mm
Gap between cutting heads	<b>DT1</b>	<b>2 mm</b>
	DT2	6 mm
	DT3	10 mm
Inclination wrt horizontal	ET1	20 deg
	<b>ET2</b>	<b>45 deg</b>
	ET3	70 deg
Vertical (plunging) velocity	<b>FT1</b>	<b>2 mm/s</b>
	FT2	3 mm/s
	FT3	4 mm/s
Rotational velocity	<b>GT1</b>	<b>2000 RPM</b>
	GT2	6000 RPM
	GT3	10000 RPM

Raw DEM simulation data were post-processed to obtain the analysis metrics. Furthermore, average values of the analysis metrics were computed for the three values of the range defined for each parameter involved in the sensitivity analysis, and then fitted via linear trend functions. Delta-values across trend functions were computed for the average value, 25<sup>th</sup> percentile, 50<sup>th</sup> percentile, and 75<sup>th</sup> percentile of the analysis metrics of each parameter (Table 4.20, Table 4.21, and Table 4.22). Delta-values are the basis for the determination of most sensitive parameters, since they provide a quantitative indication about the influence of a

parameter on the analysis metrics, thus on the granular material flow. Again, to efficiently use these results and complete the sensitivity analysis, the FOM approach was adopted. However, only  $FOM_1$  and  $FOM_2$  are used in this case, since  $FOM_3$  is specifically related to the measurement of DEM model parameters.

Results of sensitivity analysis for each analysis metric are reported in Table 4.23, Table 4.24, and Table 4.25, while Table 4.26 reports the global results of the sensitivity analysis, considering the average values of each analysis metric. Global results show a strong influence of rotational velocity on velocity magnitude, as expected. In fact, a higher rotational velocity of the Dual-Rasp cutting heads leads to a higher momentum delivered to the particles, thus a higher velocity magnitude. A similar explanation is also valid for the influence of the outer diameter on the velocity magnitude. The inclination of the Dual-Rasp cutting heads with respect to the horizontal has a medium influence on the elevation dispersion angle, as expected. In fact, the inclination of the cutting heads determines the direction of the tangential velocity vector, thus influencing the direction of particles' velocity vectors measured through the elevation angle. A similar explanation might be also valid for the influence of the inclination of the cutting heads on the azimuth dispersion angle.

**Table 4.20** Sensitivity analysis of sampling system parameters. Delta-values across trend lines for velocity magnitude analysis metric.

Parameter	Average Vel. mag. [m/s]	25 <sup>th</sup> perc. Vel. mag. [m/s]	50 <sup>th</sup> perc. Vel. mag. [m/s]	75 <sup>th</sup> perc. Vel. mag. [m/s]
$N_t$	0.0953	0.0059	0.0273	0.0688
$L_t$	0.0414	0.0058	-0.0172	-0.0125
$O_t$	0.613	0.1721	0.3702	0.735
$G_t$	-0.3095	-0.0215	-0.1233	-0.2207
$I_t$	-0.0872	0.0288	0.0555	0.0695
$V_t$	0.1204	0.019	0.0024	0.0195
$R_t$	2.2641	4.0577	4.8818	5.4878

**Table 4.21** Sensitivity analysis of sampling system parameters. Delta-values across trend lines for elevation dispersion angle analysis metric.

Parameter	Average Elev. angle [deg]	25 <sup>th</sup> perc. Elev. angle [deg]	50 <sup>th</sup> perc. Elev. angle [deg]	75 <sup>th</sup> perc. Elev. angle [deg]
$N_t$	4.1744	-4.3775	-7.5446	-11.7818
$L_t$	-0.6249	-0.6245	0.1619	-0.4458
$O_t$	4.2002	-4.0420	-6.4313	-13.8326
$G_t$	-16.5935	28.0107	44.7027	70.8518
$I_t$	-37.5796	5.0006	7.9674	24.6536
$V_t$	7.3395	-7.5735	-12.0302	-18.8817
$R_t$	-10.4275	16.0571	22.8675	46.0630

**Table 4.22** Sensitivity analysis of sampling system parameters. Delta-values across trend lines for azimuth dispersion angle analysis metric.

Parameter	Average Az. angle [deg]	25 <sup>th</sup> perc. Az. angle [deg]	50 <sup>th</sup> perc. Az. angle [deg]	75 <sup>th</sup> perc. Az. angle [deg]
$N_t$	0.3162	-2.6202	-4.4562	-3.1930
$L_t$	-0.0895	2.8135	0.4555	-4.8849
$O_t$	0.6404	-9.2377	-13.3109	-18.3265
$G_t$	2.2339	13.5991	23.7275	38.2175
$I_t$	4.1275	-13.2108	-22.0117	-15.7335
$V_t$	2.0147	2.7250	2.1130	-4.1619
$R_t$	-0.4897	2.1575	7.5051	27.4031

**Table 4.23** Sensitivity analysis of sampling system parameters. Results about velocity magnitude metrics.

		Analysis Metrics			
		Average Vel. mag.	25 <sup>th</sup> perc. Vel. mag.	50 <sup>th</sup> perc. Vel. mag.	75 <sup>th</sup> perc. Vel. mag.
Parameters	Number of teeth ( $N_t$ )	0.26	0.17	0.17	0.25
	Length ( $L_t$ )	0.17	0.17	0.17	0.17
	Outer diameter ( $O_t$ )	0.42	0.26	0.28	0.38
	Gap between cutting heads ( $G_t$ )	0.30	0.17	0.26	0.26
	Inclination wrt horizontal ( $I_t$ )	0.26	0.17	0.25	0.25
	Vertical (plunging) velocity ( $V_t$ )	0.27	0.17	0.08	0.17
	Rotational velocity ( $R_t$ )	0.67	0.67	0.67	0.67

**Table 4.24** Sensitivity analysis of sampling system parameters. Results about elevation dispersion angle metrics.

		Analysis Metrics			
		Average El. angle	25 <sup>th</sup> perc. El. angle	50 <sup>th</sup> perc. El. angle	75 <sup>th</sup> perc. El. angle
Parameters	Number of teeth ( $N_t$ )	0.12	0.14	0.14	0.14
	Length ( $L_t$ )	0.09	0.09	0.08	0.09
	Outer diameter ( $O_t$ )	0.12	0.13	0.13	0.15
	Gap between cutting heads ( $G_t$ )	0.31	0.50	0.58	0.67
	Inclination wrt horizontal ( $I_t$ )	0.58	0.14	0.14	0.28
	Vertical (plunging) velocity ( $V_t$ )	0.15	0.17	0.17	0.26
	Rotational velocity ( $R_t$ )	0.18	0.36	0.34	0.55

**Table 4.25** Sensitivity analysis of sampling system parameters. Results about azimuth dispersion angle metrics.

		Analysis Metrics			
		Average Az. angle	25 <sup>th</sup> perc. Az. angle	50 <sup>th</sup> perc. Az. angle	75 <sup>th</sup> perc. Az. angle
Parameters	Number of teeth ( $N_t$ )	0.11	0.15	0.15	0.11
	Length ( $L_t$ )	0.09	0.15	0.09	0.13
	Outer diameter ( $O_t$ )	0.14	0.31	0.27	0.33
	Gap between cutting heads ( $G_t$ )	0.26	0.42	0.50	0.58
	Inclination wrt horizontal ( $I_t$ )	0.42	0.41	0.48	0.30
	Vertical (plunging) velocity ( $V_t$ )	0.25	0.15	0.11	0.12
	Rotational velocity ( $R_t$ )	0.12	0.14	0.19	0.41

**Table 4.26** Global results of the sensitivity analysis of sampling system parameters.

		Analysis Metrics		
		Velocity magnitude	Azimuth angle	Elevation angle
Parameters	Number of teeth ( $N_t$ )	0.26	0.11	0.12
	Length ( $L_t$ )	0.17	0.09	0.09
	Outer diameter ( $O_t$ )	0.42	0.14	0.12
	Gap between cutting heads ( $G_t$ )	0.30	0.26	0.31
	Inclination wrt horizontal ( $I_t$ )	0.26	0.42	0.58
	Vertical (plunging) velocity ( $V_t$ )	0.27	0.25	0.15
	Rotational velocity ( $R_t$ )	0.67	0.12	0.18

### 4.3.1.5 Measurement of DEM model parameters

Results of the sensitivity analysis of DEM model parameters showed that the most sensitive parameters influencing the granular material flow are the particle-tool coefficient of static friction ( $\mu_{s_{pt}}$ ) and the particle-tool coefficient of restitution ( $e_{pt}$ ). The Direct Measurement Approach was selected to determine the values of those parameters. This approach requires to directly measure the parameters' values at particle or contact level, and might be very difficult to apply, depending on the parameter to measure and on the particle size. Only special cases that involve simplistic shapes in the context of controlled laboratory experiments can really take advantage of this approach. For model validation purposes, real materials composed of unconsolidated particles of the same size and shape as the simulated material were selected for apples-to-apples comparison between DEM simulation model and experimental testing. For this reason, the direct measurement can be applied and its benefits can be fully exploited, including the advantage that measured properties' values are independent on the DEM model or the specific DEM code adopted [157].

Materials shown in Table 4.27 were considered for DEM model validation, including balls and beads typically adopted for milling and grinding. Selection criteria are summarized below.

- *Particle size*, approximately 1 mm in diameter, to be compatible with simulated particle size.
- *Particle shape*, approximately spherical, to be compatible with simulated particle shape.
- *Particle color*, matt black or white, with the purpose to prevent particle glitter in high-speed video recordings, thus obtaining a high-contrast, high-defined particle shape against the background with the purpose of obtaining a more robust video post-processing for particle tracking purposes.

**Table 4.27** Materials considered for DEM model validation.

Material	Size [mm]	Shape	Color	References
Yttria Stabilized Zirconia	0.1 – 30	Spherical	Matt white	[190]
Alumina	1 – 35	Spherical	Matt white	[191]
Natural Brazilian Agate	3 – 20	Spherical	Ivory white / gray	[192]

Tungsten carbide	1 – 20	Spherical	Metallic color	[193]
304 Stainless Steel	1 – 50	Spherical	Metallic color	[194]
316 Stainless Steel	3 – 50	Spherical	Metallic color	[194]
52100 Chrome Steel	5 – 50	Spherical	Metallic color	[194]
Cellulose Acetate	1 – 12	Spherical (> 98%)	Various colors	[195]
Polyethylene	0.85 – 1 (> 90%)	Spherical (> 90%)	Fluorescent green / red	[196]
Polyethylene	0.85 – 1 (> 90%)	Spherical (> 90%)	Clear / white	[197]
Soda lime glass	0.85 – 1 (> 90%)	Spherical (> 85%)	Clear / white	[198] [199]
Borosilicate glass	0.85 – 1 (> 90%)	Spherical (> 90%)	Clear / white	[200] [201]

Two materials were selected for DEM model validation, Ytria Stabilized Zirconia (YSZ) and alumina. Both are matt white and composed of monodisperse unconsolidated 1 mm diameter spheres, hence are ideal for DEM model validation purposes according to the defined criteria. YSZ is a ceramic material made of zirconium dioxide ( $ZrO_2$ ) stabilized at room temperature by adding yttrium oxide ( $Y_2O_3$ ) [202]. Alumina, common name of the aluminum (III) oxide ( $Al_2O_3$ ), is a ceramic material and one of the most common aluminum oxides. Table 4.28 summarized physical and mechanical properties.

**Table 4.28** Properties of YSZ and alumina particles.

	YSZ	Alumina	References
Particle density	5.85 – 6.1 g/cm <sup>3</sup>	3.8 – 3.98 g/cm <sup>3</sup>	[191] [203] [204]
Particle Young's modulus	200-210 GPa	370 – 380 GPa	[191] [203] [204]
Particle Poisson's ratio	0.25 – 0.3	0.25 – 0.3	[191] [203] [204]

Particle-tool coefficient of static friction ( $\mu_{s_{pt}}$ ) and particle-tool coefficient of restitution ( $e_{pt}$ ) between YSZ/alumina particles and Dual-Rasp cutting heads material were directly measured via independent tests performed by using custom designed testbeds.

The particle-tool coefficient of static friction ( $\mu_{s_{pt}}$ ) was measured by performing an inclined plane test. The testbed designed and built for this purpose is shown in Figure 4.18 and is composed by a linear actuator that simply supports the tool plate at one of its edges and gently lift it for inclining the plate, while the inclinometer provides real-time measurement of its inclination (Figure 4.19). The tool plate is made of the same material considered for the Dual-Rasp cutting heads (i.e. Al 6061-T6). The particle plate is simply placed on top of the tool plate and not constrained. In this way, the particle plate can freely slide down as soon as the tool plate achieves the critical inclination for incipient motion. The particle plate has three particles glued to its bottom face and it is placed face down on tool plate in such a way the particles directly touch the tool plate. In this way, the static friction between particles and tool plate determines the rise of the incipient motion of particle plate when the tool plate starts inclining. The particles glued to the bottom face of the particle plate are disposed in a regular triangle shape. This configuration guarantees that all particles always touch the tool plate since there is always a plane passing through the three contact points between particles and tool plate. Since the tool plate is flat, it can be considered as a plane, thus there is no risk that one of the particles comes to no contact. Moreover, the particle plate orientation was selected to enhance stability during motion. In fact, one particle is placed close to the trailing edge of the particle plate, while the other two particles are close to the leading edge (Figure 4.20). As a result, the single particle left in the rear position acts as a stabilizer of the particle plate during its motion.

Particle-tool coefficient of static friction  $\mu_{s_{pt}}$  can be determined from measurement of the tool plate inclination  $\theta$  at particle plate incipient motion, according to Eq. (4.28) [81]

$$\mu_{s_{pt}} = \tan \theta \quad (4.28)$$

To determine the number of measurements required to achieve a statistically significant result, the confidence interval method for continuous data was adopted [205] [206] [207]. In fact, the type of data considered are continuous, since  $\theta$  can be represented by a continuous number. Moreover, the purpose is to generalize a limited sample to a broader population. In fact, the population is represented by the potentially infinite number of particle/tool plate couples, while the sample is the sub-set of the population selected to produce the results. For statistical analyses of this type, the confidence interval method is adopted.

According to the confidence interval method for continuous data, the minimum estimated sample size to achieve a statistically significant result is given by Eq. (4.29)

$$n_0 = \left( \frac{Z \sigma}{E_r} \right)^2 \quad (4.29)$$

Where

$n_0$  Estimate of minimum sample size

$Z$  Value of the Z-distribution corresponding to the selected confidence interval

$\sigma$  Estimate of standard deviation

$E_r$  Margin of error

A confidence interval of 95% was selected. This parameter identifies the range in the sample distribution within which it is expected to find the true population value, given the selected degree of confidence (i.e. 95%). The value  $Z$  of the Z-distribution related to a 95% confidence interval is equal to 1.96. The margin of error is selected to define how well the sample must represent the population. In this case, a margin of error  $E_r$  equal to 1% was selected. The estimate of standard deviation  $\sigma$  informs about the spread of measurements around the average and was not known for the sample considered. To determine  $\sigma$ , a pilot study was conducted for both YSZ and alumina particles [208]. The pilot study required to repeat measurements a number of times with the purpose to obtain a plot of standard deviation  $\sigma$  as function of sample size (Figure 4.21 for YSZ and Figure 4.22 for alumina). Plots show that the standard deviation approaches a plateau value once a certain number of measurements (i.e. sample size) is achieved. A plateau value equal to 0.0088 was found for YSZ, while a plateau values equal to 0.0066 was found for alumina. These values were used as the estimate of standard deviation  $\sigma$ .

According to the defined input parameters, Eq. (4.29) suggests a minimum estimated sample size  $n_0 = 3$  for YSZ, while it suggests a minimum estimated sample size  $n_0 = 2$  for alumina. As a conservative approach, a sample size  $n = 30$  was selected for both materials for a total of 60 samples collected.

A value of  $0.154 \pm 0.0032$  was found for the coefficient of static friction between YSZ particles and Al 6061-T6, while a value of  $0.2226 \pm 0.0024$  was found for the coefficient of static friction between alumina particles and Al 6061-T6.

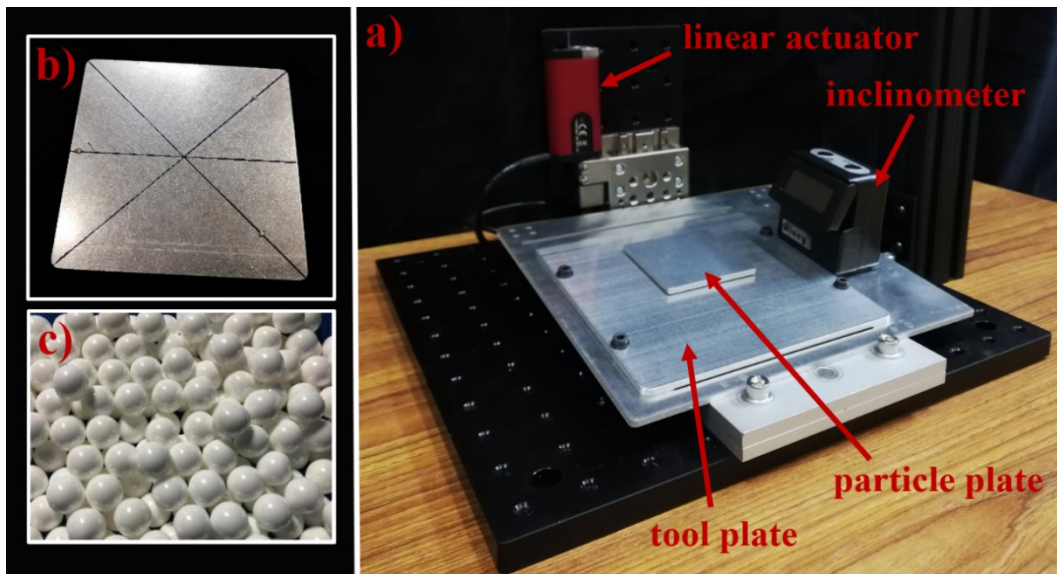


**Figure 4.18** Inclined plane testbed (a). Detail of the bottom face of the particle plate with three particles glued to it (b). YSZ particles shown as a reference (c).

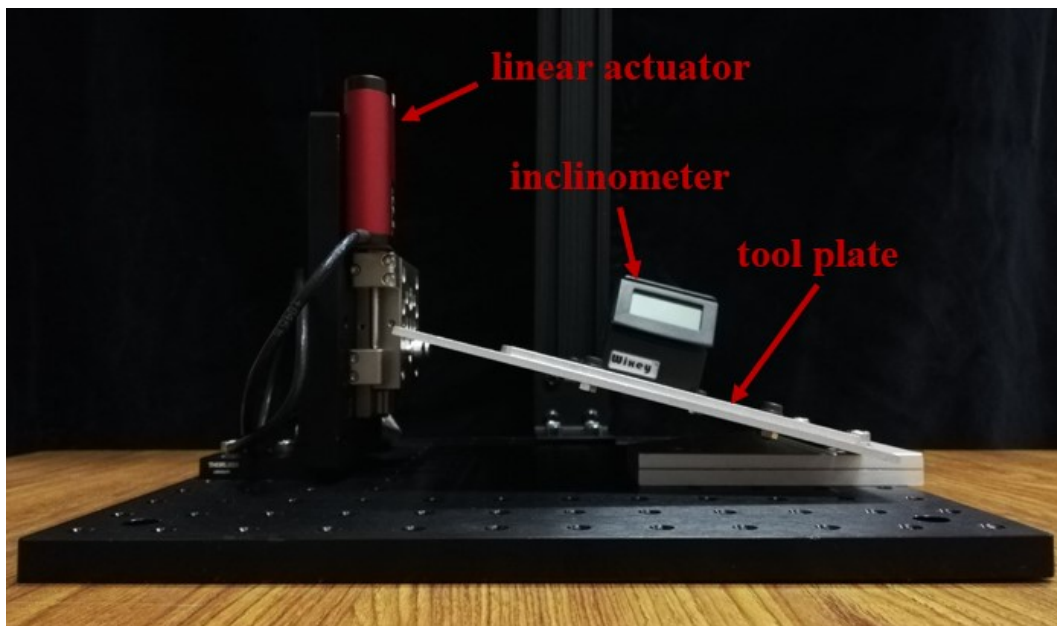


**Figure 4.19** Inclined plane testbed shown in inclined position.

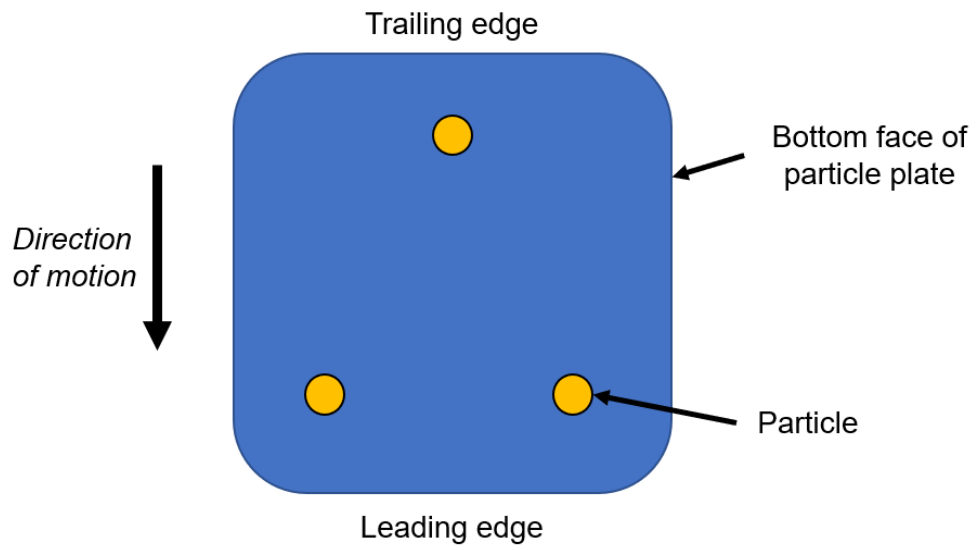


*Figure 4.20 Particle plate.*

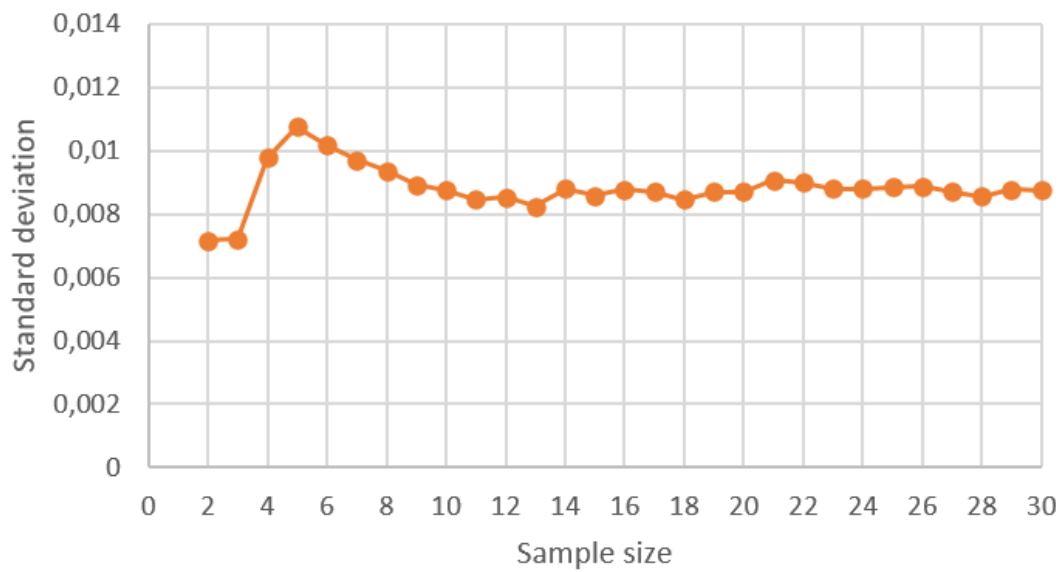


*Figure 4.21 Standard deviation as function of sample size for measurement of particle-tool coefficient of static friction of YSZ particles.*

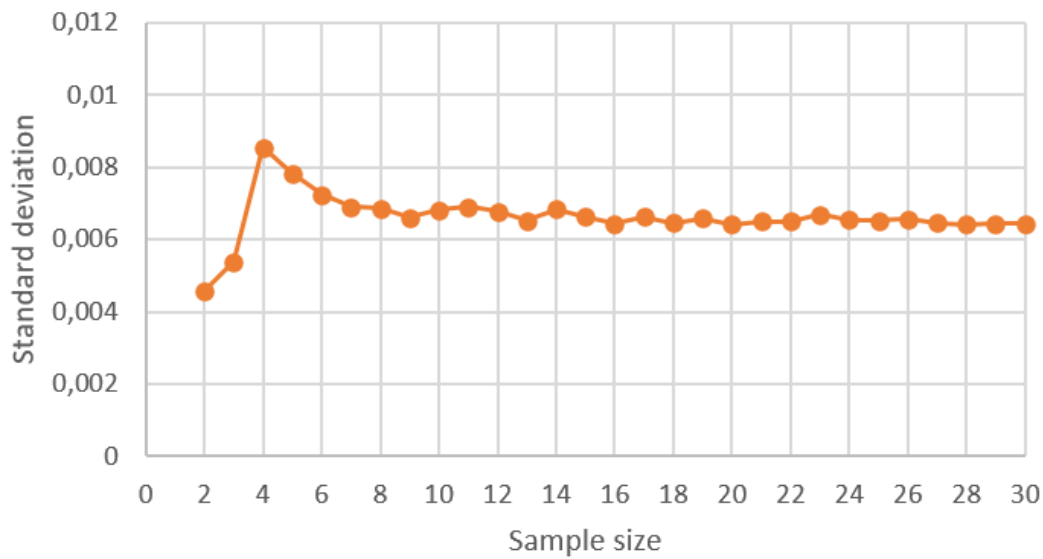


**Figure 4.22** Standard deviation as function of sample size for measurement of particle-tool coefficient of static friction of alumina particles.

The particle-tool coefficient of restitution was measured by performing a particle drop test. The apparatus designed and built for this purpose is shown in Figure 4.23. The drop tower drops one particle at the time, the particle hits the tool plate and bounces back. Again, the tool plate is made of the same material considered for the Dual-Rasp cutting heads (i.e. Al 6061-T6). The collision between particle and tool plate is recorded by using the ultra-high speed Photron FASTCAM SA-Z (Figure 4.24). This camera provides high-resolution images at frame rates up to 21000 frames per second (fps) and even greater than 2 million fps at reduced image resolution, as well as shutter speeds as short as 159 nanoseconds [209]. Figure 4.25 shows four representative frames of the particle drop test sequence, as recorded by the ultra-high speed camera.

Particle-tool coefficient of restitution  $e_{pt}$  can be determined from measurement of particles' vertical velocity right after impact  $v'$  and right before impact  $v$ , according to Eq. (4.30) [210].

$$e_{pt} = \frac{v'}{v} \quad (4.30)$$

Particle's velocity was obtained by using the official tracking software provided by the camera's vendor to post-process the ultra-high speed test recordings. Figure 4.26 shows a typical drop test data plot as obtained by performing particle's tracking in ultra-high speed test recordings.

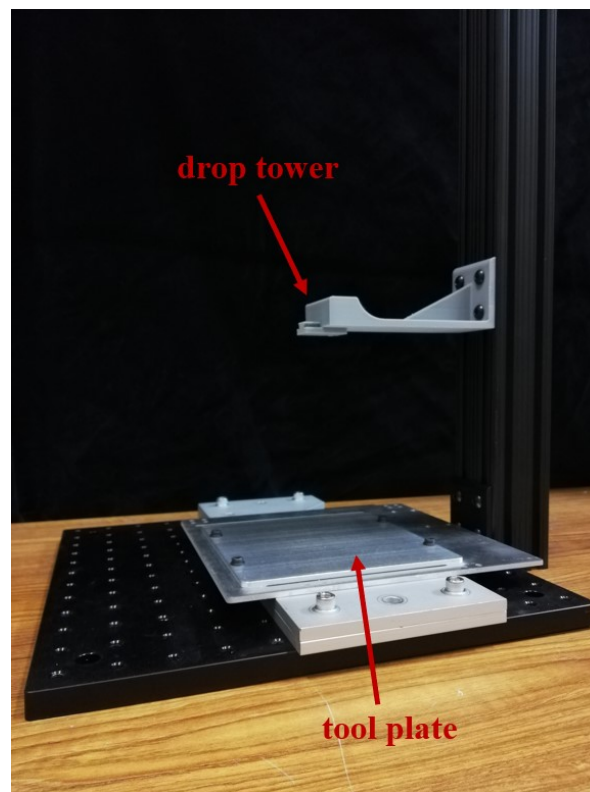


*Figure 4.23 Particle drop testbed.*

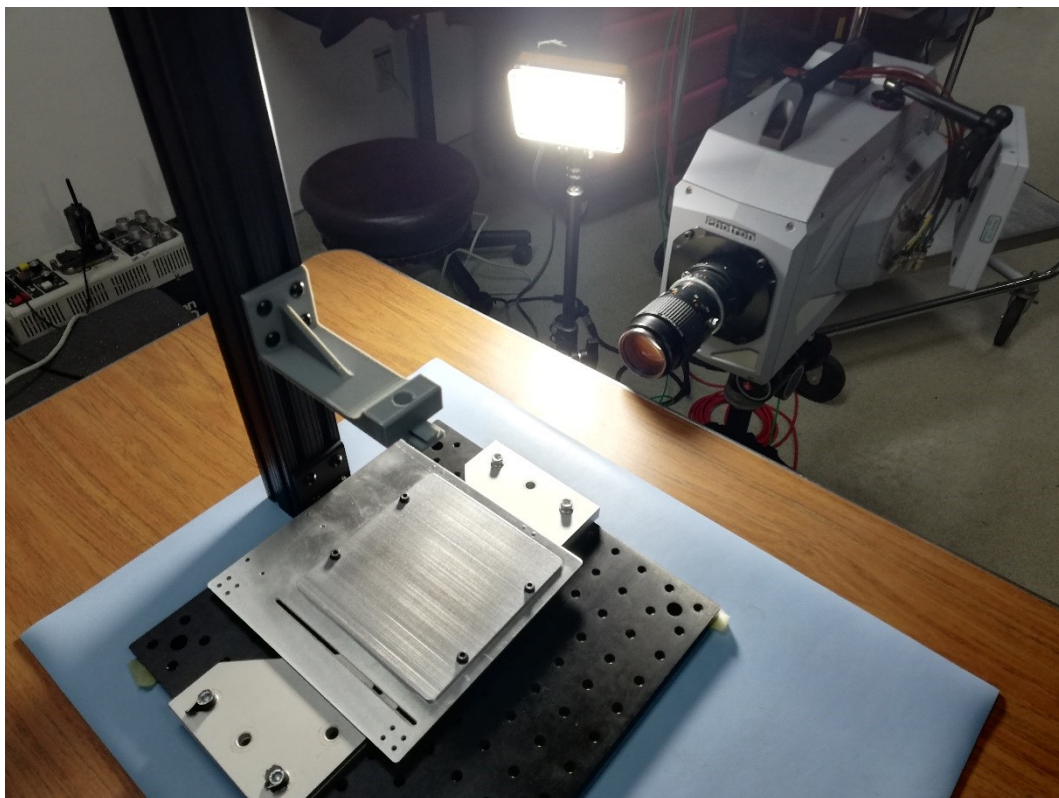


*Figure 4.24 Particle drop test setup including the ultra-high speed camera.*

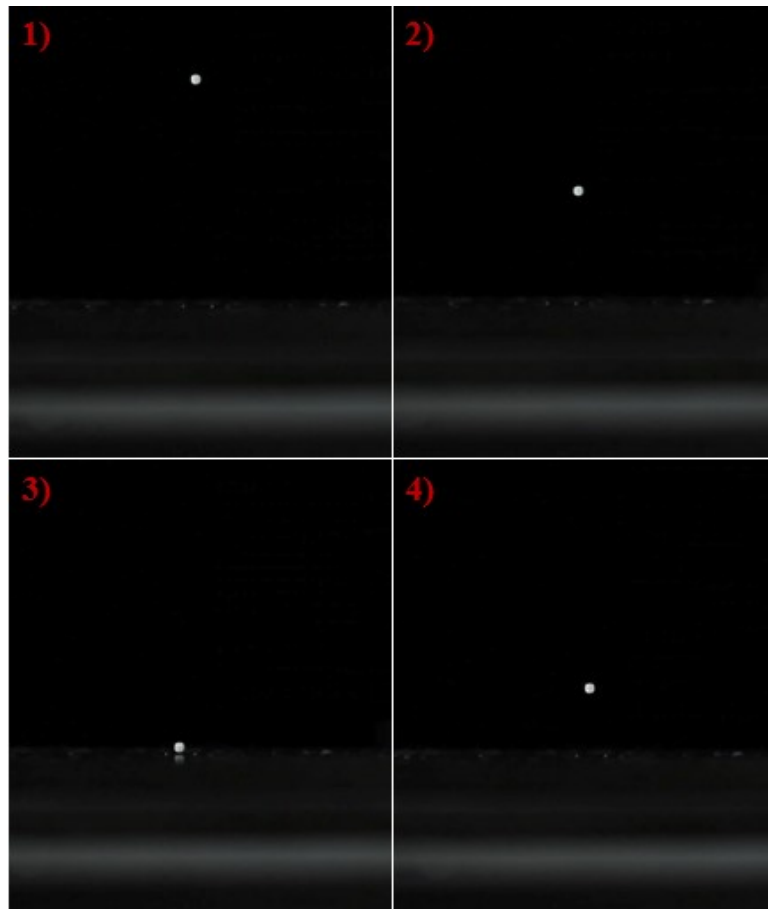


**Figure 4.25** Representative frames of particle drop test sequence, as recorded by the ultra-high speed camera. 1) and 2) show the particle falling toward the tool plate. 3) shows the contact between particle and tool plate. 4) shows particle bounce.

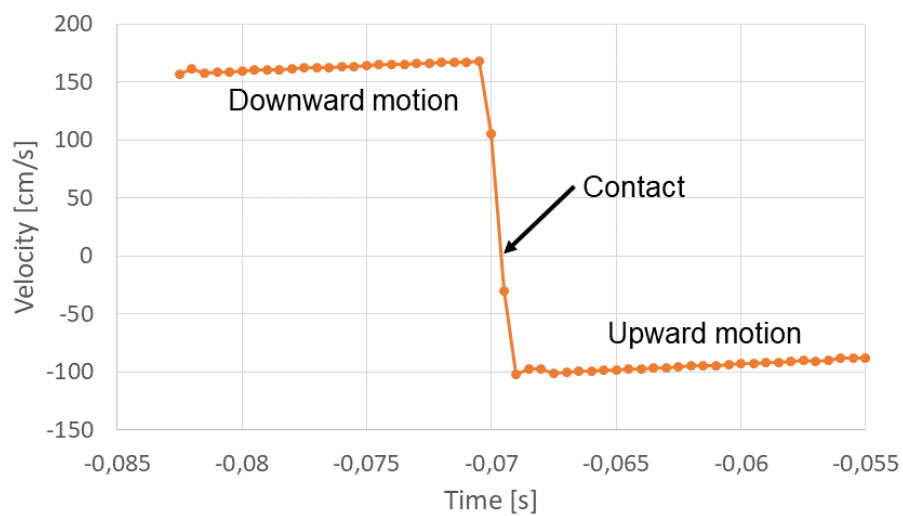


**Figure 4.26** Example of a typical drop test data plot. Particle's vertical velocity vs. time is shown, indicating downward motion, upward motion, and particle-plate contact.

To consider and evaluate the effect of particle terminal velocity on the value of the coefficient of restitution, the drop tower was designed to be adjustable in height. The particle drop was then performed from three different heights from tool plate: 150 mm, 300 mm, and 450 mm.

Similarly to previous analysis, the confidence interval method for continuous data was adopted to determine the minimum estimated sample size  $n_0$  to achieve a statically significant result. A confidence interval of 95% was selected, resulting in a value  $Z$  of the  $Z$ -distribution equal to 1.96. A margin of error  $E_r$  equal to 1% was selected. Similarly to previous analysis, a pilot study was conducted to obtain an estimate of standard deviation  $\sigma$ . Figure 4.27, Figure 4.28, and Figure 4.29 show the plots of standard deviation  $\sigma$  as function of sample size for YSZ particles dropped from 150 mm, 300 mm, and 450 mm drop heights, respectively. Figure 4.30, Figure 4.31, and Figure 4.32 show the plots of standard deviation  $\sigma$  as function of sample size for alumina particles dropped from 150 mm, 300 mm, and 450 mm drop heights, respectively. The plots show that the standard deviation approaches a plateau value once a certain number of measurements (i.e. sample size) is achieved. For YSZ particles, a plateau value equal to 0.0362, 0.0428, and 0.0287 was found for 150 mm, 300 mm, and 450 mm drop heights, respectively. For alumina particles, a plateau value equal to 0.0348, 0.0308, and 0.0363 was found for 150 mm, 300 mm, and 450 mm drop heights, respectively. These values were used as the estimate of standard deviation  $\sigma$ .

For YSZ particles, Eq. (4.29) suggests a minimum estimated sample size  $n_0$  equal to 50, 71, and 32 for 150 mm, 300 mm, and 450 mm drop heights, respectively. For alumina particles, Eq. (4.29) suggests a minimum estimated sample size  $n_0$  equal to 47, 36, and 51 for 150 mm, 300 mm, and 450 mm drop heights, respectively. As a conservative approach, a sample size  $n = 75$  was selected for both materials and all drop heights for a total of 450 samples collected.

Table 4.29 summarizes the values found for COR between YSZ / alumina particles and Al 6061-T6 at 150 mm, 300 mm, and 450 mm drop heights. Average values are also included. For YSZ particles, COR values at different drop heights lie within a maximum 2.9 % deviation from average. For alumina particles, COR values at different drop heights lie within a maximum 1.8 % deviation from average. Results show that COR is independent from drop height, thus the average value can be used as a representative value.

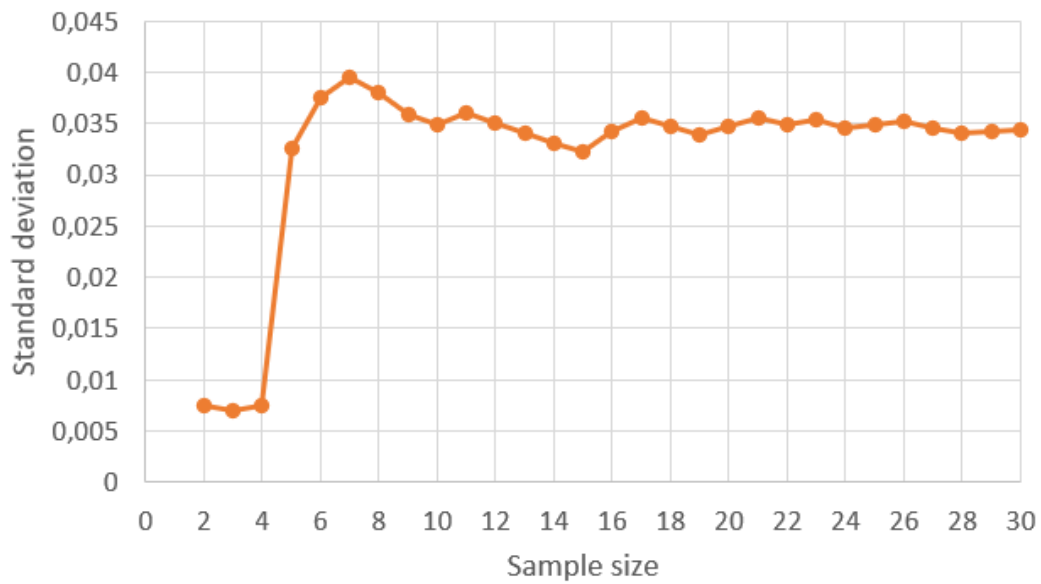


**Figure 4.27** Standard deviation as function of sample size for measurement of particle-tool coefficient of restitution considering YSZ particles dropped from 150 mm.

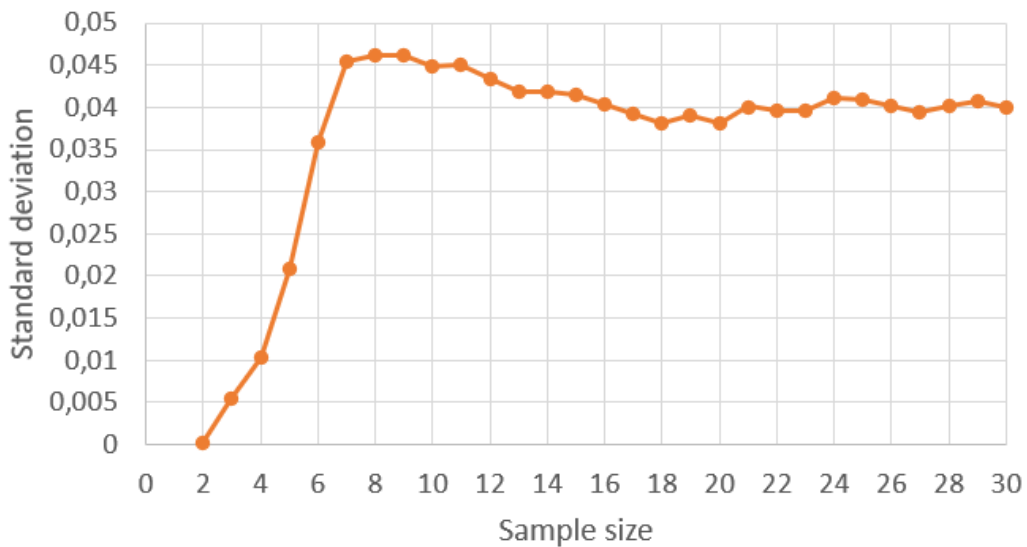


**Figure 4.28** Standard deviation as function of sample size for measurement of particle-tool coefficient of restitution considering YSZ particles dropped from 300 mm.

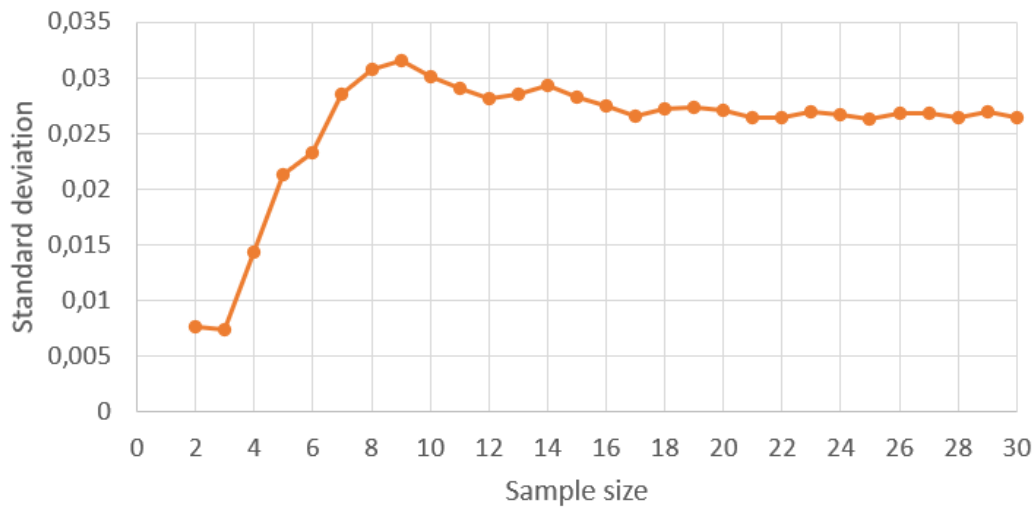


**Figure 4.29** Standard deviation as function of sample size for measurement of particle-tool coefficient of restitution considering YSZ particles dropped from 450 mm.

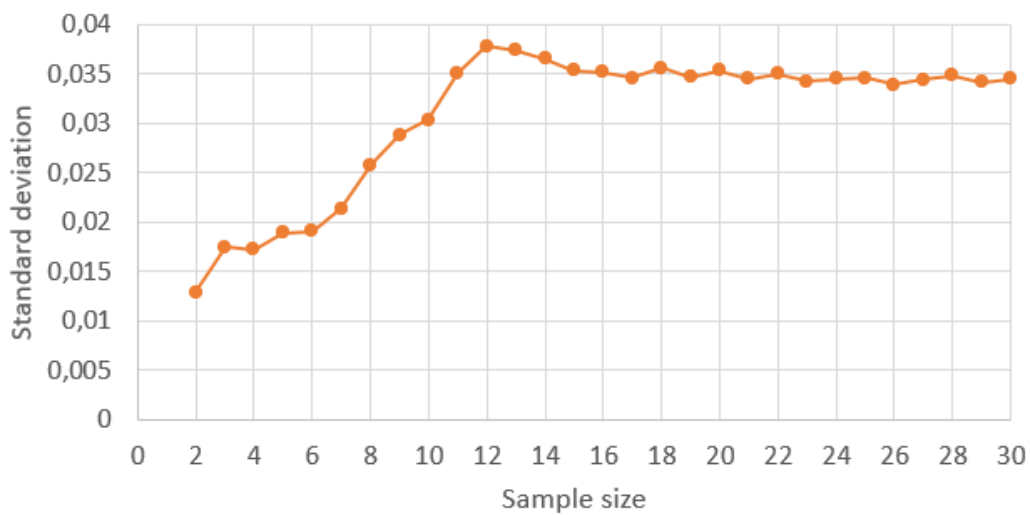


**Figure 4.30** Standard deviation as function of sample size for measurement of particle-tool coefficient of restitution considering alumina particles dropped from 150 mm.

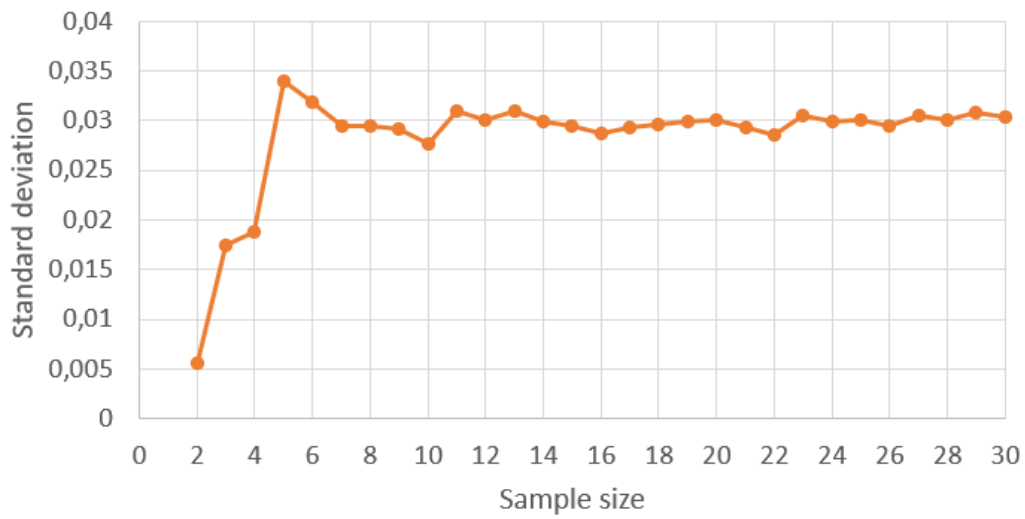


**Figure 4.31** Standard deviation as function of sample size for measurement of particle-tool coefficient of restitution considering alumina particles dropped from 300 mm.

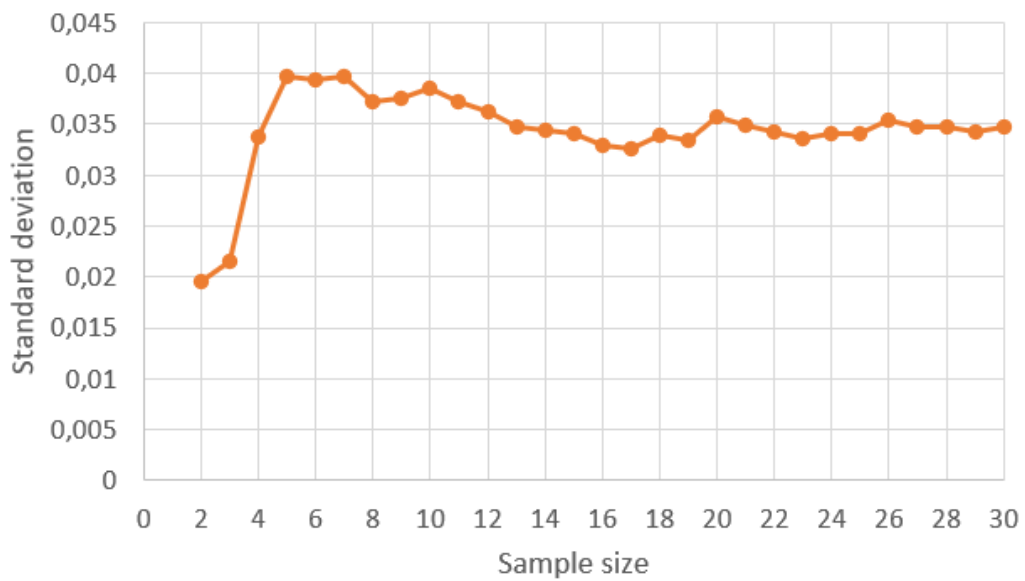


**Figure 4.32** Standard deviation as function of sample size for measurement of particle-tool coefficient of restitution considering alumina particles dropped from 450 mm.

**Table 4.29** Values of COR between YSZ / alumina particles and Al 6061-T6.

	YSZ	Alumina
<b>150 mm drop height</b>	0.6612 ± 0.0709	0.6248 ± 0.0682
<b>300 mm drop height</b>	0.6284 ± 0.0840	0.6043 ± 0.0603
<b>450 mm drop height</b>	0.6377 ± 0.0563	0.6120 ± 0.0712
<b>Average</b>	0.6424 ± 0.098	0.6137 ± 0.0793

### 4.3.2 DEM-driven design and verification of sample collection system

Characterization of granular material flow showed that the Dual-Rasp action generates a granular flow that originates from the cutting heads and evolves in the 3D space by dispersing in both elevation and azimuth angles, with a range related to the average velocity magnitude of the particles' assembly. Such a granular flow must be intercepted and driven toward a well-defined volume where the sample is collected. The whole process, from sampling to sample collection must be as much deterministic as possible to guarantee successful sample acquisition in the whole range of potential scenarios. Therefore, the same DEM numerical model adopted for the characterization of granular material flow can be exploited to drive the design of sample collection system. DEM simulation setup adopted to characterize the granular flow only included the Dual-Rasp cutting heads and the material particles free-flying in the unconstrained 3D space as result of the sampling action. However, the same DEM simulation model can be enriched with other elements to aid guiding the free granular flow into a path for collection. Such additional elements compose the sample collection system, working in conjunction with the sampling system (i.e. Dual-Rasp) to guarantee successful sampling and sample collection into a pre-defined volume. Moreover, results of granular flow characterization can be exploited to drive the design of the elements of the sample collection system. Three elements of the sample collection system were identified: the sample transport guide, the sample collection cup, and the sample retention features.

The sample transport guide, hereafter simply called guide, has the purpose of intercepting the free-flying granular flow produced by the Dual-Rasp and guide it toward the inlet of the sample collection cup. Before getting to the idea of using a purposely designed element to guide the granular flow toward the collection cup, a guide-free scenario was investigated. DEM simulations were conducted to evaluate the feasibility of collecting sample directly by just placing the collection volume in the way of the granular flow. In this case, the collection volume is

simply represented by a cube with a front large opening to let the particles entering the volume and being captured. DEM simulation results (Figure 4.33) showed that a negligible number of particles was collected, highlighting a few major weaknesses of this solution.

- The spatial dispersion angles of the free-flying, unconstrained granular flow would require a very large collection volume, thus negatively influencing the severe limitations in terms of mass and volume of the whole sample collection system.
- The random collisions between particles and surfaces of the collection volume make significantly not deterministic the sample collection process. This effect is highly influenced by the geometry of the surfaces interacting with the particles, hence there is margin for improvements.
- In a low gravity vacuum environment, the range of particle's parabolic trajectories is much larger than Earth's. As a result, it is required to capture the particles while they are still in the straight upwards portion of their trajectory, otherwise the whole sample collection system would be unreasonably large. Moreover, capturing the particles while they are still moving in a straight upwards trajectory requires orienting the collection volume accordingly, thus making more difficult sample collection and retention.

To improve sample collection, a few changes were made. The difficulty of capturing particles while moving in the straight upwards trajectory requires to add an element to guide and deflect particle's trajectories downward. This is supported by results of DEM-MBD co-simulations on the first design iteration. In fact, Figure 4.33 shows that some particles colliding with inner surfaces of collection volume are deflected downward. This behavior can be exploited to enable a more efficient sample collection.

The second design iteration included a significantly smaller collection cup shaped as a right circular cylinder and a preliminary concept of the guide to aid particles' deflection toward the collection cup. Guide and collection cup were generated as a single part for convenience. DEM-MBD co-simulation results (Figure 4.34) showed that particle's deflection toward the collection cup can be successfully achieved resulting in a significant increase in the collection efficiency. Moreover, the collection cup has a more suited size, geometry, position, and orientation. Despite the second iteration showed promising results, it should be noted that the geometry adopted for the guide has not a specific rationale and was implemented only to evaluate the feasibility of an element purposely designed to guide and deflect the particles toward the collection cup. For this reason, further improvements were made providing a rationale for the geometry of the guide.

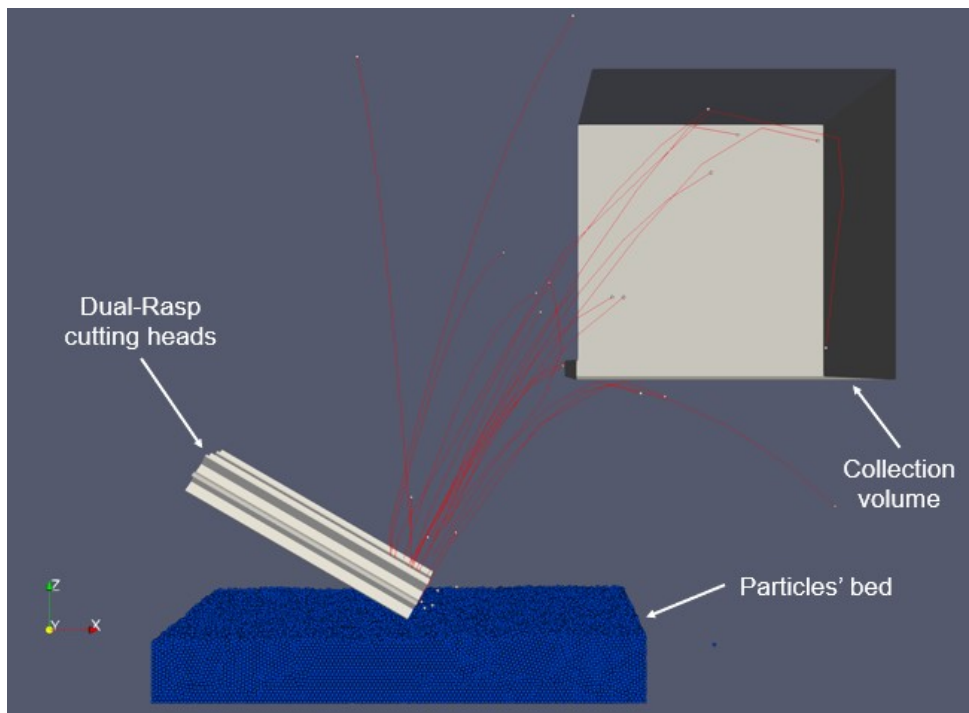


**Figure 4.33** DEM-MBD co-simulation of first design iteration of sample collection system implementing direct collection into a volume. Particles trajectories are shown in red. Please note that the collection volume is cross sectioned to show the inside. Side view shown.

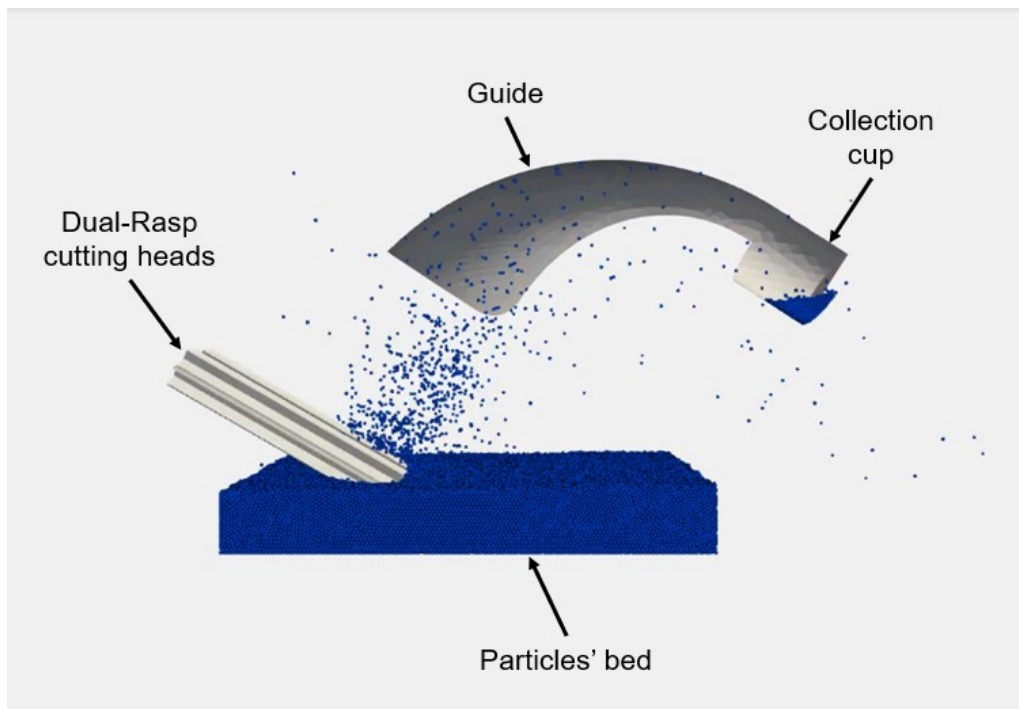


**Figure 4.34** DEM-MBD co-simulation of second design iteration of sample collection system implementing the guide concept to deflect particles toward the collection cup. Please note that both the guide and the collection cup are cross sectioned to show the inside. Side view shown.

The investigation of generation and evolution of the granular flow led to the identification of a pattern useful to define an optimized geometry for the guide. In fact, the granular flow generates by a small area in between the tips of the Dual-Rasp cutting heads. The granular flow then disperses into a larger 3D volume and needs to be intercepted, deflected and re-focused toward a smaller volume represented by the collection cup. As a result, the surface geometry of the guide should have some reflection and focusing capabilities. There are several geometries with different reflection and focusing properties, such as the rotunda, the parabola, and the ellipse (Figure 4.35). The geometrical properties of these surfaces are used in several applications where it is required to reflect and focus radiation waves (e.g. lasers, radio waves, etc.) or sound waves. A rotunda is a geometry similar to a cupola alternating pentagons and triangles around an axis [211]. This geometry is adopted in many buildings with dome-like ceilings and exhibits a guided reflection of sound waves along its surface [212]. A parabola is a geometry focusing parallel rays projected to its surface to a focal point [213]. This geometry is widely used in telecommunication, optical, and sound applications, including antennas, mirrors, and microphones [214] [215] [216]. An ellipse is a geometry with two focal points and has the property of focusing rays projected in any direction from one focal point to the other [213]. This geometry is widely used in optical applications such as mirrors [217]. Therefore, it was decided to investigate if a geometry with reflection and focusing properties can be used to deflect and re-focus the granular flow toward the collection cup. In this context, an elliptical guide is the most promising geometry since it can be designed in such a way the two focal points are coincident with the origin (i.e. the tip of the Dual-Rasp cutting heads) and the desired destination (i.e. inlet of the collection cup) of the granular material flow. The 3D guide geometry is derived by extending the ellipse geometry in the 3D space, thus obtaining a tri-axial ellipsoid. This geometry is generated by two ellipses defined on elevation and azimuth planes enabling particles ejected by the Dual-Rasp cutting heads being deflected and re-focused toward the inlet of the collection cup (Figure 4.36 and Figure 4.37). To maximize the amount of sample collected, the collection cup was designed as a right semi-elliptical cylinder to match the footprint of the guide in the azimuth plane (Figure 4.37 and Figure 4.38). In fact, the collection cup is placed just below the guide and its inlet face is parallel to the azimuth plane of the guide.

The two ellipses generating the tri-axial ellipsoid share the major axis and the focal points. The major axis is defined through the length and the inclination with respect to horizontal. Both parameters are defined considering two factors:

- The average velocity magnitude of the granular flow, that determines the region where it is desirable to intercept particles along the straight portion of their upward trajectory.

- The relative position between the Dual-Rasp and the collection cup, that is influenced by the requirement on the volume envelope of the whole sample collection system. In fact, it is required that the sample collection system has at least 18 deg of clearance with respect to the surrounding terrain all around the Dual-Rasp location. As a result, the sample collection system must fit into a conical volume envelope with a 72 deg semi-aperture around the Dual-Rasp, since it is the only element of the system that must interact with the terrain. The purpose of this requirement is to guarantee a safety margin with respect to the uncertainty on the roughness of the Enceladus surface.

On the other hand, the minor axes of the two ellipses are independently defined since they control the width of the ellipsoid in elevation and azimuth. As a result, the minor axes of the two ellipses are influenced by the dispersion angles of the granular flow in elevation and azimuth, thus determining the percentage of particles intercepted by the guide.

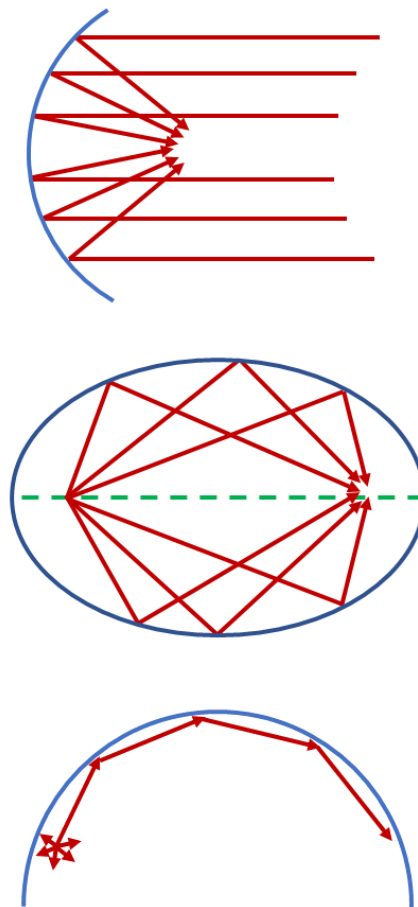


**Figure 4.35** Examples of geometries with reflection and focusing properties. From top to bottom: parabola, ellipse, and rotunda.

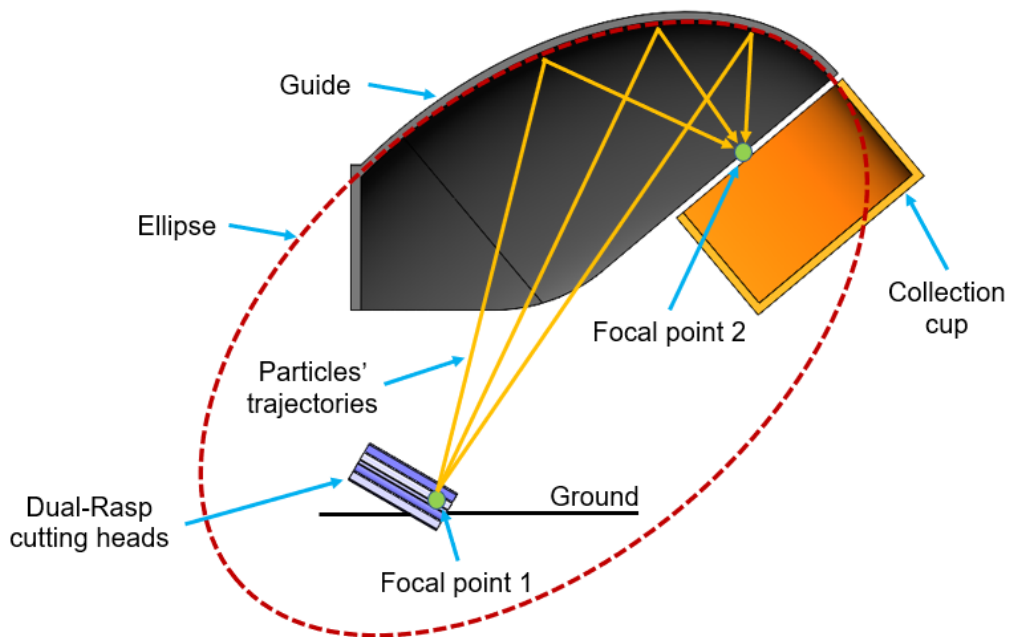


**Figure 4.36** Guide design based on the ellipsoid geometry. View of the elevation plane showing the focusing effect on particles' trajectories.

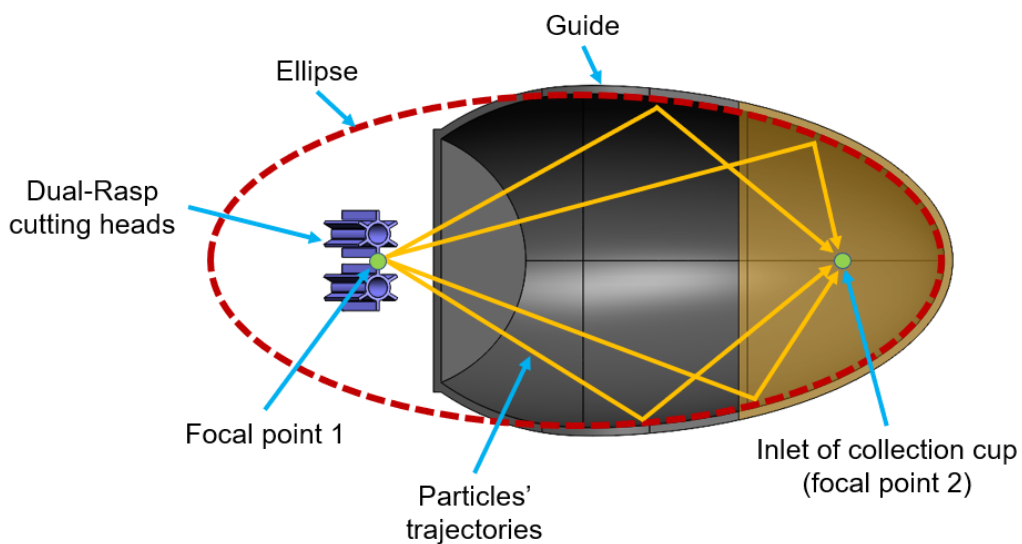


**Figure 4.37** Guide design based on the ellipsoid geometry. View of the azimuth plane showing the focusing effect on particles' trajectories. The transparent orange element represents the collection cup.

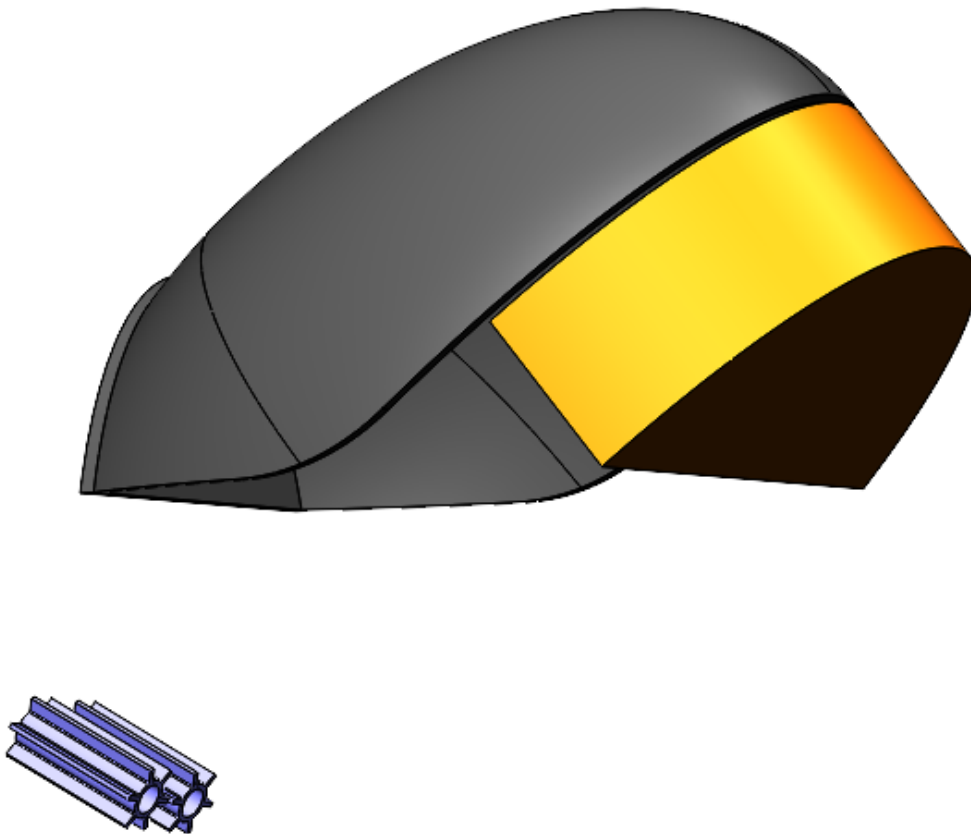


**Figure 4.38** 3D representation of the sample collection system model, including the ellipsoidal guide (black), the collection cup (orange) and the Dual-Rasp cutting heads (light blue).

Since the analysis metrics characterizing the granular flow provide crucial guidelines for the design of the guide, numerical simulations based on the DEM model presented in paragraph 4.3.1.1 were conducted to characterize the free-flying granular flow generated by the Dual-Rasp with the purpose to optimize the design of the guide. Since the characterization is performed on the free-flying granular flow, the simulations only involved the Dual-Rasp cutting heads and the particles' bed, and considered the 1g Earth's environment with the purpose to provide a design of the guide suited for laboratory testing. Because of the higher gravity, the Dual-Rasp was operated at 10000 RPM to produce a granular flow with sufficient average velocity magnitude to be intercepted by the guide in the straight portion of the upward trajectory. Table 4.30, Table 4.31, Table 4.32 summarize the parameters of DEM-MBD co-simulation performed to characterize the granular flow. Figure 4.39 shows the results of granular flow characterization through the analysis metrics extrapolated by the simulation data. The design of the sample collection system, including the geometry of the guide and the relative positioning among the elements, were driven by the DEM simulation results and adjusted to optimize the percentage of granular flow intercepted by the guide

within the constraints and margins previously discussed. As shown in Figure 4.40 and Figure 4.41, the configuration adopted for the sample collection system enables to use the guide to theoretically intercept up to 37% of the granular flow in the elevation plane and up to 50% in the azimuth plane. However, particles are more likely to be successfully deflected toward the inlet of the collection cup if intercepted in its vicinity. In this scenario, up to 25-35% of the granular flow is expected to be intercepted in both the elevation and azimuth planes. As shown in Figure 4.40, a significant portion (up to 50%) of the granular flow in the elevation plane is blocked by the body of the collection cup. This compromise was dictated by the requirement on the ground clearance of the sample collection system.

A DEM-MBD co-simulation of sample collection system was performed by using the parameters defined in Table 4.30, Table 4.31, Table 4.32, Table 4.33, Table 4.34 and related to Dual-Rasp cutting heads, particles, guide, collection cup, and environment. Simulation results (Figure 4.42) show a good agreement with expectations since particles are intercepted and deflected toward the inlet of the collection cup because of the ellipsoid geometry of the guide. This configuration makes the sample collection process much more deterministic than previous designs. Moreover, collection of particles into the cup is significantly aided by the higher gravity settling particles in the lowest corner of the cup.

**Table 4.30** Parameters of the Dual-Rasp cutting heads and environmental parameter for the DEM-MBD co-simulation of sample collection system.

Parameters of Dual-Rasp cutting heads	
<b>Geometry</b>	Cylindrical core with 6 straight uniformly spaced radial teeth
<b>Geometrical features and Position</b>	<ul style="list-style-type: none"> <li>• Core length: 30 mm</li> <li>• Core diameter: 7 mm</li> <li>• Tooth: 3 mm (length) x 1 mm (thickness)</li> <li>• Gap between cutting heads: 2 mm (at teeth's tip)</li> <li>• Inclination wrt horizontal: 30 deg</li> </ul>
<b>Prescribed motion</b>	<ul style="list-style-type: none"> <li>• Vertical motion (plunging) velocity: 2 mm/s</li> <li>• Vertical motion (plunging) displacement: 10 mm</li> <li>• Rotational speed [Earth, Enceladus]: [10000, 2000] RPM</li> </ul>
<b>Material (Al 6061-T6)</b>	<ul style="list-style-type: none"> <li>• Young's modulus (<math>E_t</math>): 68.9 GPa [183]</li> <li>• Poisson's ratio (<math>\nu_t</math>): 0.33 [183]</li> </ul>
<b>Mesh</b>	<ul style="list-style-type: none"> <li>• Shell surface mesh</li> <li>• 1 mm element size</li> <li>• 7706 total nodes</li> <li>• 3852 total elements</li> </ul>
Environmental parameter	
<b>Gravitational acceleration [Earth, Enceladus]</b>	[9.81, 0.113] m/s <sup>2</sup>

**Table 4.31** Particle parameters for the DEM-MBD co-simulation of sample collection system.

Particle parameters	
Material	YSZ / Alumina
Shape / Shape distribution	Sphere / Monodisperse
Size / Size distribution	1 mm diameter / Monodisperse
Number of particles	187500
Size of particles' bed	<ul style="list-style-type: none"> <li>• Length: 75 mm</li> <li>• Width: 75 mm</li> <li>• Height: 30 mm</li> </ul>
Young's modulus ( $E_p$ )	0.1 GPa
Poisson's ratio ( $\nu_p$ )	0.35
Density ( $\rho_p$ )	3000 kg/m <sup>3</sup>

**Table 4.32** Paired parameters for the DEM-MBD co-simulation of sample collection system.

Paired parameters	
$pp$ coefficient of static friction ( $\mu_{spp}$ )	0.5
$pt$ coefficient of static friction ( $\mu_{spt}$ ) [YSZ, Alumina]	[0.154, 0.2226]
$pp$ coefficient of rolling friction ( $\mu_{rpp}$ )	0.005
$pt$ coefficient of rolling friction ( $\mu_{rpt}$ )	0.005
$pp$ coefficient of restitution ( $e_{pp}$ )	0.5
$pt$ coefficient of restitution ( $e_{pt}$ ) [YSZ, Alumina]	[0.6424, 0.6137]

**Table 4.33** Parameters of sample transport guide for the DEM-MBD co-simulation of sample collection system.

Parameters of sample transport guide	
<b>Geometry</b>	Tri-axial ellipsoid
<b>Geometrical features and Position</b>	<ul style="list-style-type: none"> <li>• Length of semi-major axis: 108 mm</li> <li>• Inclination of semi-major axis wrt horizontal: 40 deg</li> <li>• Length of semi-minor axis in elevation plane: 68 mm</li> <li>• Length of semi-minor axis in azimuth plane: 50 mm</li> </ul>
<b>Prescribed motion</b>	<ul style="list-style-type: none"> <li>• Vertical motion (plunging) velocity: 2 mm/s</li> <li>• Vertical motion (plunging) displacement: 10 mm</li> </ul>
<b>Material (Al 6061-T6)</b>	<ul style="list-style-type: none"> <li>• Young's modulus (<math>E_t</math>): 68.9 GPa [183]</li> <li>• Poisson's ratio (<math>\nu_t</math>): 0.33 [183]</li> </ul>
<b>Mesh</b>	<ul style="list-style-type: none"> <li>• Shell surface mesh</li> <li>• 1 mm element size</li> <li>• 35735 total nodes</li> <li>• 17720 total elements</li> </ul>

**Table 4.34** Parameters of the collection cup for the DEM-MBD co-simulation of sample collection system.

Parameters of collection cup	
<b>Geometry</b>	Right semi-elliptical cylinder
<b>Geometrical features</b>	<ul style="list-style-type: none"> <li>• Length (max): 61 mm</li> <li>• Width (max): 95 mm</li> <li>• Height: 37 mm</li> </ul>
<b>Prescribed motion</b>	<ul style="list-style-type: none"> <li>• Vertical motion (plunging) velocity: 2 mm/s</li> <li>• Vertical motion (plunging) displacement: 10 mm</li> </ul>
<b>Material (Al 6061-T6)</b>	<ul style="list-style-type: none"> <li>• Young's modulus (<math>E_t</math>): 68.9 GPa [183]</li> <li>• Poisson's ratio (<math>\nu_t</math>): 0.33 [183]</li> </ul>
<b>Mesh</b>	<ul style="list-style-type: none"> <li>• Shell surface mesh</li> <li>• 1 mm element size</li> <li>• 15513 total nodes</li> <li>• 7594 total elements</li> </ul>

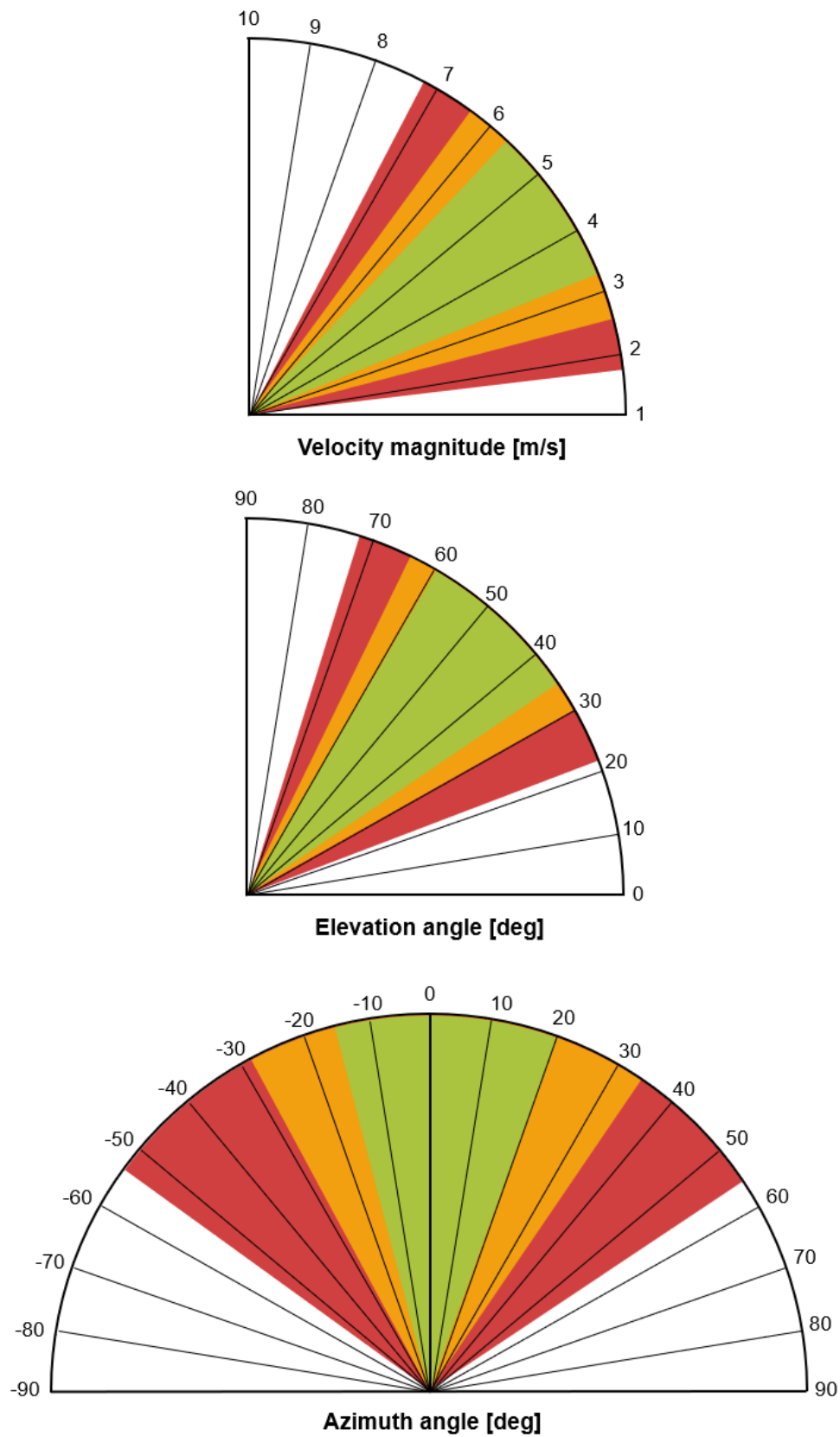


**Figure 4.39** Dual-Rasp granular flow characterization in 1g Earth's environment. Results show the dispersion of the analysis metrics including 25<sup>th</sup> percentile (green), 50<sup>th</sup> percentile (yellow), and 75<sup>th</sup> percentile (red).

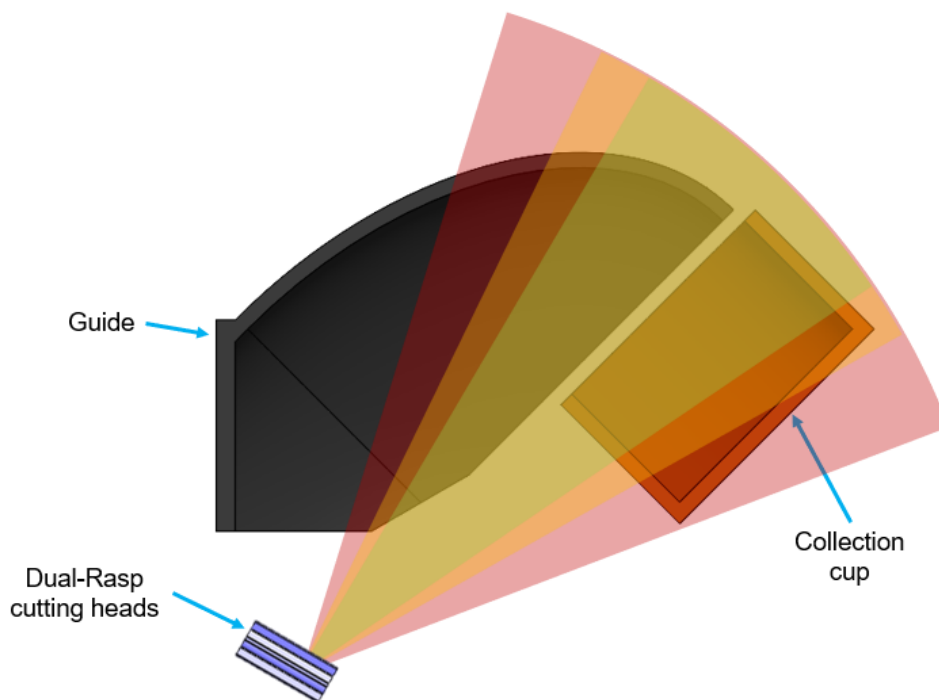


**Figure 4.40** Sample collection system design for 1g Earth's environment driven by DEM-MBD co-simulation results. Granular flow dispersion in the elevation plane is shown, including 25<sup>th</sup> percentile (green area), 50<sup>th</sup> percentile (yellow area), and 75<sup>th</sup> percentile (red area).

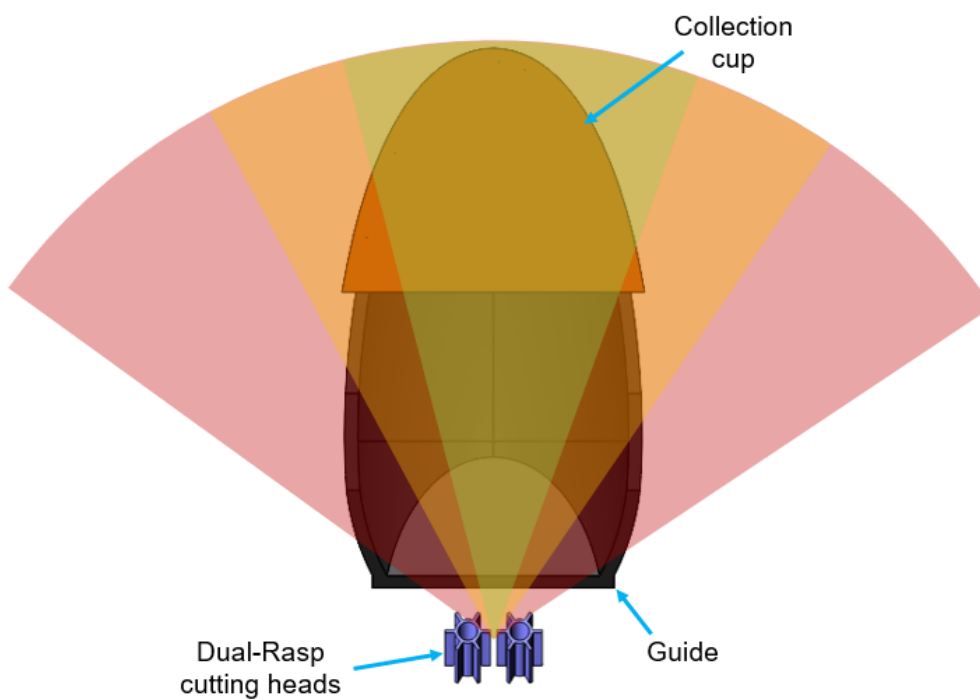


**Figure 4.41** Sample collection system design for 1g Earth's environment driven by DEM-MBD co-simulation results. Granular flow dispersion in the azimuth plane is shown, including 25<sup>th</sup> percentile (green area), 50<sup>th</sup> percentile (yellow area), and 75<sup>th</sup> percentile (red area).

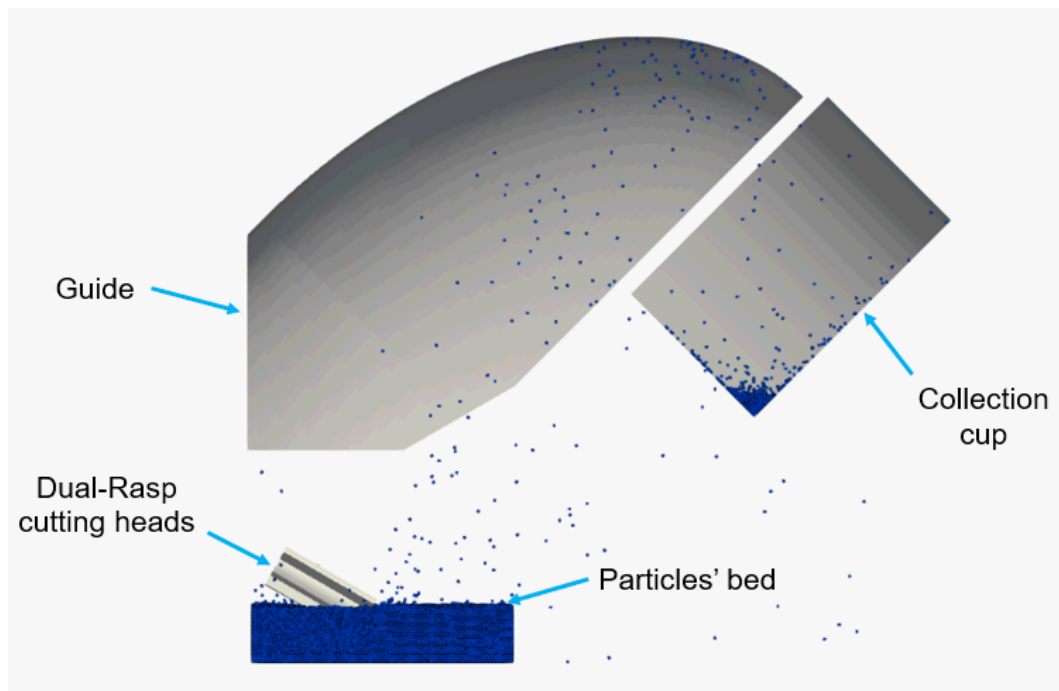


**Figure 4.42** DEM-MBD co-simulation of sample collection system in 1g Earth's environment.

The DEM-driven design process described was also applied to the sample collection system for 1%g Enceladus' environment. Because of the lower gravity, the Dual-Rasp was operated at 2000 RPM to produce a granular flow with sufficient average velocity magnitude to be intercepted by the guide in the straight portion of the upwards trajectory. Table 4.30, Table 4.31, Table 4.32 summarize the parameters of DEM-MBD co-simulation performed to characterize the granular flow. Figure 4.43 shows the results of granular flow characterization through the analysis metrics extrapolated by the simulation data. The geometry of the guide and the relative positioning among the elements of the sample collection system were adjusted to optimize the percentage of granular flow intercepted by the guide within the constraints and margins previously discussed. As shown in Figure 4.44 and Figure 4.45, the configuration adopted for the sample collection system enables to use the guide to theoretically intercept up to 37% of the granular flow in the elevation plane and up to 50% in the azimuth plane. However, particles are more likely to be successfully deflected toward the inlet of the collection cup if intercepted in its vicinity. In this scenario, up to 25-35% of the granular flow is expected to be intercepted in both the elevation and azimuth planes. As shown in Figure 4.44, also in this case a significant portion (up to 50%) of the granular flow in the elevation plane is blocked by the body of the collection cup. This compromise was dictated by the requirement on the ground clearance of the sample collection system.

A DEM-MBD co-simulation of sample collection system was performed by using the parameters defined in Table 4.30, Table 4.31, Table 4.32, Table 4.33,

Table 4.34 and related to Dual-Rasp cutting heads, particles, guide, collection cup, and environment. Simulation results (Figure 4.46) show that the particles remain in suspension much longer time because of the low gravity environment. Also in this case, particles are successfully intercepted and deflected toward the inlet of the collection cup as a result of the ellipsoid geometry of the guide. However, the low gravity environment is less effective in settling the particles and retaining them inside the collection cup. As a result, particles bounce to the inner walls of the collection cup and get out of it, leaving only a small amount of particle collected. For this reason, the collection cup must be provided with some sort of feature to aid sample retention in a low gravity environment.

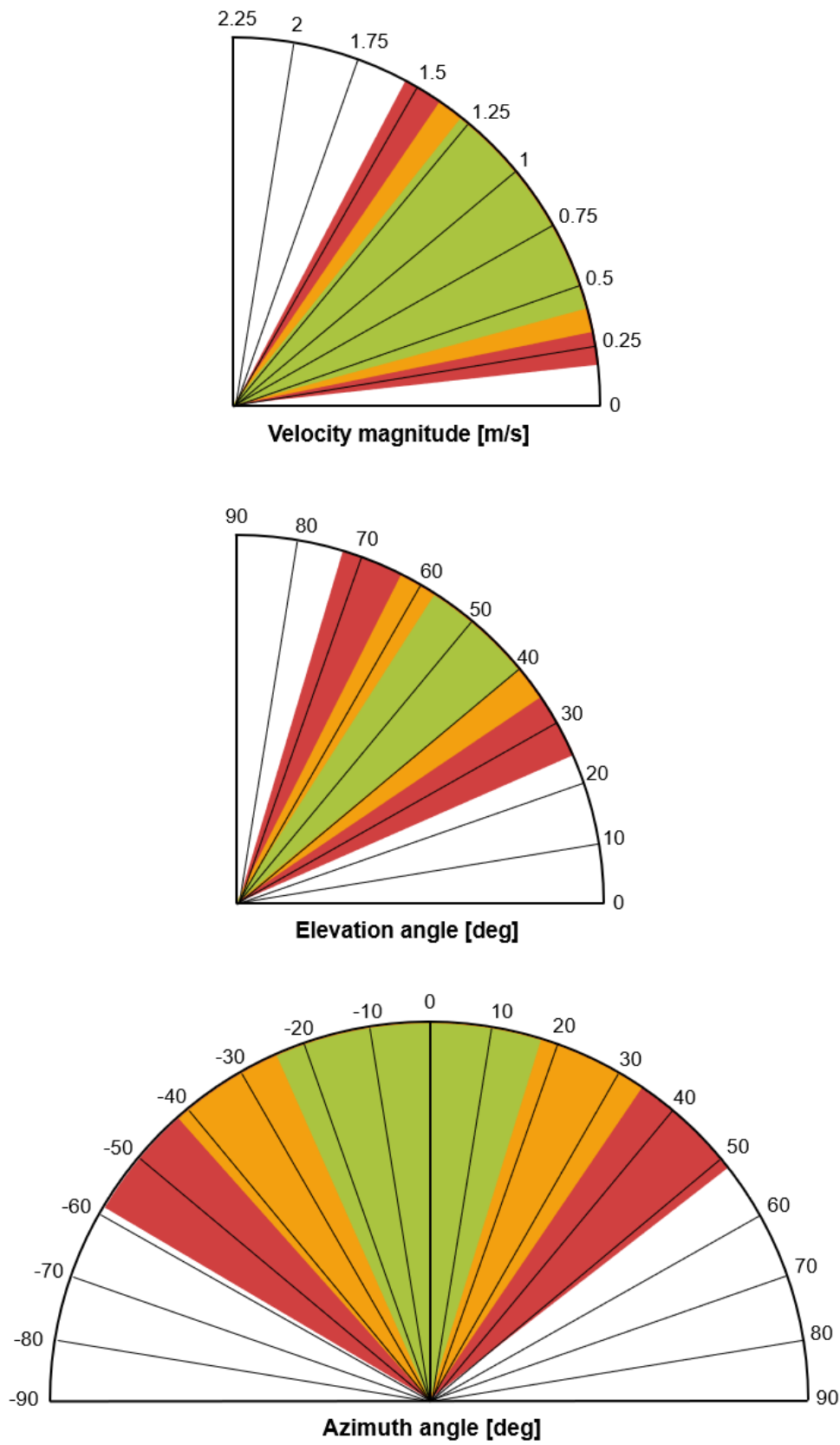


**Figure 4.43** Dual-Rasp granular flow characterization in 1%g Enceladus' environment. Results show the dispersion of the analysis metrics including 25<sup>th</sup> percentile (green), 50<sup>th</sup> percentile (yellow), and 75<sup>th</sup> percentile (red).

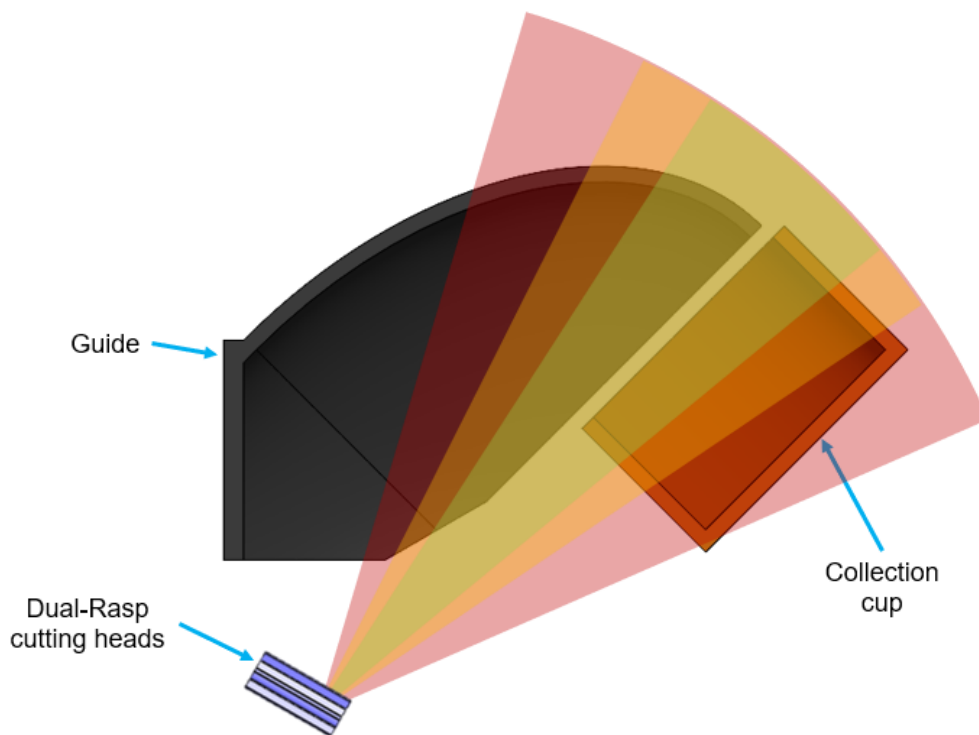


**Figure 4.44** Sample collection system design for 1%g Enceladus' environment driven by DEM-MBD co-simulation results. Granular flow dispersion in the elevation plane is shown, including 25<sup>th</sup> percentile (green area), 50<sup>th</sup> percentile (yellow area), and 75<sup>th</sup> percentile (red area).

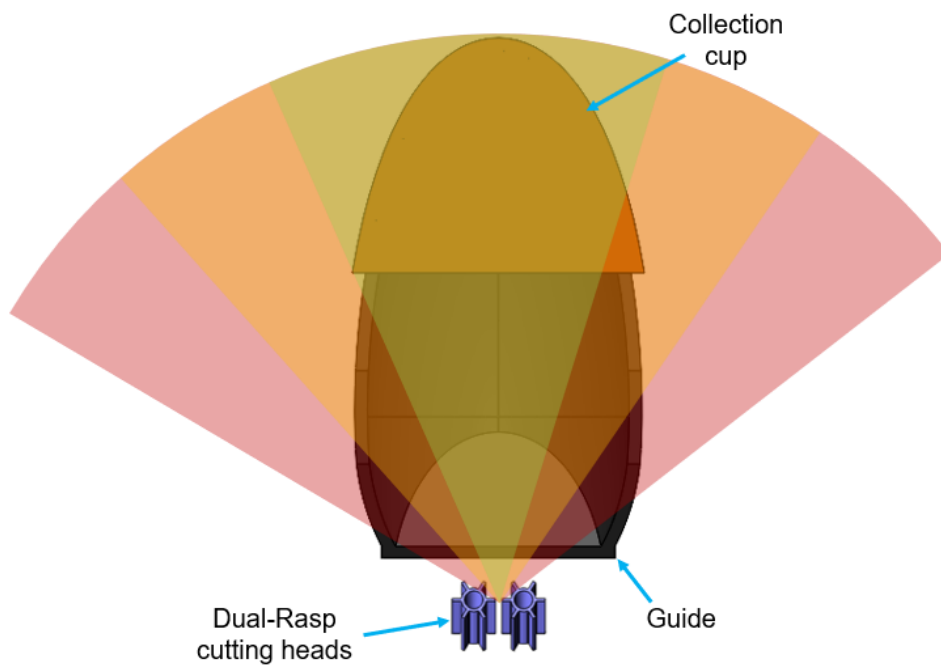


**Figure 4.45** Sample collection system design for 1%g Enceladus' environment driven by DEM-MBD co-simulation results. Granular flow dispersion in the azimuth plane is shown, including 25<sup>th</sup> percentile (green area), 50<sup>th</sup> percentile (yellow area), and 75<sup>th</sup> percentile (red area).

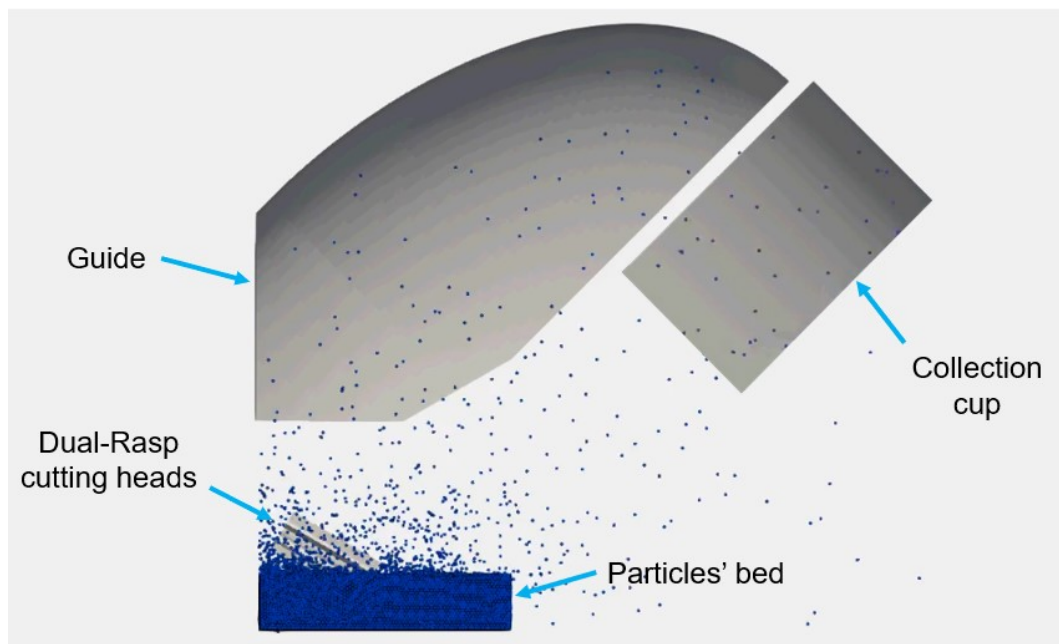


**Figure 4.46** DEM-MBD co-simulation of the sample collection system in 1% Enceladus' environment.

Several sample retention features were devised, integrated into the collection cup design, and simulated in the DEM-MBD environment. Sample retention efficiency was evaluated to compare the different solutions.

Concept #1 of collection cup design provided with sample retention features implemented barriers to create a labyrinth with the goal to trap the particles (Figure 4.47). Particles' trajectories inside the collection cup can be qualitatively anticipated by considering the classic laws of collisions and reflections governing the interaction between particles and inner walls of the collection cup. Figure 4.48 shows that some particles' trajectories can be directed toward the inside of the labyrinth generated by the barriers, thus trapping particles in a series of internal reflections that make less likely exiting the collection cup. DEM-MBD simulations confirmed this expectation by showing an estimated 60% increase in the retention efficiency with respect to the collection cup without any retention feature (Figure 4.49). Two more collection cup designs were investigated by exploring the labyrinth concept. In concept #2 (Figure 4.50), the lower corner of the collection cup was provided with a 45 deg chamfer to aid particles' reflection toward the inside of the labyrinth. Top barrier was inclined 45 deg with respect to its original orientation to make the inlet of the labyrinth wider, thus increasing the number of particles captured. In concept #3 (Figure 4.51), also the bottom barrier was inclined 45 deg with respect to its original orientation, thus creating a sharper corner to trap the particles. Concept #2 and concept #3 were simulated in the DEM-MBD environment showing little improvements in the retention efficiency with respect to concept #1 (Figure 4.52 and Figure 4.53). In fact, simulation results showed an estimated 60-65% increase in the retention efficiency with

respect to the collection cup without any retention feature. For this reason, a different approach was investigated. Figure 4.54 shows grid-style retention features embedded into the collection cup. The grid provides much more surface area to increase collisions between particles and inner walls, thus dissipating particles' kinetic energy. The grid stops before reaching the bottom of the collection cup in such a way a common area is created at the bottom of the cup. This area is meant to further stimulate particles' mixing, dissipating kinetic energy by mutual collisions. DEM-MBD co-simulation of this concept showed a significant improvement in the retention efficiency (Figure 4.55). In fact, simulation results showed an estimated 130% increase in the retention efficiency with respect to the collection cup without any retention feature.

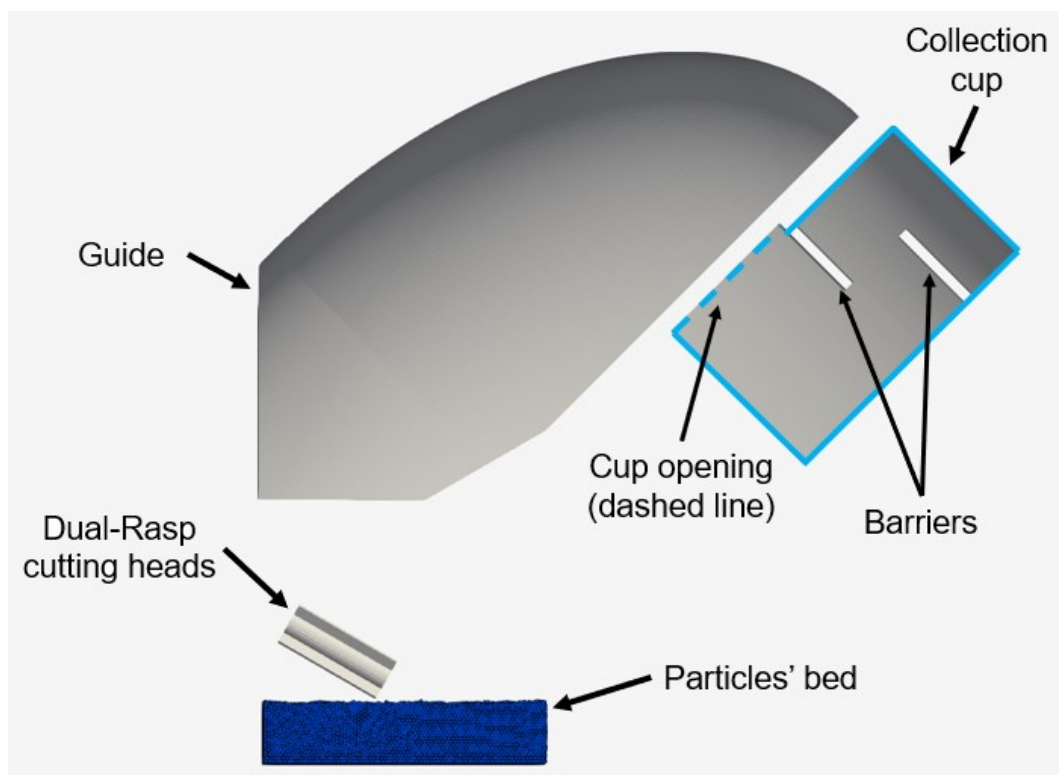


**Figure 4.47** Concept #1 of collection cup design provided with labyrinth-style sample retention features. General architecture.

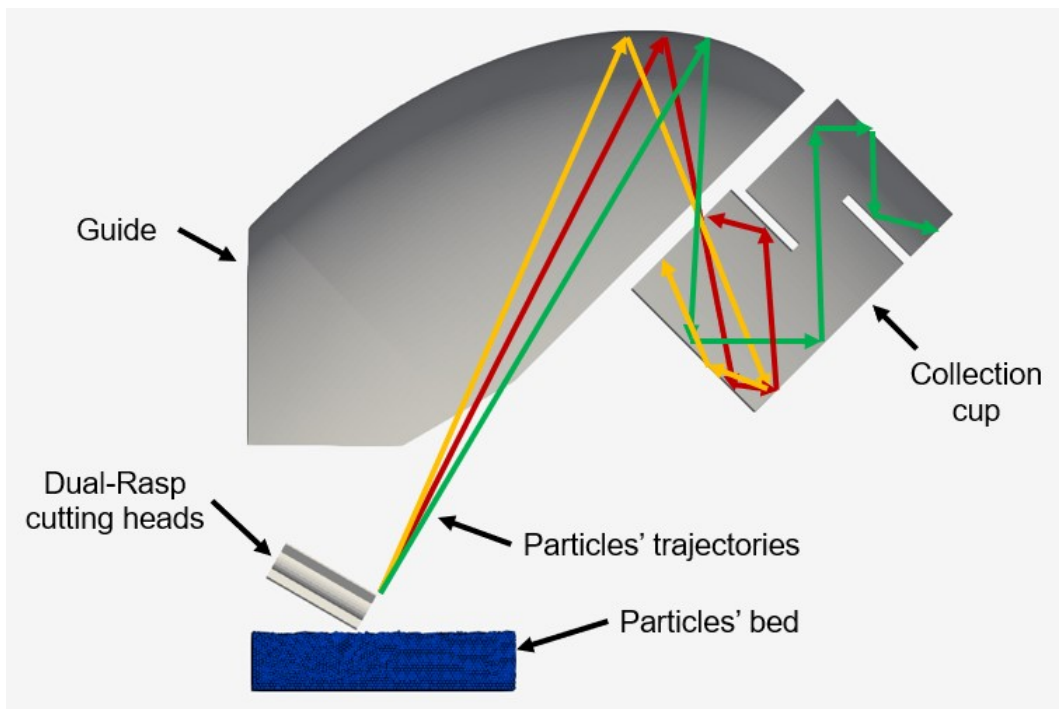


**Figure 4.48** Concept #1 of collection cup design provided with labyrinth-style sample retention features. Potential particles' trajectories. Qualitative scheme.

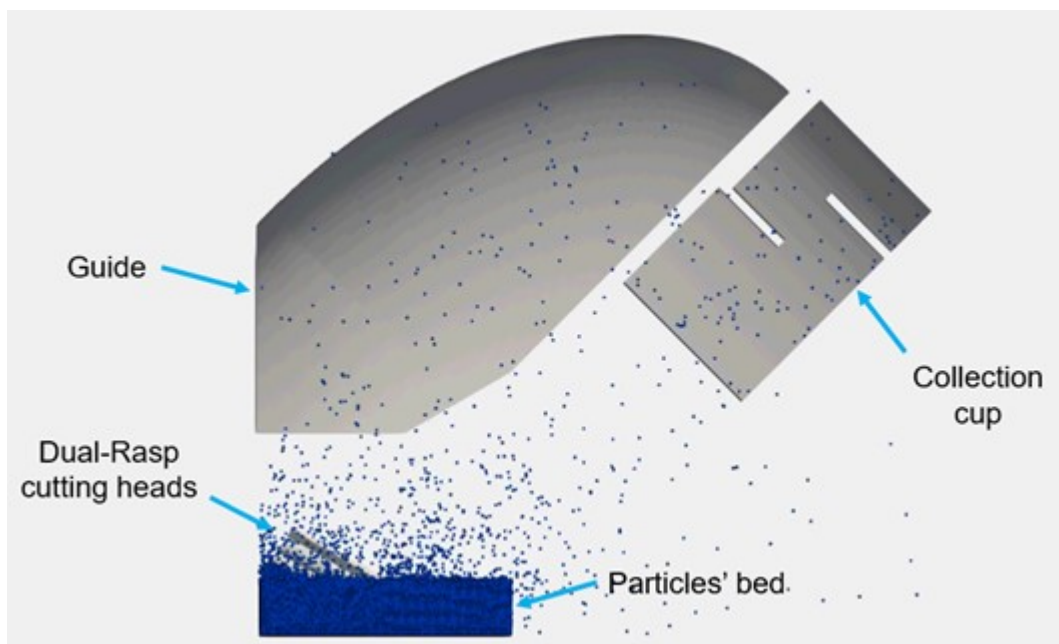


**Figure 4.49** Concept #1 of collection cup design provided with labyrinth-style sample retention features. DEM-MBD co-simulation.

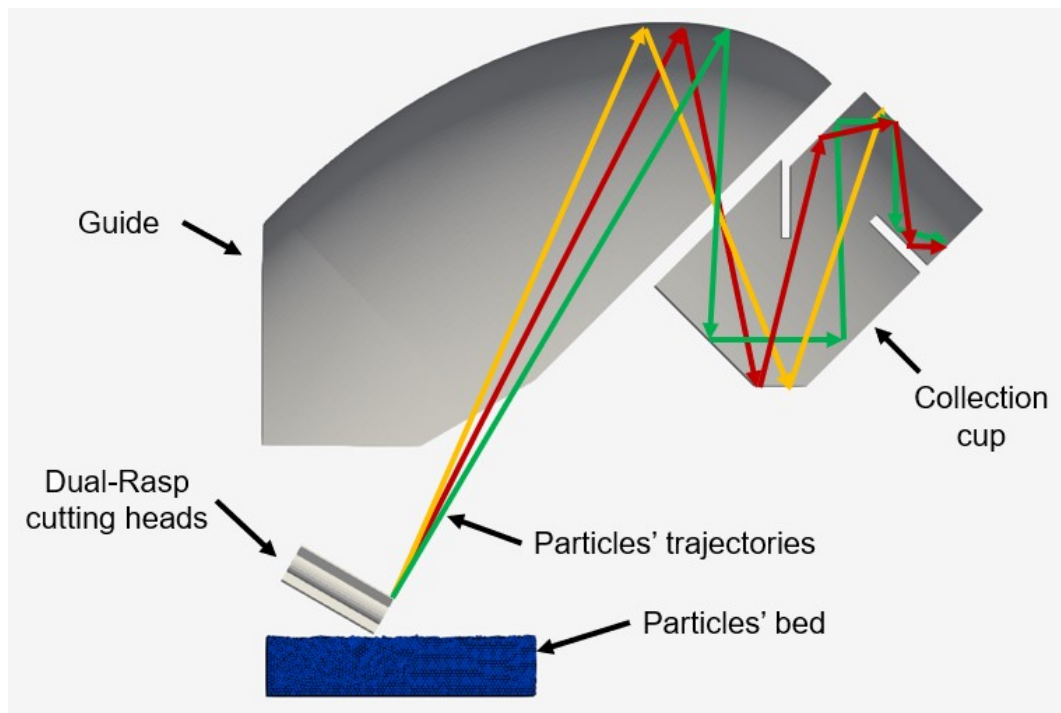


**Figure 4.50** Concept #2 of collection cup design provided with labyrinth-style sample retention features. Potential particles' trajectories. Qualitative scheme.

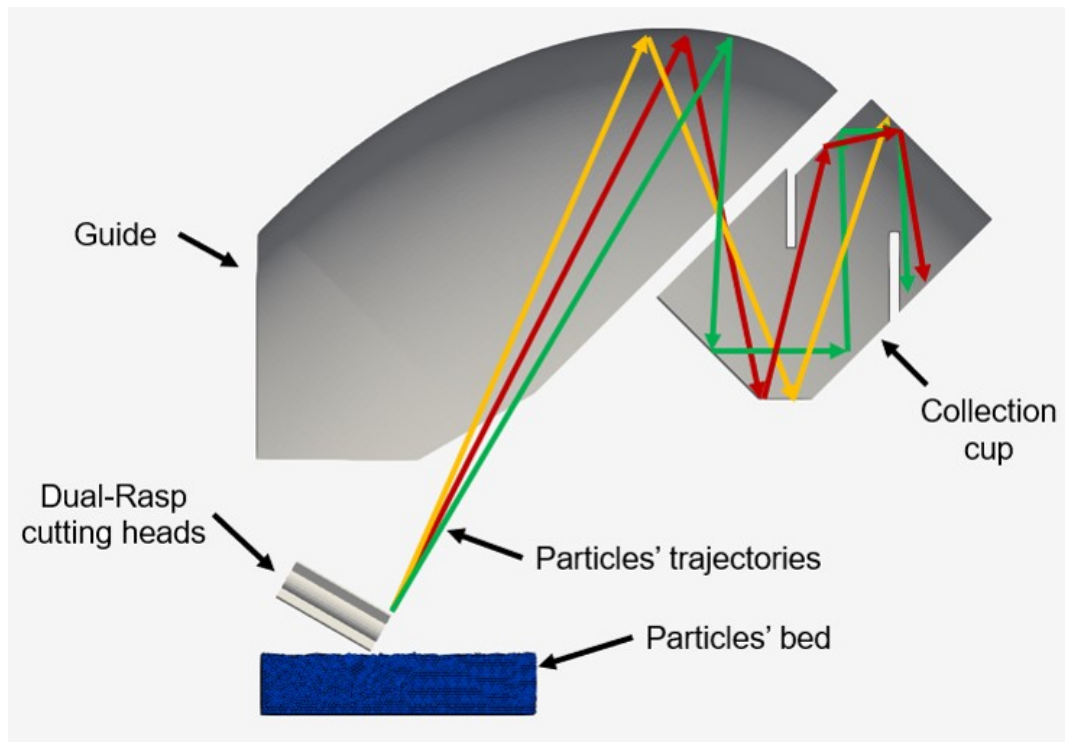


**Figure 4.51** Concept #3 of collection cup design provided with labyrinth-style sample retention features. Potential particles' trajectories. Qualitative scheme.

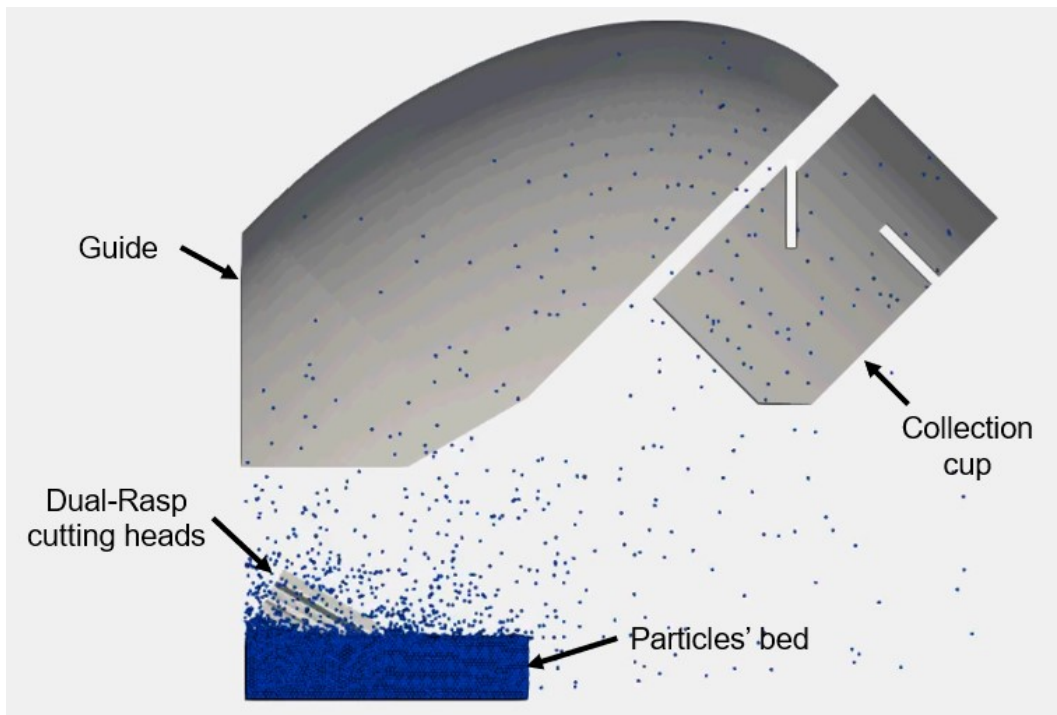


**Figure 4.52** Concept #2 of collection cup design provided with labyrinth-style sample retention features. DEM-MBD co-simulation.

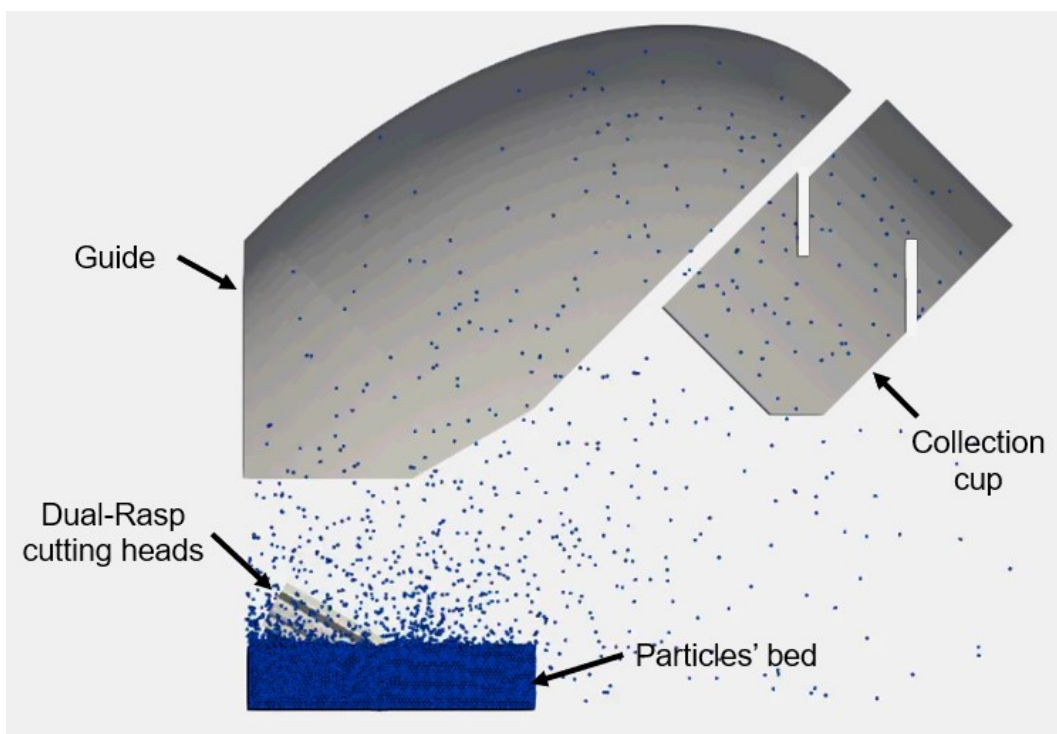


**Figure 4.53** Concept #3 of collection cup design provided with labyrinth-style sample retention features. DEM-MBD co-simulation.

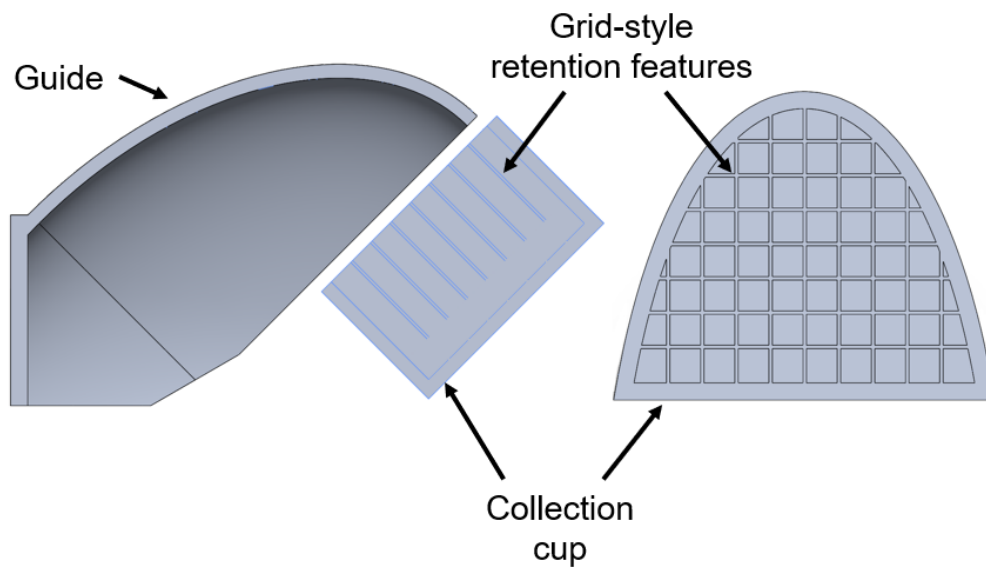


**Figure 4.54** Concept #4 of collection cup design provided with grid-style sample retention features. Side view of the integrated design (left). Top view of the collection cup (right).

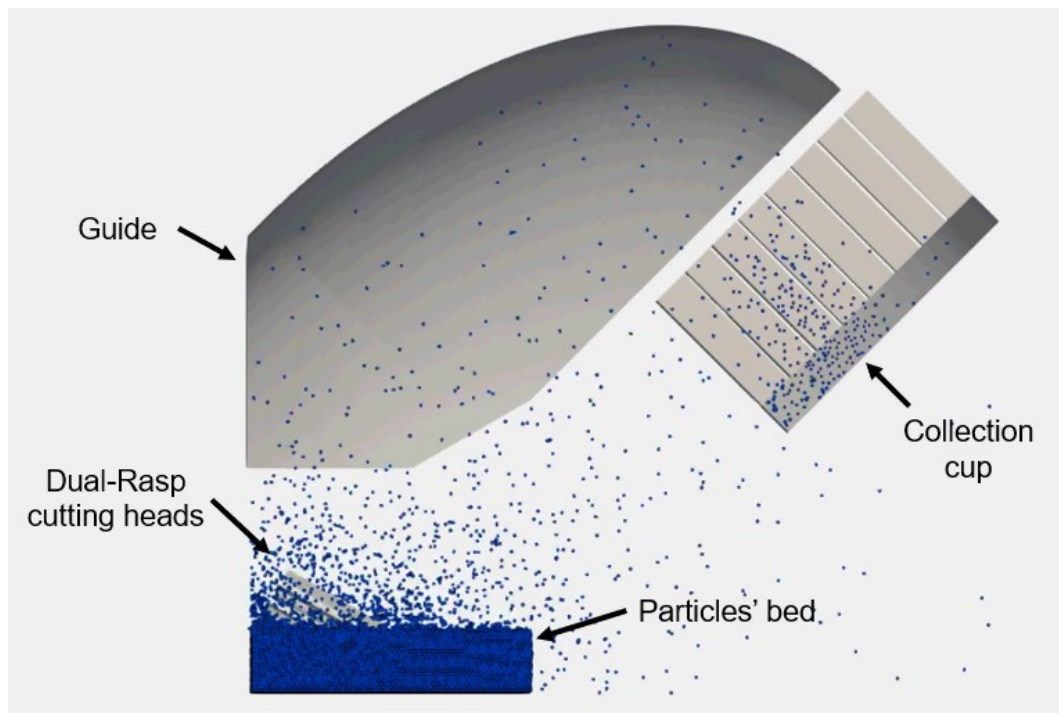


**Figure 4.55** Concept #4 of collection cup design provided with grid-style sample retention features. DEM-MBD co-simulation.

Promising simulation results led to the development and fabrication of an integrated sample collection system based on the Dual-Rasp sampling system, the ellipsoid-shaped guide, and the collection cup provided with grid-style sample retention features (Figure 4.56 and Figure 4.57).

A test campaign was performed in ground-based laboratory ambient conditions (i.e. 1g and 1 atm Earth's environment) to verify and mature the Dual-Rasp sampling system and the sample collection system to TRL 4. Several ambient analogue materials were used, covering the whole range of physical/mechanical properties considered for the design of the sampling system (Table 4.35). Test results, summarized in Table 4.36, showed good performances and versatility of the Dual-Rasp in sampling materials from weak loose to hard sintered.

Among loose analogue materials, the higher collection efficiency (i.e. about 45%) was achieved with BLC 110, a silica sand used as Mars analogue. Test results showed a good momentum transfer from Dual-Rasp cutting heads to particles, and a clear granular flow toward the guide, leading to collection into the cup. Minex 3, another silica sand analogue, showed a granular flow similar to BLC 110. However, a smaller collection efficiency (i.e. about 20%) was achieved, probably because particle's size of Minex is 10 times smaller than BLC 110. Therefore, the granular flow experience much more dispersion because of the effect of the atmospheric drag on particles' trajectories. YSZ and alumina showed a chaotic granular flow because of the high coefficient of restitution, resulting in a low collection efficiency of about 1%, improved to about 4% at lower Dual-Rasp rotational speed.

Among sintered analogue materials, all in the family of pervious concretes, the higher collection efficiency (i.e. 15-25%) was achieved with W-15-60b, W-15-80, and B-10-1. For W-15-60b and W-15-80, pervious concretes based on Wedron aggregates, test results showed larger cuttings being generated by the Dual-Rasp sampling action, as well as a good momentum transfer leading to higher granular flow average velocity. The Dual-Rasp was able to generate a granular flow with mostly uniform cutting's size and few larger particles. For B-10-1, a pervious concrete based on BLC 110 aggregates, test results showed a good collection efficiency with finer grains and no visible larger cuttings. For M-10-40, a pervious concrete based on Minex aggregates, a significant number of fine grains generated at the surface and dispersed into dust, resulting in about 9% of collection efficiency. This result was emphasized by the effect of the atmosphere drag on fine Minex grains. Only few larger cuttings ended into the cup. A similar result was obtained with M-15-60, a pervious concrete also based on Minex aggregates. The granular flow is mostly composed of finer grains slowed down by the atmospheric drag and dispersed in dust. Only larger cuttings tend to be collected into the cup.

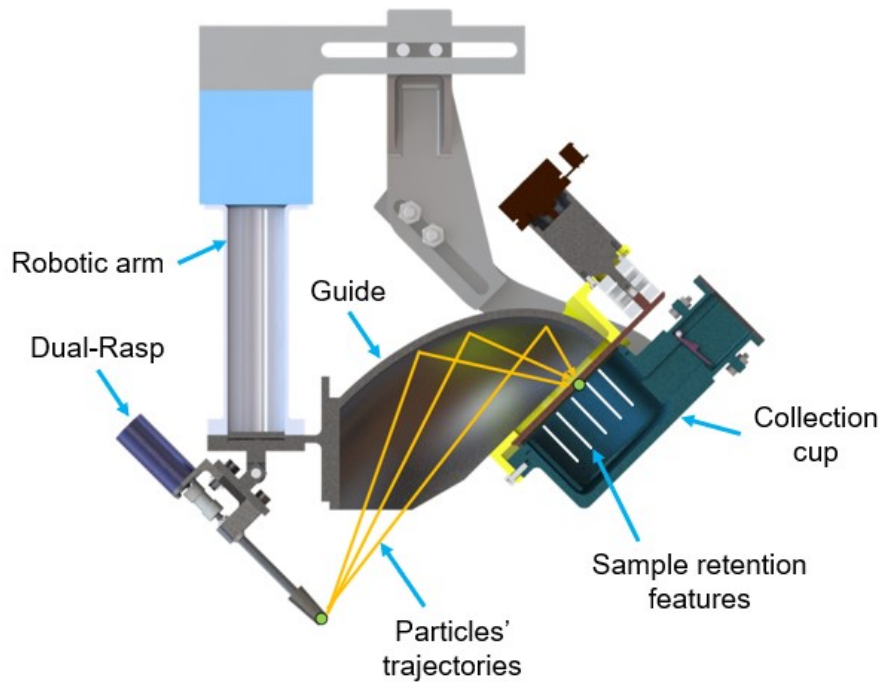


**Figure 4.56** Integrated CAD model of the sample collection system composed of the Dual-Rasp sampling system, the ellipsoid-shaped guide, and the collection cup provided with grid-style sample retention features.

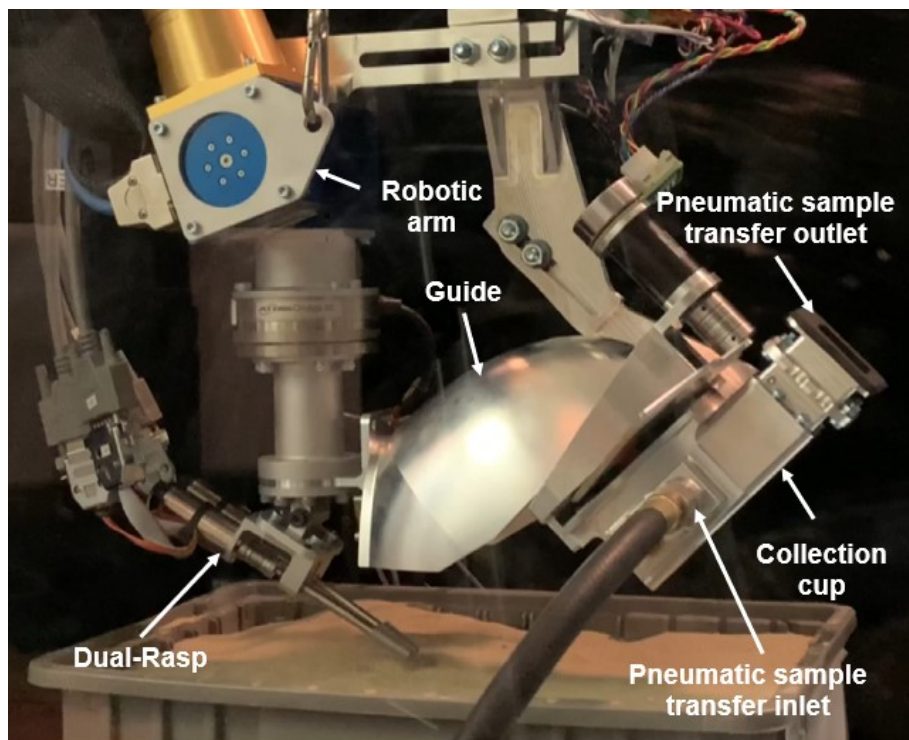


**Figure 4.57** Integrated prototype of the Dual-Rasp sampling system and the sample collection system composed of the ellipsoid-shaped guide and the collection cup. This prototype also integrates the pneumatic sample transfer system into the collection cup design (further details provided in paragraph 5.6).

**Table 4.35** Ambient analogue materials adopted for sample collection system verification campaign.

Material name	Bulk material state	Strength [MPa CPT]	Aggregate material	Grain shape	Grain size [ $\mu\text{m}$ ]
YSZ	Loose	N/A	Zirconia	Spherical	1000
Alumina	Loose	N/A	Aluminum oxide	Spherical	1000
BLC 110	Loose	N/A	Silica	Sub-rounded / Spherical	100
Minex 3	Loose	N/A	Silica	Sub-rounded / Spherical	10
M-15-60	Sintered	1 – 2	Minex 3	Sub-rounded	10
B-10-1	Sintered	1 – 2	BLC 110	Sub-rounded	50 – 100
M-10-40	Sintered	10 – 15	Minex 3	Sub-rounded	10
W-15-80	Sintered	10 – 15	Wedron	Sub-rounded	500 – 1000
W-15-60b	Sintered	30	Wedron	Sub-rounded	500

**Table 4.36** Results of sample collection system verification campaign.

Material name	Collected mass [g]	Collection efficiency [%]	Advantages	Disadvantages
YSZ	1.0 – 2.12	1 – 4	Model is based on hard, spherical particles	Particle motion is chaotic, too much energy
Alumina	0.3 – 1	/	Model is based on hard, spherical particles	Particle motion is chaotic, too much energy
BLC 110	4.6 – 6.2	45	Highest collection rate	Particle spread is high
Minex 3	0.37 – 0.46	20	/	Dust spreads everywhere

M-15-60	0.4	/	/	Too brittle, dust not collected, too low velocity
B-10-1	1.0 – 1.5	15 – 24	Larger particle size helps with distance	Does not clump together, so collected sample is fine
M-10-40	0.4 – 0.55	9	/	Too brittle, dust not collected, too low velocity
W-15-80	0.8 – 1.3	16	Larger particle size, more energy to reach the cup	/
W-15-60b	1.0 – 1.5	22 – 25	Larger particle size, more energy to reach the cup	/

### 4.3.3 Future work

A test campaign is planned to achieve the following objectives.

- To validate the DEM simulation model by comparing model predictions to experimental results obtained in the following conditions.
  - 1g Earth's gravity and vacuum conditions.
  - 1%g Earth's gravity (i.e. Enceladus' gravity) and vacuum conditions.
- To verify and mature the Dual-Rasp sampling system and the sample collection system to TRL 5 by performing experimental tests in 1%g Earth's gravity and vacuum conditions.

Earth's gravity condition can be easily achieved in ground-based laboratory testing, while Enceladus' gravity condition is achieved by performing parabolic flights. Parabolic flights are conducted by using aircrafts specifically adapted for this purpose. During a typical parabolic flight, the aircraft follows a parabolic flight path relative to the center of the Earth (Figure 4.58). The flight starts by climbing at about 50 degrees pitch angle. While following this path, the aircraft lowers its nose and gradually reduces engine thrust such that the aircraft follows a



Preliminary tests performed in 1g Earth's environment at 0.05 atm and 1 atm ambient pressure show the Dual-Rasp cutting heads generating about 10  $\mu\text{m}$  size particles that are dispersed in the 1 atm conditions (Figure 4.61) but flow more directly to the guide in the 0.05 atm conditions (Figure 4.62), as expected.

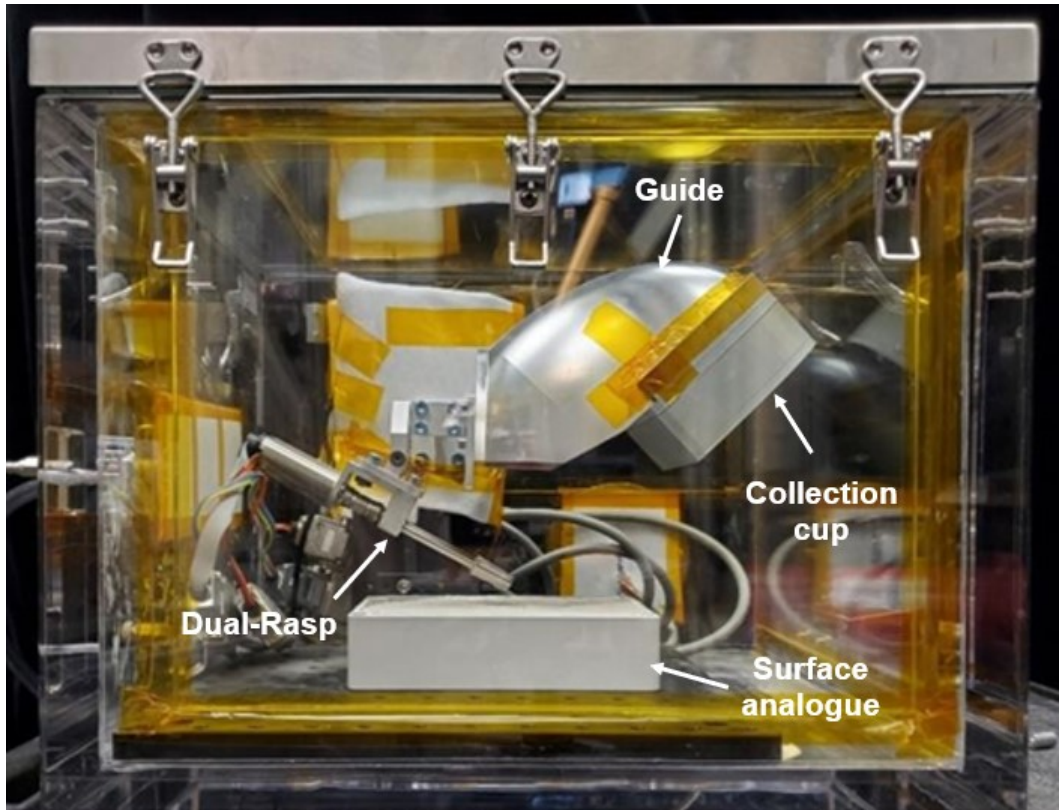


**Figure 4.59** Vacuum chamber testbed including Dual-Rasp sampling system, sample collection system and surface analogue.

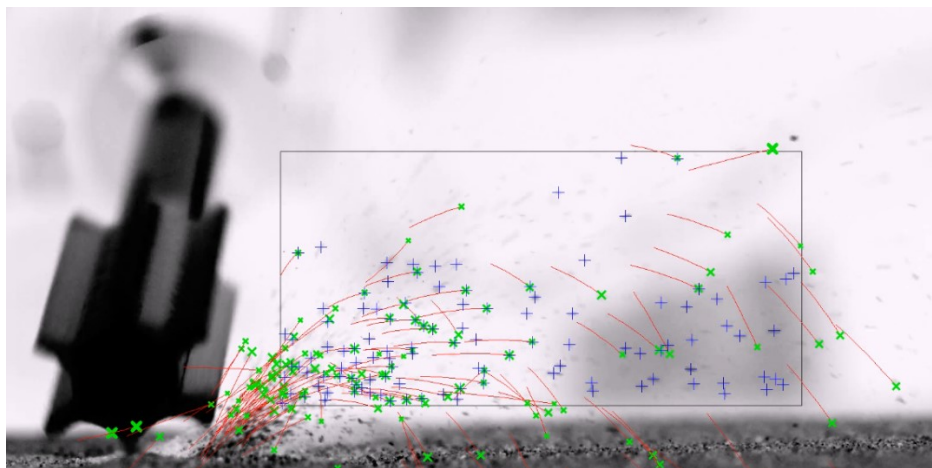


**Figure 4.60** Particle tracking software used for post-processing of high-speed recordings of the granular flow generated by a single Dual-Rasp cutting head. Particles are identified by green cross symbols, while particles' trajectories are identified by red lines.



*Figure 4.61* Sample transport of approximately  $10\ \mu\text{m}$  particles in 1 atm conditions.

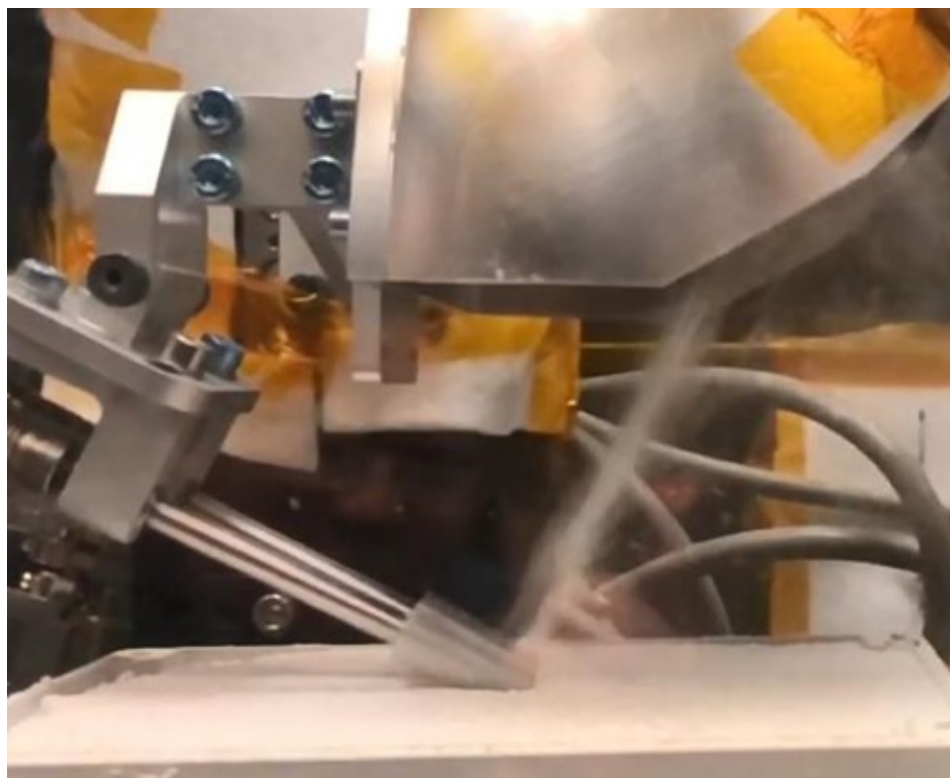


*Figure 4.62* Sample transport of approximately  $10\ \mu\text{m}$  particles in 0.05 atm conditions.

Figure 4.63 shows the vacuum chamber test setup for parabolic flight. Test plan includes performing sampling of three different surface analogues, whose samples are collected into three separate collection cups. The Dual-Rasp sampling system and the guide are bolted together, while the collection cups are separately mounted on a tray suspended on vertical springs. During sample acquisition, the vertical linear actuator plunges the Dual-Rasp into the surface analogue. Consequently, the guide follows the Dual-Rasp motion by pushing the collection cup that complies to the vertical motion by compressing the springs. Once the sample acquisition is completed, the vertical linear actuator moves to the starting position and the horizontal linear actuator moves the Dual-Rasp and the guide to the next surface analogue and collection cup. Sample acquisition operations are recorded from outside the vacuum chamber by using high-speed cameras. For this reason, half-cups were introduced with the aim to enable direct observation and recording of sample collection and retention inside the collection cups.

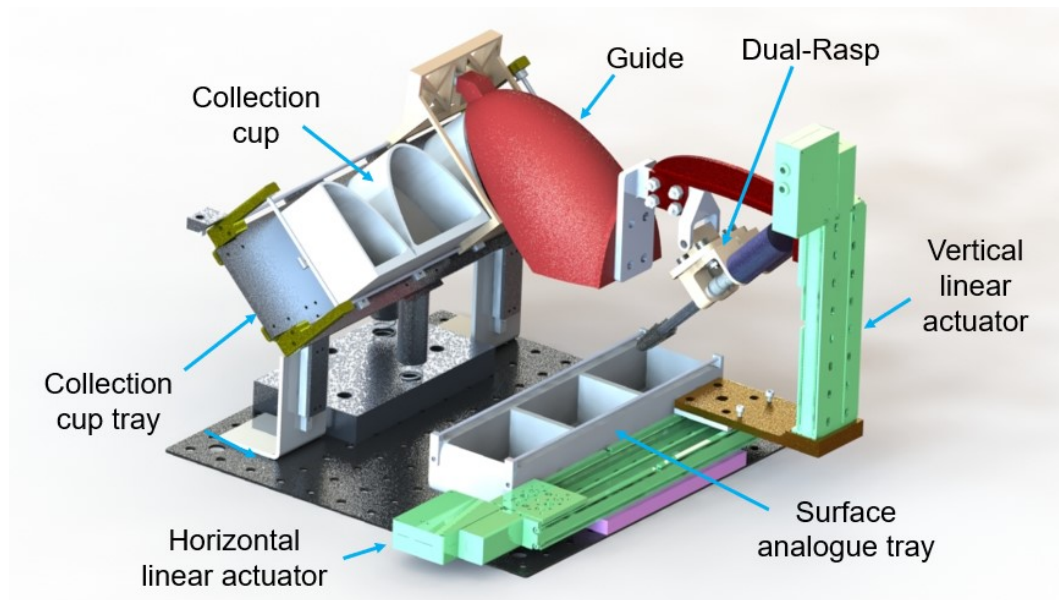


**Figure 4.63** CAD model of vacuum chamber testbed for parabolic flight. Testbed includes the Dual-Rasp sampling system, the sample collection system, and the surface analogues. Vacuum chamber surrounding the assembly not shown for convenience.

#### 4.4 Ultrasonic scoop sampling system

As presented in paragraph 3.6, the ultrasonic scoop sampling system is a piezoelectric-driven device capable to collect a predefined volume of sample and requiring 1 DOF for operation. The end-effector tool consists of a scoop with curved geometry (Figure 4.64). Sampling and sample collection operations include the deployment of ultrasonic scoop to a surface by using the RA, followed

by the activation of piezoelectric actuator while the scoop is driven along a circular path by RA wrist joint to achieve sample excavation and collection. Once sampling process is completed, the RA follows a succession of predefined movements to move the ultrasonic scoop to the delivery location for sample deposit. This can be achieved by scraping to remove collected sample material from the scoop or by activating piezoelectric actuator at a lower power level to ease the sample separation from the scoop.

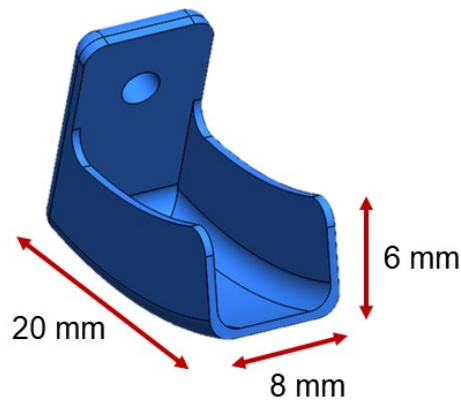


*Figure 4.64 CAD model of curved scoop.*

#### 4.4.1 Analysis method

DEM-MBD co-simulations were performed to investigate the effect of 1%g Enceladus environment on granular material dynamics while performing sample chain operations, from sampling to sample deposit. Worst-case scenarios were investigated in terms of unconstrained sample collection volume (i.e. the scoop collection volume is open during all sample chain operations) and loose material. Moreover, the effect of RA's vibrations in terms of acceleration disturbances was included.

Scoop motion during sample chain operations was discretized into four basic steps, namely scooping, ascend from surface, move to lander, deposit into science instrument chamber (Figure 4.65). DEM-MBD co-simulation were performed by using parameters defined in Table 4.37, Table 4.38, Table 4.39, Table 4.40.

Disturbances in terms of three-axial accelerations occurring during RA's motion were measured at scoop's location using IBARM while performing sample chain steps (Figure 4.66 and Table 4.41) with the goal to superimpose disturbances to basic scoop motions. To achieve so, measured acceleration disturbances were modeled as sine wave functions characterized by a peak amplitude/frequency equal to the value recorded during each motion step. Then,

acceleration disturbance functions were integrated to obtain position disturbance functions. Eq. (4.31) and Eq. (4.32) show acceleration and position functions, respectively. Simulated scoop motion was prescribed according to position functions resulting from superimposition of basic motion and RA's disturbances.

$$a(t) = A \sin(\omega t + \phi) \quad (4.31)$$

$$p(t) = -\frac{A}{(2\pi f)^2} \sin(\omega t + \phi) \quad (4.32)$$

Where

$a(t)$  Acceleration disturbance as function of time

$p(t)$  Position disturbance as function of time

$A$  Amplitude

$f$  Frequency

$\omega$  Angular frequency

$\phi$  Phase

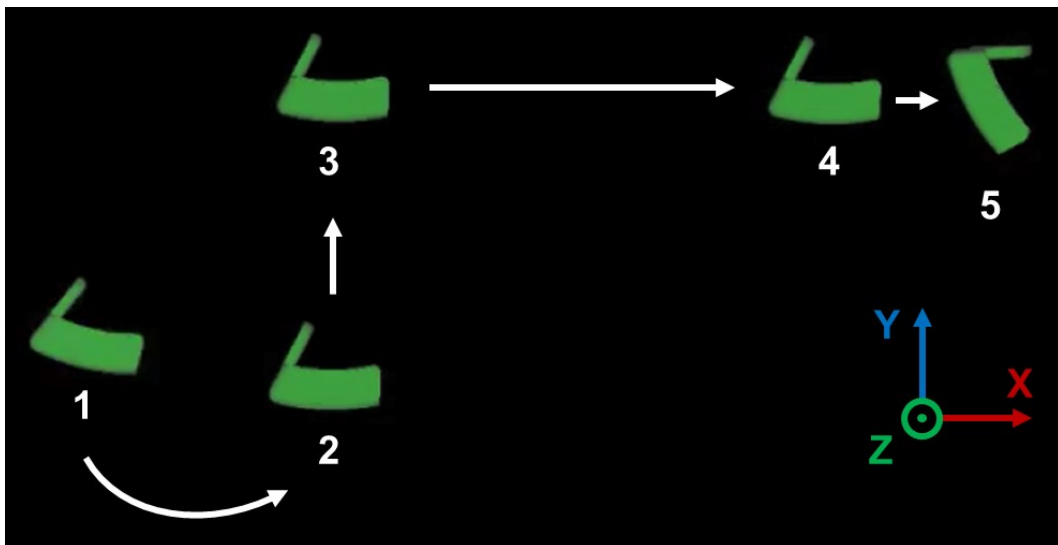


**Figure 4.65** Basic scoop motion steps. Scooping (1-2), ascend from surface (2-3), move to lander (3-4), and deposit into science instruments (5).

**Table 4.37** Computation parameters for DEM-MBD co-simulation of ultrasonic scoop sample chain steps.

DEM computation parameters	
Integrator	NVE
Time step	0.5e-05 s
Number of steps	5.8e+06
Simulation time	29 s
Contact models	<ul style="list-style-type: none"> <li>• Hertz-Mindlin (normal/tangential contact)</li> <li>• EPSD2 (rotational contact)</li> </ul>

**Table 4.38** Parameters of the ultrasonic scoop and environmental parameter for DEM-MBD co-simulation of ultrasonic scoop sample chain steps.

Parameters of ultrasonic scoop	
<b>Geometry</b>	Curved scoop
<b>Geometrical features</b>	<ul style="list-style-type: none"> <li>• Height: 6 mm</li> <li>• Length: 20 mm</li> <li>• Width: 8 mm</li> </ul>
<b>Prescribed motion</b>	<ul style="list-style-type: none"> <li>• Scooping               <ul style="list-style-type: none"> <li>○ Radius / span: 10 cm / 17 deg</li> <li>○ Angular speed: 2.5 deg/s</li> </ul> </li> <li>• Ascend from surface               <ul style="list-style-type: none"> <li>○ Span: 40 mm</li> <li>○ Linear speed: 10 mm/s</li> </ul> </li> <li>• Move to lander               <ul style="list-style-type: none"> <li>○ Span: 40 mm</li> <li>○ Linear speed: 10 mm/s</li> </ul> </li> <li>• Deposit               <ul style="list-style-type: none"> <li>○ Span: 40 deg</li> <li>○ Angular speed: 5 deg/s</li> </ul> </li> </ul>
<b>Material (Al 6061-T6)</b>	<ul style="list-style-type: none"> <li>• Young's modulus (<math>E_t</math>): 68.9 GPa [183]</li> <li>• Poisson's ratio (<math>\nu_t</math>): 0.33 [183]</li> </ul>
<b>Mesh</b>	<ul style="list-style-type: none"> <li>• Shell surface mesh</li> <li>• 1 mm element size</li> <li>• 3726 total nodes</li> <li>• 1857 total elements</li> </ul>

Environmental parameter	
Gravitational acceleration [Earth, 10% Earth's, Enceladus]	[9.81, 0.918, 0.113] m/s <sup>2</sup>

*Table 4.39 Particle parameters for DEM-MBD co-simulation of ultrasonic scoop sample chain steps.*

Particle parameters	
Shape / Shape distribution	Sphere / Monodisperse
Size / Size distribution	1 mm diameter / Monodisperse
Number of particles	187500
Size of particles' bed	<ul style="list-style-type: none"> <li>• Length: 125 mm</li> <li>• Width: 75 mm</li> <li>• Height: 30 mm</li> </ul>
Young's modulus ( $E_p$ )	0.1 GPa
Poisson's ratio ( $\nu_p$ )	0.35
Density ( $\rho_p$ )	3000 kg/m <sup>3</sup>

*Table 4.40 Paired parameters for DEM-MBD co-simulation of ultrasonic scoop sample chain steps.*

Paired parameters	
$pp$ coefficient of static friction ( $\mu_{s_{pp}}$ )	[0.1, 0.9]
$pt$ coefficient of static friction ( $\mu_{s_{pt}}$ )	[0.1, 0.9]
$pp$ coefficient of rolling friction ( $\mu_{r_{pp}}$ )	0.005
$pt$ coefficient of rolling friction ( $\mu_{r_{pt}}$ )	0.005
$pp$ coefficient of restitution ( $e_{pp}$ )	[0.1, 0.9]
$pt$ coefficient of restitution ( $e_{pt}$ )	[0.1, 0.9]

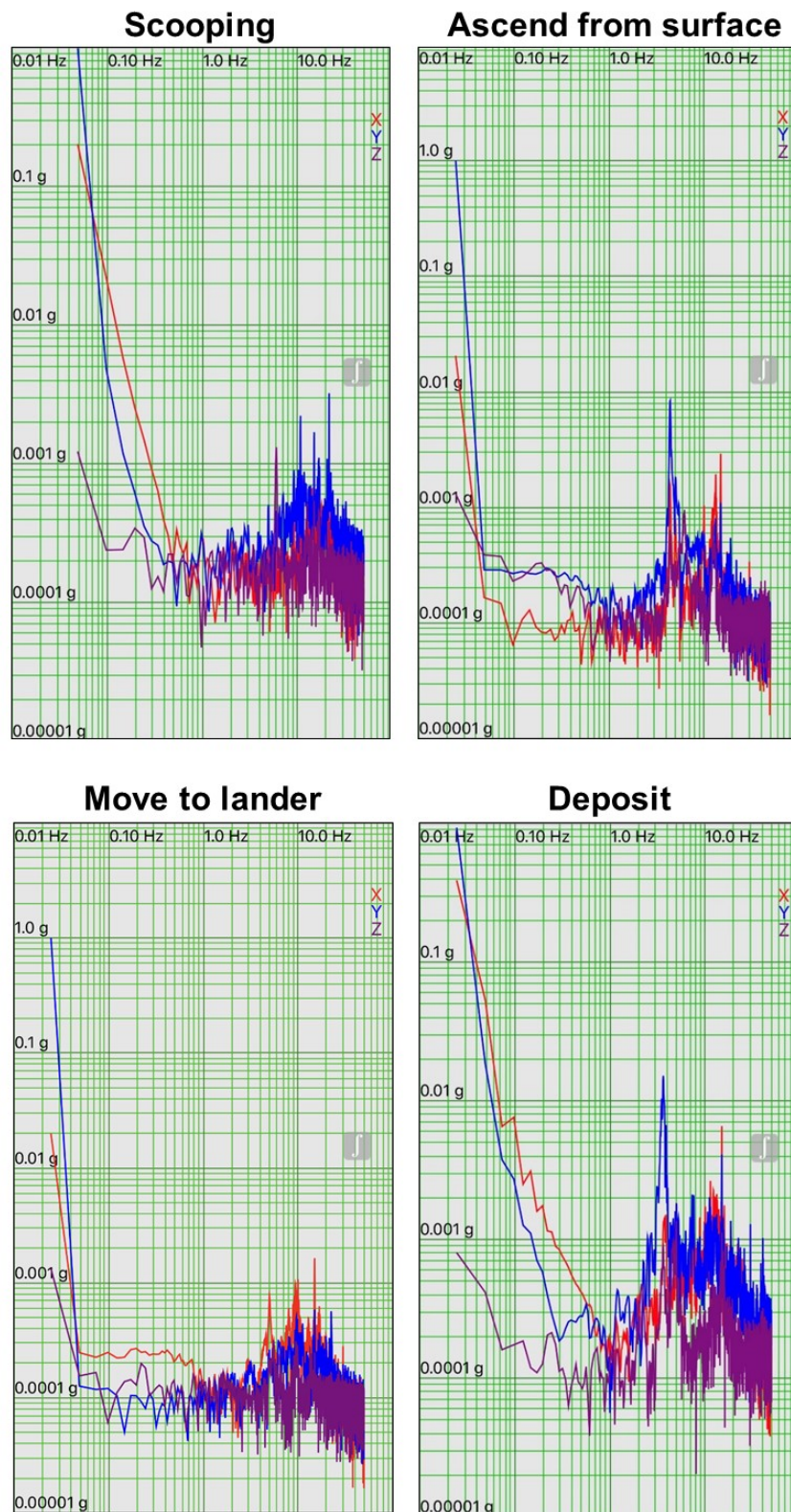


*Figure 4.66* Plots of acceleration disturbances measured at scoop's location using IBARM while performing sample chain steps.

**Table 4.41** Values of acceleration disturbances measured at scoop's location using IBARM while performing sample chain steps.

	Peak amplitude [g]	Peak frequency [Hz]	Main component
<b>Scooping</b>	0.0035	11	Y component
<b>Ascend from surface</b>	0.009	3.5	Y component
<b>Move to lander</b>	0.002	10	Y component
<b>Deposit</b>	0.015	3.5	X/Y component

Sample chain steps are simulated by prescribing scoop motion in terms of time-dependent position functions. Moreover, scoop position is defined by superimposing basic motions and position disturbances. Since measurements of disturbances were acquired in 1g Earth's environment, it is required to scale them to the desired gravitational acceleration. To do so, RA's dynamics was modeled by assuming that its stiffness  $k$  scales linearly with gravitational acceleration. It was also assumed that both RA's natural frequency  $f_n$  and frequency of disturbances  $f$  are proportional to the square root of RA's stiffness  $\sqrt{k}$ . Finally, frequency of disturbances depends on RA's natural frequency, which in turn depends on its stiffness. Specifically, natural frequency of IBARM corresponds to 3.5 Hz.

#### 4.4.2 Case studies

Three case studies were included in the analysis, depending on gravitational acceleration considered.

Case study 1 considers 1g Earth's gravity and related full RA's stiffness. Figure 4.67 shows resulting position disturbance functions at each sample chain step, defined as trapezoidal functions to guarantee smooth amplitude changes. Along Y direction (i.e. vertical direction), DPS (deposit) step is the most affected by RA's disturbances with a peak position amplitude of about 0.3 mm, followed by ASC (ascend from surface) step with a peak position amplitude of about 0.2 mm, while SCP (sampling) step is lightly affected. Along X direction (i.e. horizontal direction), DPS step is also significantly affected by RA's disturbances. Simulation results (Figure 4.68) showed that the effect of RA's disturbances on granular material dynamics is efficiently dampened by 1g Earth's gravity environment, resulting in an estimated total sample loss of less than 5%.

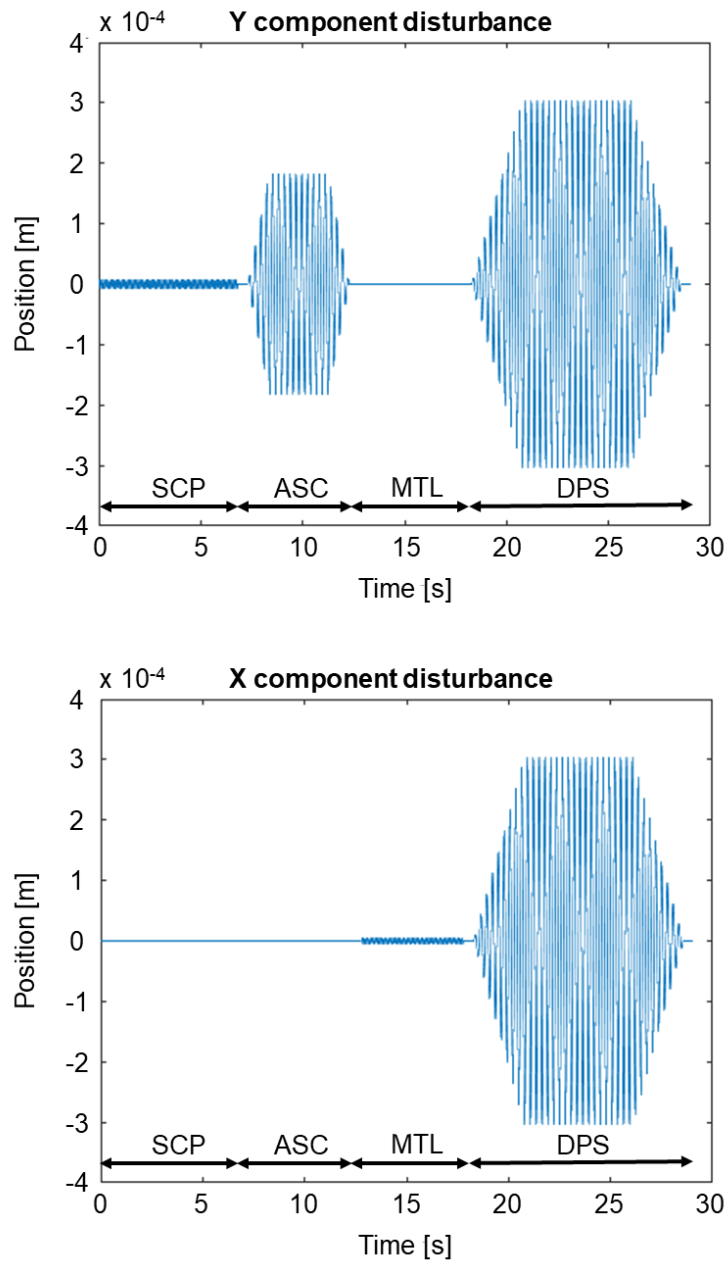


**Figure 4.67** Case study 1, 1g Earth's gravity and full RA's stiffness. Position disturbance functions shown at each sample chain step: scooping (SCP), ascend from surface (ASC), move to lander (MTL), and deposit (DPS).

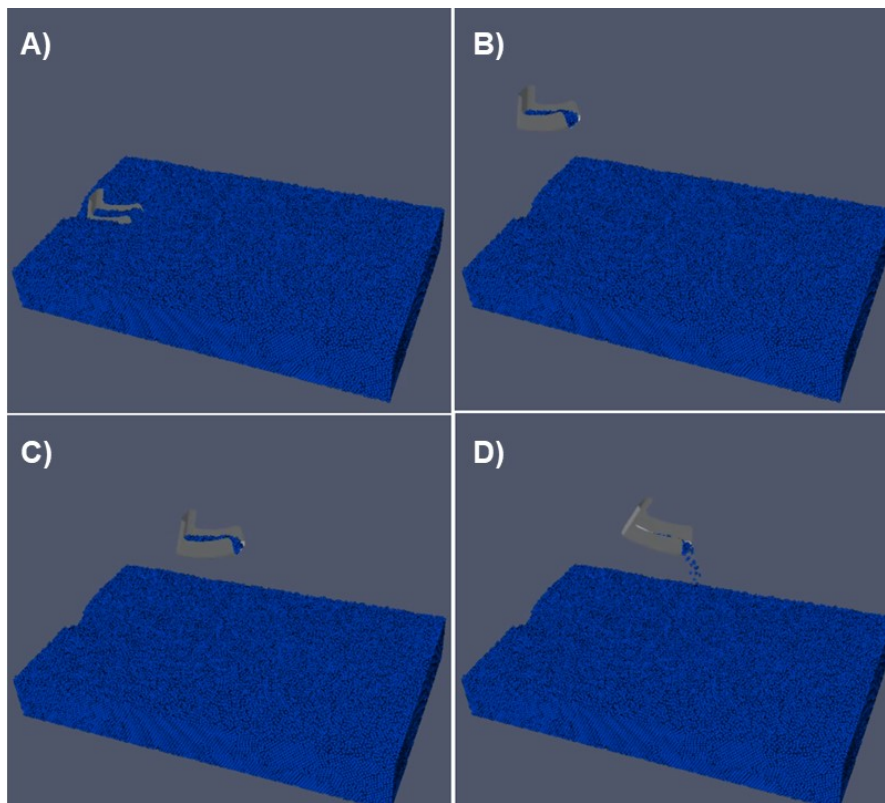


**Figure 4.68** Case study 1, 1g Earth's gravity and full RA's stiffness. DEM-MBD simulation of sample chain steps performed by the ultrasonic scoop is shown, including sampling (A), ascend from surface (B), move to lander (C), and deposit (D).

Case study 2 considers 10%g Earth's gravity and related 10% full RA's stiffness. Figure 4.69 shows resulting position disturbance functions at each sample chain step, defined as trapezoidal functions to guarantee smooth amplitude changes. As for case study 1, along Y direction (i.e. vertical direction) DPS (deposit) step is the most affected by RA's disturbances with a peak position amplitude of about 1.5 mm, followed by ASC (ascend from surface) step with a peak position amplitude of about 1 mm, while SCP (sampling) step is lightly affected. Both frequency and amplitude of position disturbances are affected by reduced RA's stiffness. Frequency of position disturbances reduced to about 30% full frequency, while amplitude increased of one order of magnitude with respect to case study 1. It should be noted that peak position amplitude along Y direction during DPS (deposit) step corresponds to 25% of total scoop's height. Along X direction (i.e. horizontal direction), DPS step is also significantly affected by RA's disturbances with a peak position amplitude of about 1.5 mm, corresponding to about 5% of total scoop's length. Simulation results (Figure 4.70) showed that RA's disturbances become relevant to granular material dynamics in a 10%g Earth's gravity environment, resulting in an estimated total sample loss of about 25%.

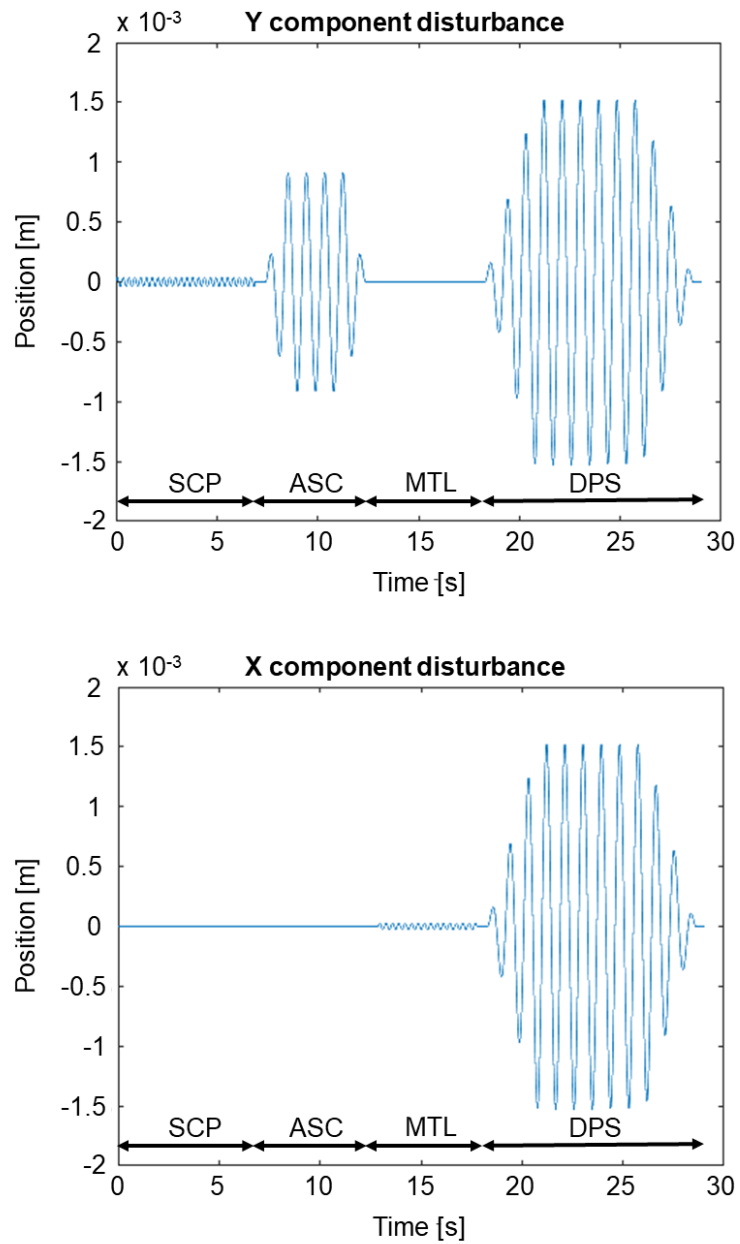


**Figure 4.69** Case study 2, 10%g Earth's gravity and 10% full RA's stiffness. Position disturbance functions shown at each sample chain step: scooping (SCP), ascend from surface (ASC), move to lander (MTL), and deposit (DPS).

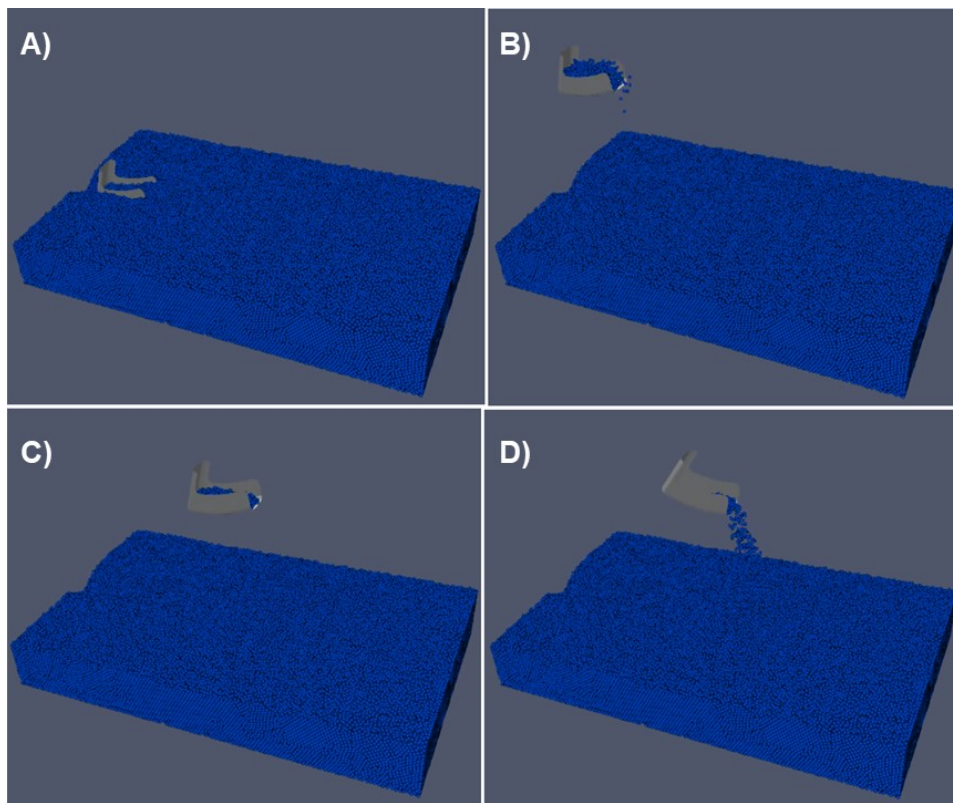


**Figure 4.70** Case study 2, 10%g Earth's gravity and 10% full RA's stiffness. DEM-MBD simulation of sample chain steps performed by the ultrasonic scoop is shown, including sampling (A), ascend from surface (B), move to lander (C), and deposit (D).

Case study 3 considers 1%g Earth's gravity (i.e. Enceladus conditions) and related 1% full RA's stiffness. Figure 4.71 shows resulting position disturbance functions at each sample chain step, defined as trapezoidal functions to guarantee smooth amplitude changes. As for case study 1 and case study 2, along Y direction (i.e. vertical direction) DPS (deposit) step is the most affected by RA's disturbances with a peak position amplitude of about 30 mm, followed by ASC (ascend from surface) step with a peak position amplitude of about 20 mm, while SCP (sampling) step is lightly affected. Both frequency and amplitude of position disturbances are affected by reduced RA's stiffness. Frequency of position disturbances reduced to about 10% full frequency, while amplitude increased of two orders of magnitude with respect to case study 1. It should be noted that peak position amplitude along Y direction during DPS (deposit) step corresponds to about 500% of total scoop's height. Along X direction (i.e. horizontal direction), DPS step is also significantly affected by RA's disturbances with a peak position amplitude of about 30 mm, corresponding to about 150% of total scoop's length. Simulation results (Figure 4.72) showed that RA's disturbances become dominant to granular material dynamics in a 1%g Earth's gravity environment, resulting in an estimated total sample loss over 95%.

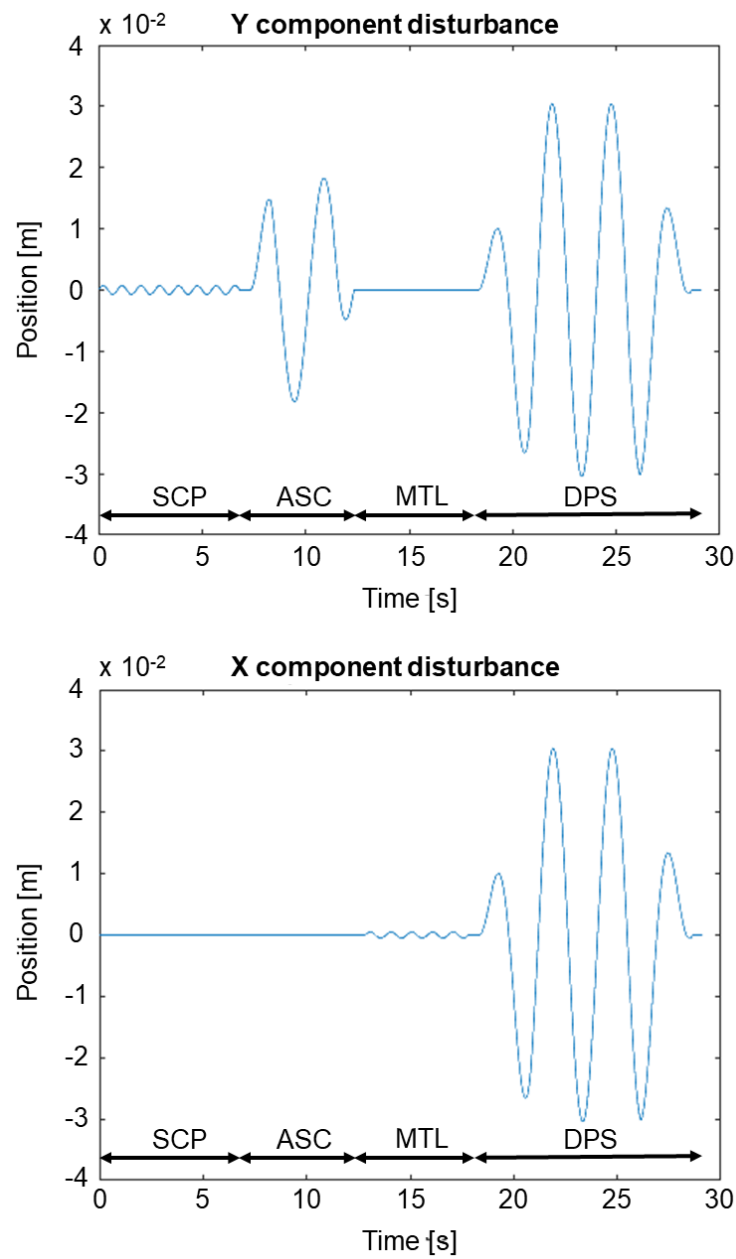


**Figure 4.71** Case study 3, 1%g Earth's gravity (i.e. Enceladus conditions) and 1% full RA's stiffness. Position disturbance functions shown at each sample chain step: scooping (SCP), ascend from surface (ASC), move to lander (MTL), and deposit (DPS).

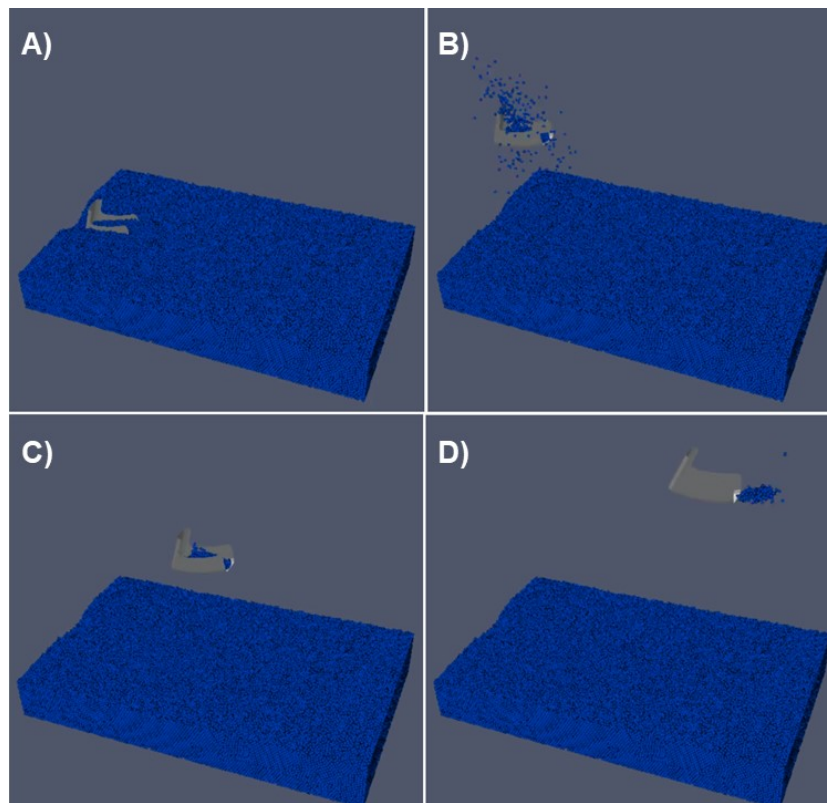


**Figure 4.72** Case study 3, 1%g Earth's gravity (i.e. Enceladus conditions) and 1% full RA's stiffness. DEM-MBD simulation of sample chain steps performed by the ultrasonic scoop is shown, including sampling (A), ascend from surface (B), move to lander (C), and deposit (D).

In conclusion, analysis of ultrasonic scoop in Enceladus gravity conditions indicated that there would be risk of particles bouncing away from the scoop during sample chain steps due to RA's accelerations. A relatively stiff arm and a potentially not achievable accurate motor acceleration control would be needed to prevent sample loss in a low gravity environment. Figure 3.12 shows the implementation of a lid to close sample collection volume during sample transfer to the lander, thus mitigating the risk of sample loss during sample transfer. However, collection volume must be opened during sample deposit step. Therefore, significant RA's disturbances during sample deposit step will still pose a risk of sample loss.

# Chapter 5

## 5 Investigation of sample transfer and deposit

Part of the content of the present chapter was published in [55] [84] [220].

### 5.1 Introduction

As introduced in chapter 3, the sample chain is typically composed of the following phases.

- *Sampling*, that is the operation of breaking up and/or disturbing the pristine material to get the sample.
- *Collection*, that is the operation of gathering the sample.
- *Transfer*, that is the operation of transporting the sample from one location to another.
- *Measurement*, that is the operation of measuring the quantity of sample collected in terms of mass, volume, etc.
- *Deposit*, that is the operation of delivering the sample to its destination (e.g. a science instrument, a storing capsule, etc.)

Chapter 4 focused on the analysis and development of sample collection system assuring the pristine sample extracted from the surface to be transported, collected, and retained into the collection cup. However, the collection cup is only a temporary storage since the sample must be transferred to its destination, represented by the science instrument. Since sample transfer aims to directly transport sample from collection cup to destination, transfer and deposit phases are merged. This chapter focuses on the challenges deriving from the need of performing the transfer/deposit phases of the sample chain in the low gravity environment found on Enceladus. Also, this chapter introduces current studies on concepts for sample measurement.

Past space missions made use of the local gravity for sample handling. The Mars Science Laboratory rover moves the robotic arm with respect to the gravity vector and adopts a combination of percussion and vibration mechanisms to transfer the sample powder from the drill to the instruments [88]. The Phoenix lander exploited the Mars gravity to deliver the sample collected to the instruments by just pouring it [96].

As shown by previous analyses, on Enceladus it is not possible to rely on gravity for sample handling. For this reason, other strategies must be considered. One of the emerging and most promising methods for sample handling in low gravity environments is the use of pneumatics [221]. Such a method was successfully adopted by the OSIRIS-REx spacecraft to sample and collect loose material from the surface of the asteroid Bennu [86]. As a result, the interest about pneumatics and its advantages is increasing, as demonstrated by several proposals for potential future applications such as the PlanetVac concept utilizing a pneumatic system for sample acquisition and delivery [222], and the P-Sampler for the Martian Moons eXploration (MMX) mission [223].

Pneumatics exploits a pressurized gas to move particles by using momentum transfer. In fact, a pressurized gas turns its energy into momentum when it is released into a lower pressure environment. Such a momentum can be transferred to the sample to make particles getting transported by the gas, thus generating a granular flow dispersed into the gas flow. Flow in disperse systems is widely used in the industry, e.g. in the production of chemicals [224] [225], pharmaceuticals [226] [227], food [228] [229], and in the treatment of minerals [230] [231] and wastes [232] [233].

This chapter introduces two approaches to the analysis of flow in disperse systems and presents the models developed to investigate the pneumatic transport of surface samples in the low gravity, vacuum, and cryogenic environment found on the Enceladus surface with the aim of providing guidelines for sample chain design. Pneumatic sample transfer system prototypes were subsequently built and tested to evaluate feasibility and mature technology.

## 5.2 Approach

Two main approaches can be identified in the literature to address the complexity of flow in disperse systems. The empirical approach is the most common and is characterized by the definition of correlations based on the evaluation of experiments and empirical data. On the other hand, the theoretical approach is based on fundamental physics governing flow phenomena in disperse systems.

### 5.2.1 Empirical approach

The empirical approach is characterized by the definition of correlations based on the evaluation of experiments and empirical data [199]. The pneumatic transport of granular solids is generally classified into two flow regimes: dilute phase flow and dense phase flow. Dilute phase flow usually applies to short pipelines, and is characterized by high gas velocity, low solids concentration and low pressure drops. In these conditions, solid particles are fully suspended in the gas and fluid-particle forces dominate. On the other side, dense phase flow is characterized by low gas velocity, high solids concentration and high pressure drops. In these conditions, solids are not fully suspended and particle-particle forces dominate. The boundary between the two flow regimes is unclear and no universally accepted definitions are available. In this context, the choking and saltation velocities are used to define the boundary between dilute phase and dense phase transport in vertical and horizontal pipelines, respectively. Figure 5.1 shows the general relationship between gas velocity and pressure gradient for a vertical pneumatic transport at different solids feed rate  $G$ . At high gas velocity, the concentration is low, and frictional resistance between gas and pipe wall predominates. As the gas velocity decreases the frictional resistance decreases as well but, since the concentration of the solids increases, the static head required to support these solids increases. If the gas velocity is sufficiently low a fluidized bed starts forming in the transport line, marking the transition from a dilute phase flow to a dense phase flow in vertical pneumatic transport pipelines. The phenomenon is known as choking. At a given solids feed rate  $G$ , the lowest velocity at which a dilute phase transport can be achieved is called choking velocity  $U_{CH}$ . The higher is the solids feed rate, the higher is the choking velocity.

An analytical model was developed to characterize the flow in disperse systems with the aim to support the integrated design of pneumatic systems to be tested and matured in laboratory ambient conditions. The model considers commonly used empirical correlations adopted to address the problem in the technological practice [234]. In particular, Eq. (5.1) and Eq. (5.2) were adopted to predict the choking condition [235] [236]. Eq. (5.1) and Eq. (5.2) must be solved simultaneously by trial and error to determine  $\epsilon_{CH}$  and  $U_{CH}$ .

$$\frac{U_{CH}}{\epsilon_{CH}} - U_T = \frac{G}{\rho_p(1 - \epsilon_{CH})} \quad (5.1)$$

$$\rho_f^{0.77} = \frac{2250 D (\epsilon_{CH}^{-4.7} - 1)}{\left(\frac{U_{CH}}{\epsilon_{CH}} - U_T\right)^2} \quad (5.2)$$

Where

$\epsilon_{CH}$  Voidage or volume fraction occupied by the gas in the pipe at the choking velocity  $U_{CH}$

$\rho_p$  Particle density

$\rho_f$  Gas density

$D$  Pipe diameter

$G$  Mass flux of solids

$U_T$  Terminal velocity of a single particle in the gas

Figure 5.2 shows the general relationship between gas velocity and pressure gradient for a horizontal pneumatic transport at different solids feed rate  $G$ . At high gas velocity, all the solids are carried in very dilute suspension. As the gas velocity decreases, the solids start settle at the bottom of the pipe. The gas velocity at which this occurs is named saltation velocity  $U_{salt}$ , marking the boundary between dilute phase and dense phase flow regime. The higher is the solids feed rate, the higher is the saltation velocity. Eq. (5.3) was adopted to predict the saltation condition [237].

$$\frac{M_p}{\rho_f U_{salt} A} = \left( \frac{1}{10^{(1440 d + 1.96)}} \right) \left( \frac{U_{salt}}{\sqrt{g D}} \right)^{(1100 d + 2.5)} \quad (5.3)$$

Where

$M_p$  Mass flow rate of solids

$g$  Gravity acceleration

$A$  Cross section area of the pipe

Once choking and saltation velocities are determined it is possible to determine the flow rates of solids ( $M_p$ ) and gas ( $M_f$ ) by using the fundamental relationships governing the flow of gas and solids and represented by Eq. (5.4) and Eq. (5.5). Finally, the pressure drop can be expressed through Eq. (5.6), referring to a transport line segment of length  $L$  and inclined at an angle  $\theta$  with respect to the horizontal.

$$M_p = A U_p (1 - \epsilon) \rho_p \quad (5.4)$$

$$M_f = A U_f \epsilon \rho_f \quad (5.5)$$

$$\Delta p = \underbrace{\frac{1}{2} \epsilon \rho_f U_f^2}_{(1)} + \underbrace{\frac{1}{2} (1 - \epsilon) \rho_o U_p^2}_{(2)} + \underbrace{F_{fw} L}_{(3)} + \underbrace{F_{pw} L}_{(4)} + \underbrace{\rho_f L \epsilon g \sin \theta}_{(5)} + \underbrace{\rho_p L (1 - \epsilon) g \sin \theta}_{(6)} \quad (5.6)$$

The total pressure drop  $\Delta p$  is composed of several terms.

- (1) Pressure drop due to gas acceleration.
- (2) Pressure drop due to particle acceleration.
- (3) Pressure drop due to gas-to-wall friction.  $F_{fw}$  is the gas-to-wall friction force per unit volume of pipe.
- (4) Pressure drop related to solids-to-wall friction.  $F_{pw}$  is the solids-to-wall friction force per unit volume of pipe.
- (5) Pressure drop due to the static head of the gas.
- (6) Pressure drop due to the static head of the solids.

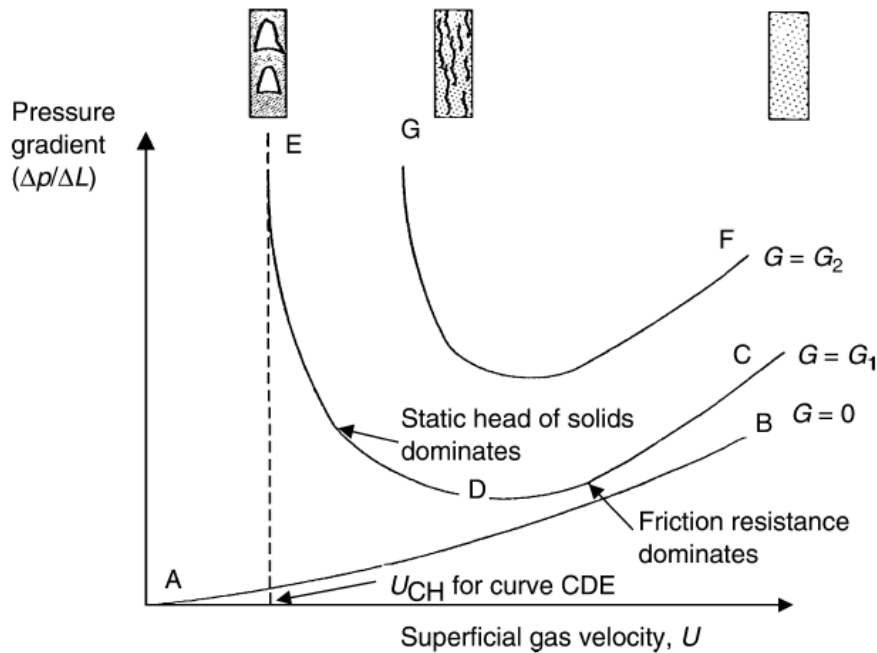


**Figure 5.1** Phase diagram for dilute phase vertical pneumatic transport [234].

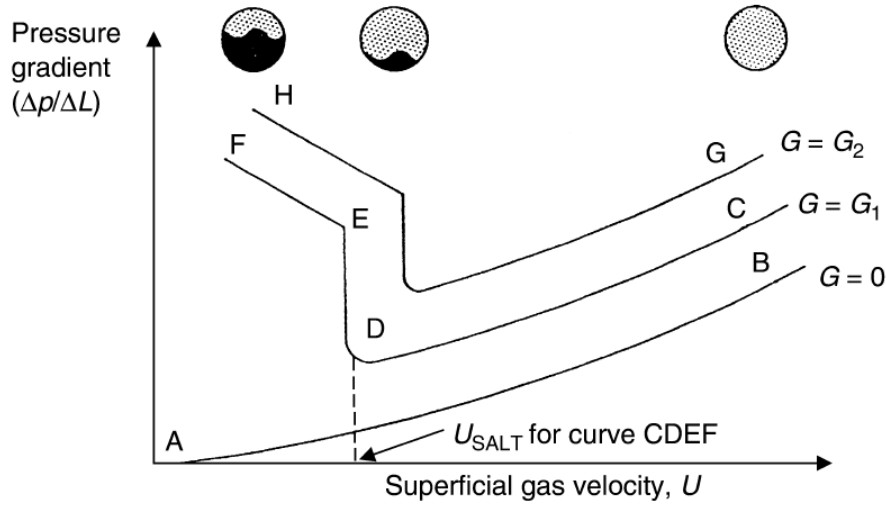


**Figure 5.2** Phase diagram for dilute phase horizontal pneumatic transport [234].

## 5.2.2 Theoretical approach

On the opposite extreme with respect to the empirical approach, the theoretical approach exploits the fundamental physics governing flow phenomena of disperse systems [238]. The aim is to define quantities, named non-dimensional parameters, and group of quantities, named non-dimensional groups, conceived to provide a generally valid representation of flow phenomena in disperse systems and which can be appropriately adapted to fit the specific problem of interest [239]. Non-dimensional groups arise from fundamental physics governing fluid-particle interaction. Considering a single particle suspended into a carrying fluid, forces and moments the fluid exerts on the particle can be represented by non-dimensional groups showed in Eq. (5.7) and Eq. (5.8). As a result, the motion of the center of gravity of a suspended particles can be defined through the non-dimensional groups showed in Eq. (5.9), taking into consideration also the influence of particle's rotation.

$$\frac{F}{\rho_f d_p^2 v_{rel}^2} = C_F \left( \frac{v_{rel} d_p}{v}; \frac{\omega_{rel} d_p}{v_{rel}} \right) \quad (5.7)$$

$$\frac{F}{\rho_f d_p^3 v_{rel}^2} = C_M \left( \frac{v_{rel} d_p}{v}; \frac{\omega_{rel} d_p}{v_{rel}} \right) \quad (5.8)$$

$$F_c \left\{ \frac{v_{rel}^2}{\left( \frac{\rho_s}{\rho_f} - 1 \right) d_p g}; \frac{v_{rel} d_p}{v}; \frac{\rho_s}{\rho_s - \rho_f} \frac{v^2}{L g}; \frac{\rho_f}{\rho_f} \left( \frac{L v_{rel}}{d_p v} \right) \right\} = 0 \quad (5.9)$$

Where

$C_F$  Force coefficient.

$C_M$  Moment coefficient.

$\rho_f$  Gas density.

$\rho_s$  Particle density.

$d_p$  Particle diameter.

$v_{rel}$  Magnitude of relative velocity between fluid and particle.

$\omega_{rel}$  Magnitude of relative angular velocity between fluid and particle.

$v$  Characteristic velocity of the flow field.

$L$  Characteristic length of the flow field.

$g$  Gravitational acceleration.

A step forward in the representation of flow in disperse systems is the introduction of multiple particles forming a bed. Three flow regimes are generally identified when a gas flow passes through a particles' bed. At low flow gas velocities, gravity force overcomes gas force, thus the bed remains fixed. At higher gas flow velocities, gas starts passing through voids between particles and gas forces start reacting to gravity, resulting in a gradually increasing separation between particles. At critical conditions, gas forces balance gravity and particles become suspended in the gas. In this state, a fluidized bed is created, and the solid/gas mixture behaves as a fluid. At higher gas flow velocities, gas forces dominate over gravity, thus particles are fully suspended and carried over by the gas.

The representation of the behavior of a fluidized bed can be given by the non-dimensional group shown in Eq. (5.10).

$$F_{fl} \left( \frac{3}{4} Fr \frac{\rho_f}{\rho_s - \rho_f}; Re; \frac{\rho_s}{\rho_f}; \epsilon \right) = 0 \quad (5.10)$$

Where

$Fr$  Froude number, defined as  $Fr = \frac{u^2}{d_p g}$

$Re$  Reynolds number, defined as  $Re = \frac{u d_p}{\nu}$

- $u$  Superficial gas velocity.
- $\nu$  Kinematic viscosity.
- $\epsilon$  Voidage or volume fraction occupied by the gas.

The introduction of the Froude number provides an important non-dimensional parameter weighting the contribution of inertial force and gravitational force. In particular, the Froude number determines the transition from a fixed bed exhibiting a particulate behavior, to a fluidized bed exhibiting a fluid behavior. Experiments showed that this limit is defined by  $Fr \approx 0.13$  [240]. Similarly, the Reynolds number is a non-dimensional parameter weighting the contribution of inertial force and viscous force.

The combination of non-dimensional parameters of Eq. (5.10) provides the characterization of flow regimes, resulting in the definition of flow state diagrams of disperse systems (Figure 5.3). The significance of Froude and Reynolds numbers makes them an ideal choice as non-dimensional parameters to define the flow state diagram (Figure 5.4). Moreover, in the technology practice the non-dimensional parameter  $\rho_s/\rho_f$  is not a true variable since it is usually restricted to a defined range i.e. 2 to 5 in the case of liquid-solid systems,  $(2 \text{ to } 5) \cdot 10^3$  in the case of gas-solid systems.

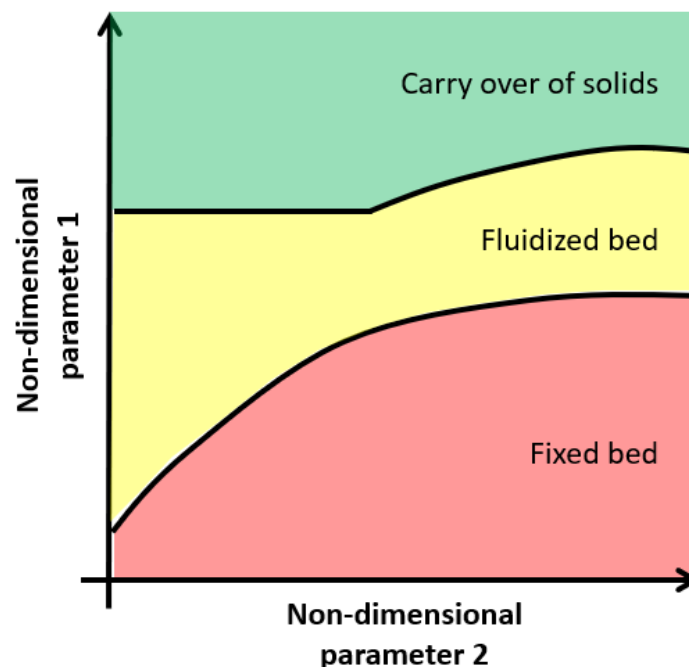


**Figure 5.3** Example of state diagram representing flow regimes in disperse systems and defined through the use of non-dimensional parameters.

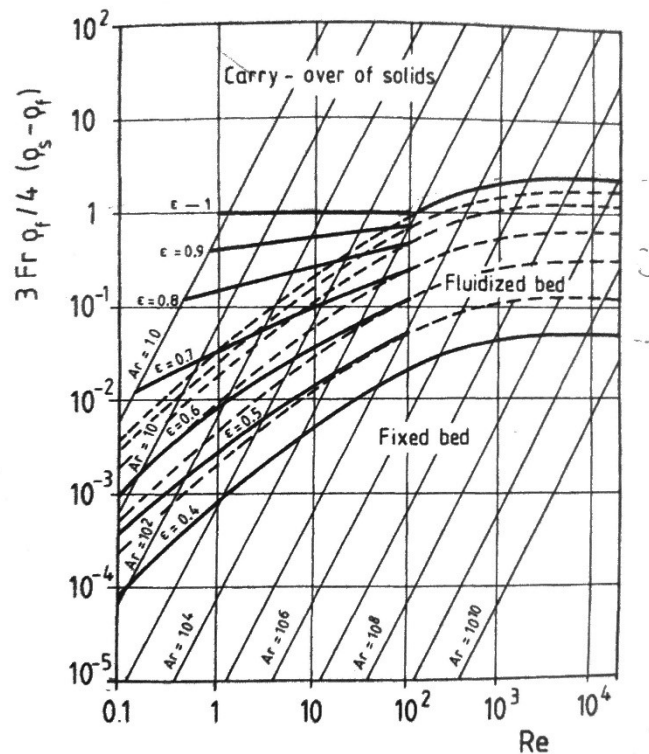


**Figure 5.4** Example of state diagram for liquid-solid and for non-pressurized gas-solid systems. The heavy solid lines represent gas-solid systems, while the heavy dotted lines represent liquid-solid systems [241].

### 5.3 Integrated sample chain testbed

A pneumatic sample transfer testbed was designed and integrated with the IBARM manipulation testbed to enable end-to-end demonstration of sample chain operations, including sampling from analogue surface material, sample collection, and transfer to a mock-up lander's deck provided with a science instrument chamber.

The same general pneumatic transport system architecture was devised for application to all sampling systems considered for the integration of pneumatic sample transfer capabilities (i.e. Full-face drill, Rasp, and Dual-Rasp). The pneumatic sample transfer system is composed of three main components: the pressurized gas tank, the sampling system, and the science instrument chamber. The gas tank provides storage for the pneumatic transfer medium. The sampling systems are attached as end-effector of the IBARM manipulation testbed and all integrate a collection chamber where the sample is temporarily stored while completing sampling operations. The science instrument chamber is the destination where the sample must be transferred to and is located on a mock-up lander's deck. Specific science instrument chambers and sealed docking interface

architectures were designed and integrated on the mock-up lander's deck to comply with the specific designs of the sampling systems. Moreover, docking interfaces do not require perfect seals.

Two specific architectures were developed for the pneumatic sample transfer system. Figure 5.5 shows the architecture adopted for both the Full-face drill and the Rasp sampling systems. In this architecture, the sampling system docks with the pneumatic sample transfer system in two points to close the pneumatic circuit, thus enabling pneumatic sample transfer. Figure 5.6 shows the architecture adopted for the Dual-Rasp sampling system. In this architecture, the pneumatic line carrying the gas and coming from the pressurized tank directly interfaces with the sampling system through a fixed connection. As a result, the sampling system must be only docked to the interface with the science instrument chamber to enable pneumatic sample transfer. Further details on these architectures will be provided in the following paragraphs.

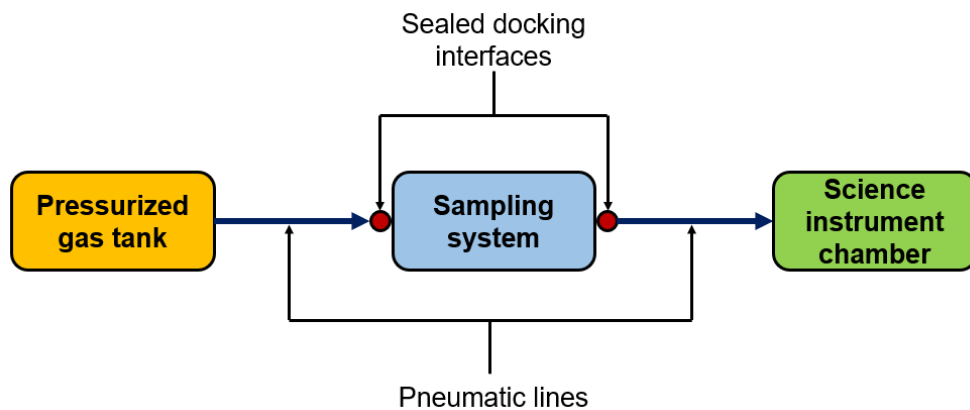


**Figure 5.5** Qualitative scheme of the pneumatic sample transfer system for both the Full-face and Rasp sampling systems. The sampling systems dock with the pneumatic sample transfer system in two points to close the pneumatic circuit.

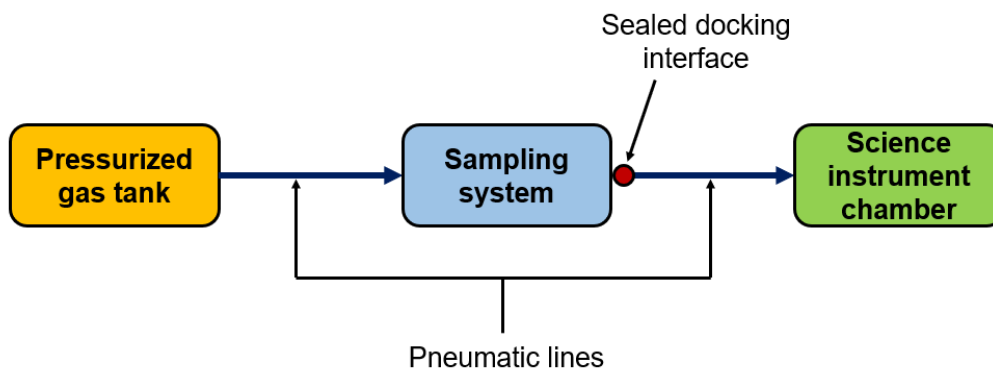


**Figure 5.6** Qualitative scheme of the pneumatic sample transfer system for the Dual-Rasp sampling system. The sampling system docks with the pneumatic sample transfer system only in one point to close the pneumatic circuit.

## 5.4 Sample transfer system applied to Full-face drill sampling system

As presented in paragraph 3.4, the full-face drill sampling system is a rotary hammer tool with a powder bit with full-face cutting ability that drives the cuttings toward the bit rotation axis and stores the cuttings inside the bit. The bit has a conical shape provided with a concave frontal face and the teeth placement follow an arc or parabola segment where the angle of the tangent to the locating curve with the central symmetry plane is proportional to the radial distance from the central axis.

Due to the low gravity environment on the surface of Enceladus, sample transfer cannot rely on simple dumping or pouring since sample would not tend to flow downwards and would just float around inside the collection chamber. Moreover, the Enceladus' gravity is sufficiently low that it cannot be relied upon to provide enough force to overcome small scale forces such as electrostatic and friction when attempting to transfer the material out of the collection chamber. Therefore, the bit was designed with integrated features to enable both sample collection and pneumatic transfer in a low gravity environment. Specifically, the bit was provided with a lid shaping the internal bit cavity for sample retention during sampling and subsequent pneumatic sample transfer (Figure 5.7).

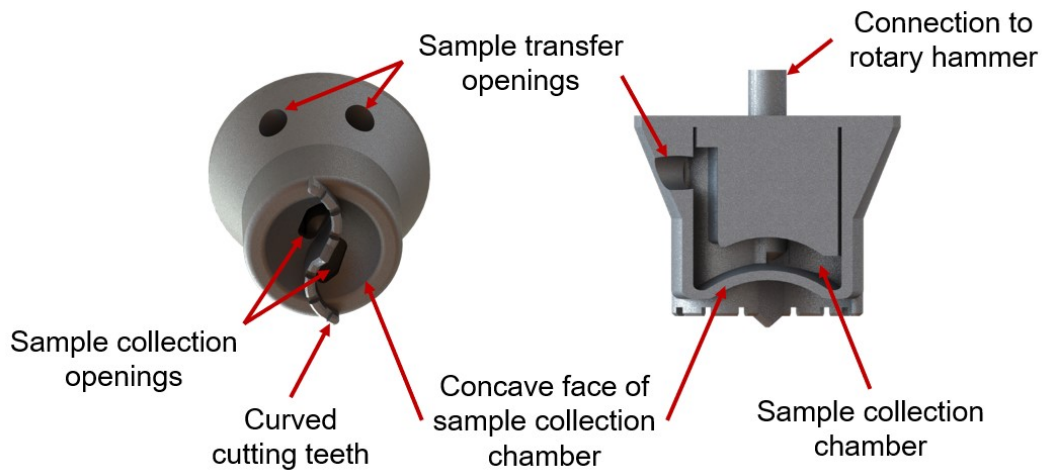


**Figure 5.7** Full-face drill sampling system with integrated pneumatic sample transfer features.

Once sampling and sample collection operations are complete, the IBARM moves the Full-face drill from sampling position to sample transfer position, thus docking the Full-face drill to the sealed docking interfaces on the mock-up lander's deck (Figure 5.8 and Figure 5.9). Figure 5.10 shows the pneumatic sample transfer system built. Docking operation is performed in a single step. The

IBARM pushes the Full-face drill against the bottom interface, provided with a cylindrical seal to host the conical body of the drill bit. This operation constraints the body of the drill bit and passively aligns the sample transfer openings on the drill bit with the side interface, thus closing the pneumatic circuit. As a result, the sample collection openings of the Full-face drill match the bottom interface and are exploited as gas inlet during pneumatic sample transfer. On the other end, the sample transfer openings of the Full-face drill match the side interface, shaped to aid transport of sample dispersed into the gas, thus closing the pneumatic circuit. Moreover, the side interface is directly connected to the science instrument chamber where the sample is delivered.

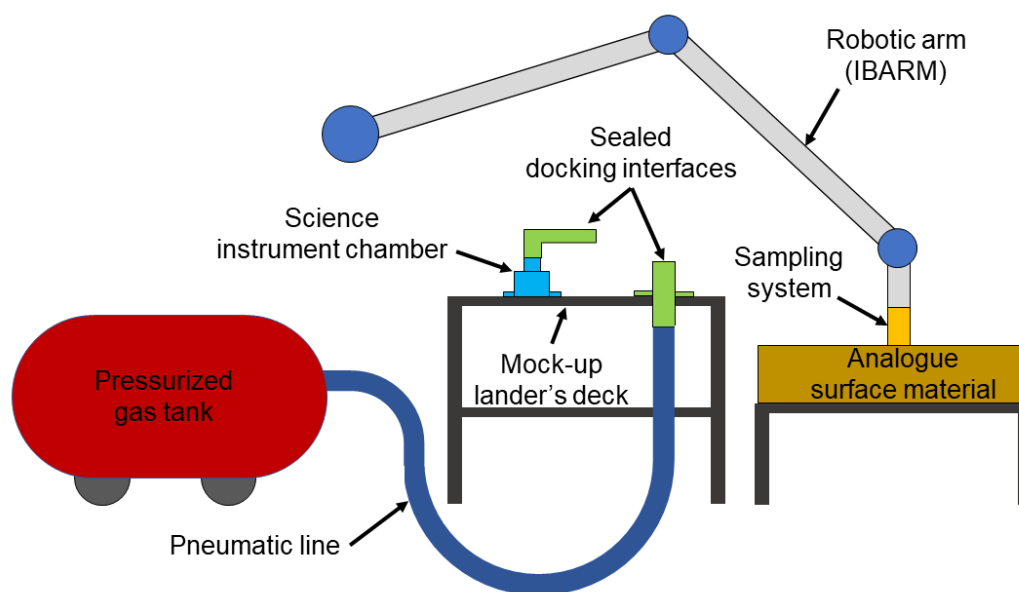


**Figure 5.8** Integrated sample chain architecture for Full-face drill sampling system. Sampling position shown. Qualitative scheme, not to scale.

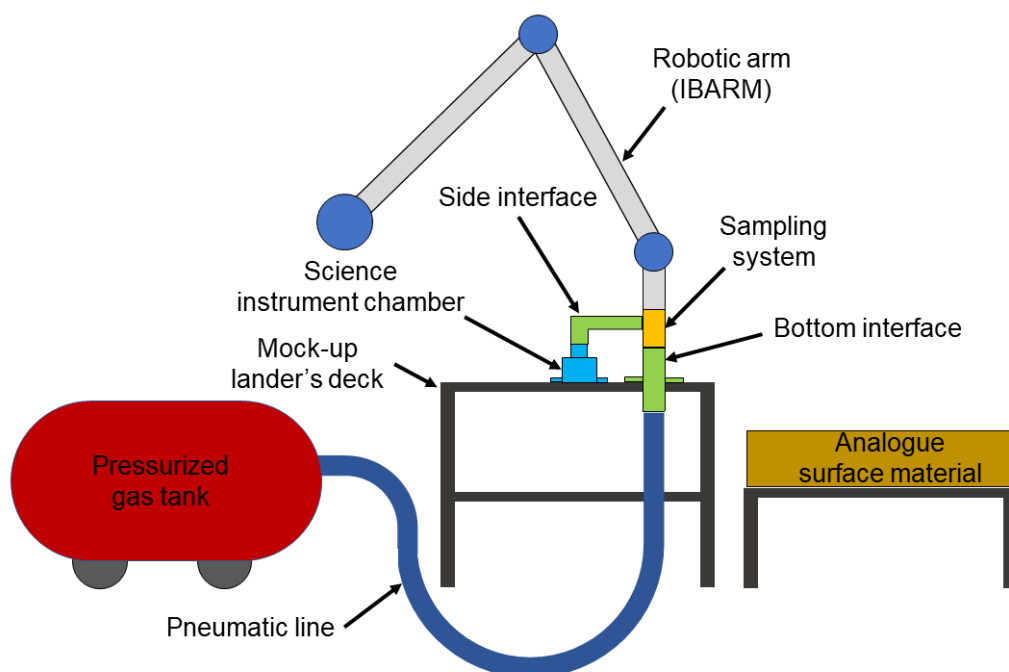


**Figure 5.9** Integrated sample chain architecture for Full-face drill sampling system. Sample transfer position shown. Qualitative scheme, not to scale.

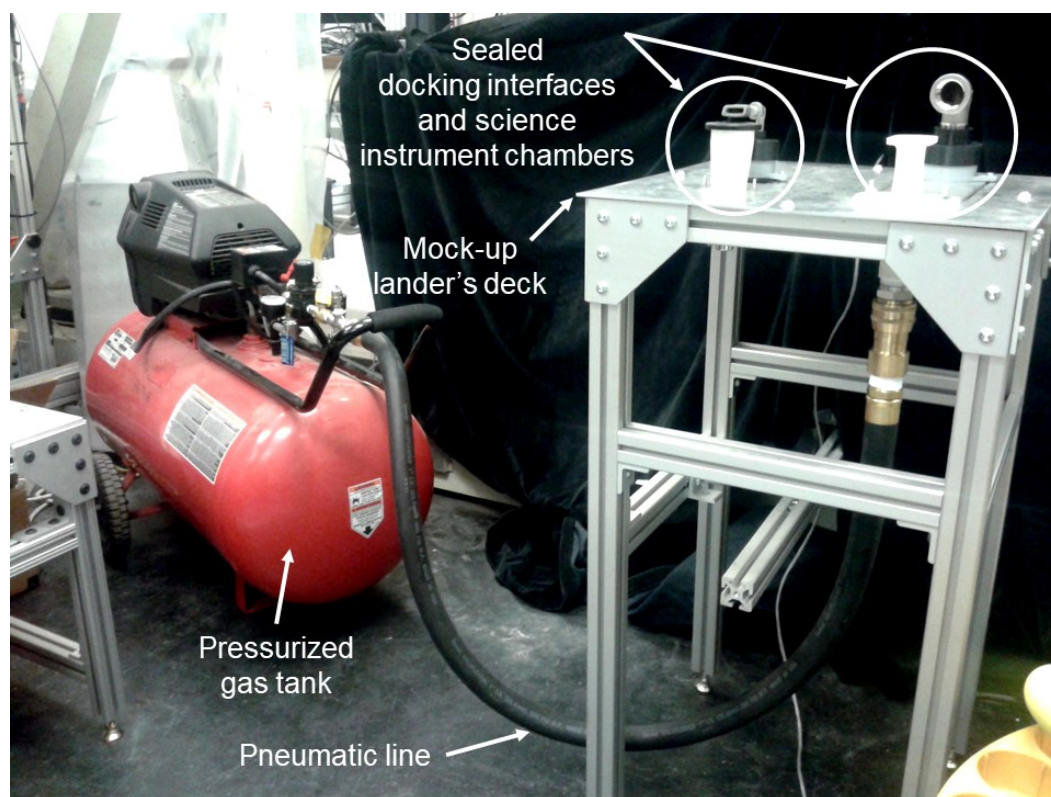


**Figure 5.10** Pneumatic sample transfer system within the integrated sample chain testbed. Configuration for Full-face drill and Rasp sampling systems shown. Robotic arm (IBARM) and sampling systems not shown.

Once docking operation is complete, the gas is released from the pressurized tank and is driven by the pneumatic line to the sample collection openings. Then, the gas enters the collection chamber of the Full-face drill where the sample is temporarily stored. A dispersion of solids into gas is thus created and the sample is transported along the pneumatic circuit, out of the collection chamber, through the sample transfer openings, and into the science instrument chamber, which is provided of venting holes and a filter to let the gas escape outside, still holding the sample inside (Figure 5.11).

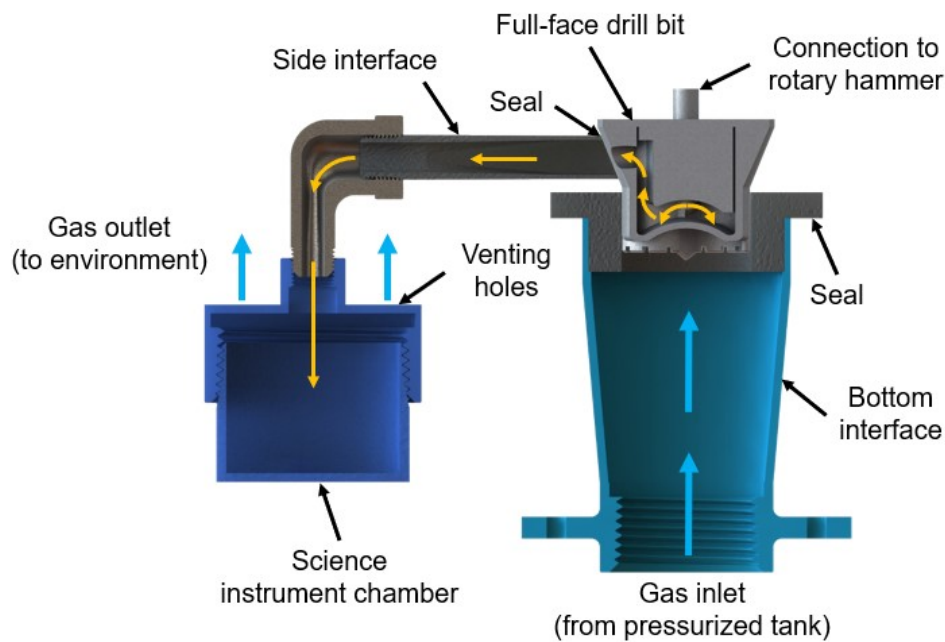


**Figure 5.11** Cross-section of pneumatic sample transfer system applied to the Full-face drill sampling system. Bold blue arrows represent the flow of gas, while bold orange arrows represent the flow of gas/solids mixture.

Since the case study under investigation considers low solids quantity (1 to 5 cm<sup>3</sup>) to be transported along a short route, a dilute phase flow regime was considered. The empirical model presented in paragraph 5.2.1 was adopted to support the preliminary design of the pneumatic sample transfer system.

The empirical model was included into a purposely developed software tool to enable rapid and integrated system's design iterations to determine the most suited configuration. Figure 5.12 shows the block diagram of the software tool developed to perform the iterative analysis and design process of the pneumatic sample transfer system. The resulting design was obtained by considering a trade-off among pressure losses, flow velocity required to achieve a dilute phase transport of sample, and physical and integration constraints. System's design includes a pipeline with an average inner diameter of 10 mm and composed of an

80 mm long horizontal flat conical section, a 50 mm long vertical circular section, and a single 90 deg bend.

The analysis of the pneumatic transport system was conducted for both Earth's and Enceladus' environment. For the Enceladus' environment, nitrogen was considered as medium for sample transport. In fact, the selected medium must be capable to sustain the gaseous phase also in the cryogenic and vacuum conditions found on the surface of Enceladus. Nitrogen is a viable solution for this application since its phase diagram confirms that it maintains the gaseous phase also under the pressure and temperature conditions under investigation (Figure 5.13). Table 5.1 summarizes the analysis results.

End-to-end sample chain operations, including sampling, sample collection and pneumatic transfer to the notional science instrument chamber located on the mock-up lander's deck, were successfully demonstrated for the Full-face drill sampling system (Figure 5.14) with the goal to mature the pneumatic sample transfer system to TRL 3. Main sample losses were observed at docking interfaces because of non-perfect seals, still assuring at least 75% pneumatic sample transfer efficiency.

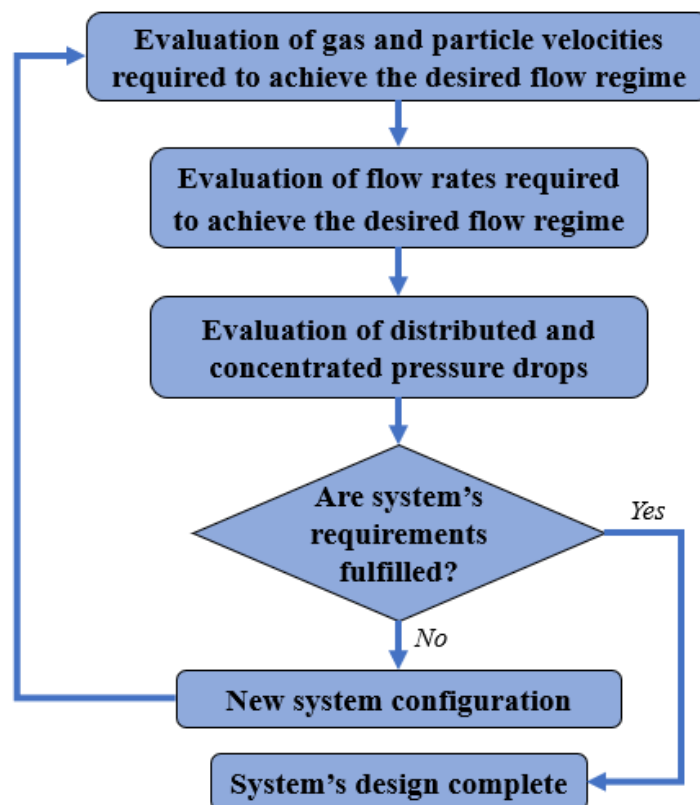


**Figure 5.12** Block diagram of the software tool developed for pneumatic sample transfer system analysis and design.

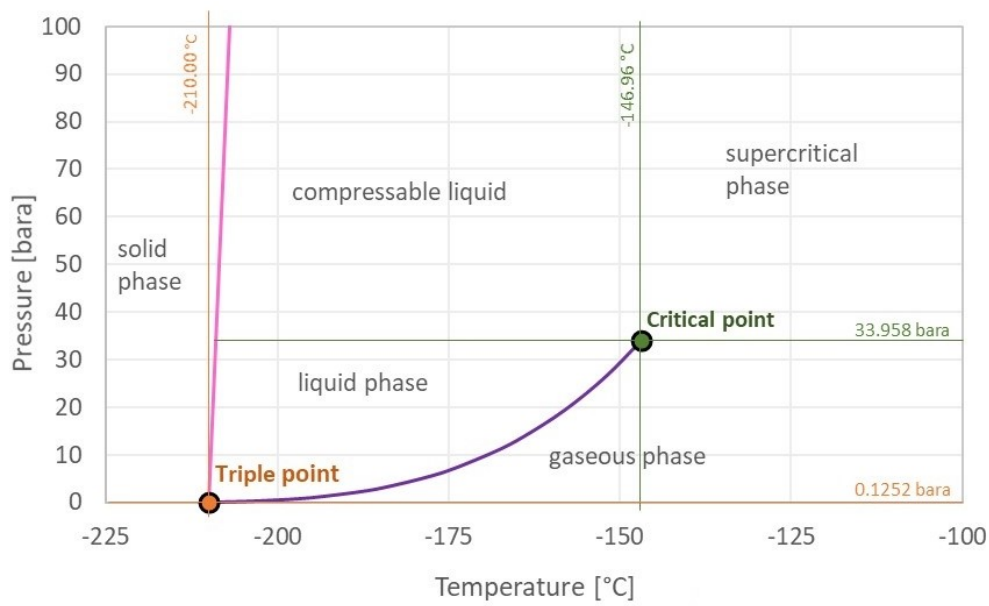


*Figure 5.13 Nitrogen phase diagram [242].*

*Table 5.1 Results of the analysis of TRL 3 pneumatic sample transfer system applied to the Full-face drill sampling system.*

		Earth's environment	Enceladus' environment
Gas	Medium	Air	Nitrogen
	Gravitational acceleration	9.81 m/s <sup>2</sup>	0.113 m/s <sup>2</sup>
	Temperature	293 K	100 K
	Tank pressure	10 atm	10 atm
	Regulator's outlet pressure	6.8 atm	2.7 atm
	Expected total pressure loss	1.5 atm	0.4 atm
	Volume flow rate	104 cm <sup>3</sup> /s	52 cm <sup>3</sup> /s
Solids	Particle diameter	500 μm	
	Particle density	2500 kg/m <sup>3</sup>	
	Mass flow rate	10 g/s	

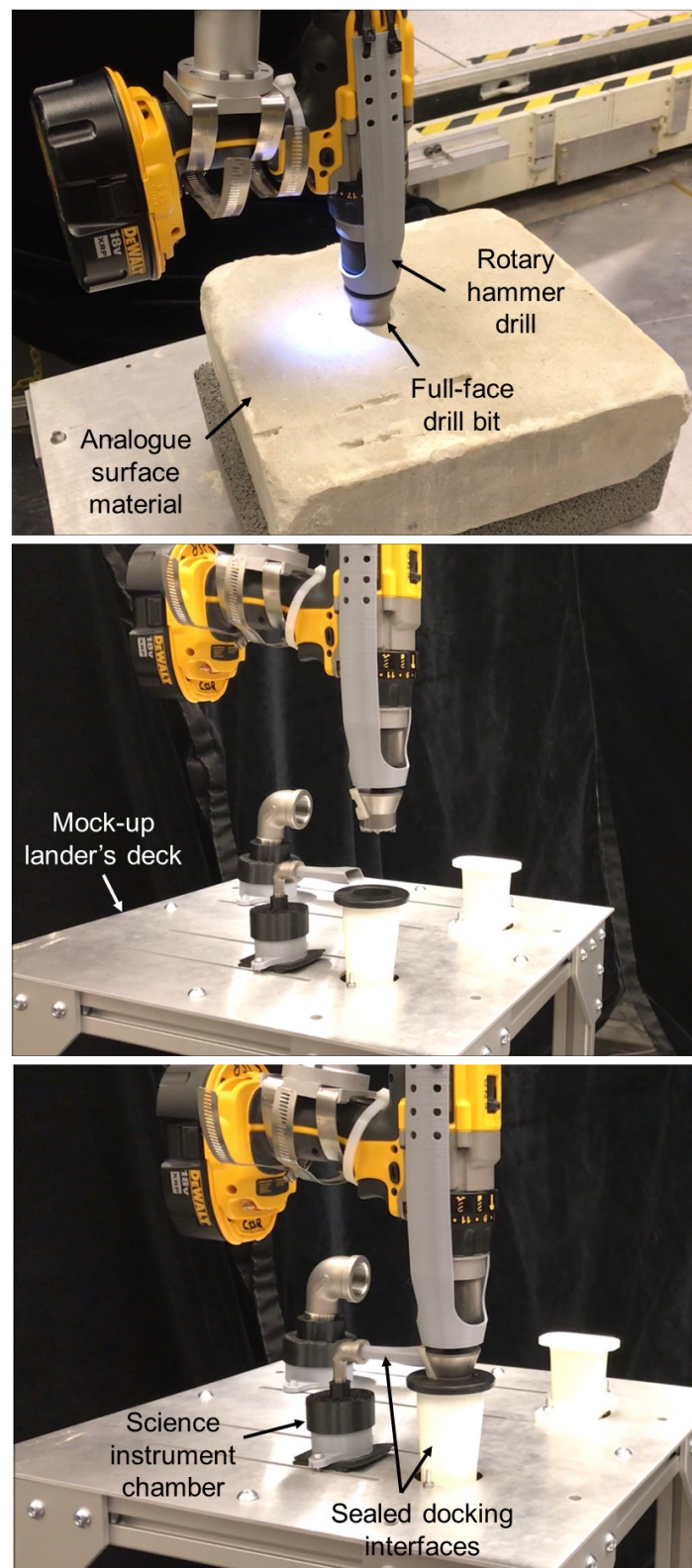


**Figure 5.14** End-to-end sample chain operations for the Full-face drill sampling system. Top picture shows Full-face drill in sampling position. Middle picture shows the Full-face drill in an intermediate position prior to completion of docking operation. Bottom picture shows the Full-face drill docked to sealed interfaces and in sample transfer position.

## 5.5 Sample transfer system applied to Rasp sampling system

As presented in paragraph 3.7, the Rasp is a rotary cutter-based sampling system that relies on high cutter rotational rates to impart momentum into cuttings that are flung into a sample collection chamber located immediately above the spinning cutter. The collected sample is then transferred from the collection chamber to its destination (i.e. the science instrument on the lander).

Also in this case, the Enceladus' gravity is sufficiently low that it cannot be relied upon to enable sample transfer by just dumping or pouring. Therefore, the Rasp sampling system was designed with integrated features to enable both sample collection and pneumatic transfer in a low gravity environment (Figure 5.15).

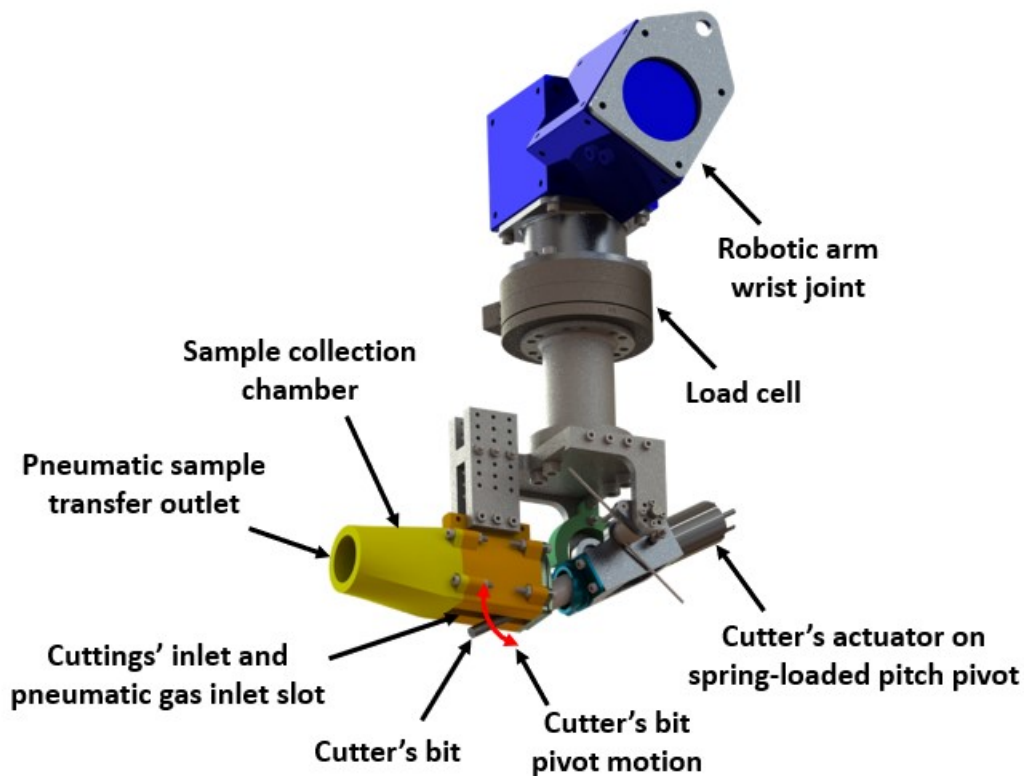


*Figure 5.15 Rasp sampling system with integrated pneumatic sample transfer features.*

Once sampling and sample collection operations are complete, the IBARM moves the Rasp from sampling position to sample transfer position (Figure 5.16 and Figure 5.17). As a result, the Rasp is docked to the sealed docking interfaces on the mock-up lander's deck. Docking operations are performed in two steps: first, the IBARM pushes the Rasp against the bottom interface to constrain the

vertical DOF of the robotic arm, then the IBARM pulls the Rasp against the side interface to constrain the horizontal DOF of the robotic arm. As a result, the cuttings' inlet of the Rasp matches the bottom interface and is exploited as gas inlet during pneumatic sample transfer. On the other end, the sample collection chamber of the Rasp matches the side interface and is shaped to aid transport of sample dispersed into the gas, thus closing the pneumatic circuit. Moreover, the side interface is directly connected to the science instrument chamber where the sample is delivered.

Once docking operations are complete, the gas is released from the pressurized tank and is driven by the pneumatic line to the cuttings' inlet. Then, the gas enters the Rasp's collection chamber where the sample is temporarily stored. A dispersion of solids into gas is thus created and the sample is transported along the pneumatic circuit, out of the collection chamber and into the science instrument chamber, which is provided of venting holes and a filter to let the gas escape outside, still holding the sample inside (Figure 5.18).

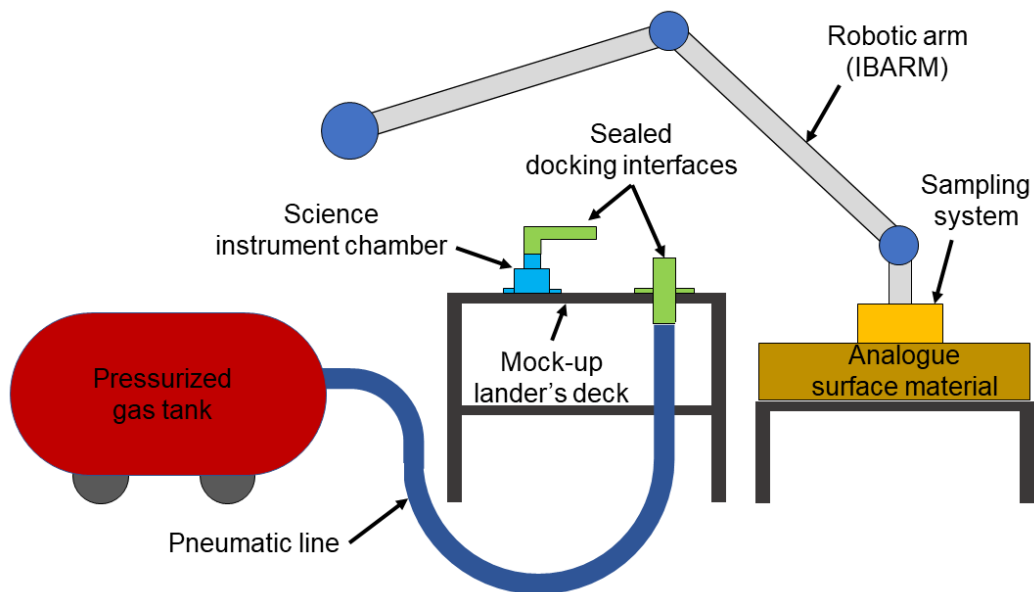


**Figure 5.16** Integrated sample chain architecture for Rasp sampling system. Sampling position shown. Qualitative scheme, not to scale.

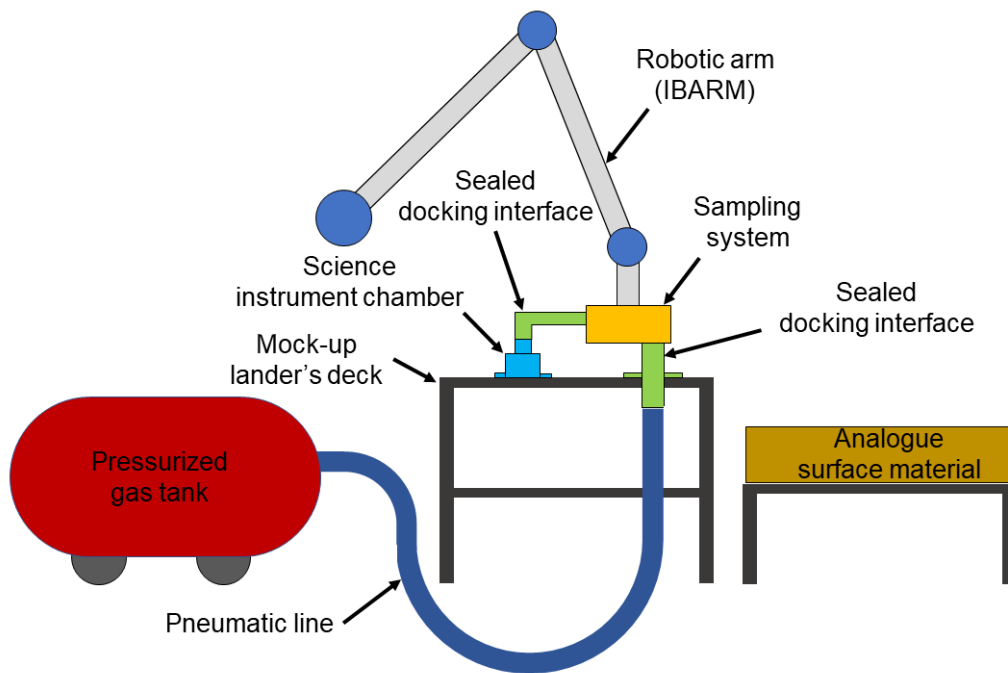


**Figure 5.17** Integrated sample chain architecture for Rasp sampling system. Sample transfer position shown. Qualitative scheme, not to scale.

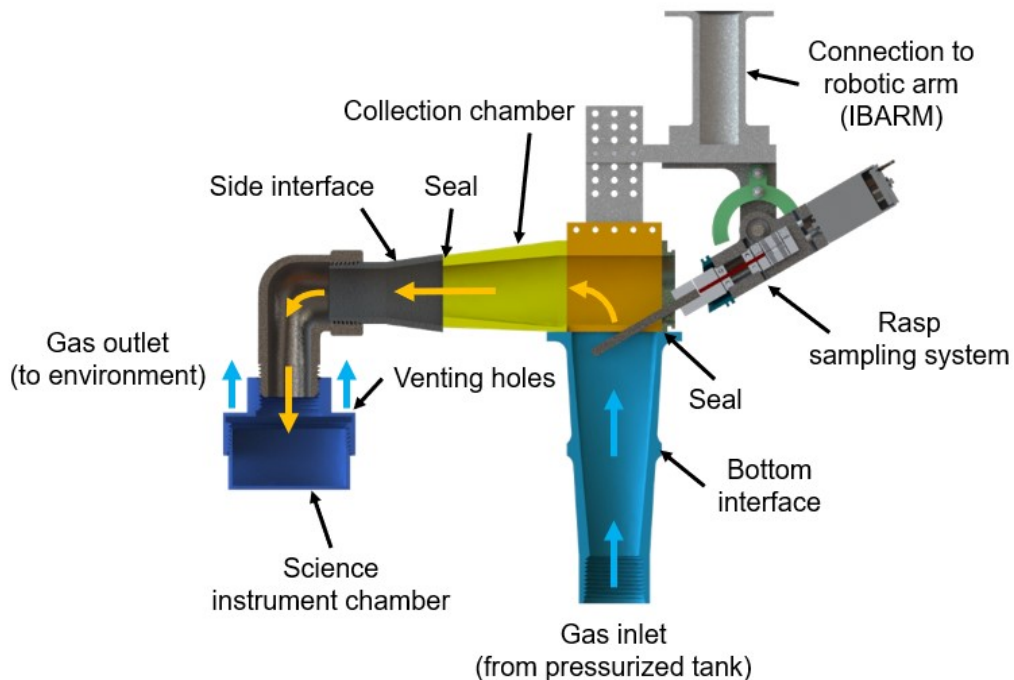


**Figure 5.18** Cross-section of pneumatic sample transfer system applied to the Rasp sampling system. Bold blue arrows represent the flow of gas, while bold orange arrows represent the flow of gas/solids mixture.

Similarly to the Full-face drill sampling system presented in the previous paragraph, a dilute phase flow regime was considered. The same software tool implementing the empirical model to enable rapid and integrated system's design iterations was adopted to support the preliminary design of the pneumatic sample transfer system. The resulting design was obtained by considering a trade-off among pressure losses, flow velocity required to achieve a dilute phase transport of sample, and physical and integration constraints. System's design includes a pipeline with an average inner diameter of 20 mm and composed of a 100 mm long horizontal conical section, a 50 mm long vertical circular to slot section, and a single 90 deg bend. The analysis of the pneumatic transport system was conducted for both Earth's and Enceladus' environment, again considering nitrogen as medium for sample transport in the Enceladus' environment. Table 5.2 summarizes analysis results. End-to-end sample chain operations, including sampling, sample collection and pneumatic transfer to the notional science instrument chamber located on the mock-up lander's deck, were successfully demonstrated for the Rasp sampling system (Figure 5.19) with the goal to mature the pneumatic sample transfer system to TRL 3. Main sample losses were observed at docking interfaces because of non-perfect seals, still assuring at least 80% pneumatic sample transfer efficiency.

**Table 5.2** Results of the analysis of TRL 3 pneumatic sample transfer system applied to the Rasp sampling system.

		Earth's environment	Enceladus' environment
Gas	Medium	Air	Nitrogen
	Gravitational acceleration	9.81 m/s <sup>2</sup>	0.113 m/s <sup>2</sup>
	Temperature	293 K	100 K
	Tank pressure	10 atm	10 atm
	Regulator's outlet pressure	4 atm	2 atm
	Expected total pressure loss	1.15 atm	0.02 atm
	Volume flow rate	7080 cm <sup>3</sup> /s	944 cm <sup>3</sup> /s
Solids	Particle diameter	500 μm	
	Particle density	2500 kg/m <sup>3</sup>	
	Mass flow rate	10 g/s	

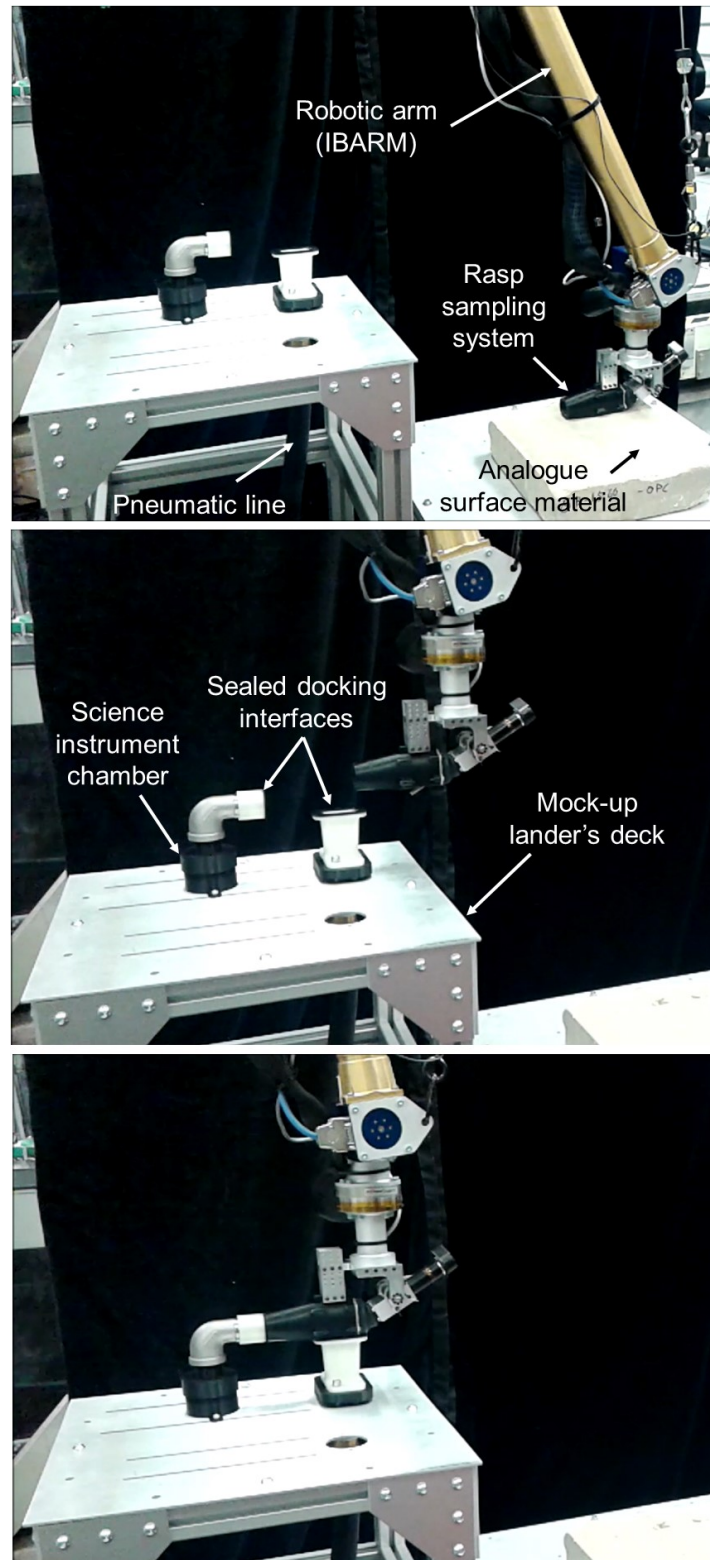


**Figure 5.19** End-to-end sample chain operations for the Rasp sampling system. Top picture shows the Rasp in sampling position. Middle picture shows the Rasp in an intermediate position prior to completion of docking operations. Bottom picture shows the Rasp docked to sealed interfaces and in sample transfer position.

## 5.6 Sample transfer system applied to Dual-Rasp sampling system

As presented in paragraph 3.8 and detailed in paragraph 4.3, the Dual-Rasp is a rotary cutter-based sampling system that relies on the action of two counter-rotating cutting heads to impart momentum into cuttings that are flung into a path for collection, through the guide and into the sample collection chamber. The collected sample is then transferred from the collection chamber to its destination (i.e. the science instrument on the lander).

Also in this case, the Enceladus' gravity is sufficiently low that it cannot be relied upon to enable sample transfer by just dumping or pouring. Therefore, the Dual-Rasp sampling system was designed with integrated features to enable both sample collection and pneumatic transfer in a low gravity environment (Figure 5.20).

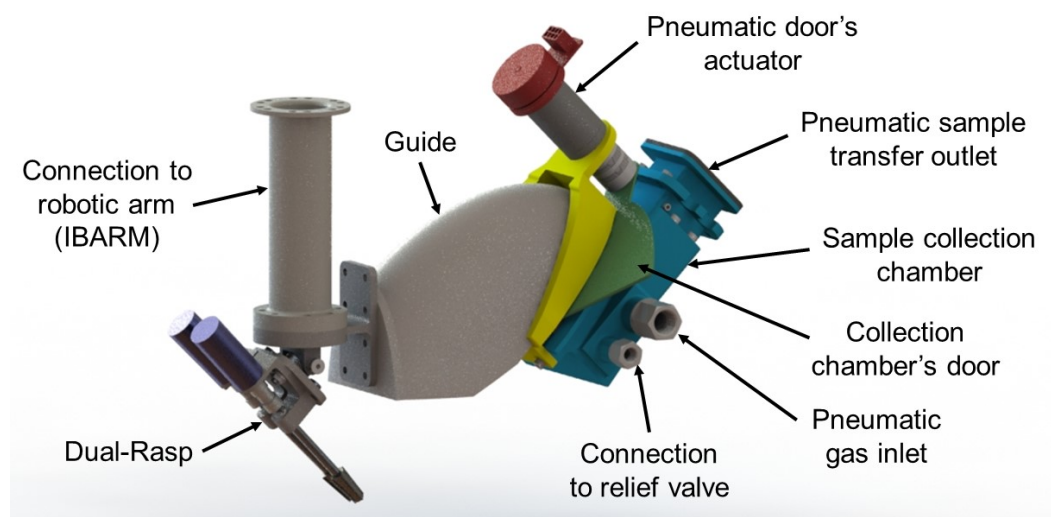


**Figure 5.20** Dual-Rasp sampling system with integrated pneumatic sample transfer features. Collection chamber's door shown in partially open position.

Once sampling and sample collection operations are complete, the main opening of the sample collection chamber, exploited to collect sample during sampling operations, is closed by using a door driven by a rotary actuator. Then, IBARM moves the Dual-Rasp from sampling position to sample transfer position (Figure 5.21 and Figure 5.22). In this architecture, the pneumatic line carrying the gas coming from pressurized tank directly interfaces with the Dual-Rasp through a fixed connection. As a result, docking operation is performed in a single step, with the IBARM pushing the Dual-Rasp against the sealed interface. As a result, the sample transfer outlet of the Dual-Rasp aligns with the inlet of the science instrument chamber, thus closing the pneumatic circuit.

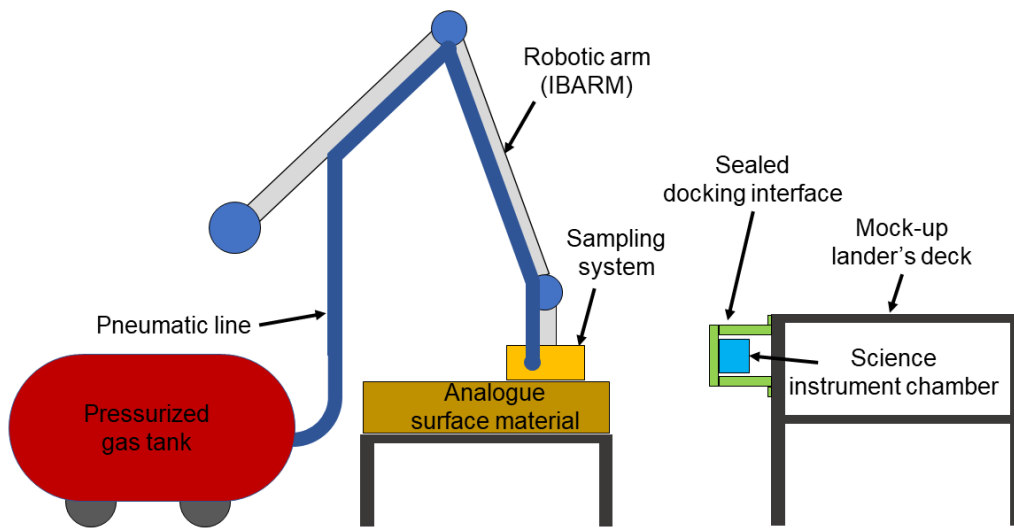


**Figure 5.21** Integrated sample chain architecture for Dual-Rasp sampling system. Sampling position shown. Qualitative scheme, not to scale.

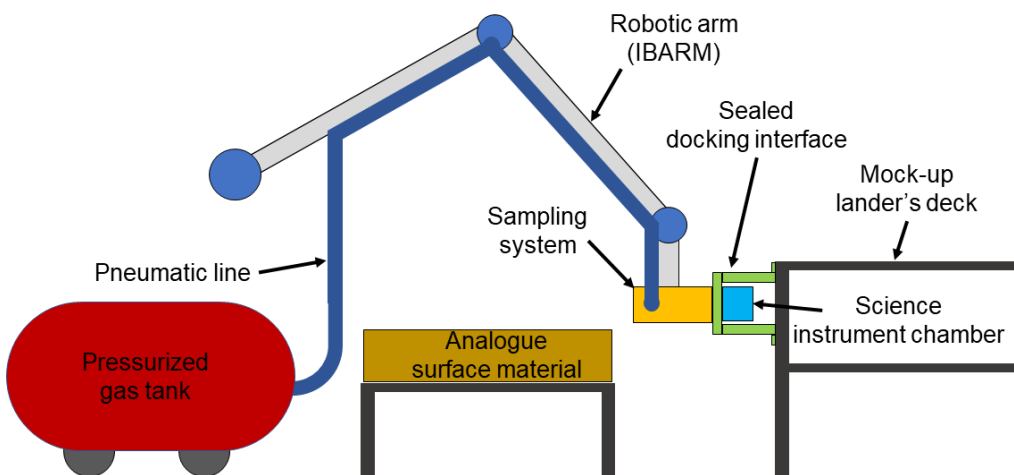


**Figure 5.22** Integrated sample chain architecture for Dual-Rasp sampling system. Sample transfer position shown. Qualitative scheme, not to scale.

Once docking operation is complete, the gas is released from the pressurized tank and is driven by the pneumatic line directly into the sample collection chamber through the fixed gas inlet. A dispersion of solids into gas is thus created and the sample is transported along the pneumatic circuit, out of the collection chamber and into the science instrument chamber (Figure 5.23). It should be noted that once sampling and sample collection operations are complete, the internal volume of sample collection chamber is closed by the collection chamber's door, closing the main opening, and by a small pneumatic door, closing the outlet. This strategy guarantees to retain the sample inside the collection chamber while

moving the Dual-Rasp from sampling position to sample transfer position. Specifically, the pneumatic door is spring-actuated and is normally closed. The door opens under the pressure differential generated when releasing the gas into the collection chamber. This enables the gas/solids mixture of exiting the collection chamber to reach the science instrument chamber.

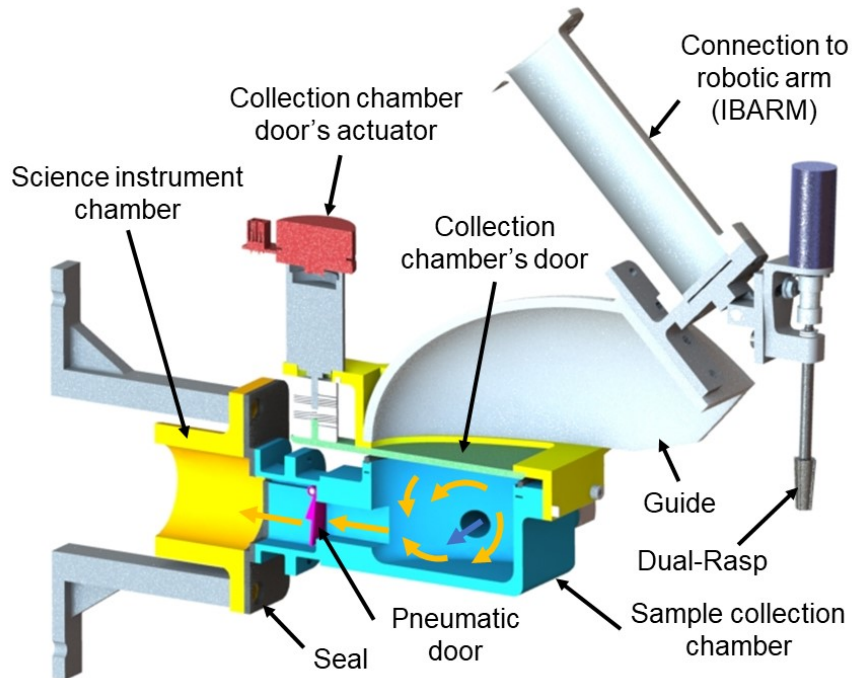


**Figure 5.23** Cross-section of pneumatic sample transfer system applied to the Dual-Rasp sampling system. Bold blue arrow represents the flow of gas, while bold orange arrows represent the flow of gas/solids mixture.

Similarly to previous cases involving both the Full-face and the Rasp drill sampling systems, a dilute phase flow regime was considered. The same software tool implementing the empirical model to enable rapid and integrated system's design iterations was adopted to support the preliminary design of the pneumatic sample transfer system.

The resulting design was obtained by considering a trade-off among pressure losses, flow velocity required to achieve a dilute phase transport of sample, and physical and integration constraints. System's design includes a pipeline with an average inner diameter of 45 mm and composed of a 200 mm long straight horizontal square to circular section.

The analysis of the pneumatic transport system was conducted for both Earth's and Enceladus' environment, again considering nitrogen as medium for sample transport. Table 5.2 summarizes the analysis results.

End-to-end sample chain operations, including sampling, sample collection and pneumatic transfer to the notional science instrument chamber located on the

mock-up lander's deck, were successfully demonstrated for the Dual-Rasp sampling system (Figure 5.19) with the goal to mature the pneumatic sample transfer system to TRL 4. Main sample losses were observed at docking interface because of non-perfect seal, still assuring at least 90% pneumatic sample transfer efficiency.

**Table 5.3** Results of the analysis of TRL 4 pneumatic sample transfer system applied to the Dual-Rasp sampling system.

		Earth's environment	Enceladus' environment
Gas	Medium	Air	Nitrogen
	Gravitational acceleration	9.81 m/s <sup>2</sup>	0.113 m/s <sup>2</sup>
	Temperature	293 K	100 K
	Tank pressure	10 atm	10 atm
	Regulator's outlet pressure	2.4 atm	1.12 atm
	Expected total pressure loss	0.87 atm	0.011 atm
	Volume flow rate	28062 cm <sup>3</sup> /s	3268 cm <sup>3</sup> /s
Solids	Particle diameter	500 μm	
	Particle density	2500 kg/m <sup>3</sup>	
	Mass flow rate	10 g/s	

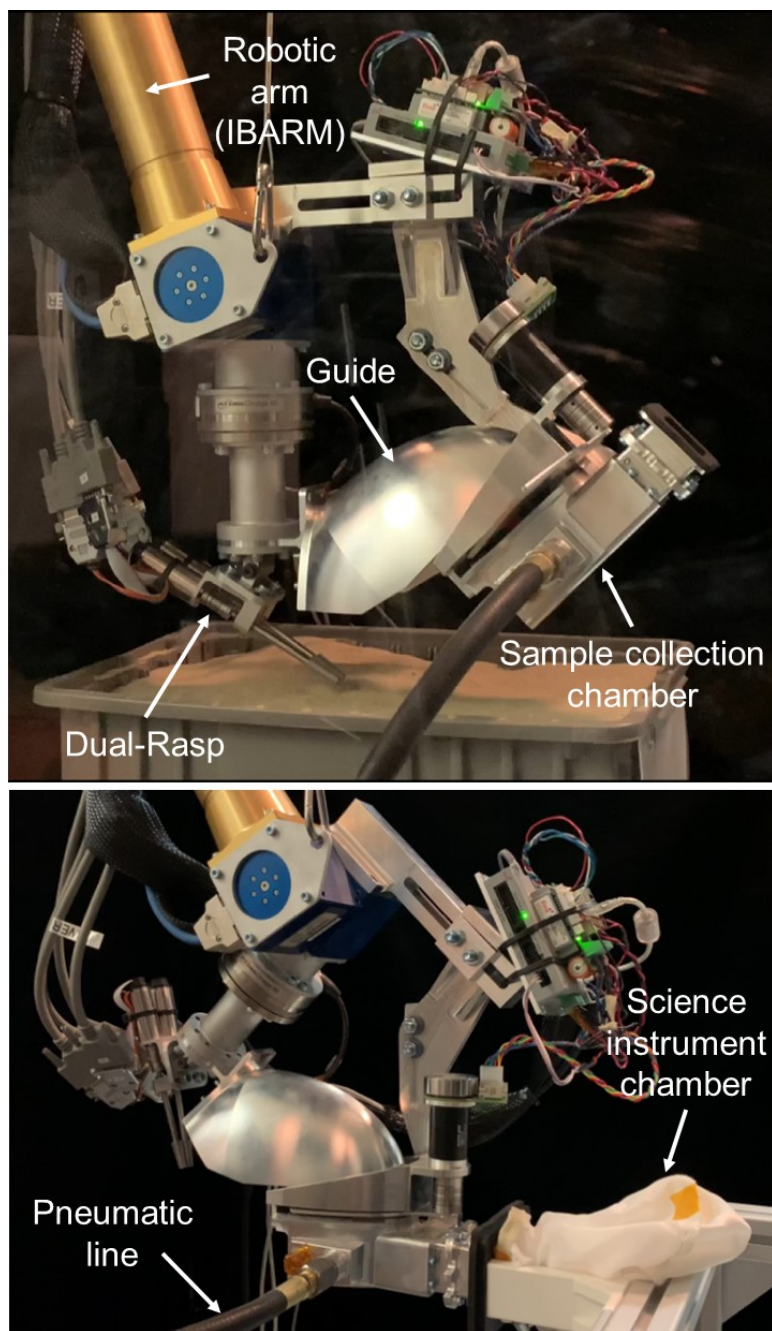


**Figure 5.24** End-to-end TRL 4 sample chain operations for the Dual-Rasp sampling system. Top picture shows the Dual-Rasp in sampling position. Bottom picture shows the Dual-Rasp docked to sealed interface and in sample transfer position. In this case, the science instrument chamber is represented by a soft bag supported by a rigid cylindrical structure.

Preliminary Enceladus mission architecture includes using a two DOF RA that would deploy the Dual-Rasp to enable surface sampling across an arc in front of the lander (Figure 5.25). For this reason, the pneumatic sample transfer system was adapted to the architecture of the two DOF RA and re-designed to undergo environmental verification testing expected to be performed in a thermal vacuum

chamber with the goal to achieve TRL 5 by reproducing relevant Enceladus surface conditions, including cryogenic temperatures and vacuum.

The new architecture implemented solutions to cope with the weaknesses of previous designs. Specifically, docking events were previously implemented to enable sample transfer from the collection chamber, located at the end-effector of the RA, to the science instrument chamber, located on the lander. However, docking events might be operationally demanding, complex and risky, and might require the compliance to critical interface and integration requirements. For this reason, the new architecture was devised to remove any need of performing docking operations. To achieve so, sample transfer was enabled by using an outlet pneumatic line with a fixed interface to the collection chamber and running along the RA with a direct fixed inlet into the science instrument chamber. On the other end, the inlet pneumatic line directly carries gas from the pressurized tank to the collection chamber through a fixed interface, similarly to the previously implemented and successfully tested solution. This architecture enables a simpler and more reliable pneumatic sample transfer system that does not require any docking operation. However, it is still required to perform a transition from sampling operations to sample transfer operations. In the new architecture, this transition is enabled by re-positioning the guide. In fact, during sampling operations, the guide is positioned to aid sample interception and re-direction toward the collection chamber (Figure 5.26). Once sampling operations are complete and the sample is temporarily stored and retained into the collection chamber, the guide is moved on top of it to close the collection volume. The motion of the guide is achieved by using a four-bar linkage mechanism driven by a rotary actuator (Figure 5.27). At this point, sample transfer operation starts by releasing gas from the pressurized tank into the inlet pneumatic line, through the guide and into the collection chamber where it mixes with the sample. The gas/solids mixture exits the collection chamber, through the outlet pneumatic line running along the RA, and into the science instrument chamber (Figure 5.28). As the gas/solids mixture flows into the science instrument chamber, a filter would cause the sample to remain in the chamber as the gas exits through the filter. A prototype filter in a clear wall science instrument chamber was designed and built for TRL 5 pneumatic sample transfer system (Figure 5.29).

CFD analyses were performed to optimize the collection chamber design for pneumatic flow. Specifically, gas flow from inlet, through the guide and into the collection chamber was simulated with the aim to define a proper geometry that facilitates gas/solids mixing and minimizes generation of flow recirculation areas that might trap particles, thus preventing them of being transported (Figure 5.30). Moreover, two rotary union joints are implemented in series to allow gas transfer from stationary pneumatic line through rotary DOFs of RA, still preserving and isolating the pneumatic connection (Figure 5.31) [243].

Figure 5.32 shows full integrated TRL 5 sample chain including the two DOFs RA, Dual-Rasp sampling, sample collection, and sample transfer systems.

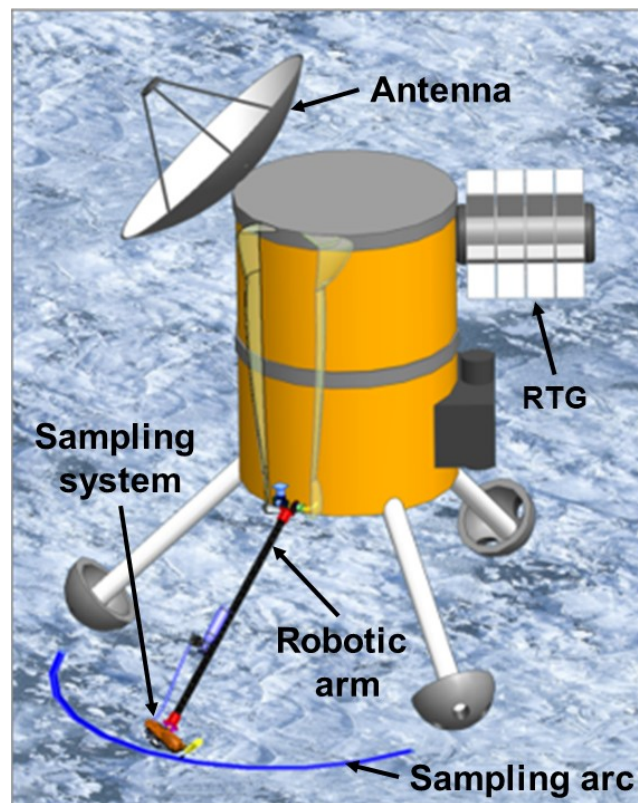


*Figure 5.25* Artistic concept of the Enceladus lander.

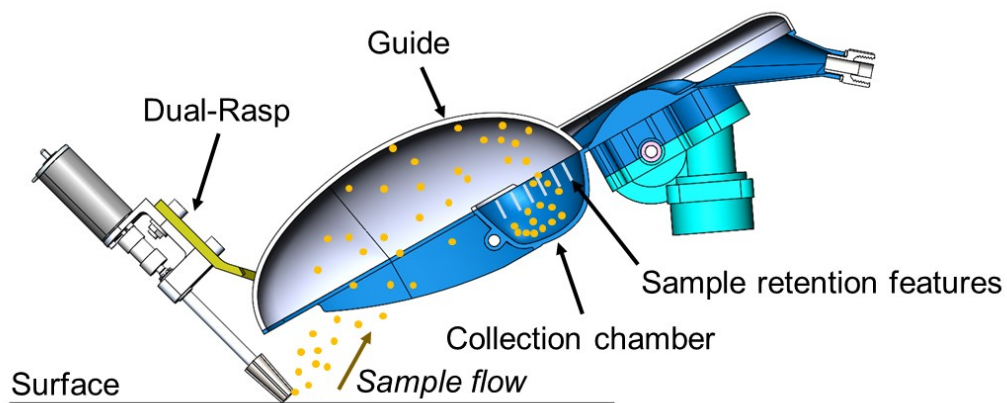


*Figure 5.26* Sample collection in the Dual-Rasp TRL 5 sample chain. The sample material removed from the surface flows from the Dual-Rasp, through the guide into the collection chamber provided with sample retention features.

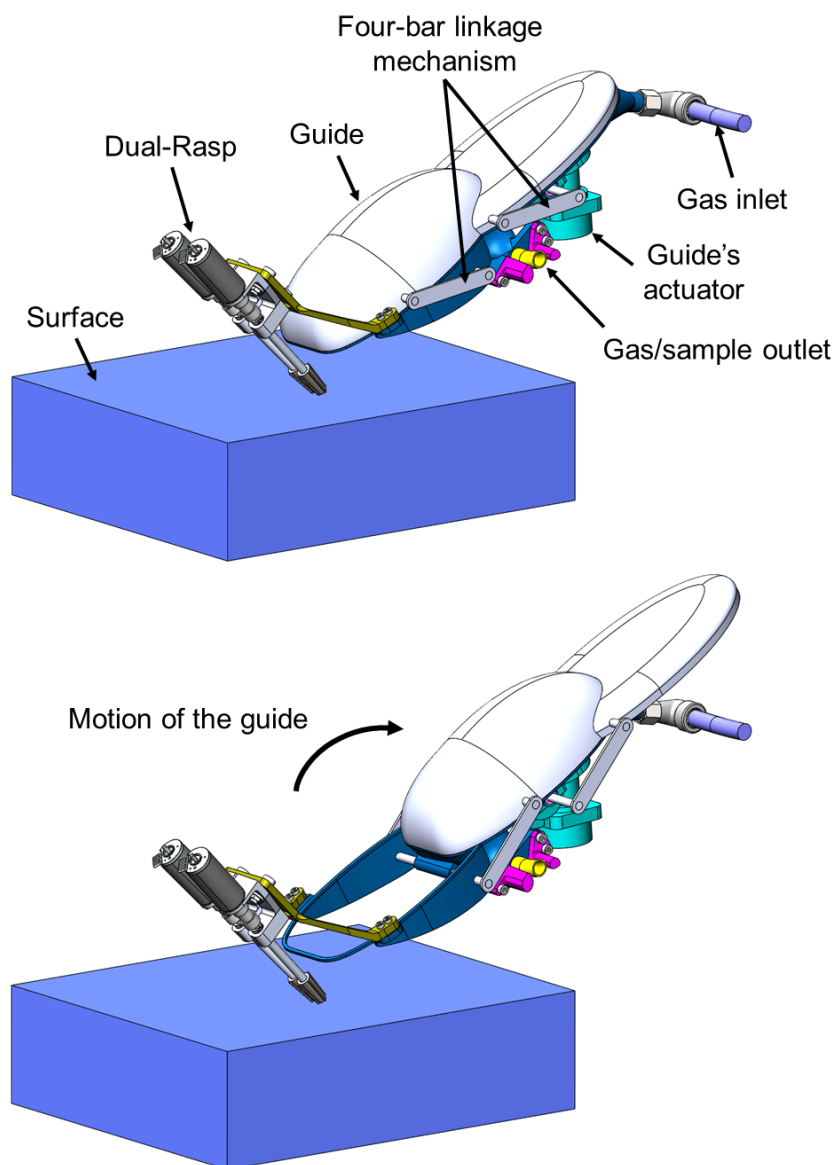


**Figure 5.27** Preparation to sample transfer in the Dual-Rasp TRL 5 sample chain. Once the sample is collected into the collection chamber (Top), the guide moves on top of it to enable pneumatic sample transfer to science instrument chamber (Bottom).

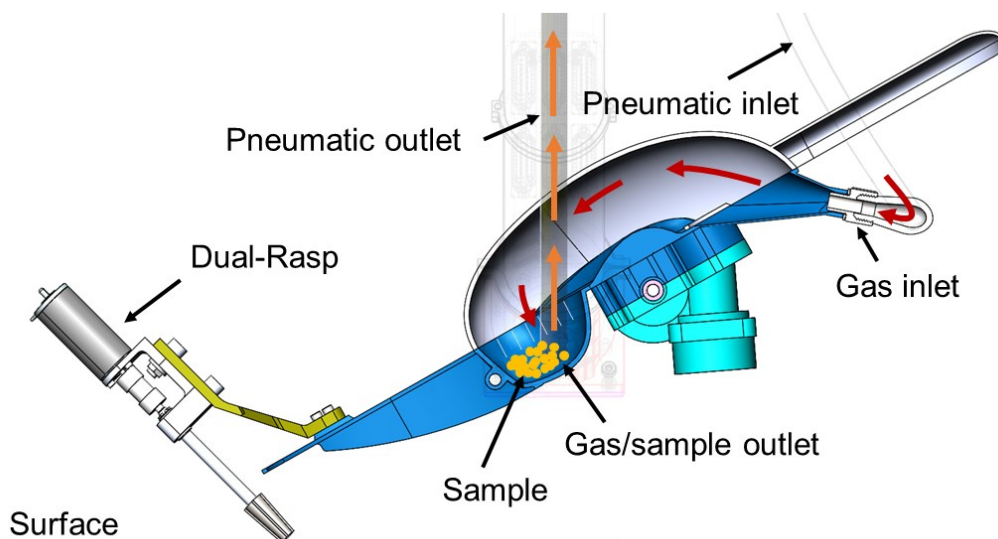


**Figure 5.28** Pneumatic sample transfer in the Dual-Rasp TRL 5 sample chain. Once the collection volume is closed by the guide, the gas is released into the inlet pneumatic line, flows through the guide and into the collection chamber (red arrows). The mix of gas and sample exits the collection chamber through the outlet pneumatic line to reach the science instrument chamber (orange arrows).

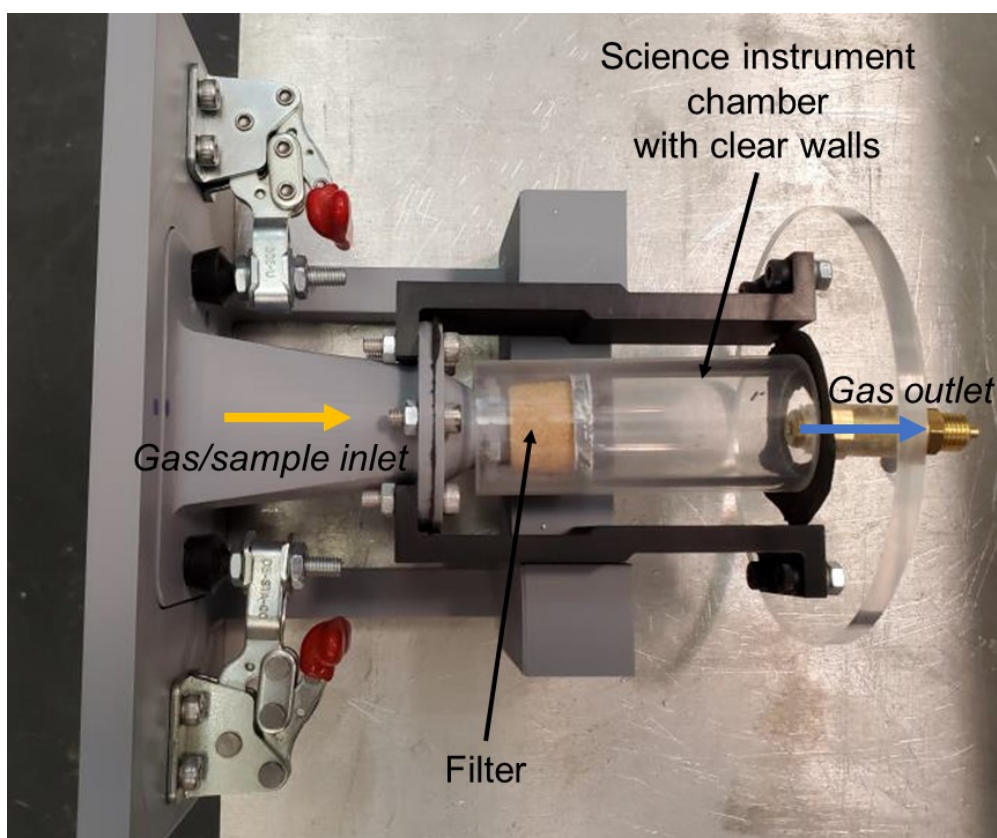


**Figure 5.29** Prototype of science instrument chamber for TRL 5 pneumatic sample transfer system.

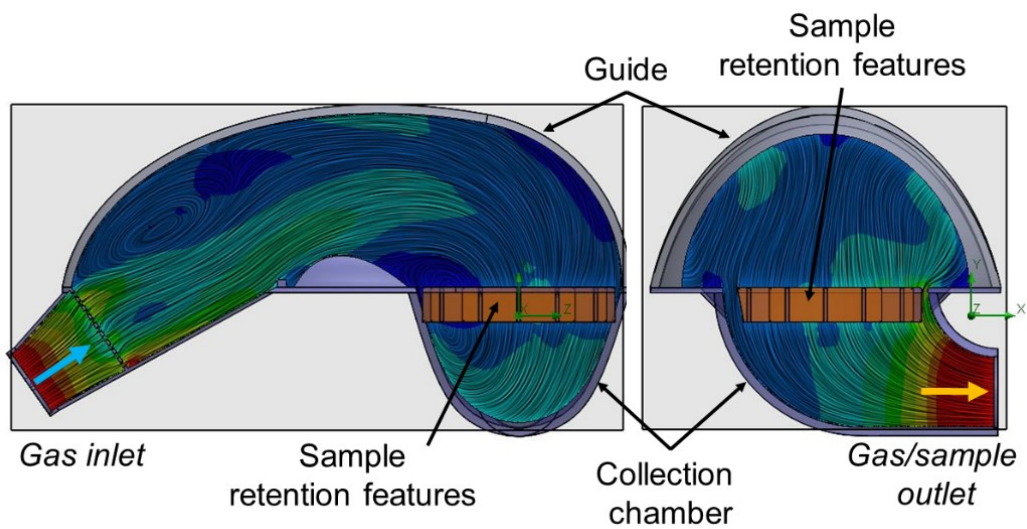


**Figure 5.30** CFD analysis of gas flow from inlet, through the guide and into the collection chamber. Front (Left) and side (Right) cross-section views representing streamlines are shown.

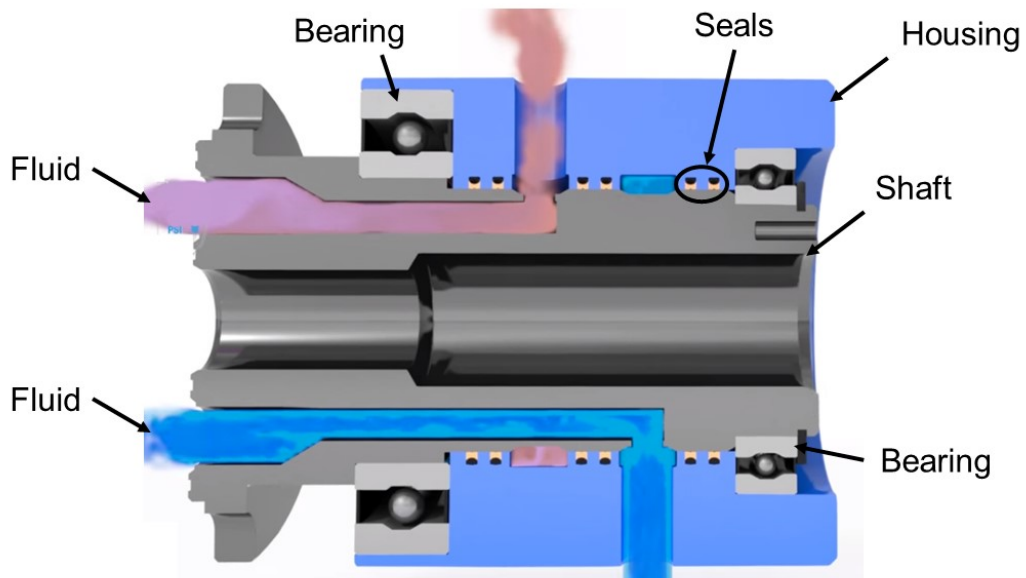


**Figure 5.31** Main components of a typical rotary union joint [243].

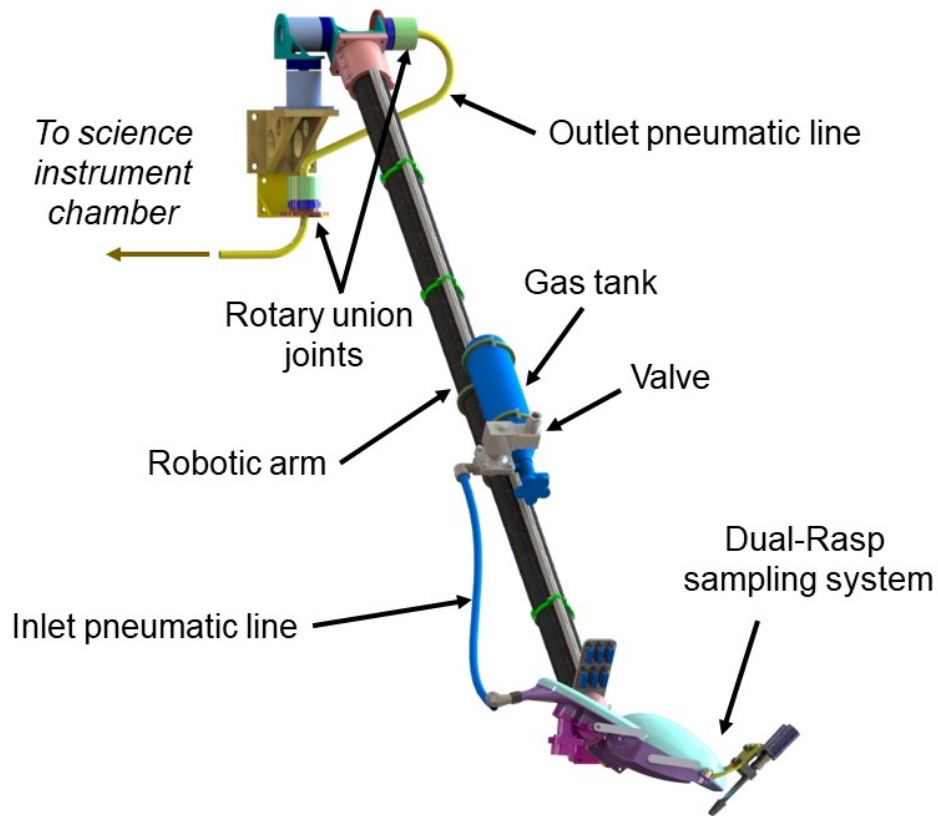


**Figure 5.32** TRL 5 sample chain elements, including RA, Dual-Rasp sampling, sample collection, and sample transfer systems.

Design of pneumatic sample transfer system was driven by the results provided by an analytical tool developed at JPL. The tool implements the theory of non-dimensional groups presented in paragraph 5.2.2 to determine the state diagram and related flow regimes of gas/solids disperse system. Moreover, Fanno flow equations [244] were implemented to determine the evolution of flow parameters along the pneumatic system, modeled as an adiabatic flow in a pipeline considering the effect of friction.

To perform the analysis of gas/solids disperse system, the architecture represented in Figure 5.32 was modeled as represented in Figure 5.33. The analysis was conducted for Earth's gravity, cryogenic temperatures, and vacuum conditions. Conversely to previous architectures, helium was considered as medium for sample transport instead of nitrogen. As for nitrogen, helium phase diagram confirms that it maintains the gaseous phase also under the pressure and temperature conditions under investigation (Figure 5.34). However, helium is inert and is thus better suited to comply with critical planetary protection and contamination control requirements at play when handling samples of potentially high biological interest.

Figure 5.35 shows the state diagram of gas/solids disperse system and includes indication of flow regimes obtained considering both low and high ends of the range of particle's properties considered, namely diameter and density. Moreover, Figure 5.36 shows the evolution of flow parameters along the pneumatic system, namely gas density  $\rho_f$ , gas velocity  $U_f$ , and gas Mach number  $M_f$ . As expected, since gas flow exhausts in vacuum, it achieves the sonic condition at the outlet of the pneumatic line because of the action of friction.

The resulting pneumatic sample transfer system design was obtained by considering a trade-off including flow velocity required to achieve carry over of particles, as well as physical and integration constraints.

Table 5.4 summarizes main design parameters of resulting pneumatic sample transfer system.

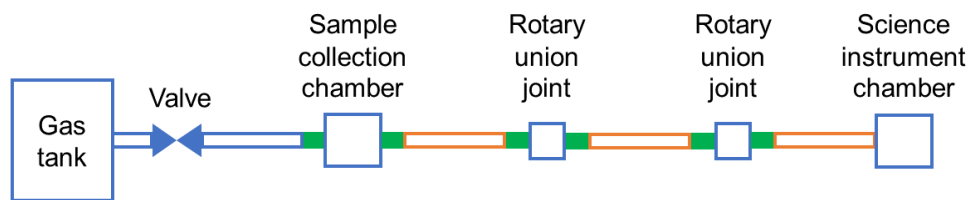


**Figure 5.33** Architecture of TRL 5 pneumatic sample transfer system.

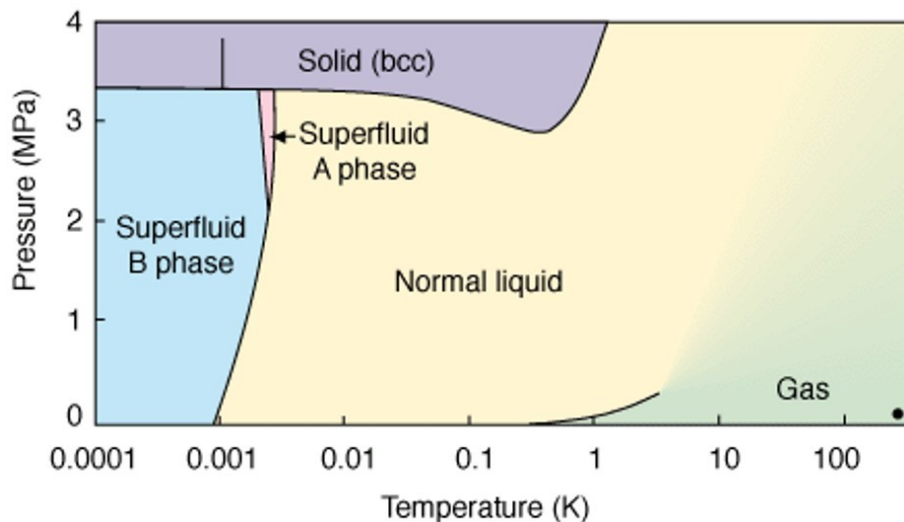


**Figure 5.34** Helium phase diagram [245].

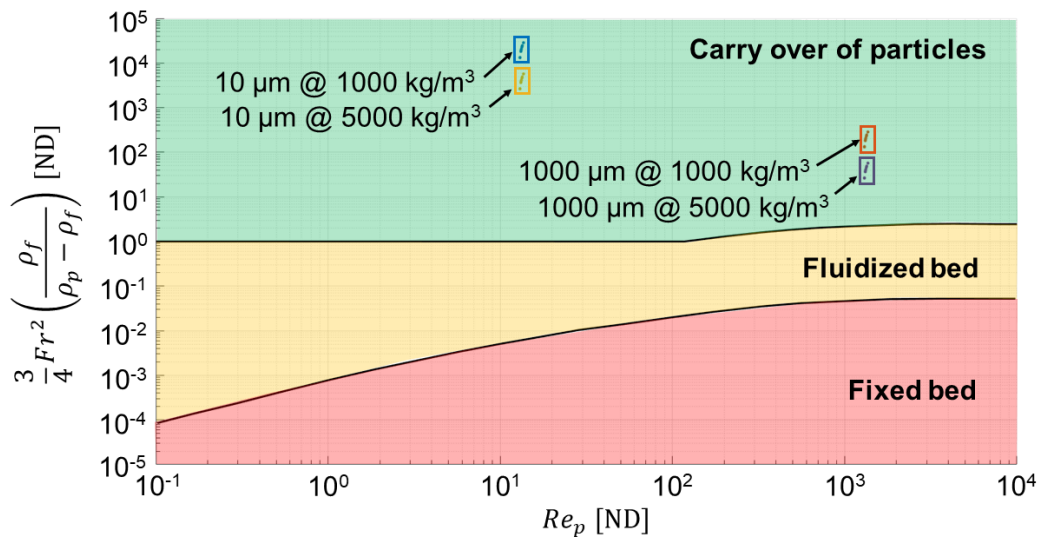


**Figure 5.35** State diagram of gas/solids dispersion for TRL 5 pneumatic sample transfer system.

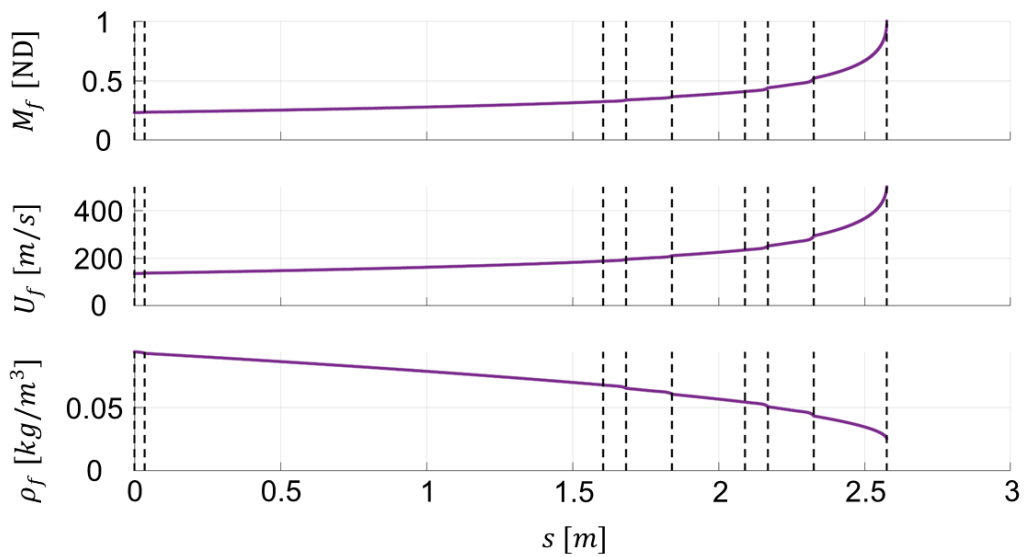


**Figure 5.36** Flow properties along the TRL 5 pneumatic sample transfer system, namely gas density  $\rho_f$ , gas velocity  $U_f$ , and gas Mach number  $M_f$ .

**Table 5.4** Main features of TRL 5 pneumatic sample transfer system.

<b>Pneumatic line</b>	<b>Length</b>	2.57 m
	<b>Inner diameter</b>	10 mm
	<b>Roughness of inner walls</b>	5E-6
	<b>Number of bends</b>	7
	<b>Radius of bends</b>	50 mm
<b>Gas</b>	<b>Medium</b>	Helium
	<b>Gravitational acceleration</b>	9.81 m/s <sup>2</sup>
	<b>Temperature</b>	100 K
	<b>Tank pressure</b>	3 atm
	<b>Expected total pressure loss</b>	0.87 atm
	<b>Mass flow rate</b>	1 g/s
<b>Solids</b>	<b>Diameter</b>	[10, 1000] $\mu\text{m}$
	<b>Density</b>	[1000, 5000] kg/m <sup>3</sup>

## 5.7 Sample measurement

The sample measurement concept is to measure the volume of sample as it flows through the pneumatic transfer system on its way to the science instrument chamber. Therefore, a reliable, on-line, and indirect measurement method is required.

Measurement of solids' flow rate in pneumatic conveying pipelines has become increasingly significant in the industry with the aim to achieve accuracy, reliability, and efficient utilization of energy and to reduce losses. Indirect measurement methods proposed for measuring volumetric concentration and velocity of solids in pneumatic conveying systems are reported in Table 5.5 and Table 5.6, respectively [246]. A trade space study was conducted on main sample measurement technologies to identify the most suited with respect to mission requirements (Table 5.7), including capability to work in a vacuum environment, resiliency to potential material building up and accumulating into the pneumatic line, and capability to measure volume concentration or velocity.

**Table 5.5** Methods for indirect measurement of volumetric concentration of solids in pneumatic conveying pipelines [246].

Method	Sensing technique
Electrical methods	<ul style="list-style-type: none"> <li>• Capacitive</li> <li>• Electrostatic</li> </ul>
Attenuation and scattering	<ul style="list-style-type: none"> <li>• <math>\gamma</math> Rays</li> <li>• Microwaves</li> <li>• Optical</li> <li>• Acoustic / Ultrasonic</li> </ul>
Resonance	<ul style="list-style-type: none"> <li>• Magnetic</li> <li>• Microwave</li> <li>• Acoustic</li> </ul>
Flow tomography	<ul style="list-style-type: none"> <li>• Capacitance / resistance</li> <li>• Optical</li> <li>• <math>\gamma</math> Rays</li> </ul>
Digital imaging	<ul style="list-style-type: none"> <li>• Laser sheet</li> <li>• CCD camera</li> </ul>

**Table 5.6** Methods for indirect measurement of solids' velocity in pneumatic conveying pipelines [246].

Method	Sensing technique
Cross correlation	<ul style="list-style-type: none"> <li>• Optical</li> <li>• Electrostatic</li> <li>• Capacitive</li> <li>• <math>\gamma</math> Rays</li> </ul>
Electrical sensors and new signal processing methods	<ul style="list-style-type: none"> <li>• Electrostatic sensor and wavelet analysis</li> <li>• Capacitive sensor and Fourier transform</li> </ul>
Doppler	<ul style="list-style-type: none"> <li>• Laser Doppler</li> <li>• Microwave Doppler</li> </ul>
Spatial filtering	<ul style="list-style-type: none"> <li>• Capacitive / electrostatic</li> <li>• Optical</li> <li>• Microwave</li> </ul>

**Table 5.7** Trade space study on sample measurement technologies.

Technology						Limitations
	Non-contact	Vacuum compatible	Resilient to particle build-up	Measures concentration	Measures velocity	
Capacitive	Green	Green	Red	Green	Green	Non-uniform field
Electrostatic	Green	Green	Red	Green	Green	Sensitive to ambient factors
Microwave	Green	Green	Green	Green	Green	Costly, sensitive to particle size
Optical	Green	Green	Red	Green	Green	Non-uniform field, low sensitivity
Acoustic	Green	Red	Green	Green	Red	Calibrated to particle size
Magnetic	Green	Green	Red	Green	Red	Dependent on relaxation time of nuclei, costly
Laser sheet + CCD	Green	Green	Red	Green	Green	Only for dilute phase flows

Trade space study has shown that microwave technology is best suited to the application. Specifically, microwave Doppler approach is being evaluated for sample measurement. Such a sensor emits low energy microwaves to the particles flowing through the pneumatic line. Sensor measures the intensity of Doppler-shifted energy of microwaves reflected by particles, which is related to flow concentration and velocity, and converts it into a current signal, and then into flow rate by adopting specific algorithms (Figure 5.37). As a result, only moving particles are measured and build-up of material has little influence upon measurement. Preliminary laboratory testing clearly showed a dual correlation between cumulative voltage resulting from Doppler-shifted energy of microwaves reflected by particles and both sample mass and particle's flow velocity (Figure 5.38). Future activities include further investigation on algorithms to determine sample volume from sensor's reading, as well as verification and validation tests in both laboratory and relevant environment.

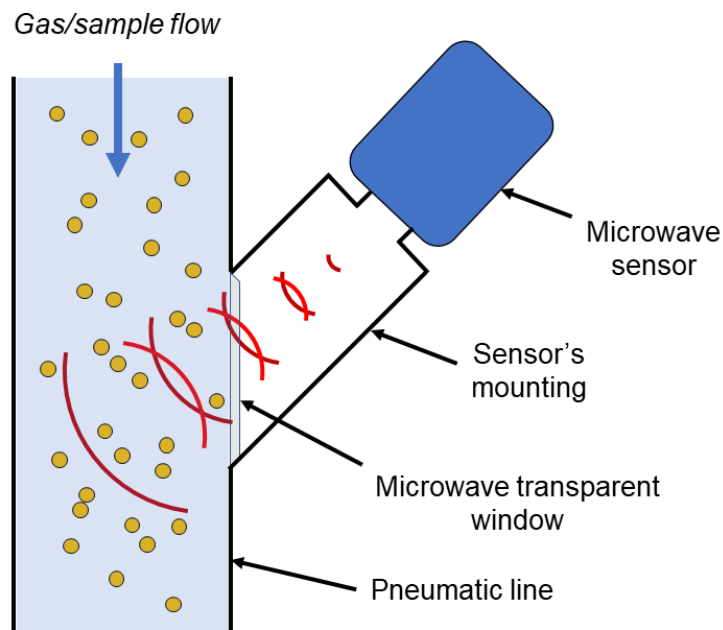


**Figure 5.37** Working principle of microwave Doppler technique for measuring concentration and velocity of particles in a pneumatic conveying system. The sensor emits microwaves and measures the Doppler-shift energy of microwaves reflected by particles in the gas/sample dispersion flowing in the pneumatic line. Doppler-shift energy relates to flow rate of particles.

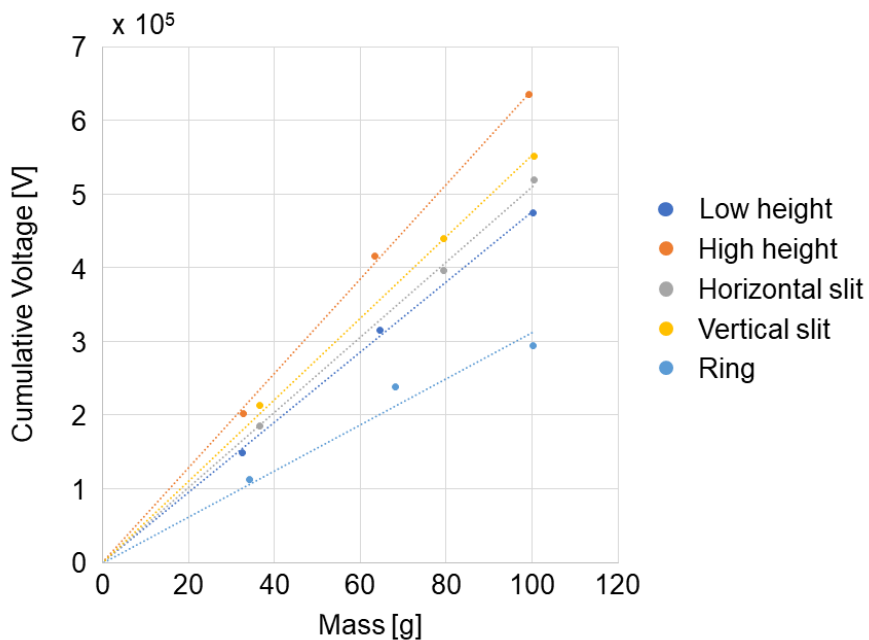


**Figure 5.38** Cumulative voltage vs. sample mass correlation for microwave Doppler technique applied to BLC 110 analogue material. Various flow conditions are represented, also showing a correlation between voltage and flow velocity.

## 5.8 Ocean Worlds Life Surveyor Project

The NASA JPL's Ocean Worlds Life Surveyor (OWLS) Project aims to develop a science instrument to perform molecular and cellular analyses for a potential life detection mission to ocean worlds such as Enceladus and Europa [247] [248].

Molecular analyses are performed by using several detection methods, including the Capillary Electrophoresis-Laser Induced Florescence (CE-LIF) to detect amino acids and carboxylic acids, the Capillary Electrophoresis Capacitively-Coupled Contactless Conductivity Detector (CE-C4D) to detect charged species, and the Capillary Electrophoresis-Electrospray Ionization coupled to Mass Spectrometry (CESI-MS) to detect collections of organic molecules. On the other hand, cellular analyses are performed by using a Digital Holographic Microscope (DHM) capable to record videos and detect motion of particles, and the Volume Fluorescence Imager (VFI) to identify potential biomolecules in the videos captured via DHM. These techniques will enable the acquisition of multiple independent evidence for the presence of life on ocean worlds, should we encounter it during a potential future mission of exploration.

Transmitting raw science data from Enceladus back to Earth would require a significant amount of electrical power because of the high distance. For this reason, the total data transmission budget is severely limited to only about 0.01% of the raw data collected. However, the OWLS Project aims to develop an autonomous software to overcome this obstacle. The software will be designed to analyze, summarize, and prioritize science data to be transmitted back for scientific analysis.

# Conclusions

Saturn's moon Enceladus is among the most promising candidates in the Solar System to host life beyond Earth. A potential mission to the surface of Saturn's moon Enceladus could determine if biosignatures or life traces exist there. Such a mission is currently under investigation at NASA Jet Propulsion Laboratory (JPL). The objective of JPL's activity is to develop and mature a sample chain for the acquisition of material from plume fallback on the surface of Enceladus with the goal to perform in-situ measurement.

Ph.D. research supported JPL's activity by pursuing the following objectives.

- To define the high-level requirements on the sampling system to guarantee the stability of the lander while performing the sampling operation.
- To investigate and characterize sample collection and transfer operations in the Enceladus gravity, cryogenic, and vacuum environmental conditions.
- To provide sample chain design guidelines to fulfill sample acquisition requirements.

Ph.D. research objectives were pursued by performing the following activities.

- The novel analytical tool MISTRAL was developed to support the definition of the high-level requirements on both the sampling system and the lander system to guarantee successful sampling operations. MISTRAL was conceived for trade space exploration during early conceptual and preliminary design phases, where a rapid and broad evaluation is required for a very high number of configurations and boundary conditions. The tool rapidly determines the preliminary design envelope of a sampling apparatus to guarantee the stability condition of the lander. The tool also provides the capability to infer high-level requirements concerning other elements of the lander critical to its stability, such as the footpads.
- A numerical model based on DEM was developed to investigate sample collection operation. The model enabled simulation of granular material flow generated by the Dual-Rasp sampling system through computation of motion and effect of a large number of particles. A set of analysis metrics was developed to characterize the granular material flow generated during sampling operation. The analysis metrics were devised to be used for both numerical analysis and experimental

testing, providing a framework for apples-to-apples comparison. Particle-tool coefficient of static friction and particle-tool COR were identified as the most sensitive model parameters by performing a sensitivity analysis. Most sensitive parameters were directly measured by performing inclined plane tests to measure particle-tool coefficient of static friction, and drop tests to measure particle-tool COR. Custom testbeds were designed and built to perform measurement of parameters.

- DEM results were adopted to drive the design of sample collection system. Main elements investigated include a sample transport guide whose concept and geometry were developed and optimized to intercept and re-focus the granular flow generated by the Dual-Rasp sampling system toward the inlet of the sample collection chamber. Grid-style sample retention features were devised and developed to aid sample retention in the collection chamber in a low gravity environment. Sample collection system was prototyped and subject to verification tests in 1g Earth's gravity to achieve TRL 4.
- A test campaign is planned for DEM model validation and Dual-Rasp sampling system and sample collection verification to achieve TRL 5 via parabolic flights in 1%g Earth's gravity and vacuum conditions. Custom test hardware and software was developed to support the campaign, including an acrylic vacuum chamber with clear walls and a particle tracking software to post-process high-speed recordings of sampling and sample collection operations.
- An analytical model was developed to investigate pneumatic sample transport of particles dispersed into a gas. The model allows the integrated design of the pneumatic system in both Earth's and Enceladus' environmental conditions by exploring the design space to determine the optimal design parameters to achieve a dilute phase transport of sample. Analysis results were adopted to drive the design of a pneumatic sample transfer system applied to Full-face drill, Rasp, and Dual-Rasp sampling systems. Verification tests were performed in 1g Earth's gravity to achieve TRL 4.
- Designed and developed a two DOF RA with integrated Dual-Rasp sampling system, sample collection, and sample transfer systems to a notional science instrument chamber with the aim to perform end-to-end sample chain verification in 1g Earth's gravity and Enceladus-like thermal vacuum environment to achieve TRL 5.

# References

- [1] W.-H. Ip, J. Yan, C.-H. Li and Z.-Y. Ouyang, "Preface: The Chang'e-3 lander and rover mission to the Moon," *Research in Astronomy and Astrophysics*, vol. 14, no. 12, 2014.
- [2] O. Wang and J. Liu, "A Chang'e 4 mission concept and vision of future Chinese lunar exploration activities," *Acta Astronautica*, vol. 127, pp. 678-683, 2016.
- [3] R. Arvidson, J. Gooding and H. Moore, "The Martian surface as imaged, sampled and analyzed by the Viking landers," *Reviews of Geophysics*, vol. 27, no. 1, pp. 39-60, 1989.
- [4] M. Golombek, "Overview of the Mars Pathfinder Mission: Launch through landing, surface operations, data sets, and science results," *Journal of Geophysical Research: Planets*, vol. 104, no. E4, pp. 8523-8553, 1999.
- [5] J. Guinn, M. Garcia and K. Talley, "Mission design of the Phoenix Mars Scout mission," *Journal of Geophysical Research: Planets*, vol. 113, no. E3, 2008.
- [6] W. Banerdt, "InSight: a discovery mission to explore the interior of Mars," in *44th Lunar and Planetary Science Conference*, The Woodlands, Texas, USA, 2013.
- [7] J. P. Lebreton and D. L. Matson, "The Huygens Probe: Science, Payload and Mission Overview," *Space Science Reviews*, vol. 104, pp. 59-100, 2002.
- [8] S. Ulamec and et al., "Rosetta Lander – Landing and operations on comet 67P/Churyumov-Gerasimenko," *Acta Astronautica*, vol. 125, pp. 80-91, 2016.
- [9] S. Ulamec and et al., "Landing on small bodies: From the Rosetta Lander to MASCOT and beyond," *Acta Astronautica*, vol. 93, pp. 460-466, 2014.
- [10] National Research Council, "Vision and Voyages for Planetary Science in the Decade 2013-2022," The National Academies Press, 2011.
- [11] A. R. Hendrix and et al., "The NASA Roadmap to Ocean Worlds," *Astrobiology*, vol. 19, no. 1, 2019.
- [12] C. B. Phillips and R. T. Pappalardo, "Europa Clipper Mission Concept: Exploring Jupiter's Ocean Moon," *Eos, Transactions American Geophysical*

- Union*, vol. 95, no. 20, 2014.
- [13] R. Gershman, E. Nilsen and R. Oberto, "Europa Lander," *Acta Astronautica*, vol. 52, no. 2-6, pp. 253-258, 2003.
- [14] R. D. Lorenz and et al., "Dragonfly: A rotorcraft lander concept for scientific exploration at Titan," *Johns Hopkins APL Technical Digest*, vol. 34, no. 3, 2018.
- [15] P. Tsou and et al., "LIFE - Enceladus Plume Sample Return via Discovery," in *45th Lunar and Planetary Science Conference*, The Woodlands (Texas, USA), 2014.
- [16] M. Choukroun, P. Backes, M. Cable, R. Hodyss, M. Badescu, E. Marteau, J. Molaro, S. Moreland, T. Nordheim, T. Okamoto, D. Riccobono and K. Zacny, "Sampling Ocean Materials, Traces of Life or Biosignatures in Plume Deposits on Enceladus' Surface," White Paper to Planetary Science and Astrobiology Decadal Survey 2023-2032, 2020.
- [17] P. Thomas, R. Tajeddine, M. Tiscareno, J. Burns, J. Joseph, T. Lored, P. Helfenstein and C. Porco, "Enceladus's measured physical libration requires a global subsurface ocean," *Icarus*, vol. 264, pp. 37-47, 2016.
- [18] L. Iess, D. Stevenson, M. Parisi, D. Hemingway, R. Jacobson, J. Lunine, F. Nimmo, J. Armstrong, S. Asmar, M. Ducci and P. Tortora, "The Gravity Field and Interior Structure of Enceladus," *Science*, vol. 344, no. 6179, pp. 78-80, 2014.
- [19] C. Porco, P. Helfenstein, P. Thomas, A. Ingersoll, J. Wisdom, R. West, G. Neukum, T. Denk, R. Wagner, T. Roatsch, S. Kieffer, E. Turtle, A. McEwen, T. Johnson, J. Rathbun, J. Veverka, D. Wilson, J. Perry, J. Spitale, A. Brahic, J. Burns, A. DelGenio, L. Dones, C. Murray and S. Squyres, "Cassini Observes the Active South Pole of Enceladus," *Science*, vol. 311, no. 5766, pp. 1393-1401, 2006.
- [20] J. Spitale and C. Porco, "Association of the jets of Enceladus with the warmest regions on its south-polar fractures," *Nature*, vol. 449, pp. 695-697, 2007.
- [21] C. Howett, J. Spencer, J. Pearl and M. Segura, "High heat flow from Enceladus' south polar region measured using 10–600 cm<sup>-1</sup> Cassini/CIRS data," *Journal of Geophysical Research: Planets*, vol. 116, no. E3, 2011.
- [22] J. Spencer, J. Pearl, M. Segura, F. Flasar, A. Mamoutkine, P. Romani, B. Buratti, A. Hendrix, L. Spilker and R. Lopes, "Cassini Encounters Enceladus: Background and the Discovery of a South Polar Hot Spot," vol. 311, no. 5766, pp. 1401-1405, 2006.

- [23] J. Spencer, A. Barr, L. Esposito, P. Helfenstein, A. Ingersoll, R. Jaumann, C. McKay, F. Nimmo and J. Hunter Waite, "Enceladus: An active cryovolcanic satellite," in *Saturn from Cassini-Huygens*, Springer, 2009, pp. 683-724.
- [24] C. Howett, J. Spencer, J. Pearl and M. Segura, "Thermal inertia and bolometric Bond albedo values for Mimas, Enceladus, Tethys, Dione, Rhea and Iapetus as derived from Cassini/CIRS measurements," *Icarus*, vol. 206, no. 2, pp. 573-593, 2010.
- [25] F. Nimmo, J. Spencer, R. Pappalardo and M. Mullen, "Shear heating as the origin of the plumes and heat flux on Enceladus," *Natura*, vol. 447, no. 7142, pp. 289-291, 2007.
- [26] J. Spencer and F. Nimmo, "Enceladus: An Active Ice World in the Saturn System," *Annual Review of Earth and Planetary Sciences*, vol. 41, pp. 693-717, 2013.
- [27] P. Haff, A. Eviatar and G. Siscoe, "Ring and plasma: The enigmas of Enceladus," *Icarus*, vol. 56, no. 3, pp. 426-438, 1983.
- [28] D. Hemingway, L. Maxwell and M. Manga, "Cascading parallel fractures on Enceladus," *Nature Astronomy*, vol. 4, no. 3, pp. 234-239, 2020.
- [29] V. Lainey, L. Casajus, J. Fuller, M. Zannoni, P. Tortora, N. Cooper, C. Murray, D. Modenini, R. Park, V. Robert and Q. Zhang, "Resonance locking in giant planets indicated by the rapid orbital expansion of Titan," *Nature Astronomy*, pp. 1-6, 2020.
- [30] S. Kempf, U. Beckmann and J. Schmidt, "How the Enceladus dust plume feeds Saturn's E ring," *Icarus*, vol. 206, no. 2, pp. 446-457, 2010.
- [31] F. Postberg, S. Kempf, J. Schmidt, N. Brilliantov, A. Beinsen, B. Abel, U. Buck and R. Srama, "Sodium salts in E-ring ice grains from an ocean below the surface of Enceladus," *Nature*, vol. 459, pp. 1098-1101, 2009.
- [32] F. Postberg, J. Schmidt, J. Hillier, S. Kempf and R. Srama, "A salt-water reservoir as the source of a compositionally stratified plume on Enceladus," *Nature*, vol. 474, pp. 620-622, 2011.
- [33] F. Postberg, N. Khawaja, B. Abel, G. Choblet, C. Glein, M. Gudipati, B. Henderson, H.-W. Hsu, S. Kempf, F. Klenner, G. Moragas-Klostermeyer, B. Magee, L. Nölle, M. Perry, R. Reviol, J. Schmidt, R. Srama, F. Stolz, G. Tobie, M. Trieloff and J. Hunter Waite, "Macromolecular organic compounds from the depths of Enceladus," *Nature*, vol. 558, no. 7711, pp. 564-568, 2018.
- [34] J. Waite Jr, W. Lewis, B. Magee, J. Lunine, W. McKinnon, C. Glein, O. Mousis, D. Young, T. Brockwell, J. Westlake, M. Nguyen, B. Teolis, H.

- Niemann, R. McNutt Jr, M. Perry and W. Ip, "Liquid water on Enceladus from observations of ammonia and 40 Ar in the plume," *Nature*, vol. 460, pp. 487-490, 2009.
- [35] J. Waite Jr, C. Glein, R. Perryman, B. Teolis, B. Magee, G. Miller, J. Grimes, M. Perry, K. Miller, A. Bouquet, J. Lunine, T. Brockwell and S. Bolton, "Cassini finds molecular hydrogen in the Enceladus plume: evidence for hydrothermal processes," *Science*, vol. 356, no. 6334, pp. 155-159, 2017.
- [36] C. Glein and J. Hunter Waite, "The Carbonate Geochemistry of Enceladus' Ocean," *Geophysical Review Letters*, vol. 47, no. 3, 2020.
- [37] P. Schenk, R. Clark, C. Howett, A. Verbiscer and J. Hunter Waite, *Enceladus and the Icy Moons of Saturn*, University of Arizona Press, 2018.
- [38] C. McKay, A. Anbar, C. Porco and P. Tsou, "Follow the plume: The habitability of Enceladus," *Astrobiology*, vol. 14, no. 4, pp. 352-355, 2014.
- [39] C. McKay, C. Porco, T. Altheide, W. Davis and T. Kral, "The possible origin and persistence of life on Enceladus and detection of biomarkers in the plume," *Astrobiology*, vol. 8, no. 5, pp. 909-919, 2008.
- [40] A. Ingersoll and E. Shawn, "Total particulate mass in Enceladus plumes and mass of Saturn's E ring inferred from Cassini ISS images," *Icarus*, vol. 216, no. 2, pp. 492-506, 2011.
- [41] J. Schmidt, N. Brilliantov, F. Spahn and S. Kempf, "Slow dust in Enceladus' plume from condensation and wall collisions in tiger stripe fractures," *Nature*, vol. 451, pp. 685-688, 2008.
- [42] B. Southworth, S. Kempf and J. Spitale, "Surface deposition of the Enceladus plume and the zenith angle of emissions," *Icarus*, vol. 319, pp. 33-42, 2019.
- [43] C. Porco, L. Dones and C. Mitchell, "Could it be snowing microbes on Enceladus? Assessing conditions in its plume and implications for future missions," *Astrobiology*, vol. 17, no. 9, pp. 876-901, 2017.
- [44] M. Guzman, R. Lorenz, D. Hurley, W. Farrell, J. Spencer, C. Hansen, T. Hurford, J. Ibea, P. Carlson and C. McKay, "Collecting amino acids in the Enceladus plume," *International Journal of Astrobiology*, vol. 18, no. 1, pp. 47-59, 2019.
- [45] J. Waite Jr, M. Combi, W. Ip, T. Cravens, R. McNutt Jr, W. Kasprzak, R. Yelle, J. Luhmann, H. Niemann, D. Gell, B. Magee, G. Fletcher, J. Lunine and W.-L. Tseng, "Cassini ion and neutral mass spectrometer: Enceladus plume composition and structure," *Science*, vol. 311, no. 5766, pp. 1419-

- 1422, 2006.
- [46] T. Nordheim, K. Hand, C. Paranicas, C. Howett, A. Hendrix, G. Jones and A. Coates, "The near-surface electron radiation environment of Saturn's moon Mimas," *Icarus*, vol. 286, pp. 56-68, 2017.
- [47] S. Warren, "Optical constants of ice from the ultraviolet to the microwave," *Applied Optics*, vol. 23, no. 8, pp. 1206-1225, 1984.
- [48] P. Johnson, R. Hodyss, V. Chernow, D. Lipscomb and J. Goguen, "Ultraviolet photolysis of amino acids on the surface of icy Solar System bodies," *Icarus*, vol. 221, no. 2, pp. 800-805, 2012.
- [49] J. Eigenbrode, G. Robert, C. McKay, T. Hurford and D. Alfonso, "Searching for Life in an Ocean World: The Enceladus Life Signatures and Habitability (ELSAH) mission concept," in *42nd COSPAR Scientific Assembly*, Pasadena (California, USA), 2018.
- [50] K. Hand, "Report of the Europa Lander science definition team," National Aeronautics and Space Administration, 2017.
- [51] M. Neveu, L. Hays, M. Voytek, M. New and M. Schulte, "The Ladder of Life Detection," *Astrobiology*, vol. 18, no. 11, pp. 1375-1402, 2018.
- [52] National Aeronautics and Space Administration, "Technology Readiness Level," [Online]. Available: [https://www.nasa.gov/directorates/heo/scan/engineering/technology/txt\\_accordion1.html](https://www.nasa.gov/directorates/heo/scan/engineering/technology/txt_accordion1.html). [Accessed 14 November 2020].
- [53] National Aeronautics and Space Administration, "Technology Readiness Level Definitions," [Online]. Available: [https://www.nasa.gov/pdf/458490main\\_TRL\\_Definitions.pdf](https://www.nasa.gov/pdf/458490main_TRL_Definitions.pdf). [Accessed 14 November 2020].
- [54] D. Riccobono, G. Genta, S. Moreland and P. Backes, "A multidisciplinary design tool for robotic systems involved in sampling operations on planetary bodies," *CEAS Space Journal*, 2020.
- [55] M. Badescu, P. Backes, S. Moreland, A. Brinkman, D. Riccobono, M. Dotson, N. Csomay-Shanklin, S. Ubellacker, J. Molaro, M. Choukroun and G. Genta, "Sampling tool concepts for Enceladus lander in-situ analysis," in *IEEE Aerospace Conference*, Big Sky (Montana, USA), 2019.
- [56] A. Ellery, *Planetary Rovers: Robotic Exploration of the Solar System*, First ed., Springer, 2016.
- [57] A. Ball, J. Garry, R. Lorenz and V. Kerzhanovich, *Planetary Landers and*

- Entry Probes, First ed., Cambridge University Press, 2010.
- [58] G. Genta, *Introduction to the Mechanics of Space Robots*, First ed., Springer Nature, 2012.
- [59] K. Zacny, R. Mueller, J. Craft and J. Wilson, "Five-Step Parametric Prediction and Optimization Tool for Lunar Surface Systems Excavation Tasks," in *12th Biennial International Conference on Engineering, Construction, and Operations in Challenging Environments*, Honolulu (Hawaii, USA), 2010.
- [60] A. Wilkinson and A. DeGennaro, "Digging and pushing lunar regolith: Classical soil mechanics and the forces needed for excavation and traction," *Journal of Terramechanics*, vol. 44, no. 2, pp. 133-152, 2007.
- [61] D. Pullan, M. Sims, I. Wright, C. Pillinger and R. Trautner, "Beagle 2: the exobiological lander of Mars Express, Mars Express: the scientific payload," *ESA Publications Division*, Vols. ESA SP-1240, pp. 165-204, 2004.
- [62] NASA Space Science Data Center, "Venera 13," [Online]. Available: <https://nssdc.gsfc.nasa.gov/nmc/spacecraft/display.action?id=1981-106D>. [Accessed 13 December 2020].
- [63] NASA Space Science Data Center, "Surveyor 3," [Online]. Available: <https://nssdc.gsfc.nasa.gov/nmc/spacecraft/display.action?id=1967-035A>. [Accessed 13 December 2020].
- [64] NASA Space Science Data Center, "Surveyor 4," [Online]. Available: <https://nssdc.gsfc.nasa.gov/nmc/spacecraft/display.action?id=1967-068A>. [Accessed 13 December 2020].
- [65] NASA Space Science Data Center, "Surveyor 5," [Online]. Available: <https://nssdc.gsfc.nasa.gov/nmc/spacecraft/display.action?id=1967-084A>. [Accessed 13 December 2020].
- [66] NASA Space Science Data Center, "Surveyor 6," [Online]. Available: <https://nssdc.gsfc.nasa.gov/nmc/spacecraft/display.action?id=1967-112A>. [Accessed 13 December 2020].
- [67] NASA Space Science Data Center, "Surveyor 7," [Online]. Available: <https://nssdc.gsfc.nasa.gov/nmc/spacecraft/display.action?id=1968-001A>. [Accessed 13 December 2020].
- [68] G. Soffen and C. Snyder, "First Viking mission to Mars," *Science*, vol. 193, pp. 759-766, 1976.
- [69] G. Soffen, "The Viking project," *Journal of Geophysical Research*, vol. 82,

- no. 28, pp. 3959-3970, 1977.
- [70] National Aeronautics and Space Administration, "Press Kit/December 1999—Mars Polar Lander/Deep Space 2," [Online]. Available: [https://www.jpl.nasa.gov/news/press\\_kits/mplds2hq.pdf](https://www.jpl.nasa.gov/news/press_kits/mplds2hq.pdf). [Accessed 13 December 2020].
- [71] H. Boehnhardt, "The Philae lander mission and science overview," *Philosophical Transactions of the Royal Society A: Mathematical, Physical and Engineering Sciences*, 2017.
- [72] NASA Space Science Data Center, "Luna 16," [Online]. Available: <https://nssdc.gsfc.nasa.gov/nmc/spacecraft/display.action?id=1970-072A>. [Accessed 13 December 2020].
- [73] NASA Space Science Data Center, "Luna 20," [Online]. Available: <https://nssdc.gsfc.nasa.gov/nmc/spacecraft/display.action?id=1972-007A>. [Accessed 13 December 2020].
- [74] NASA Space Science Data Center, "Luna 24," [Online]. Available: <https://nssdc.gsfc.nasa.gov/nmc/spacecraft/display.action?id=1976-081A>. [Accessed 13 December 2020].
- [75] G. E. Forsythe, M. A. Malcolm and C. B. Moler, *Computer Methods for Mathematical Computations*, Englewood Cliffs: NJ: Prentice Hall, 1976.
- [76] R. P. Brent, *Algorithms for Minimization without Derivatives*, Englewood Cliffs: NJ: Prentice-Hall, 1973.
- [77] R. E. Arvidson, R. G. Bonitz, M. L. Robinson, J. L. Carsten, R. A. Volpe, A. Trebi-Ollennu, M. T. Mellon, P. C. Chu, K. R. Davis, J. J. Wilson, A. S. Shaw, R. N. Greenberger, K. L. Siebach, T. C. Stein, S. C. Cull, W. Goetz, R. V. Morris, D. W. Ming, H. U. Keller, M. T. Lemmon, H. G. Sizemore and M. Mehta, "Results from the Mars Phoenix Lander Robotic Arm experiment," *Journal of Geophysical Research*, vol. 114, no. 5685, 2009.
- [78] R. Bonitz, L. Shiraishi, M. Robinson, J. Carsten, R. Volpe, A. Trebi-Ollennu, R. E. Arvidson, P. C. Chu, J. J. Wilson and K. R. Davis, "The Phoenix Mars Lander Robotic Arm," in *IEEE Aerospace Conference*, Big Sky (Montana, USA), 2009.
- [79] A. Shaw, R. Arvidson, R. Bonitz, J. Carsten, H. Keller, M. Lemmon, M. Mellon, M. Robinson and A. Trebi-Ollennu, "Phoenix soil physical properties investigation," *Journal of Geophysical Research: Planets*, vol. 114, no. E1, 2009.
- [80] National Aeronautics and Space Administration, "Press Kit/August 2007 – Phoenix Launch: Mission to the Martian Polar North," August 2007.

- [Online]. Available: [https://www.jpl.nasa.gov/news/press\\_kits/phoenix-launch-presskit.pdf](https://www.jpl.nasa.gov/news/press_kits/phoenix-launch-presskit.pdf). [Accessed 30 September 2020].
- [81] M. Budhu, *Soil Mechanics and Foundations*, Third ed., Wiley & Sons, 2010.
- [82] M. Mellon, R. Arvidson, H. Sizemore, M. Searls, D. Blaney, S. Cull, M. Hecht, T. Heet, H. Uwe Keller, M. Lemmon, W. Markiewicz, D. Ming, R. Morris, W. Pike and A. Zent, "Ground ice at the Phoenix Landing Site: Stability state and origin," *Journal of Geophysical Research: Planets*, vol. 114, no. E1, 2009.
- [83] M. Mellon, M. Malin, R. Arvidson, M. Searls, H. Sizemore, T. Heet, M. Lemmon, H. Uwe Keller and J. Marshall, "The periglacial landscape at the Phoenix landing site," vol. 114, no. E1, 2009.
- [84] P. Backes, S. Moreland, M. Badescu, D. Riccobono, A. Brinkman, M. Choukroun, J. Molaro, R. Aggerwal, T. Newbold, A. Ahmad and S. Ubellacker, "The Dual-Rasp Sampling System for an Enceladus Lander," in *IEEE Aerospace Conference*, Big Sky (Montana, USA), 2020.
- [85] J. Molaro, M. Choukroun, C. Phillips, E. Phelps, R. Hodyss, K. Mitchell, J. Lora and G. Meirion-Griffith, "The Microstructural Evolution of Water Ice in the Solar System Through Sintering," *Journal of Geophysical Review: Planets*, vol. 124, no. 2, pp. 243-277, 2019.
- [86] E. Beshore, D. Lauretta, W. Boynton, C. Shinohara, B. Sutter, D. Everett, J. Gal-Edd, R. Mink, M. Moreau and J. Dworkin, "The OSIRIS-REx asteroid sample return mission," in *IEEE Aerospace Conference*, Big Sky (Montana, USA), 2015.
- [87] S. Squyres, K. Nakamura-Messenger, D. Mitchell, V. Moran, M. Houghton, D. Glavin, A. Hayes, D. Lauretta and CAESAR Project Team, "The CAESAR New Frontiers Mission: 1. Overview", in *49th Lunar And Planetary Science Conference*, 2018.
- [88] R. Anderson, L. Jandura, A. Okon, D. Sunshine, C. Roumeliotis, L. Beegle, J. Hurowitz, B. Kennedy, D. Limonadi, S. McCloskey, M. Robinson, M. Seybold and K. Brown, "Collecting samples in Gale Crater, Mars; an overview of the Mars Science Laboratory sample acquisition, sample processing and handling system," *Space Science Reviews*, vol. 170, pp. 57-75, 2012.
- [89] S. Moreland, P. Backes, M. Badescu, D. Riccobono, M. Mongelli, P. Viera, A. Brinkman, F. Rehnmark, R. Wei, G. Adams, R. Toda, W. Cervantes and K. Zacny, "Full-scale dynamic touch-and-go validation of the BiBlade comet surface sample chain," in *IEEE Aerospace Conference*, Big Sky (Montana, USA), 2018.

- [90] P. Backes, C. McQuin, M. Badescu, A. Ganino, H. Manohara, Y. Bae, R. Toda, N. Wiltsie, S. Moreland, J. Grimes-York, P. Walkemeyer, E. Kulczycki, C. Dandino, R. Smith, M. Williamson, D. Wai, R. Bonitz, A. San Martin and B. Wilcox, "Sampling System Concepts for a Touch-and-Go Architecture Comet Surface Sample Return Mission," in *AIAA SPACE 2014 Conference and Exposition*, 2014.
- [91] R. Bonitz, "The brush wheel sampler - A sampling device for small-body touch-and-go missions," in *IEEE Aerospace Conference*, Big Sky (Montana, USA), 2012.
- [92] A. Ercoli Finzi, F. Bernelli Zazzera, C. Dainese, F. Malnati, P. Magnani, E. Re, P. Bologna, S. Espinasse and A. Olivieri, "SD2 - How to Sample a Comet," *Space Science Reviews*, vol. 128, pp. 281-299, 2007.
- [93] K. Seweryn, J. Grygorczuk, H. Rickmann, M. Morawski, S. Aleksashkin, M. Banaszkiwicz, M. Drogosz, J. Gurgurewicz, O. Kozlov, M. Krolikowska-Soltan, S. Sutugin, R. Wawrzaszek, L. Wisniewski and A. Wisniewski, "CHOMIK -Sampling Device of Penetrating Type for Russian Phobos Sample Return Mission," in *38th COSPAR Scientific Assembly*, 2010.
- [94] S. Watanabe, Y. Tsuda, M. Yoshikawa, S. Tanaka, T. Saiki and S. Nakazawa, "Hayabusa 2 Mission Overview," *Space Science Reviews*, vol. 208, pp. 3-16, 2017.
- [95] K. Edelberg, P. Backes, J. Biesiadecki, S. Brooks, D. Helmick, W. Kim, B. Metz, J. Reid, A. Sirota, W. Ubellacker and P. Vieira, "Software System for the Mars 2020 Mission Sampling and Caching Testbeds," in *IEEE Aerospace Conference*, Big Sky (Montata, USA), 2018.
- [96] R. Bonitz, L. Shiraishi, M. Robinson, R. Arvidson, P. Chu, J. Wilson, K. Davis, G. Paulsen, A. Kusack, D. Archer and P. Smith, "NASA Mars 2007 Phoenix Lander robotic arm and icy soil acquisition device," *Journal of Geophysical Research*, vol. 113, 2008.
- [97] E. Gallego, A. Ruiz and P. Aguado, "Simulation of silo filling and discharge using ANSYS and comparison with experimental data," *Computers and Electronics in Agriculture*, vol. 118, pp. 281-289, 2015.
- [98] O. Zienkiewicz, R. Taylor and J. Zhu, *The Finite Element Method: Its Basis and Fundamentals*, Butterworth-Heinemann, 2013.
- [99] T. Hughes, *The Finite Element Method: Linear Static and Dynamic Finite Element Analysis*, Prentice Hall, 1987.
- [100] H. Mang, *Numerical methods in finite element analysis*, Prentice-Hall, 1976.
- [101] J. Chaskalovic, *Finite Element Methods for Engineering Sciences*, Springer-

- ] Verlag Berlin Heidelberg, 2008.
- [102 A. Shahani and M. Amini Fasakhodi, "Finite element analysis of dynamic crack propagation using remeshing technique," *Materials & Design*, vol. 30, no. 4, pp. 1032-1041, 2009.
- [103 A. Trädegård, F. Nilsson and S. Östlund, "FEM-remeshing technique applied to crack growth problems," *Computer Methods in Applied Mechanics and Engineering*, vol. 160, no. 1-2, pp. 115-131, 1998.
- [104 N. Moës, J. Dolbow and T. Belytschko, "A finite element method for crack growth without remeshing," *International Journal for Numerical Methods in Engineering*, vol. 46, no. 1, pp. 131-150, 1999.
- [105 N. Sukumar, J. Dolbow and N. Moës, "Extended finite element method in computational fracture mechanics: a retrospective examination," *International Journal of Fracture*, vol. 196, pp. 189-206, 2015.
- [106 C. Coetzee, "Discrete and continuum modelling of soil cutting," *Computational Particle Mechanics*, vol. 1, pp. 409-423, 2014.
- [107 C. Coetzee, A. Basson and P. Vermeer, "Discrete and continuum modelling of excavator bucket filling," *Journal of Terramechanics*, vol. 44, no. 2, pp. 177-186, 2007.
- [108 C. Wozniak, "Discrete and continuum modelling of delamination processes," *Ingenieur-Archiv*, vol. 60, pp. 335-344, 1990.
- [109 B. Alder and T. Wainwright, "Studies in Molecular Dynamics. I. General Method," *The Journal of Chemical Physics*, vol. 31, 1959.
- [110 M. Griebel, S. Knapek and G. Zumbusch, *Numerical Simulation in Molecular Dynamics*, Springer-Verlag Berlin Heidelberg, 2007.
- [111 J. Haile, *Molecular Dynamics Simulation: Elementary Methods*, Wiley, 1997.
- [112 S. Plimpton, "Fast Parallel Algorithms for Short-Range Molecular Dynamics," *Journal of Computational Physics*, vol. 117, no. 1, pp. 1-19, 1995.
- [113 W. Brown, P. Wang, S. Plimpton and A. Tharrington, "Implementing Molecular Dynamics on Hybrid High Performance Computers - Short Range Forces," *Computer Physics Communications*, vol. 182, no. 4, pp. 898-911, 2011.
- [114 W. Brown, A. Kohlmeyer, S. Plimpton and A. Tharrington, "Implementing molecular dynamics on hybrid high performance computers – Particle–

- particle particle-mesh," *Computer Physics Communications*, vol. 183, no. 3, pp. 449-459, 2012.
- [115 P. Cundall and O. Strack, "A discrete numerical model for granular assemblies," *Géotechnique*, vol. 29, no. 1, pp. 47-65, 1979.]
- [116 F. Radjaï and F. Dubois, *Discrete-element Modeling of Granular Materials*, Wiley, 2011.]
- [117 T. Pöschel and T. Schwager, *Computational Granular Dynamics*, Springer-Verlag Berlin Heidelberg, 2005.]
- [118 H. Zhu, Z. Zhou, R. Yang and A. Yu, "Discrete particle simulation of particulate systems: A review of major applications and findings," *Chemical Engineering Science*, vol. 63, no. 23, pp. 5728-5770, 2008.]
- [119 Z. Asaf, D. Rubinstein and J. Shmulevich, "Determination of discrete element model parameters required for soil tillage," *Soil and Tillage Research*, vol. 92, no. 1-2, pp. 227-242, 2007.]
- [120 Y. Chen, L. Munkholm and T. Nyord, "A discrete element model for soil-sweep interaction in three different soils," *Soil and Tillage Research*, vol. 126, pp. 34-41, 2013.]
- [121 C. Coetzee and D. Els, "Calibration of discrete element parameters and the modelling of silo discharge and bucket filling," *Computers and Electronics in Agriculture*, vol. 65, no. 2, pp. 198-212, 2009.]
- [122 C. Coetzee and D. Els, "Calibration of granular material parameters for DEM modelling and numerical verification by blade-granular material interaction," *Journal of Terramechanics*, vol. 46, no. 1, pp. 15-26, 2009.]
- [123 C. Coetzee and D. Els, "The numerical modelling of excavator bucket filling using DEM," *Journal of Terramechanics*, vol. 46, no. 5, pp. 217-227, 2009.]
- [124 C. Coetzee, D. Els and G. Dymond, "Discrete element parameter calibration and the modelling of dragline bucket filling," *Journal of Terramechanics*, vol. 47, no. 1, pp. 33-44, 2010.]
- [125 K. Kafui, C. Thornton and M. Adams, "Discrete particle-continuum fluid modelling of gas-solid fluidised beds," *Chemical Engineering Science*, vol. 57, no. 13, pp. 2395-2410, 2002.]
- [126 S. Deb and D. Tafti, "Investigation of flat bottomed spouted bed with multiple jets using DEM-CFD framework," *Powder Technology*, vol. 254, pp. 387-402, 2014.]
- [127 J. Zhao and T. Shan, "Coupled CFD-DEM simulation of fluid-particle

- ] interaction in geomechanics," *Powder Technology*, vol. 239, pp. 248-258, 2013.
- [128 A. Di Renzo and F. Di Maio, "Comparison of contact-force models for the simulation of collisions in DEM-based granular flow codes," *Chemical Engineering Science*, vol. 59, no. 3, pp. 525-541, 2004.
- [129 N. Brilliantov, F. Spahn, J.-M. Hertzsch and T. Pöschel, "Model for collisions in granular gases," *Physical Review E*, vol. 53, pp. 5382-5392, 1996.
- [130 T. Schwager and T. Poschel, "Coefficient of restitution and linear dashpot model revisited," *Granular Matter*, vol. 9, pp. 465-469, 2007.
- [131 L. Silbert, D. Ertas, G. Grest, T. Halsey, D. Levine and S. Plimpton, "Granular flow down an inclined plane: Bagnold scaling and rheology," *Physical Review E*, vol. 64, 2001.
- [132 H. Zhang and H. Makse, "Jamming transition in emulsions and granular materials," *Physical Review E*, vol. 72, 2005.
- [133 R. Mindlin, "Compliance of elastic bodies in contact," *Journal of Applied Mechanics*, vol. 16, pp. 259-268, 1949.
- [134 R. Mindlin and H. Deresiewicz, "Elastic Spheres in Contact under Varying Oblique Force," *Journal of Applied Mechanics*, vol. 20, pp. 327-344, 1953.
- [135 C. Wensrich and A. Katterfeld, "Rolling friction as a technique for modelling particle shape in DEM," *Powder Technology*, vol. 217, pp. 409-417, 2012.
- [136 D. Markauskas and R. Kačianauskas, "Investigation of rice grain flow by multi-sphere particle model with rolling resistance," *Granular Matter*, vol. 13, pp. 143-148, 2011.
- [137 J. Ai, J.-F. Chen, J. Rotter and J. Ooi, "Assessment of rolling resistance models in discrete element simulations," *Powder Technology*, vol. 206, no. 3, pp. 269-282, 2011.
- [138 M. Kuhn and K. Bagi, "Contact rolling and deformation in granular media," *International Journal of Solids and Structures*, vol. 41, no. 21, pp. 2593-5820, 2005.
- [139 L. Easo and C. Wassgren, "Comparison of Liquid Bridge Volume Models in DEM Simulations," in *AIChE Annual Meeting*, 2013.
- [140 G. Lian, C. Thornton and M. Adams, "A Theoretical Study of the Liquid Bridge Forces between Two Rigid Spherical Bodies," *Journal of Colloid and*

- Interface Science*, vol. 161, no. 1, pp. 138-147, 1993.
- [141 S. Nase, W. Vargas, A. Abatan and J. McCarthy, "Discrete Characterization  
] Tools for Wet Granular Media," *Powder Technology*, vol. 116, no. 2-3, pp.  
214-223, 2001.
- [142 D. Shi and J. McCarthy, "Numerical Simulation Of Liquid Transfer Between  
] Particles," *Powder Technology*, vol. 184, no. 1, pp. 64-75, 2008.
- [143 F. Soulié, F. Cherblanc, M. El Yousoufi and C. Saix, "Influence of liquid  
] bridges on the mechanical behaviour of polydisperse granular materials,"  
*International Journal for Numerical and Analytical Methods in  
Geomechanics*, vol. 30, no. 3, 2005.
- [144 K. Johnson, K. Kendall and A. Roberts, "Surface energy and the contact of  
] elastic solids," *Proceedings of the Royal Society A*, vol. 324, no. 1558, pp.  
301-313, 1971.
- [145 B. Derjaguin, V. Muller and Y. Toporov, "Effect of contact deformations on  
] the adhesion of particles," *Journal of Colloid and Interface Science*, vol. 53,  
no. 2, pp. 314-326, 1975.
- [146 S. Luding, "Cohesive, frictional powders: contact models for tension,"  
] *Granular Matter*, vol. 10, no. 4, p. 235, 2008.
- [147 J. Marshall, "Discrete-element modeling of particulate aerosol flows,"  
] *Journal of Computational Physics*, vol. 228, no. 5, pp. 1541-1561, 2009.
- [148 C. Thornton, "Interparticle sliding in the presence of adhesion," *Journal of  
] Physics D: Applied Physics*, vol. 24, 1991.
- [149 C. Coetzee, "Calibration of the Discrete Element Method and the effect of  
] particle shape," *Powder Technology*, vol. 297, pp. 50-70, 2016.
- [150 D. Höhner, S. Wirtz and V. Scherer, "Experimental and numerical  
] investigation on the influence of particle shape and shape approximation on  
hopper discharge using the discrete element method," vol. 235, pp. 614-627,  
2013.
- [151 D. Höhner, S. Wirtz and V. Scherer, "A study on the influence of particle  
] shape on the mechanical interactions of granular media in a hopper using the  
Discrete Element Method," *Powder Technology*, vol. 278, pp. 286-305,  
2015.
- [152 D. Markauskas, A. Ramírez-Gómez, R. Kačianauskas and E. Zdancevičius,  
] "Maize grain shape approaches for DEM modelling," *Computers and  
Electronics in Agriculture*, vol. 118, pp. 247-258, 2015.

- [153 K. Williams, W. Chen, S. Weeger and T. Donohue, "Particle shape characterisation and its application to discrete element modelling," *Particuology*, vol. 12, pp. 80-89, 2014.
- [154 C. Krumbein and L. Sloss, *Stratigraphy and Sedimentation*, Second ed., San Francisco (California, USA): Freeman and Company, 1963.
- [155 S. Zhao, X. Zhou and W. Liu, "Discrete element simulations of direct shear tests with particle angularity effect," *Granular Matter*, vol. 17, pp. 793-806, 2015.
- [156 M. Sinnott and P. Cleary, "The effect of particle shape on mixing in a high shear mixer," *Computational Particle Mechanics*, vol. 3, pp. 477-504, 2016.
- [157 C. Coetzee, "Review: Calibration of the discrete element method," *Powder Technology*, vol. 310, pp. 104-142, 2017.
- [158 CFDEM®project, "LIGGGHTS® Open Source Discrete Element Method Particle Simulation Code," [Online]. Available: <https://www.cfdem.com/liggghtsr-open-source-discrete-element-method-particle-simulation-code>. [Accessed 17 October 2020].
- [159 CFDEM®project, "CFDEM® Coupling Open Source CFD-DEM Framework," [Online]. Available: <https://www.cfdem.com/cfdemrcoupling-open-source-cfd-dem-framework>. [Accessed 17 October 2020].
- [160 R. Mukherjee, S. Myint, J. Chang, I. Kim, J. Craft, M. Pomerantz, J. Kim and L. Peterson, "M3tk: A Robot Mobility and Manipulation Modeling Toolkit," in *ASME 2014 International Design Engineering Technical Conferences and Computers and Information in Engineering Conference*, Buffalo (New York, USA), 2014.
- [161 C. Kloss, C. Goniva, A. Hager and S. Amberger, "Models, algorithms and validation for opensource DEM and CFD-DEM," *Progress in Computational Fluid Dynamics An International Journal*, vol. 12, pp. 140-152, 2012.
- [162 K. Hanley and C. O'Sullivan, "Analytical study of the accuracy of discrete element simulations," *International Journal for Numerical Methods in Engineering*, vol. 55, pp. 947-971, 2016.
- [163 R. Hart, P. Cundall and J. Lemos, "Formulation of a three-dimensional distinct element model—Part II. Mechanical calculations for motion and interaction of a system composed of many polyhedral blocks," *International Journal of Rock Mechanics and Mining Sciences & Geomechanics Abstracts*, vol. 25, no. 3, pp. 177-125, 1988.
- [164 A. Jensen, K. Fraser and G. Laird, "Improving the Precision of Discrete Element Simulations through Calibration Models," in *13th International LS -*

*DYNA Users Conference*, Detroit (Michigan, USA), 2014.

- [165 X. Tu and J. Andrade, "Criteria for static equilibrium in particulate  
] mechanics computations," *International Journal for Numerical Methods in Engineering*, vol. 75, pp. 1581-1606, 2008.
- [166 J. Boac, K. Ambrose, M. Casada and R. Maghirang, "Applications of  
] Discrete Element Method in Modeling of Grain Postharvest Operations," *Food Engineering Reviews*, vol. 6, pp. 128-149, 2014.
- [167 Y. Li, Y. Xu and C. Thornton, "A comparison of discrete element  
] simulations and experiments for 'sandpiles' composed of spherical particles," *Powder Technology*, vol. 160, no. 3, pp. 219-228, 2005.
- [168 C. Thornton and C. Randall, "Applications of Theoretical Contact Mechanics  
] to Solid Particle System Simulation," *Studies in Applied Mechanics*, vol. 20, pp. 133-142, 1988.
- [169 C. Thornton, "Numerical simulations of deviatoric shear deformation of  
] granular media," *Géotechnique*, vol. 50, pp. 43-53, 2000.
- [170 M. Otsubo, C. O'Sullivan and T. Shire, "Empirical assessment of the critical  
] time increment in explicit particulate discrete element method simulations," *Computers and Geotechnics*, vol. 86, pp. 67-79, 2007.
- [171 K. Iwashita and M. Oda, "Rolling Resistance at Contacts in Simulation of  
] Shear Band Development by DEM," *Journal of Engineering Mechanics*, vol. 124, no. 3, 1998.
- [172 H. Nakashima, H. Fujii, A. Oida, M. Momozu, Y. Kawase, H. Kanamori, S.  
] Aoki and T. Yokoyama, "Parametric analysis of lugged wheel performance for a lunar microrover by means of DEM," *Journal of Terramechanics*, vol. 44, no. 2, pp. 153-162, 2007.
- [173 W. Li, Y. Huang, Y. Cui, S. Dong and J. Wang, "Trafficability analysis of  
] lunar mare terrain by means of the discrete element method for wheeled rover locomotion," *Journal of Terramechanics*, vol. 47, no. 3, pp. 161-172, 2010.
- [174 M. Obermayr, C. Vrettos and P. Eberhard, "A discrete element model for  
] cohesive," in *III International Conference on Particle-based Methods. Fundamentals and Applications - Particles 2013*, Stuttgart (Germany), 2013.
- [175 C. Ergenzinger, R. Seifried and P. Eberhard, "A discrete element model  
] predicting the strength of ballast stones," *Computers & Structures*, Vols. 108-109, pp. 3-13, 2012.
- [176 R. Lichtenheldt, "A novel systematic method to estimate the contact

- ] parameters of particles in discrete element simulations of soil," in *4th International Conference on Particle-based Methods - Particles 2015*, Barcelona (Spain), 2015.
- [177 R. Lichtenheldt and B. Schäfer, "Locomotion on Soft Granular Soils: A Discrete Element based Approach for Simulations in Planetary Exploration," in *12th Symposium on Advanced Space Technologies in Robotics and Automation*, Noordwijk (Netherlands), 2013.
- [178 R. Lichtenheldt, B. Schäfer and O. Krömer, "Hammering beneath the surface of Mars – Modeling and simulation of the impact-driven locomotion of the HP3-Mole by coupling enhanced multi-body dynamics and discrete element method," in *Shaping the future by engineering: 58th Ilmenau Scientific Colloquium IWK*, Ilmenau (Germany), 2014.
- [179 S. Derakhshani, D. Schott and G. Lodewijks, "Micro–macro properties of quartz sand: Experimental investigation and DEM simulation," *Powder Technology*, vol. 269, pp. 127-138, 2015.
- [180 M. Combarros Garcia, H. Feise, S. Strege and A. Kwade, "Segregation in heaps and silos: Comparison between experiment, simulation and continuum model," *Powder Technology*, vol. 293, pp. 26-36, 2016.
- [181 J. Schwarz and W. Weeks, "Engineering Properties of Sea Ice," *Journal of Glaciology*, vol. 19, no. 81, pp. 499-531, 1977.
- [182 E. Schulson and A. Fortt, "Friction of ice on ice," *Journal of Geophysical Research: Solid Earth*, vol. 117, no. B12, 2012.
- [183 Aerospace Specification Metals Inc., "Aluminum 6061-T6; 6061-T651," [Online]. Available: <http://asm.matweb.com/search/SpecificMaterial.asp?bassnum=MA6061T6>. [Accessed 19 October 2020].
- [184 Texas Advanced Computing Center, "TACC Home," [Online]. Available: <https://www.tacc.utexas.edu/>. [Accessed 21 October 2020].
- [185 Texas Advanced Computing Center, "Lonestar5 User Guide," [Online]. Available: <https://portal.tacc.utexas.edu/user-guides/lonestar5>. [Accessed 21 October 2020].
- [186 Texas Advanced Computing Center, "Lonestar5, second petascale system deployed at TACC," [Online]. Available: <https://www.tacc.utexas.edu/systems/lonestar>. [Accessed 21 October 2020].
- [187 W. Cirillo, K. Earle, K. Goodliff, J. Reeves, C. Stromgren, M. Andraschko and R. Merrill, "Strategic Analysis Overview," in *AIAA Space*, San Diego

(California, USA), 2008.

- [188 A. Olivieri and M. Graciela, Practical Three-Way Calibration, Elsevier, ] 2014.
- [189 D. Halliday, R. Resnick and J. Walker, Fundamentals of Physics Extended, ] 10th ed., Wiley, 2013.
- [190 MSE Supplies, "Yttrium stabilized zirconia beads," [Online]. Available: ] <https://www.msesupplies.com/collections/yttrium-stabilized-zirconia-beads>. [Accessed 26 October 2020].
- [191 MSE Supplies, "Alumina Milling Media," [Online]. Available: ] <https://www.msesupplies.com/collections/alumina-milling-media>. [Accessed 26 October 2020].
- [192 MSE Supplies, "Agate Milling Media," [Online]. Available: ] <https://www.msesupplies.com/collections/agate-milling-media>. [Accessed 26 October 2020].
- [193 MSE Supplies, "Tungsten Carbide Milling Media Balls," [Online]. ] Available: <https://www.msesupplies.com/collections/tungsten-carbide-milling-media-balls>. [Accessed 26 October 2020].
- [194 MSE Supplies, "Stainless Steel Milling Media," [Online]. Available: ] <https://www.msesupplies.com/collections/stainless-steel-milling-media>. [Accessed 26 October 2020].
- [195 Cospheric, "Cellulose Acetate Polymer Spheres," [Online]. Available: ] [https://www.cospheric.com/Cellulose\\_Acetate\\_polymer\\_Spheres\\_all\\_sizes\\_all\\_colors.htm](https://www.cospheric.com/Cellulose_Acetate_polymer_Spheres_all_sizes_all_colors.htm). [Accessed 26 October 2020].
- [196 Cospheric, "UV fluorescent microspheres beads powders," [Online]. ] Available: [https://www.cospheric.com/UV\\_fluorescent\\_microspheres\\_beads\\_powders.htm](https://www.cospheric.com/UV_fluorescent_microspheres_beads_powders.htm). [Accessed 26 October 2020].
- [197 Cospheric, "CPMS polymer clear microspheres," [Online]. Available: ] [https://www.cospheric.com/CPMS\\_polymer\\_clear\\_microspheres\\_density096.htm](https://www.cospheric.com/CPMS_polymer_clear_microspheres_density096.htm). [Accessed 26 October 2020].
- [198 Cospheric, "SLGMSc solid glass spheres beads," [Online]. Available: ] [https://www.cospheric.com/SLGMSc\\_solid\\_glass\\_spheres\\_beads\\_microns.htm](https://www.cospheric.com/SLGMSc_solid_glass_spheres_beads_microns.htm). [Accessed 26 October 2020].
- [199 Cospheric, "Solid Borosilicate Glass Polished Spheres," [Online]. Available: ] <https://www.cospheric.com/Solid-Borosilicate-Glass-Polished-Spheres-2-2g->

- cc-Precision-Grades-2mm-to-7mm.htm. [Accessed 26 October 2020].
- [200 Cospheric, "BSGMS solid glass spheres beads," [Online]. Available:  
] [https://www.cospheric.com/BSGMS\\_solid\\_glass\\_spheres\\_beads\\_microns.htm](https://www.cospheric.com/BSGMS_solid_glass_spheres_beads_microns.htm). [Accessed 26 October 2020].
- [201 Cospheric, "Solid Borosilicate Glass Polished Spheres Precision Grades,"  
] [Online]. Available: <https://www.cospheric.com/Solid-Borosilicate-Glass-Polished-Spheres-2-2g-cc-Precision-Grades-2mm-to-7mm.htm>. [Accessed 26 October 2020].
- [202 H. Yanagida, K. Koumoto and M. Miyayama, *The Chemistry of Ceramics*,  
] Wiley, 1996.
- [203 M. Shirooyeh A., "Mechanical properties of yttria-stabilized zirconia  
] ceramics," Doctor of Philosophy Dissertation, University of Southern California Libraries, Los Angeles (California, USA), 2011.
- [204 Superior Technical Ceramics, "Yttria Stabilized Zirconia (YTZP)," [Online].  
] Available: <https://www.ceramics.net/ceramic-materials-solutions/zirconias/ytzp>. [Accessed 27 October 2020].
- [205 W. Cochran, *Sampling Techniques*, 3rd ed., New York: Wiley, 1977.  
]
- [206 J. Bartlett, J. Kotrlik and C. Higgins, "Organizational Research: Determining  
] Appropriate Sample Size in Survey Research," *Information Technology, Learning, and Performance Journal*, vol. 19, no. 1, pp. 43-50, 2001.
- [207 R. Lenth, "Some Practical Guidelines for Effective Sample Size  
] Determination," *The American Statistician*, vol. 55, pp. 187-193, 2001.
- [208 V. Teffo and N. Naudé, "Determination of the coefficients of restitution,  
] static and rolling friction of Eskom-grade coal for discrete element modelling," *Journal of the South African Institute of Mining and Metallurgy*, vol. 113, no. 4, pp. 351-356, 2013.
- [209 Photron, "FASTCAM SA-Z," [Online]. Available:  
] <https://photron.com/fastcam-sa-z/>. [Accessed 29 October 2020].
- [210 C. Mangwandi, Y. Cheong, M. Adams, M. Hounslow and A. Salman, "The  
] coefficient of restitution of different representative types of granules," *Chemical Engineering Science*, vol. 62, no. 1-2, pp. 437-450, 2007.
- [211 N. Johnson, "Convex polyhedra with regular faces," *Canadian Journal of  
] Mathematics*, vol. 18, no. 1, pp. 169-200, 1966.
- [212 C. Moritz and R. Bruce, "An acoustical study of a large rotunda," *The*

- ] *Journal of the Acoustical Society of America*, vol. 92, 1992.
- [213 E. Lockwood, *Book of Curves*, Cambridge University Press, 1961.  
]
- [214 C. Cutler, "Parabolic-Antenna Design for Microwave," *Proceedings of the IRE*, vol. 35, no. 11, pp. 1284 - 1294, 1947.  
]
- [215 J. Stadler, C. Stanciu, C. Stupperich and A. Meixner, "Tighter focusing with a parabolic mirror," *Optics Letters*, vol. 33, no. 7, pp. 681-683, 2008.  
]
- [216 R. Little, "Acoustic Properties of Parabolic Reflectors," *The Journal of the Acoustical Society of America*, vol. 40, 1966.  
]
- [217 J. Liu, J. Tan, T. Wilson and C. Zhong, "Rigorous theory on elliptical mirror focusing for point scanning microscopy," *Optics Express*, vol. 20, no. 6, pp. 6175-6184, 2012.
- [218 AirZeroG, "How Parabolic Flights Work," [Online]. Available: <https://www.airzerog.com/zero-g-flights-how-it-works/>. [Accessed 18 December 2020].
- [219 National Aeronautics and Space Administration, "STMD: Flight Opportunities," [Online]. Available: <https://www.nasa.gov/directorates/spacetech/flightopportunities/index.html>. [Accessed 14 November 2020].
- [220 D. Riccobono, S. Moreland, P. Backes and G. Genta, "Modelling of Pneumatic Sample Transport Systems for Enceladus Surface Acquisition," in *11th IAA Symposium on the Future of Space Exploration: Moon, Mars and Beyond: Becoming an Interplanetary Civilization*, Torino, Italy, 2019.
- [221 K. Zacny, R. Lorenz, F. Rehnmark, T. Costa, J. Sparta, V. Sanigepalli, Z. Mank, B. Yen, D. Yu, J. Bailey, D. Bergman and W. Hovik, "Application of Pneumatics in Delivering Samples to Instruments on Planetary Missions," in *IEEE Aerospace Conference*, Big Sky (Montana, USA), 2019.
- [222 K. Zacny, B. Betts, M. Hedlund, P. Long, M. Gramlich, K. Tura, P. Chu, A. Jacob and A. Garcia, "PlanetVac: Pneumatic regolith sampling system," in *IEEE Aerospace Conference*, Big Sky, Montana (USA), 2014.
- [223 K. Zacny, L. Thomas, G. Paulsen, D. Van Dyne, S. Lam, H. Williams, D. Sabahi, P. Ng and Y. Satou, "Pneumatic Sampler (P-Sampler) for the Martian Moons eXploration (MMX) Mission," in *IEEE Aerospace Conference*, Big Sky, Montana (USA), 2020.
- [224 L. Lysenko, N. Mishchuk and E. Rynda, "Intensification of the electroosmotic flow of aqueous solutions in concentrated disperse systems,"

- Journal of Water Chemistry and Technology*, vol. 33, pp. 140-146, 2011.
- [225 R. Schnabel and D. Fitting, "Analysis of Chemical Kinetics Data from Dilute, Dispersed, Well-mixed Flow-through Systems," *Soil Science Society of America Journal*, vol. 52, no. 5, 1988.
- [226 V. Villari and N. Micali, "Light Scattering as Spectroscopic Tool for the Study of Disperse Systems Useful in Pharmaceutical Sciences," *Journal of Pharmaceutical Sciences*, vol. 97, no. 5, pp. 1703-1730, 2008.
- [227 A. Allahham, P. Stewart, J. Marriott and D. Mainwaring, "Flow and injection characteristics of pharmaceutical parenteral formulations using a micro-capillary rheometer," *International Journal of Pharmaceutics*, vol. 270, no. 1-2, pp. 139-148, 2004.
- [228 M. Corradini and M. Peleg, "Consistency of dispersed food systems and its evaluation by squeezing flow viscometry," *Journal of Texture Studies*, vol. 36, no. 5-6, 2005.
- [229 M. Aliev, R. Aliev, A. Aliev and O. Bolshakov, "A mathematical model for convective mass and heat transfer between flows of finely dispersed food media in adjacent channels with a permeable wall," *Journal of Food Engineering*, vol. 65, no. 3, pp. 341-348, 2004.
- [230 O. Smirnova, "Evaluation of superplasticizer effect in mineral disperse systems based on quarry dust," *International Journal of Civil Engineering and Technology*, vol. 9, no. 8, pp. 1733-1740, 2018.
- [231 P. Usachev, "Ferrohydrodynamics of disperse systems and new combined processes of mineral ore separation," *Soviet Mining*, vol. 17, pp. 570-580, 1981.
- [232 J. Kapilesh and J. Kapilesh, "Assaying coliform removal in waste stabilisation ponds system through the dispersed flow regime," *International Journal of Environmental Technology and Management*, vol. 21, no. 1-2, 2018.
- [233 A. Dhale and V. Mahajani, "Studies in treatment of disperse dye waste: membrane-wet oxidation process," *Waste Management*, vol. 20, no. 1, pp. 85-92.
- [234 M. Rhodes, *Introduction to Particle Technology*, Second ed., Wiley, 2008.
- [235 D. Punwani, M. Modi and P. Tarman, "A generalized correlation for estimating choking velocity in vertical solids transport," in *International Powder and Bulk Solids Handling and Processing Conference*, Chicago, Illinois (USA), 1976.

- [236 T. Knowlton, "Solids transfer in fluidized systems," in *Gas Fluidization Technology*, Wiley, 1986.
- [237 F. Rizk, "Pneumatic conveying of plastic coarse material in horizontal ducts, taking into consideration the influence of height in connection with the properties of the solid and the pipe materials, especially in the optimal operating zone," Dissertation, University of Karlsruhe, 1976.
- [238 O. Molerus, *Principles of flow in disperse systems*, London: Chapman & Hall, 1993.
- [239 O. Molerus, "Appropriately defined dimensionless groups for the description of flow phenomena in disperse systems," *Chemical Engineering Science*, vol. 53, no. 4, pp. 753-759, 1998.
- [240 R. Wilhelm and M. Kwauk, "Fluidization of Solid Particles," *Chemical Engineering Progress*, vol. 44, no. 201, 1948.
- [241 L. Reh, "Verbrennung in der Wirbelschicht," *Chemie Ingenieur Technik*, vol. 40, no. 11, pp. 509-515, 1968.
- [242 The Engineering ToolBox, "Nitrogen - Thermophysical Properties," [Online]. Available: [https://www.engineeringtoolbox.com/nitrogen-d\\_1421.html](https://www.engineeringtoolbox.com/nitrogen-d_1421.html). [Accessed 19 December 2020].
- [243 Servotecnica, "What is a rotary union," [Online]. Available: <https://www.servotecnica.com/en/resources/news-mobile-en/what-is-a-rotary-union/>. [Accessed 1 December 2020].
- [244 J. Anderson, *Modern Compressible Flow: With Historical Perspective*, McGraw-Hill, 2003.
- [245 Zhang-Yu Nie and Hui Zeng, "P-T phase diagram of a holographic s+p model from Gauss-Bonnet gravity," *Journal of High Energy Physics*, vol. 47, 2015.
- [246 Y. Zheng and Q. Liu, "Review of techniques for the mass flow rate measurement of pneumatically conveyed solids," *Measurement*, vol. 44, no. 4, pp. 589-604, 2011.
- [247 NASA Jet Propulsion Laboratory, "OWLS Project," [Online]. Available: <https://microdevices.jpl.nasa.gov/capabilities/in-situ-instruments-chemical-analysis/owls-project/>. [Accessed 9 December 2020].
- [248 NASA Jet Propulsion Laboratory, "Ocean Worlds Life Surveyor (OWLS)," [Online]. Available: <https://ml.jpl.nasa.gov/projects/owls/owls.html>. [Accessed 9 December 2020].

